



TU WIEN

PHD THESIS

Modeling the fluid-structure interaction of micro-plate-resonators in viscous fluids

Author:

Andre Loch Gesing, M.Sc.
Matr.Nr.: 11838922

Supervisor:

Prof. Dr. Ulrich Schmid

submitted in fulfillment of the requirements for the degree

Doctor in technical sciences (Ph.D.)

in the

Faculty of Electrical Engineering and Information Technology, TU Wien

Vienna, December 2023

Defense: Vienna, 20/12/2023

Supervisor: Univ. Prof. Dr.rer.nat. Ulrich Schmid
TU Wien, Österreich

Reviewer: Univ. Prof. Dr. Gabriele Schrag
Technische Universität München, Deutschland

Reviewer: Univ. Prof. Dr. Manfred Kaltenbacher
Technische Universität Graz, Österreich

Copyright © 2023 by A. L. Gesing, Vienna, Austria. All rights reserved. No parts of this thesis may be reproduced, stored in a retrieval system or transmitted in any form or by any means without permission of the author. This document is freely available at [repositUM](https://repositum.tu-wien.ac.at/).

Affidavit

I declare in lieu of oath, that I wrote this thesis and performed the associated research myself, using only literature cited in this volume. If text passages from sources are used literally, they are marked as such. I confirm that this work is original and has not been submitted elsewhere for any examination, nor is it currently under consideration for a thesis elsewhere. I confirm, that going to press of this thesis needs the confirmation of the examination committee.

I acknowledge that the submitted work will be checked electronically-technically using suitable and state-of-the-art means (plagiarism detection software). On the one hand, this ensures that the submitted work was prepared according to the high-quality standards within the applicable rules to ensure good scientific practice “Code of Conduct” at the TU Wien. On the other hand, a comparison with other student theses avoids violations of my personal copyright.

Vienna, December 2023

Andre Loch Gesing

Acknowledgments

I thank my doctoral supervisor Prof. Ulrich Schmid and the postdoctoral researcher Daniel Platz. When I met them in August 2018, I felt very welcomed at the Institute of Sensors and Actuator Systems at TU Wien, and the decision to join TU Wien was largely based on the impression I had of both in this first encounter. Joining ISAS proved to be the right decision and their support remained a constant throughout our research collaboration. I also gratefully acknowledge the funding by the Innovative Projects program at TU Wien, and the team at the Vienna Scientific Cluster (VSC) for the support.

I would like to thank the colleagues who received me with open arms when I first arrived in Austria: Jonas, Hendrik, Fabian, Ali, Florian, Franz, Pedram and Paul. And of course, the colleagues with whom we built the best office in ISAS, Ioan, MinHee and Rauf. Special thanks go to Yijie, who was not in our office, but is an honorary office member. I also thank the students who trusted me to co-advise them in their bachelor's and master's theses: Marco Stixenberger, Thomas Tran, David Demattio and Erwin Gietl.

Above all, I want to thank my family for the support all the way from Brazil and my wife, Camilla. Thanks to Camilla's encouragement I was able to pursue a PhD abroad, and only with Camilla by my side was I able to conclude the research. My apartment in Austria only became a home after Camilla moved here with me, and I can not thank her enough for all her support through the years. Last, I want to thank my cats (Frida, Zara, Juvi and Nori) who are just too cute and can cure any bad day.

Abstract

Cantilevered thin structures are among the most common building block of micro-resonators. In fluidic environments, the surrounding fluid dissipates energy from the micro-resonator. The underlying viscous fluid-structure interaction is well understood for slender resonator geometries. However, for non-slender resonator geometries determining fluid losses remains challenging with both analytical and numerical approaches. Here, we present a semi-numerical method for determining the steady-state dynamics of wide micro-plate resonators in viscous fluids. The method is based on the Kirchhoff plate equation to solve for the plate's dynamics, while the hydrodynamic force acting on the plate is determined from the Stokes equations with a boundary integral formulation. The boundary integral formulation avoids discretizing the entire fluid domain and thus avoids multi-scale issues. Two fluid flow formulations are introduced here, the first in which a two-dimensional fluid flow is assumed, and the second formulation allows for a three-dimensional fluid flow. The equation of motion is solved with the finite element method. In numerical examples, the method is convergent with an exponent of the convergence rate equal to 2. We determine quality factors of micro-plates in liquids and observe excellent agreement with experimental data. Since the proposed method goes beyond existing semi-analytical methods by accounting for two-dimensional vibrational modes, novel unseen effects are investigated. For instance, in gases, the Euler-Bernoulli (EB) modes (modes with nodal lines only along the plate's width) exhibit the lowest Q-factors, while non-EB modes exhibit the highest Q-factors. The opposite is found in liquids, as EB modes show the highest Q-factors, and non-EB modes lower Q-factors. We name this opposite Q-factor pattern in gases and liquids the gas-liquid-Q-inversion (GL-Q-inversion). Experiments in water and air showed a Q-factor agreement with the GL-Q-inversion, and differences in Q-factor between simulation and experiments were below 25%. Differences in the resonance frequency are high for the EB modes in water due to the two-dimensional fluid flow approximation. The second method is proposed, in which a three-dimensional fluid flow is investigated using the unsteady Stokeslet. Results with the 3D fluid flow method exhibit even better agreement between simulation and experiments. The results and methods shown here will pave the way to efficiently exploit the two-dimensional vibrational modes of non-slender resonators to improve MEMS performance in gaseous and liquid environments.

Contents

1	Introduction	1
1.1	MEMS resonators	1
1.2	MEMS resonators in fluids	4
1.3	Modeling the dynamics of micro-beams and micro-plates in fluids	6
1.4	Objective	11
1.5	Thesis outline	12
I	A semi-numerical method for micro-plates in viscous fluids with a two-dimensional fluid flow formulation	15
2	Mathematical formulation	17
2.1	Elastic body dynamics	17
2.2	Fluid flow dynamics	21
2.2.1	Rarefaction	21
2.2.2	Compressibility	22
2.2.3	Inertial and viscous forces	26
2.3	Mathematical formulation of a micro-plate in a viscous fluid	29
2.4	Conclusions	33
3	Numerical methods for the plate equation	35
3.1	Isotropic and anisotropic material models	35
3.2	Boundary conditions	36
3.3	Finite element method for the plate equation	37
3.3.1	Interior Penalty Method	42
3.3.2	Lifting operator	42
3.4	Numerical results	43
3.4.1	Static simply supported square plate	43
3.4.2	Cantilevered plate with a sinusoidal force	46
3.4.3	Generalized eigenvalue problem	49
3.5	Conclusions	51
4	Hydrodynamic forces on a micro-plate	53
4.1	Boundary integral equation method	53
4.2	Hydrodynamic force due to different vibrational modes	57
4.3	Integration of the hydrodynamic force	59
4.3.1	Numerical integration in y -direction	61
4.3.2	Numerical integration in x -direction	64

4.3.3	Convergence of the two-dimensional integration	65
4.4	Conclusions	66
5	A semi-numerical method for micro-plates in viscous fluids	69
5.1	Convergence	70
5.1.1	Convergence with the FE-mesh	71
5.1.2	Convergence with the fluid grid	71
5.2	Validation with semi-analytic methods	72
5.2.1	Spectral displacement	73
5.2.2	Quality factor	74
5.2.3	Added-mass effect	77
5.3	Validation with purely numerical results	78
5.4	Validation with experimental results	79
5.5	Conclusions	81
II	Numerical and experimental results	83
6	Viscous losses in the beam-plate transition	85
6.1	Air	85
6.1.1	Displacement spectrum	85
6.1.2	Q-factor	88
6.2	Water	89
6.2.1	Displacement spectrum	89
6.2.2	Q-factor	89
6.3	Added-mass effect and the damping coefficient	91
6.4	Fluid flow, kinetic energy and viscous dissipation	95
6.5	Oscillatory Reynolds number	100
6.6	Conclusions	102
7	Gas-Liquid modal Q-factor inversion	105
7.1	Galerkin mode decomposition (GMD)	105
7.2	Convergence and validation	107
7.3	Q-factor in gases	109
7.4	Q-factor in liquids	111
7.5	Physical mechanism underlying the Gas-Liquid modal Q-factor-inversion	113
7.6	Conclusions	120
8	Experimental analysis	123
8.1	Fabrication of silicon MEMS resonators	123
8.2	Experiments in water	124

8.3	Experiments in air	127
8.4	Minimizing the influence of acoustic losses	130
8.5	Conclusions	132

III Beyond two-dimensional 133

9 Hydrodynamic force on a micro-plate due to a three-dimensional fluid flow 135

9.1	The unsteady Stokeslet	135
9.2	The boundary integral equation	136
9.3	Integration of the Stokeslet	141
9.4	Hydrodynamic force due to different vibrational modes	142
9.5	Conclusions	145

10 A semi-numerical method for micro-plates in viscous fluids considering a three-dimensional fluid flow 149

10.1	Numerical integration of the hydrodynamic force	149
10.2	Convergence	151
10.2.1	Convergence with the FE-mesh	151
10.2.2	Convergence with the fluid grid	152
10.3	Validation	153
10.3.1	Spectral displacement	154
10.3.2	Q-factor and damped resonance frequency	154
10.4	Conclusions	156

11 On the limits between two-dimensional and three-dimensional fluid flow 159

11.1	Spectral displacement and damped resonance frequency in water	159
11.2	Three-dimensional fluid flow in water	162
11.3	Q-factor in the beam-plate transition in water	163
11.4	Q-factor in the beam-plate transition in air	168
11.5	Comparison to experiments	169
11.6	Conclusions	172

IV Conclusions and outlook 173

12 Conclusions and outlook 175

12.1	Conclusions	175
12.2	Outlook	176

Appendices 178

A Fluid properties	181
B Convergence of the Q-factor and damped resonance frequency	183
B.1 Convergence of the Q-factor shown in the validation	183
B.2 Convergence of the Q-factor in the beam-plate transition in air	184
B.3 Convergence of the Q-factor in the beam-plate transition in water	187
C Influence of the Stokeslet numerical integration	191
D Convergence in the 3D method	193
D.1 Convergence of the Q-factor in the beam-plate transition in air	193
D.2 Convergence of the Q-factor in the beam-plate transition in water	196
D.3 Experimental results	198
List of Figures	207
List of Tables	209
List of symbols	211
List of acronyms	219

Die approbierte gedruckte Originalversion dieser Dissertation ist an der TU Wien Bibliothek verfügbar.
The approved original version of this doctoral thesis is available in print at TU Wien Bibliothek.

Chapter Contents

1.1	MEMS resonators	1
1.2	MEMS resonators in fluids	4
1.3	Modeling the dynamics of micro-beams and micro-plates in fluids	6
1.4	Objective	11
1.5	Thesis outline	12

1.1 MEMS resonators

Microelectromechanical systems (MEMS) are micrometer-scale devices that feature as basic elements electrical and mechanical sensitive transducers integrated into individual components. Silicon MEMS are fabricated using well-established integrated circuits (IC) and other batch processing techniques, e.g., physical and chemical vapor deposition, lithography as well as dry and wet etching. The batch fabrication process incurs the potential for mass production at low cost and ease of integration with complex integrated circuits at the chip level. Further advantages of silicon MEMS over macro-devices include low power consumption, reliability, and, of course, small dimensions [1, 2, 3].

MEMS connect the physical world with the digital domain by converting the motion of a micro-structure to electrical signals [4]. Most MEMS sense or actuate their environment through the use of the dynamic response of a micro-structure, rather than its static response, because dynamic MEMS transducers usually outperform static MEMS transducers in responsivity, sensitivity, and accuracy [3]. In the cases of MEMS operating at the elastic structure's resonance frequencies, the devices are called MEMS resonators, or resonant MEMS [5]. Resonant MEMS cover a wide range of applications such as atomic force microscopy (AFM) [6, 7, 8], energy harvesting [9], bio-mimetic robotic propulsion [10, 11, 12], viscosity sensors [13, 14, 15], micro-pumps [16], gas composition sensors [17, 18] and micro-fanning [19].

While resonant MEMS span a wide range in geometric layout, materials, circuits and packaging, they all employ three main principles based on the structure's dynamic response. They are: resonant amplification, resonance frequency shifting and Q-factor alteration [2, 5].

To introduce these three principles, we approximate the dynamic response of an elastic structure with the damped harmonic oscillator (DHO) [20] equation, yielding

$$\hat{w} = \frac{\hat{F}/m}{f^2 - f_0^2 + j f f_0/Q}, \quad (1.1)$$

where \hat{w} is the structure's spectral displacement, \hat{F} is the applied force, m is the structure's mass, f is frequency, f_0 is the structure's resonance frequency, j is the imaginary unit and Q is the quality factor. Resonant amplification is the increase in the amplitude of the spectral displacement \hat{w} per applied force \hat{F} when the structure is excited at the resonance frequency f_0 . The resonant amplification is shown in the spectral displacement shown in Fig. 1.1a for a Q-factor equals 100 which results in resonance amplification of 100 at $f = f_0$. One example of a resonant amplification device is AFM, where a laser beam is reflected on the surface of a slender cantilever vibrating at f_0 . From the measurement of the reflected light, the tip-surface force is reconstructed which allows determining the sample's surface [7, 21, 22].

Resonance shifting is the alteration of the structure's resonance frequency f_0 by an amount Δf_0 as exemplified in Fig. 1.1b. This effect is used to measure, for example, particle suspension in a fluid [23, 15] and fluid's density variation [17, 18], among other applications. Q-factor variation refers to the change in the spectral response \hat{w} without (or with small) variation in f_0 as shown in Fig. 1.1. Different quantities, such as a fluid's viscosity for instance, can be determined by MEMS resonators by quantifying the Q-factor alteration of the structure's spectral response around f_0 [24, 25].

For most MEMS resonators, a high Q-factor is desired. A higher Q-factor leads to an enhanced resonant amplification, thus yielding a higher signal-to-noise ratio [26]. A higher Q-factor also means a sharper resonance peak in the frequency spectrum, crucial for measurements based on the resonance frequency shift such as in chemical [27] or particle sensing [15]. Furthermore, a higher Q-factor is desirable for methods based on the Q-factor variation.

The Q-factor is the ratio of the maximum energy stored in the MEMS resonator E_{st} and the energy dissipated in one cycle of oscillation E_d [28] as

$$Q = 2\pi \frac{E_{st}}{E_d}. \quad (1.2)$$

Different dissipation mechanisms contribute to E_d and therefore limit the Q-factor of MEMS resonators. Dissipation mechanisms are categorized as intrinsic and extrinsic. The intrinsic dissipated energy encompasses surface losses $E_{d,surface}$, material losses

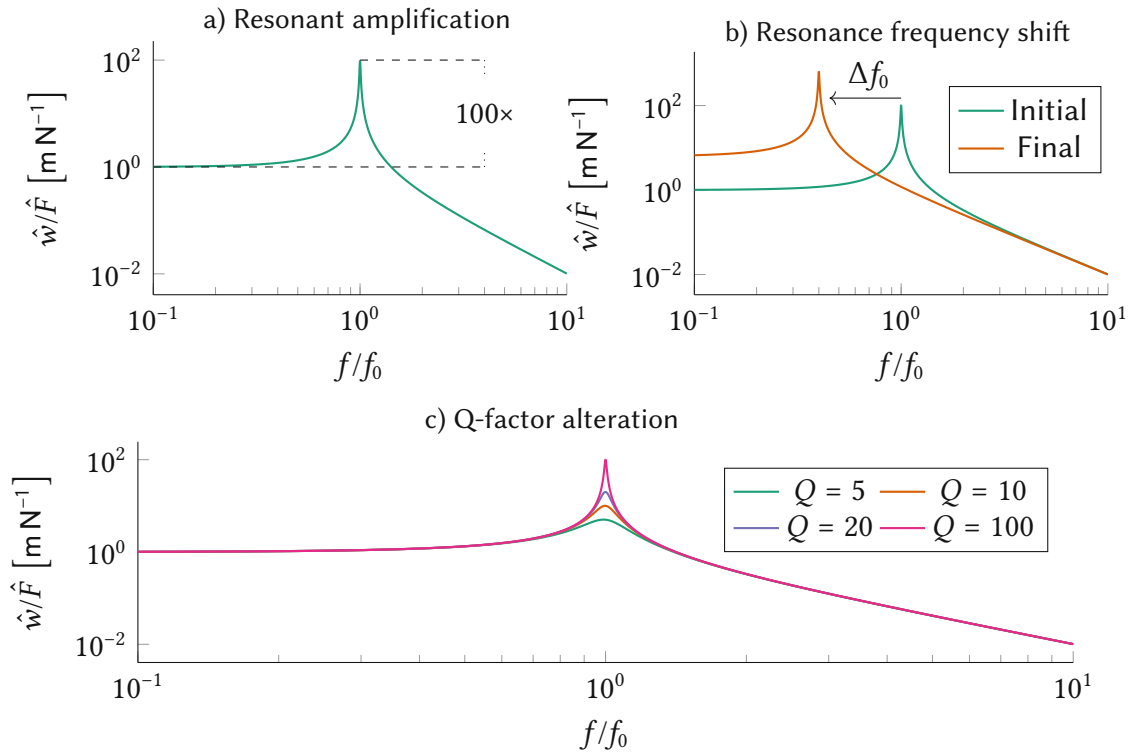


Figure 1.1: Different effects explored in MEMS resonators as a) resonant amplification, b) resonance frequency shift and c) Q-factor alteration shown in the spectral displacement \hat{w} as a function of the normalized frequency f/f_0 .

$E_{d,\text{material}}$, anchor losses $E_{d,\text{anchor}}$ and thermoelastic dissipation (TED) $E_{d,\text{TED}}$ [26, 28]. Anchor losses refer to the energy loss of the vibrating structure to the substrate through the anchoring region as shown in Fig. 1.2a. Thermoelastic dissipation is the energy loss resulting from the heat flux between compressive-stressed and tensile-stressed regions of the structure [29] as depicted in Fig. 1.2b.

Extrinsic dissipation mechanisms include all losses which occur outside the MEMS resonator. MEMS resonators are commonly immersed in a fluid (either gas or liquid). As the elastic structure of the MEMS resonator moves through the fluid, a fluid flow is induced as shown schematically in Fig. 1.2c. The fluid dissipates energy through viscous and acoustic losses [5, 30], quantified by $E_{d,\text{viscous}}$ and $E_{d,\text{acoustic}}$, respectively. The dissipated energy is the result of the summation of all different energy losses, which yields

$$Q = 2\pi \frac{E_{st}}{E_{d,\text{surface}} + E_{d,\text{material}} + E_{d,\text{anchor}} + E_{d,\text{TED}} + E_{d,\text{viscous}} + E_{d,\text{acoustic}}}. \quad (1.3)$$

While specific MEMS applications require low-pressure environments due to the absence of fluidic viscous and acoustic losses, a significant number of applications necessarily occur in liquids or gases at ambient conditions. At the dimensions regime of

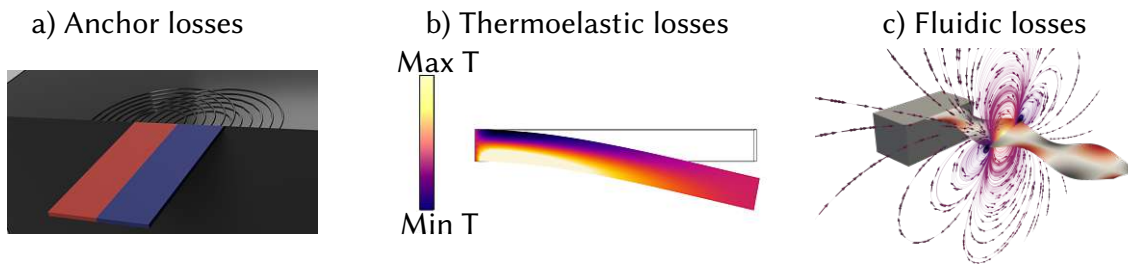


Figure 1.2: Common forms of energy dissipation in MEMS resonators include a) anchor losses, b) thermoelastic losses and c) fluidic losses. In a), a beam exhibits displacement in opposite directions in blue and red, and the beam's displacement generates elastic waves into the substrate (in dark gray), which dissipate energy from the beam to the substrate as anchor losses. In b), the beam's displacement generates regions of higher temperature T and regions of lower temperature and the heat between these regions acts as a dissipation mechanism. In c), a beam is represented with a torsional mode and the fluid flow is represented around a cross-section of the beam. Maximum velocity is represented by yellow and minimum by dark blue.

the elastic structures of MEMS resonators, which range from a couple of micrometers wide to hundreds of micrometers, when the resonators are immersed in a liquid, the viscous fluidic losses dominate over intrinsic loss mechanisms, e.g., surface, material, anchor, and thermoelastic losses, and the Q-factor of the MEMS resonator is defined mainly through the fluidic viscous losses. In gases at ambient conditions, viscous fluidic losses are expected of the same magnitude as other dissipation mechanisms [31, 32, 33]. Therefore, for MEMS resonator's applications in fluids, determining the fluidic viscous losses and strategies to minimize such losses are essential.

1.2 MEMS resonators in fluids

Different elastic structures were investigated to develop high Q-factor MEMS resonators in fluids [4, 34]. These micro-structures are typically based on thin structures, e.g., beams, plates, membranes, and strings. Beams are slender, thin structures and are the most commonly used. When beams are clamped at one end and free at all others, they are called cantilevered beams or cantilevers. Because of the cantilever's geometric features, their vibrational modes are restricted to effectively one-dimensional modes, e.g., transverse, torsional, lateral and extensional. Transverse and torsional are out-of-plane modes, whereas lateral and extensional are in-plane modes. The out-of-plane modes are characterized by the beam's displacement predominantly in the normal direction to its larger surface (z -direction) as illustrated in Fig. 1.3a and 1.3b. The transverse mode has a displacement $w(x)$, which is constant along the beam's width (y -direction), while torsional modes are described by their torsion angle $\theta(x)$ around the x -axis. Lateral

in-plane bending exhibits displacement $v(x)$ in y -direction primarily, while extensional in-plane modes exhibit predominantly velocity $u(x)$ in x -direction.

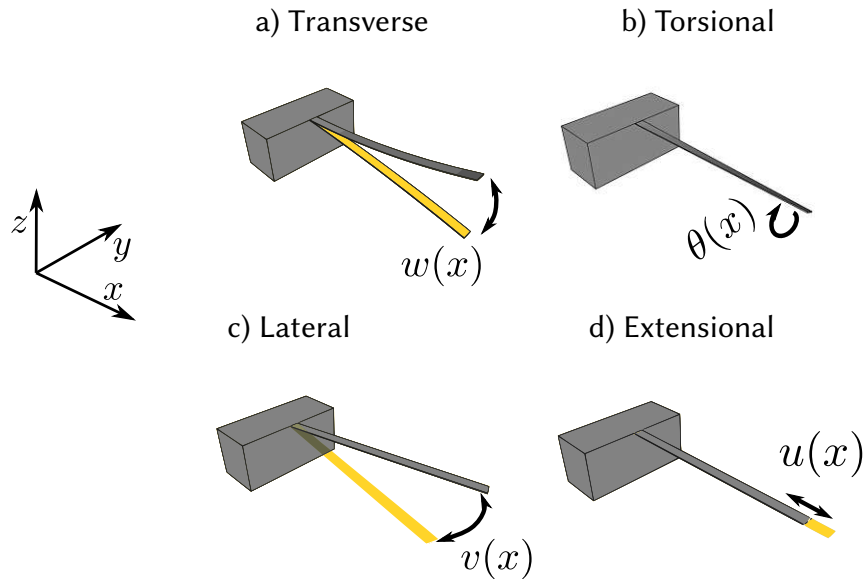


Figure 1.3: One-dimensional vibrational modes of beams are the a) transverse, b) torsional, c) lateral or d) extensional modes.

The transverse modes of cantilevers are widely used in gas environments where the viscous dissipation is small and the Q -factors are high. However, in liquids, transverse modes of cantilevers show a remarkably low Q -factor. For instance, in water, transverse modes exhibit Q -factors ranging from 1 to 10 in the first vibrational modes and below 50 for higher-order modes [35, 19, 36, 37], as shown in Fig. 1.4. Torsional and lateral modes exhibit similar Q -factors to the transverse modes at a similar frequency range, as seen in Fig. 1.4. Extensional modes are the highest Q -factor modes of slender beams. However, their resonance frequencies are much higher than the other modes. A further limitation intrinsic to all the beam-based resonators is the small surface area of beams, which limits the output signal height and the interaction surface, thus preventing applications such as chemical and particle sensing. From data in Fig. 1.4, it is evident that achieving high Q -factors (in order of hundreds) in liquids is cumbersome when using slender, thin beams.

One alternative to slender beams for MEMS resonators in fluids is non-slender geometries, whose most simple example is micro-plates. Micro-plates are thin planar structures that, different than beams, are not required to have small width. As a result, the transverse vibrational modes of a micro-plate are not effectively one-dimensional but rather two-dimensional. For instance, Fig. 1.5 shows fifteen transverse modes of a cantilevered square plate. The vibrational modes are shown using Leissa's notation [43],

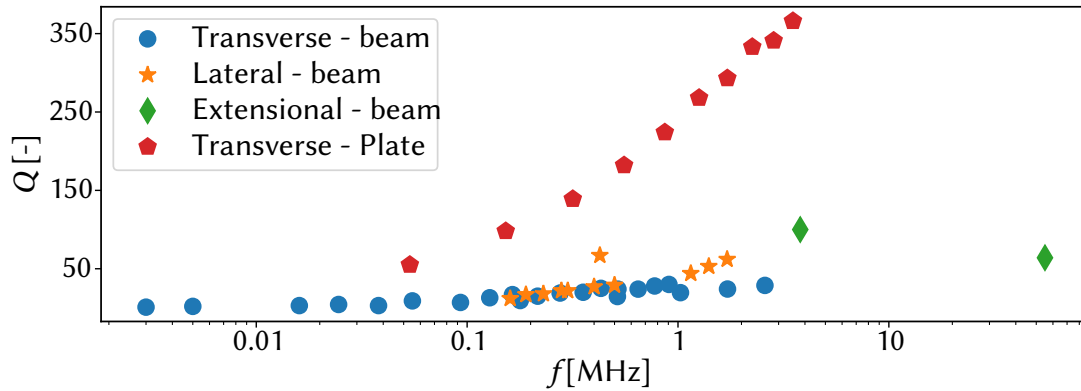


Figure 1.4: Experimental Q-factor of beams and plates in water. Beam data: transverse modes from [35, 36], lateral modes from [27, 38, 39] and extensional modes from [40]. Plate data: transverse modes from [41, 42].

which categorizes the vibrational modes according to their nodal lines as $n_x : n_y$. n_x is the number of nodal lines perpendicular to the plate's length, and n_y is the nodal lines perpendicular to its length as depicted in Fig. 1.5. Note that the transverse vibrational modes of plates encompass Euler-Bernoulli (EB) modes which are $n_x : 0$ modes, as well as torsional modes, which are $n_x : 1$. Vibrational modes with two or more nodal lines parallel to the plate's length ($n_y \geq 2$) and only one nodal line parallel to the plate's width ($n_x = 1$), are the roof tile-shaped (RTS) modes. Other plate modes, with $n_y \geq 2$ and $n_x \geq 2$, we name higher-order plate (HOP) modes.

Recently it has been discovered experimentally that the transverse modes of wide micro-plates exhibit very high Q-factors in liquids [41, 42, 24, 30]. Experimentally, a Q-factor of 360 was obtained in water at three MHz as shown in Fig. 1.4. Due to the complexity of the experimental analysis, the experiments with wide micro-plates focused on the roof tile-shaped modes. Despite the experimental findings of the high Q-factor of roof tile-shaped modes, the application of micro-plates in liquids has been so far limited to only a few studies [41, 15, 30, 24]. One reason for the yet limited use of micro-plates for liquid applications is the lack of methods for efficiently predicting micro-plates' dynamics in viscous fluids.

1.3 Modeling the dynamics of micro-beams and micro-plates in fluids

For modeling the dynamic of slender micro-beams in viscous fluids, numerous semi-analytic methods exist and are summarized in Table 1.1. Semi-analytic methods are here

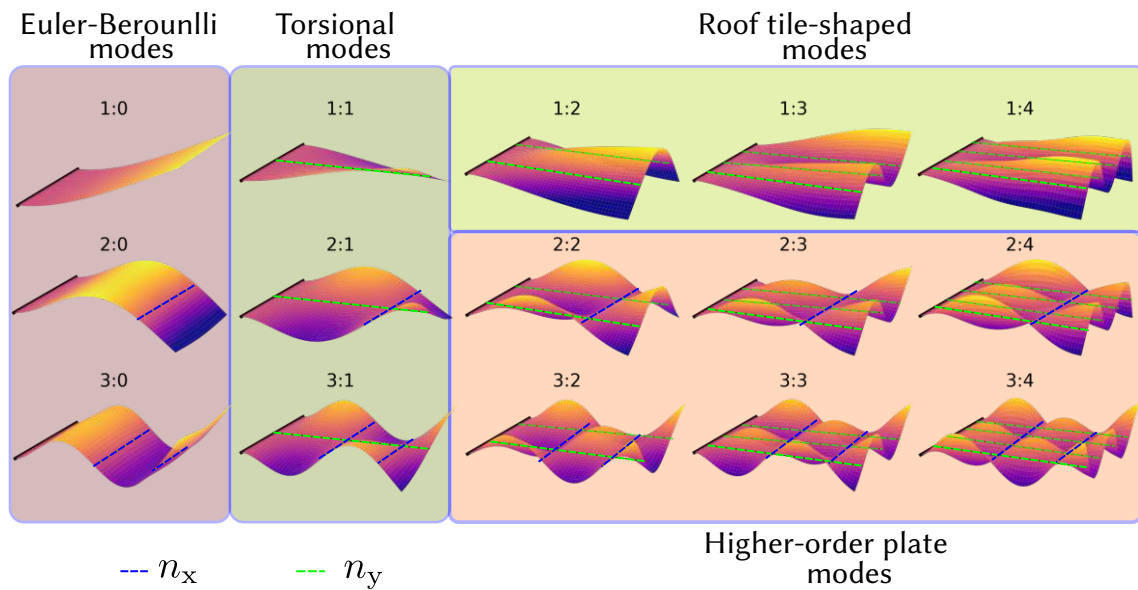


Figure 1.5: Fifteen vibrational modes of a cantilevered square plate identified using Leissa's notation. The black solid line represents the nodal line at the clamped region. Blue dashed lines are the nodal lines perpendicular to the plate's length, and green dashed lines are parallel to the plate's width.

defined as methods in which the vibrational mode of the elastic structure is obtained analytically (usually in vacuum). In contrast, a numerical method is applied to determine the force acting on the structure due to the fluid flow. This fluid force acting on the structure in the context of MEMS-fluid interaction is usually named the hydrodynamic force [31, 44, 32]. One of the first semi-analytic methods used to determine beam-fluid dynamics accounted for solely the inertial forces (IF) in the fluid (inviscid fluid model), which reduces the resonance frequency of an immersed cantilever due to the added-mass effect [45, 46]. Due to the inviscid assumption, Chu's model can only predict the beam's resonance frequencies f_0 of the beam in fluids, not the Q-factor.

Sader [31] proposed a landmark semi-analytic method to determine the dynamics of a slender micro-beam vibrating in transverse modes in a viscous fluid. The hydrodynamic force, composed of inertial forces and viscous forces (VF), on the beam, is calculated by introducing a correction to the hydrodynamic force on a circular cylinder. The fluid velocity along the beam's length is considered negligible, allowing for a two-dimensional (2D) formulation of the fluid flow as illustrated in Fig. 1.6. Subsequent semi-analytic methods (which also used the EB vibrational modes) incorporated more aspects in the scope of the micro-beam fluid interaction problem for the two-dimensional fluid flow formulation. For instance, semi-analytic methods were proposed for determining the dynamics of a beam near rigid or elastic surfaces [48, 49, 50], or even for determining the dynamics of arrays of cantilevers in the fluid [51, 52, 53].

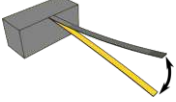

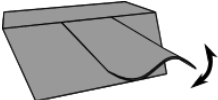
Geometry and mode	Semi-analytic methods	
	2D	3D
Beam - Transverse 	Inertial forces (IF) + Viscous Forces (VF) [31] IF + VF + nearby surfaces[48, 49, 50] IF + VF + array of beams[51, 52, 53]	Inertial forces (IF)[45, 46] IF + VF [47, 44] IF + VF + compressibility [54]
Beam - Torsional 	IF + VF[33, 55] IF + VF + nearby surface[32] IF + VF + Nearby wall [48, 56, 57]	IF + VF [47] IF + VF + compressibility [54]
Beam - Extensional	IF + VF [38, 27]	
Beam - Lateral	IF + VF [38, 27, 58, 59]	
Plate - Transverse 	IF + VF + Infinitely wide plate [60, 61]	

Table 1.1: Summary of existing semi-analytic methods for micro-beams and micro-plates in fluids. IF stands for inertial forces, and VF for viscous forces. 2D and 3D stand for two-dimensional and three-dimensional fluid flow formulation, respectively.

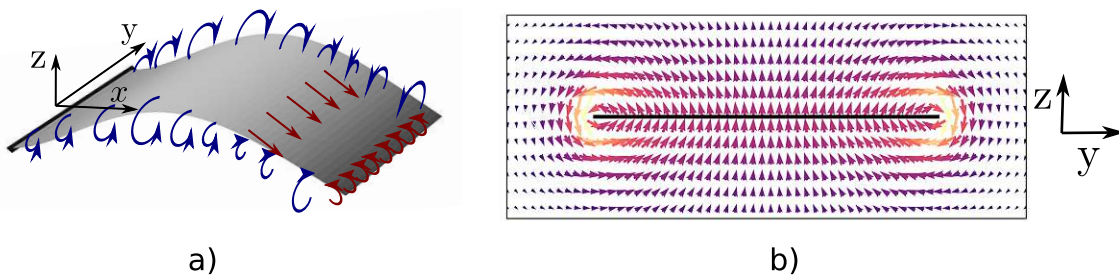


Figure 1.6: a) Illustration of the fluid flow around a plate. Blue arrows represent regions with higher fluid velocities. Red arrows represent where the fluid flow can have higher axial velocity. b) Fluid flow around a cross-section of a beam that vibrates in a flexural mode. Bright yellow is the maximum velocity, and purple is the minimum.

A more recently proposed semi-analytic method for transverse modes of cantilevers considered the three-dimensional (3D) nature of the fluid flow for incompressible [47] and compressible flow [54]. The extent of validity of the two-dimensional fluid flow approximation was the target of several studies, which use purely numerical methods to investigate the beam-fluid interaction problem [62, 35, 63, 19]. By purely numerical methods, here we define the methods in which the fluid and elastic domains are both discretized, which leads to large computational costs. Comparison between purely numerical and semi-analytic methods show that the 2D flow formulation accurately predicts the hydrodynamic force on the plate everywhere except near the cantilever's

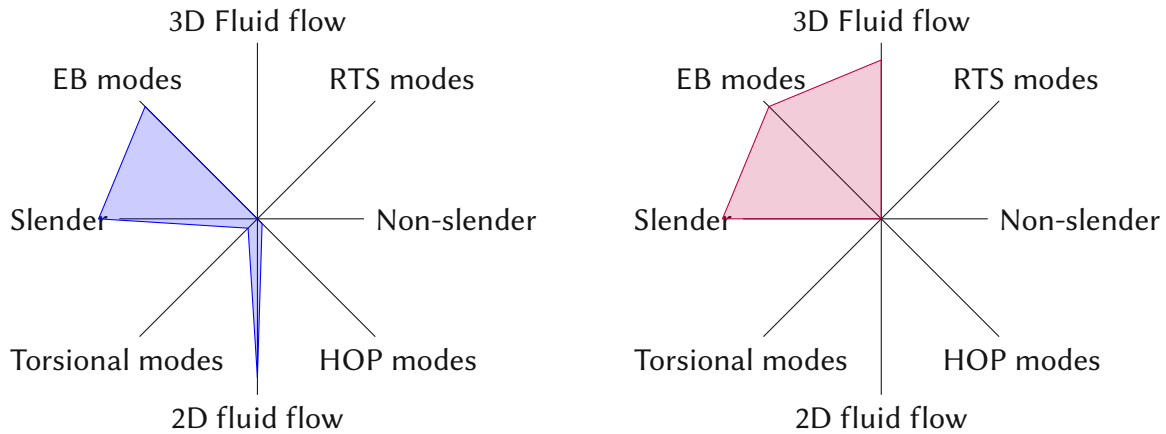
free edge [64]. The two-dimensional fluid model overestimates the hydrodynamic force near the cantilever's free edge. Consequently, 2D fluid flow approximation is expected to underestimate both the beam's resonance frequency and the Q-factor compared to purely numerical predictions. These differences were smaller than 5% up to the third transverse mode and increased to 20% in the sixth transverse mode [35].

For torsional modes also, there are semi-analytic modes that consider inertial and viscous forces in 2D [33, 55] and 3D [47] fluid flow formulations, as well as the effect of nearby surfaces [32] and compressibility effects [54] as summarized in Table 1.1. Recently semi-analytic methods focusing on the viscous forces were also proposed for extensional modes [38, 27] and lateral modes [38, 27, 58, 59].

For non-slender geometries in viscous fluids, existing semi-analytic methods are applicable only for infinitely wide plates, which limits the vibrational modes to transverse modes similar to those present in Euler-Bernoulli beams [60]. The limits of the semi-analytic methods are more clearly made visible through the radar plots in Fig. 1.7, which summarizes the semi-analytic methods for the transverse modes of micro-beams and micro-plates in terms of the fluid flow approximation (2D or 3D formulations); the structure is categorized in beams (slender structures) or plates (wide structures); and the vibrational modes are divided in EB, torsional, RTS and HOP. Note that the RTS and HOP modes are not predicted by any semi-analytic method.

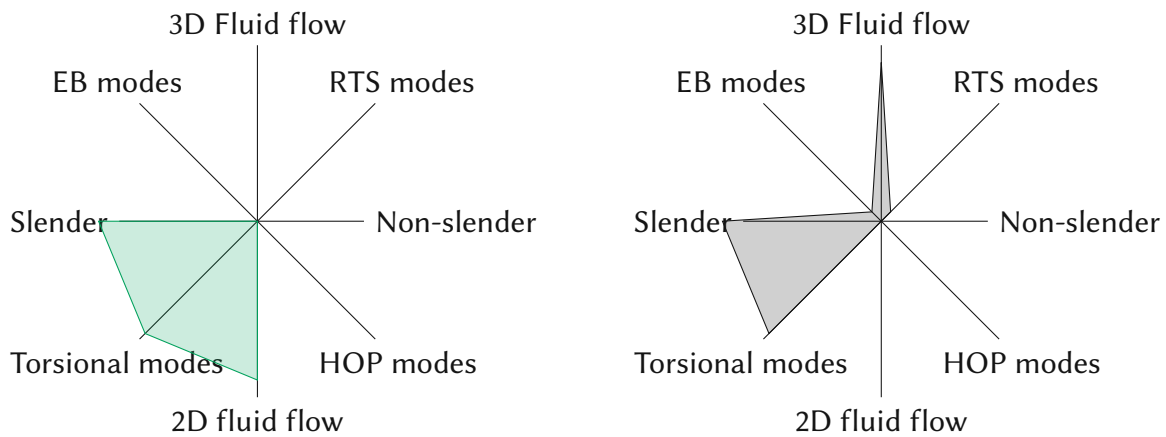
The lack of semi-analytic methods for non-slender MEMS resonators in viscous fluids occurs because solving for the dynamics of wide resonators in arbitrary modes implies a departure from the assumptions that make the semi-analytic approaches possible. For instance, to solve for the plate dynamics, either an elasticity theory or a plate theory is required. In either case, for cantilevered boundary conditions, analytic solutions are unknown and thus numeric techniques are required [65], thus preventing the existence of a semi-analytic method for plate-fluid interactions. Due to the complexity of solving the plate-fluid interaction problem, a few studies favored solving this fluid-structure interaction problem with the Finite Element Method (FEM) in a monolithic form (by discretizing both the elastic domain and the fluid domain [66, 42, 64, 67])¹. Results obtained with FEM agree with experimental data within 10% for low order modes both using 2D and 3D fluid flow [66, 66, 67]. However, due to the high computational cost, only the 2D fluid flow simulations were capable of solving RTS and HOP modes and an agreement within 50% with experimental data was reported for the eighth RTS mode [42, 66]. Solving the plate-fluid interaction problem in a monolithic form with

¹In [42, 66, 64] the transient dynamics of the plate is solved with the software ADINA or Comsol Multiphysics when a single vibrational mode is imposed as an initial condition. In [67], the eigenvalue problem is solved with Comsol Multiphysics.



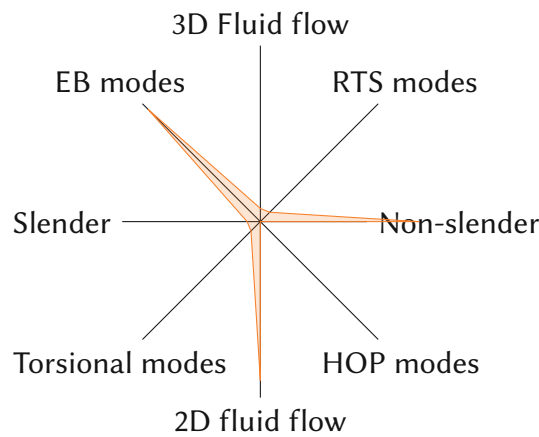
(a) Semi-analytic methods [31, 48, 49, 50, 51, 52, 53].

(b) Semi-analytic methods [45, 46, 47, 44, 54].



(c) Semi-analytic methods [33, 55, 32, 48, 56, 57]

(d) Semi-analytic methods [47, 54].



(e) Semi-analytic methods [60, 61].

Figure 1.7: Semi-analytic methods for the transverse modes of slender and non-slender MEMS resonators in viscous fluids.

FEM requires fine fluid meshing over a huge volume compared to the size of a fluid mesh cell. Moreover, micro-plates' in-plane dimensions are much larger than the occurring transverse deflections. This multi-scale character of the problem results in discretization requirements that are difficult to fulfill [68]. Also, the pressure gradient near the edges of the micro-plate is high [69] which imposes additional discretization requirements in these regions. These aspects limit the applicability of purely numerical methods for solving the plate-fluid interaction problem.

1.4 Objective

The objective of this thesis is to numerically investigate the dynamics of non-slender MEMS resonators in viscous fluids, thus expanding the scope of geometries available for fluidic operating MEMS devices. For that purpose, we propose a semi-numerical method for determining the steady-state dynamics of micro-plate resonators immersed in viscous fluids. Fig. 1.8 highlights graphically the objective of the proposed semi-numerical methods. The proposed method overcomes the limitations of the existent beam-based semi-analytic methods by accounting for two-dimensional vibrational modes (roof tile-shaped modes and higher-order plate modes) of non-slender MEMS resonators, whose dynamics in viscous fluids remain elusive. Given that several semi-analytic methods for beams assume a two-dimensional fluid flow, in this thesis we investigate a 2D fluid flow formulation, as well as a 3D fluid flow formulation. Using both formulations allows for determining the limits of the two-dimensional flow approximation and its effects on MEMS resonators.

With the proposed semi-numerical methods, we seek to determine which vibrational modes exhibit the highest Q-factor in liquids and gases and the underlying dynamics leading to the high Q-factor. Also, since the method is valid in the entire range from slender beams to plates, investigating the structure's dynamics and the fluid flow as the elastic structure changes dimensions is of great interest, as it provides insight into crucial differences between slender and non-slender resonators. Moreover, we aim to find novel effects in the micro-resonator-fluid interaction that are not present in the beam-fluid interaction. Note that this range of analysis in non-slender MEMS resonators is not feasible with a purely numerical method, given the huge computation cost associated with this multi-scale fluid-structure interaction problem, and is only with the proposed methods made possible.

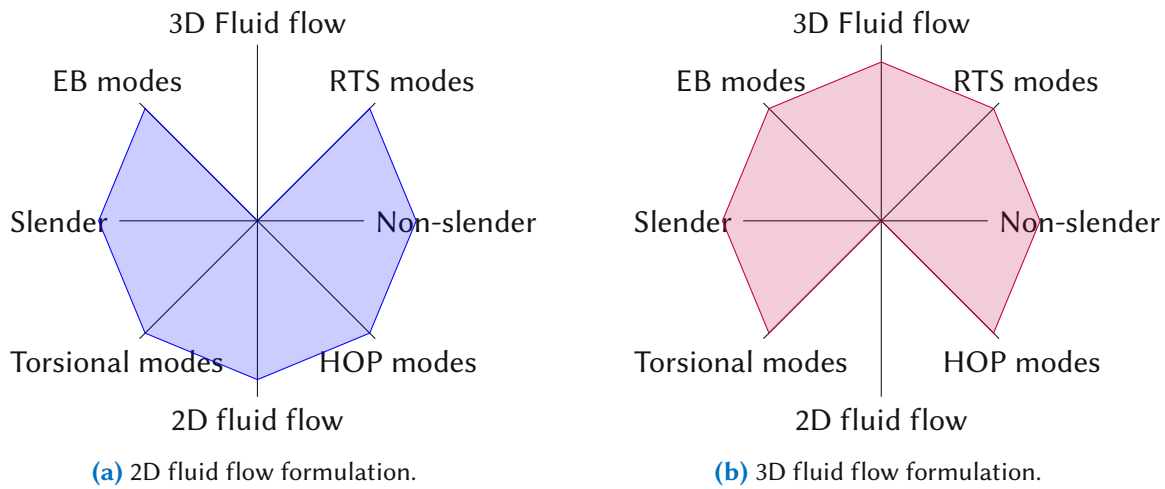


Figure 1.8: Two different semi-numerical methods are proposed for investigating the dynamics of non-slender geometries in viscous fluids: a) assuming a two-dimensional fluid flow and b) assuming a three-dimensional fluid flow.

1.5 Thesis outline

This thesis is divided into three main sections. Section I comprises chapters 2 to 5 and refers to developing the 2D fluid flow method. In Chapter 2, a dimensional analysis is performed, and the mathematical formulation for the micro-plate-fluid interaction problem is defined. In Chapter 3, numerical methods to solve the plate dynamics (without a fluid) are defined, and in Chapter 4, the boundary integral formulation for the 2D fluid flow is introduced. Chapter 5 presents the convergence and validation of the proposed method with literature data.

Section II of this thesis applies the proposed method and reports on the results and limitations found. In Chapter 6, the method is applied to determine the Q-factor and added-mass effect as the structure ranges from a beam to a plate and the resulting fluid flow in each case to understand the beam-plate transition. In Chapter 7, a wide plate is considered in gases and liquids. This analysis revealed the existence of a phenomenon that we define as the Gas-Liquid modal Q-factor inversion. An experimental analysis is carried out in liquids and gases in Chapter 8, indicating the 2D flow's validity and limits.

Section III of this thesis overcomes the limit of two-dimensional fluid flow formulation and the three-dimensional fluid flow around plate resonators is investigated. Chapter 9 introduces the three-dimensional fundamental solution to the Stokes equations, and the semi-numerical method, which accounts for the three-dimensional fluid flow, is defined. Chapter 10 concerns the convergence and validation of the new proposed

method. Chapter 11 analyzes the two semi-numerical methods proposed to identify the limits of the 2D and 3D fluid flow and its effects on the Q-factor prediction for the different plate vibrational modes. Chapter 12 is the conclusions and outlook of the thesis.

Parts of this thesis were published in similar form in the author's works [70, 71, 72].

Part I

A semi-numerical method for micro-plates in viscous fluids with a two-dimensional fluid flow formulation

2 Mathematical formulation

To define a suitable mathematical formulation for the micro-plate-fluid interaction problem, a dimensional analysis is necessary. With the dimensional analysis, we define the governing equation for the fluid flow dynamics and for the elastic body dynamics, as well as the interface conditions between the elastic body and fluid. Throughout the dimensional analysis, an elastic body with width b , length l and thickness h , completely immersed in a viscous fluid as illustrated in Fig. 2.1 is considered.

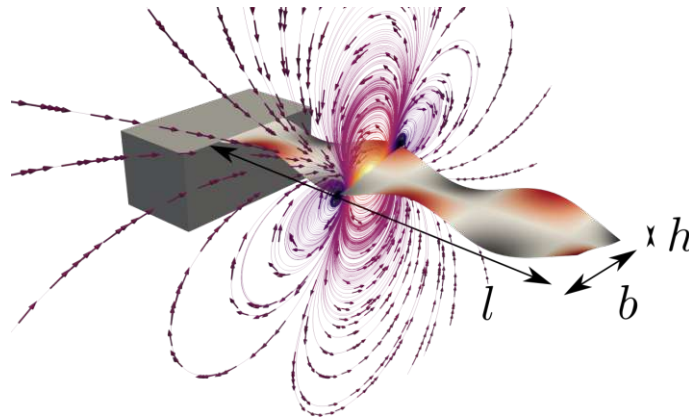


Figure 2.1: Elastic structure immersed in a viscous fluid. The structure has a length l , width b and thickness h and is represented vibrating in a torsional mode. A fluid flow is represented around a cross-section of the structure. Maximum fluid velocity is represented by bright yellow and minimum by dark blue.

2.1 Elastic body dynamics

The dynamics of an elastic body of arbitrary shape are commonly determined using a linear elasticity equation. However, most MEMS structures are rather simple in geometry. For example, beams, membranes and plates are common structures used in MEMS resonators [4]. For such structures, simplified elastic models exist which facilitate the development of methods for solving the structure's dynamics.

A classic example of simplified elasticity models for elastic bodies is the Euler-Bernoulli beam theory. The Euler-Bernoulli beam theory is valid for long slender beams whose length l greatly exceeds the beam's width b and thickness h . The Euler-Bernoulli beam theory assumes that a cross-section of the beam remains perpendicular to the beam's neutral axis when deformed as represented in Fig. 2.2a. The resulting partial differential equation (PDE) for the out-of-plane displacement w of the beam with the Euler-Bernoulli theory is

$$EI \frac{\partial^4 w}{\partial x^4} + \rho b h \frac{\partial^2 w}{\partial t^2} = F, \quad (2.1)$$

where E is the Young's modulus, I is the moment of inertia, ρ is the beam's density and F is the external force.

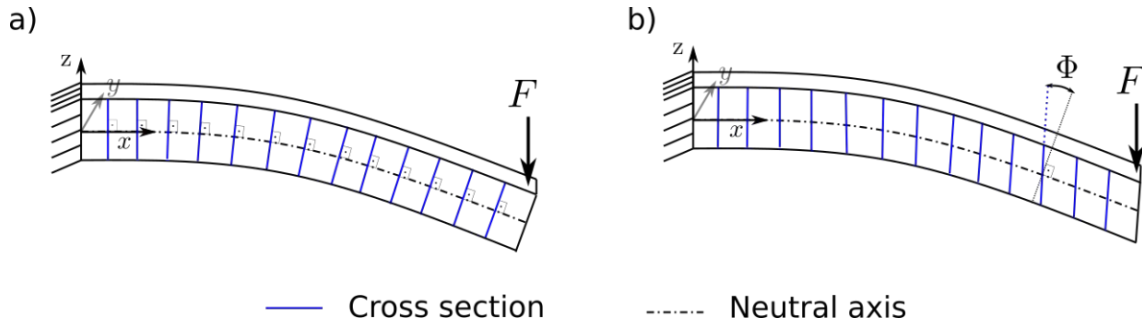


Figure 2.2: Representation of the neutral axis and cross-sections in a) Euler-Bernoulli beam and b) Timoshenko beam. The beam is in both cases considered cantilevered on the left edge.

If the beam's thickness is increased, the effect of shear forces along the beam's thickness must be considered, resulting in a cross-section no longer perpendicular to the neutral axis as depicted in Fig. 2.2b where Θ is the deformation angle due to the shear forces. The simplified theory for thick beams is the Timoshenko beam theory. A non-dimensional quantity that is typically used to classify the beam as a thin beam or thick beam is the shear coefficient Sf given by

$$SF = \frac{3Eh^2}{\kappa l^2 G}, \quad (2.2)$$

where κ is Timoshenko shear coefficient (5/6 for rectangular cross-sections) and G is the shear modulus. SF is obtained from the static Timoshenko beam equation and we apply it here as a guide, not as a strict rule since the dynamic effects alter the limit between the thin beam and the thick beam theory. For $SF > 0.01$, Timoshenko's beam theory must be applied, otherwise, $SF \leq 0.01$ the beam is considered thin and the Euler-Bernoulli equation accurately predicts the beam's dynamics.

Note that SF does not account for the beam's width b , since both theories assume $b \ll l$. If the beam becomes wider, the Euler-Bernoulli beam theory and Timoshenko beam theories are no longer valid and a two-dimensional simplified elasticity theory must be used. The generalization of Euler Bernoulli's theory for a wide structure is the Kirchhoff plate theory. The assumptions in the Kirchhoff plate theory are that the perpendicular straight lines before deformation (in blue in Fig. 2.3) remain straight after deformation, and they experience no elongation. Furthermore, the transverse normal n_p are perpendicular to the plate's neutral plane Ω_p (also called midplane) either in the undeformed or in the deformed states [65]. With these assumptions, the displacement of the plate's midplane $w(x, y)$ fully describes the plate dynamics and the displacement is independent of the z -direction. The Kirchhoff plate theory is also known as the classical plate theory, or thin plate theory [65]. For an isotropic plate undergoing purely out-of-plane displacement w , the Kirchhoff plate equation is

$$\frac{Eh^3}{(1-\nu^2)12} \left(\frac{\partial^4 w}{\partial x^4} + 2 \frac{\partial^4 w}{\partial x^2 \partial y^2} + \frac{\partial^4 w}{\partial y^4} \right) + \rho h \frac{\partial^2 w}{\partial t^2} = F, \quad (2.3)$$

where ν is the Poisson coefficient.

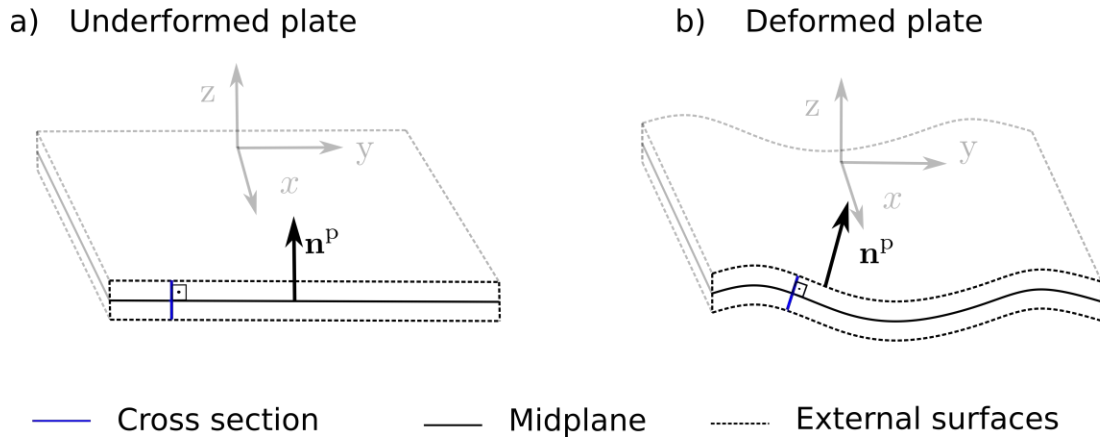


Figure 2.3: Representation of a) undeformed and b) deformed thin plate. \mathbf{n}_p is the neutral plane's normal vector.

When the plate's thickness is increased, shear forces in each cross-section may no longer be neglected and the Kirchhoff-Love plate theory is no longer valid. A simplified elasticity theory for thick plates is the Reissner-Mindlin plate theory [65]. The Reissner-Mindlin plate theory is the generalization of the Timoshenko beam theory for wide structures.

To determine the more appropriate simplified elasticity equation for the micro-plate fluid interaction problem let us introduce different geometries used in previous studies in MEMS resonators whose dimensions are listed in Table 2.1. The thickness of the elastic structures used in the micro-resonators ranges from hundreds of nanometers to tens of micrometers, whereas their in-plane dimensions (length and width) vary between tens of micrometers to millimeters [5].

Along with the dimensions, also the structures' aspect ratio $r_a = l/b$ and the thickness ratio $r_t = h/b$ are given in Table 2.1. Thin plate theory must be used when the plate's aspect ratio r_a is smaller than 10 [65] and the thickness ratio is small enough so that $SF < 0.01$. For Silicon, $SF = 0.01$ occurs for a thickness ratio of $r_t = 0.12$ using the properties given in Table 2.2.

Fig. 2.4 shows the shear coefficient Sf as a function of the aspect ratio r_a and thickness ratio r_t for a silicon structure. Also in Fig. 2.4 a gray dash-dotted line marks the aspect ratio of 10 which divides the structures into beams and plates. Points in white in Fig. 2.4 stand for the r_a and r_t pair of different geometries used in MEMS resonators whose dimensions are listed in Table 2.1. Note that the majority of resonators are in the thin plate regime with $r_a < 10$ and $r_t < 0.12$. Fig. 2.4 highlights that even beam resonators that vibrate in conventional Euler-Bernoulli modes would be more accurately modeled using a plate theory due to their high aspect ratio.

From the analysis here presented, it is evident that a thin plate theory accurately models the elastic structure's dynamics of a wide range of micro-resonators geometries

Letter	Study	Length [μm]	Width [μm]	Thickness [μm]	r_a [-]	r_t [-]
a	Kim [73]	150	10	0.2	15	0.02
b	Tung [48]	250	25	1	10	0.04
c	Clark [53]	197	29	2	6.8	0.068
d	Chen [22]	90	35	2	2.57	0.057
e	Chen [22]	130	35	2	3.71	0.057
f	Chen [22]	250	35	2	7.14	0.057
g	Chen [22]	350	35	2	10	0.057
h	Kim [73]	458	51	2	8.9	0.04
i	Ruiz-Diez [42]	500	300	11.5	1.67	0.04
j	Patocka [15]	1250	1000	21	1.25	0.02
k	Kucera [41]	2524	1274	22	1.98	0.17

Table 2.1: Dimensions of selected beams and plates used in MEMS resonators in previous studies. Arranged in the order of increasing width.

Property	Young's modulus	Poisson coefficient	Shear modulus
Variable	E	ν	G
Value	169 GPa	0.064	79 GPa

Table 2.2: Silicon properties approximated as an isotropic material [74].

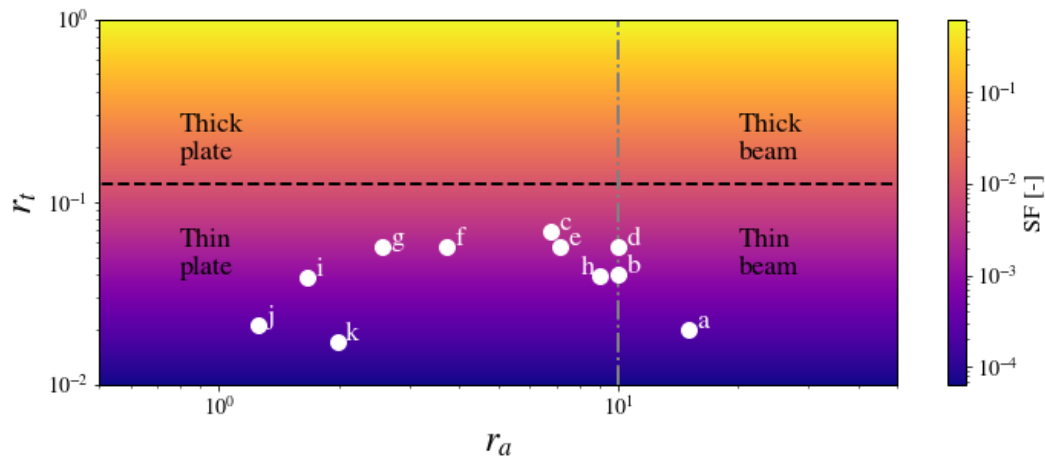


Figure 2.4: Shear coefficient S_f as a function of the aspect ratio r_a and thickness ratio r_t . The gray dash-dotted line marks the limit between beam and plate theories. The black dashed line serves as a guide to define the limit between thin and thick elasticity theories. Points a to k refer to different beams and plates used in previous studies of MEMS resonators.

A thin plate theory not only allows for the modeling of two-dimensional vibrational

modes of plates but is also more accurate for determining the dynamics of the slender structures with aspect ratio $r_a < 10$ which are encountered in MEMS.

2.2 Fluid flow dynamics

The fluid flow around micro-plates occurs in different flow regimes depending on the structure's dimensions and the fluid properties [75]. In essence, these regimes are due to the rarefaction, compressibility and ratio of inertial per viscous forces in the fluid flow. Depending on the type of fluid flow, a different set of governing equations is used to determine the fluid flow.

2.2.1 Rarefaction

The rarefaction of the fluid flow around MEMS is associated with the mean free path length λ_{mfp} in the fluid. Rarefaction effects occur when the gas molecules are so far apart from each other that the fluid can not be considered a continuum. The mean free path length is the average distance a particle moves between two consecutive collisions with other fluid particles. The non-dimensional parameter that characterizes the rarefaction of the fluid flow is the Knudsen number Kn , defined as

$$\text{Kn} = \frac{\lambda_{\text{mfp}}}{l_{\text{char}}} \quad (2.4)$$

where l_{char} is a characteristic length of the system [76, 75].

Kn is used to determine whether the flow regime is in the free molecular flow, transition flow, slip flow or continuum flow. The four types of flow regimes due to rarefaction are represented in Fig. 2.5 for a free stream flow with velocity U_0 around a structure with characteristic length l_{char} . For $\text{Kn} < 0.01$ the fluid flow is considered in the continuum, the fluid particles constantly hit each other and transfer momentum among themselves. As a result, the fluid is described with average fluid properties such as density ρ_f , dynamic viscosity μ_f and kinematic viscosity ν_f . In the continuum regime, the Navier-Stokes equations accurately describe the fluid flow dynamics [75, 76]. Furthermore, the no-slip boundary condition is valid, thus the fluid flow velocity at the wall of the structure u_{wall} is zero and a boundary layer is formed in which the fluid velocity ranges from 0 at the wall to the free-stream velocity U_0 .

For $0.01 < \text{Kn} < 0.1$, the fluid flow is categorized as slip flow. In the slip flow regime, the Navier-Stokes equations are still valid to solve for the fluid dynamics, however, the no-slip boundary condition does not provide a good agreement between experimental and theoretical results. A slip boundary condition must be applied in which $u_{\text{wall}} \neq 0$ [77, 75]. The transition regime is defined for $0.1 < \text{Kn} < 10$. In the transition regime, free stream particles collide with reflected particles transferring momentum to each other, however, the continuum and thermodynamic assumptions break down and the Navier-Stokes equations are no longer valid [76]. For $10 < \text{Kn}$, the flow is considered free molecular flow and the collisions between free stream particles and reflected particles

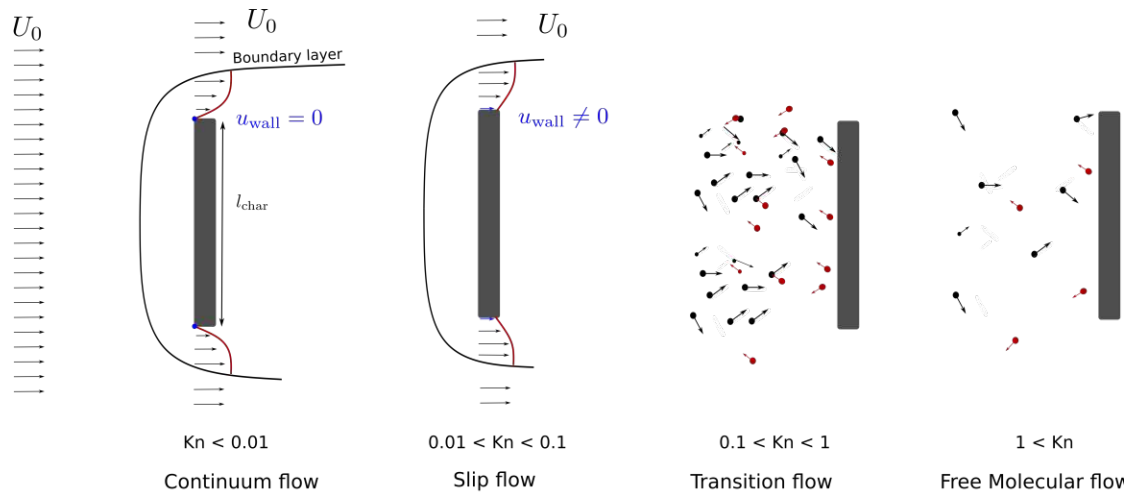


Figure 2.5: Fluid flow regimes around a structure with characteristic length l_{char} divided in a) continuum flow, b) slip flow, c) transition flow and d) free-molecular flow according to the Knudsen number Kn . The solid black line represents the boundary layer, and the red solid line the velocity profile inside the boundary layer. Black circles represent free stream particles and red circles the reflected particles.

are negligible, that is, the free stream particles are influenced by the structure only after the particle collides with the wall.

The flow around MEMS resonators immersed in air at standard ambient temperature and pressure (SATP)¹ is in the continuum regime for structures whose characteristic length is above $6.5 \mu\text{m}$ ($l_{\text{char}} > 6.5 \mu\text{m}$), as shown in Fig. 2.6. MEMS with $0.5 \mu\text{m} < l_{\text{char}} < 6.5 \mu\text{m}$ in air at SATP are in the slip flow regime. Non-continuum flows occur more commonly in gases because λ_{mfp} is larger in gases than in liquids. For instance, air at SATP has a mean free path equals to 61.1 nm , while water's λ_{mfp} is 0.13 nm [78]. Table 2.3 summarizes the properties of air and water at SATP.

For micro-beams and micro-plates, the characteristic length is usually the structure's width b [76]. Fig. 2.6 shows the points a to k in black dots which refer to the Knudsen number of different beams and plates used in previous studies of MEMS resonators whose dimensions are shown in Table 2.1. From this analysis, it is evident that the flow around micro-plates is most commonly in the continuum regime both in air and in water. The exception is for very small structures ($l_{\text{char}} < 6.5 \mu\text{m}$) in gases².

2.2.2 Compressibility

Compressibility is the effect that the fluid's density ρ_f alters depending on applied pressure. If the applied pressure is dynamic, it leads to a pressure wave that propagates through the fluid. There are two aspects to determine whether a flow is compressible

¹In SATP, the standard temperature is 298.15 K and the standard pressure is 100 kPa .

²Certain MEMS applications do not occur at SATP, but rather in gases at low-pressure conditions. For these applications, the validity of the method must be verified given that the mean free path is inversely proportional to the pressure

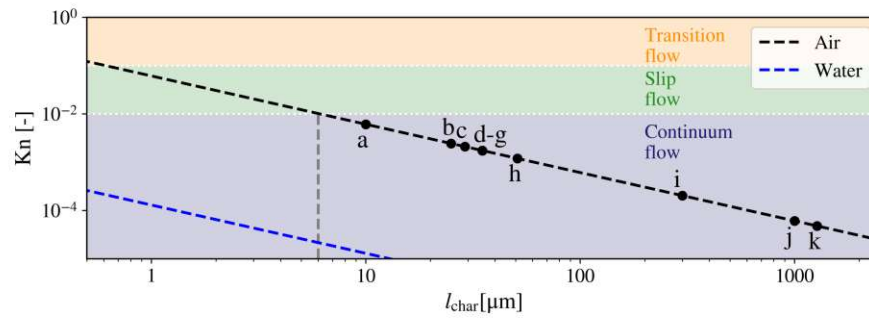


Figure 2.6: Knudsen number of the fluid flow around micro-plates with different l_{char} in air. Points a to k refer to different beams and plates used in previous studies of MEMS resonators.

Property	Variable	Air	Water
Mean free path	λ_{mfp}	61 nm	0.37 nm
Density	ρ_f	1.223 kg m^{-3}	997 kg m^{-3}
Dynamic viscosity	μ_f	$18.1 \text{ }\mu\text{Pa s}$	$890 \text{ }\mu\text{Pa s}$
Kinematic viscosity	ν_f	$15.08 \text{ mm}^2 \text{ s}^{-1}$	$0.892 \text{ mm}^2 \text{ s}^{-1}$
Speed of sound	c_s	343 m s^{-1}	1500 m s^{-1}

Table 2.3: Properties of air and water at SATP used in the dimensional analysis of the fluid flow regimes around MEMS resonators [78, 79].

or incompressible. First, if the Mach number Ma is higher than 0.3, the flow is considered compressible. Second, if the acoustic wavelength λ_{ac} is smaller than the spatial wavelength of the MEMS structure λ_{st} , compressibility effects are considered significant [79].

The Mach number is the ratio of a characteristic velocity of the structure u_{char} and the speed of sound in the fluid c_s as

$$Ma = \frac{u_{\text{char}}}{c_s}. \quad (2.5)$$

The characteristic velocity u_{char} for beams and plates can be defined from the characteristic length l_{char} assuming harmonic oscillation resulting in $u_{\text{char}} = 2\pi f \epsilon l_{\text{char}}$, where ϵ is a constant. Here, we consider $\epsilon = 0.01$, which means the plate's maximum displacement is 1% the characteristic length). With these assumptions, plates with $l_{\text{char}} \leq 100 \text{ }\mu\text{m}$ in air at SATP are in the incompressible regime up to 10 MHz as shown in Fig. 2.7. The flow around a wide MEMS resonator with $l_{\text{char}} = 1000 \text{ }\mu\text{m}$ is in the compressible regime for frequencies higher than 1.7 MHz. Thus, for wide structure at $f > 1.7 \text{ MHz}$ acoustic losses may no longer be neglected as a dissipation mechanism [30].

A high Ma number is uncommon in MEMS resonators and the most common scenario for acoustic losses is due to the match between acoustic and structural wave-

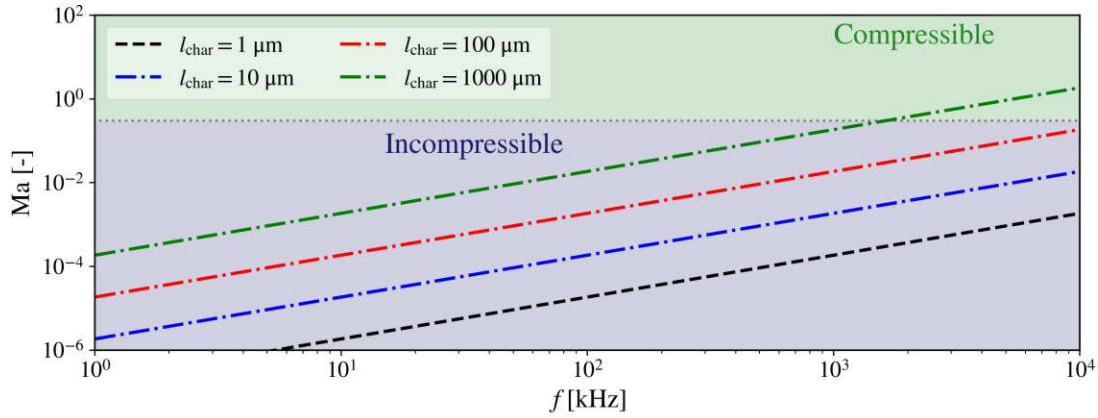


Figure 2.7: Mach number of the fluid flow around MEMS resonators as a function of frequency.

lengths. The acoustic wavelength is inversely proportional to frequency as [79]

$$\lambda_{ac} = \frac{c_s}{f}. \quad (2.6)$$

Hence, at low frequencies, λ_{ac} is large and is usually larger than λ_{st} , until a frequency f_c is reached in which $\lambda_{ac} = \lambda_{st}$. f_c is the limiting frequency of the incompressible flow.

The flexural wavelength λ_{st} depends on the structure of the MEMS resonators and on the vibrational mode. For a cantilevered beam or plate vibrating in the EB modes, λ_{st} approximated for each mode as

$$\lambda_{st,i} \approx \frac{4l}{2i-1} \quad (2.7)$$

where i is a positive natural number that denotes the mode number. Fig. 2.8 shows the lowest three EB modes and the resulting λ_{st} .

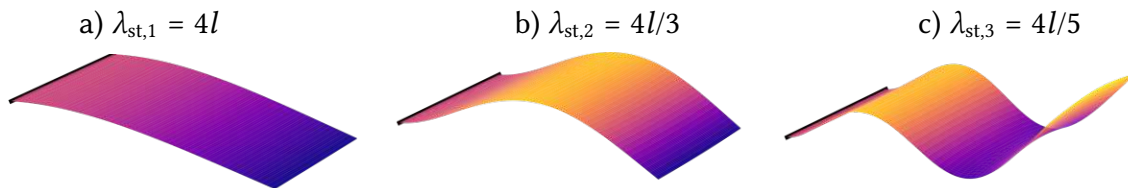


Figure 2.8: Structural wavelength λ_{st} of the first three modes of a cantilevered plate vibrating in only Euler-Bernoulli modes.

Since λ_{st} depends on the mode number i while λ_{ac} is frequency dependent, it is necessary to define the resonance frequency of each Euler-Bernoulli mode in a fluid. Limiting the vibrational modes of the plate to the Euler-Bernoulli modes and determining the plate's dynamics with the Euler-Bernoulli theory results in the resonance frequencies

in vacuum f^{vac} as

$$f_{\text{vac},i} = \frac{1}{2\pi} \frac{C_i^2}{l^2} \sqrt{\frac{Eh^2}{12\rho_p}}, \quad (2.8)$$

where C_i is the i -th root of the transcendental equation $1 + \cos c \cosh c = 0$ [31]. Note that with the Euler-Bernoulli equation, the plate's width b does not alter the mode's resonance frequencies. The resonance frequencies of the Euler-Bernoulli modes in fluids f^f are approximated using an inviscid fluid flow model [45, 46] as

$$f_i^f = f_i^{\text{vac}} \left(1 + \frac{\pi\rho_f b}{4\rho_p h} \right)^{-1/2}, \quad (2.9)$$

where ρ_f is the fluid's density.

Considering micro-plates with different lengths $l = 10 \mu\text{m}$, $l = 100 \mu\text{m}$ and $l = 1000 \mu\text{m}$ results in the λ_{st} over frequency f shown in Fig. 2.9. The plate's material is isotropic silicon with properties given in Table 2.2. For this analysis, air is considered at SATP conditions with properties as in Table 2.3. The plate's width b is set to be half the length ($b = l/2$) and the plate's thickness h is $l/100$. For the shortest plate with $l = 10 \mu\text{m}$, λ_{st} and λ_{ac} are equal for $f_c \approx 80 \text{ MHz}$. Therefore, only for frequencies lower than 80 MHz, compressibility effects are negligible for this beam with $l = 10 \mu\text{m}$. For a longer plate with $l = 100 \mu\text{m}$, this limiting frequency is 8 MHz, and for a very long plate with $l = 1000 \mu\text{m}$ the fluid is compressible for $f > 0.8 \text{ MHz}$. Therefore, longer plates have lower f_c than shorter plates.

Using the dimensions of plates and beams used in previously studied (whose dimensions are given in Table 2.1) it is possible to obtain the limiting frequency f_c for the Euler-Bernoulli modes of these structures in air which results in Fig. 2.10a. Structures a to h are in the incompressible regime up to at least 2 MHz, while the longer structures i, j and k are in the incompressible regime only up to a few hundred kilohertz in air. In parenthesis in Fig. 2.10 is shown the mode number at which f_c occurs. In water at SATP conditions, the acoustic wavelength is larger than in air due to water's higher speed of sound. In addition, the resonance frequencies of structures in liquids are smaller than in air due to the added-mass effect. For instance, using the same beams and plates as in the previous example in air renders a much higher limiting frequency f_c as shown in Fig. 2.10b. In water, minimum limiting frequencies of 30 MHz are obtained.

Here we established that the fluid flow around micro-plate-resonators is in the incompressible regime provided the Mach number is smaller than 0.3, and in frequencies where $\lambda_{\text{st}} < \lambda_{\text{ac}}$. In water, the incompressible regime extends to tens of Megahertz, while in air micro-plates may leave the incompressible regime in frequencies below 1 MHz.

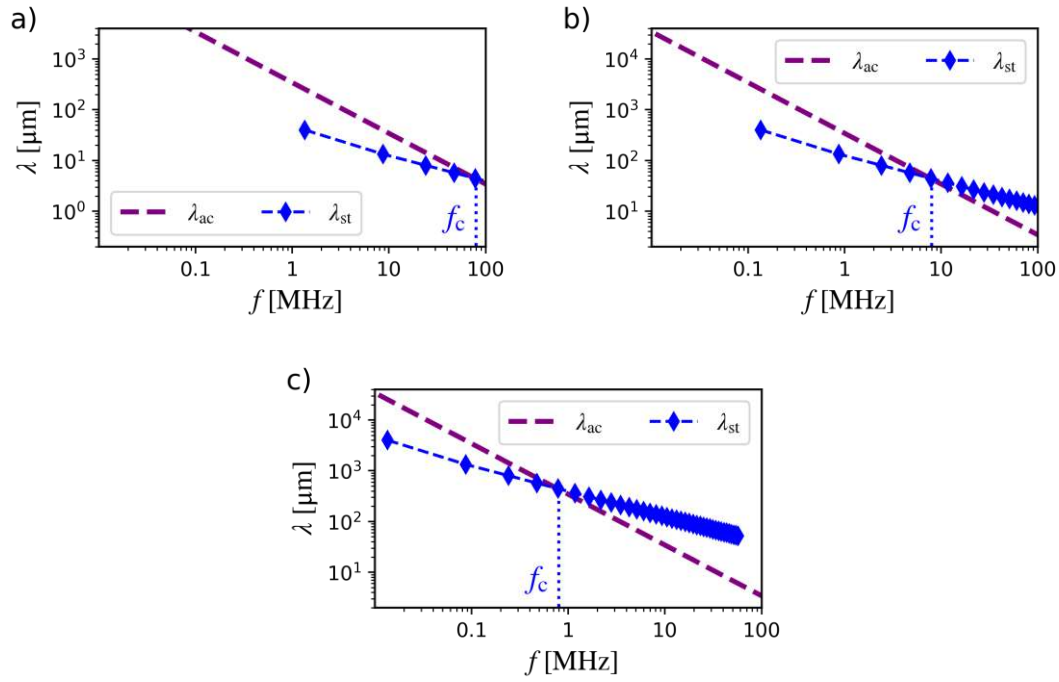


Figure 2.9: Acoustic and flexural wavelengths of different plates with a) $l = 10 \mu\text{m}$, b) $l = 100 \mu\text{m}$ and c) $l = 1000 \mu\text{m}$, in air. λ_{st} is shown for each mode, starting from the first ($i = 1$) at the lowest frequency.

2.2.3 Inertial and viscous forces

The governing equations for an incompressible Newtonian fluid are the Navier-Stokes equations [80]

$$\begin{aligned} \frac{\partial \mathbf{u}}{\partial t} + (\mathbf{u} \cdot \nabla) \mathbf{u} - \nu_f \nabla^2 \mathbf{u} &= -\frac{1}{\rho_f} \nabla p, \\ \nabla \cdot \mathbf{u} &= 0, \end{aligned} \quad (2.10)$$

where \mathbf{u} is the velocity field, p is pressure, ν_f is the fluid's dynamic viscosity and ρ_f is the fluid's density.

It is possible to write the Navier-Stokes equations in non-dimensional form using the characteristic velocity u_{char} and characteristic length l_{char} , using

$$\mathbf{u}' = \frac{\mathbf{u}}{u_{\text{char}}}, \quad t' = \frac{t u_{\text{char}}}{l_{\text{char}}}, \quad \nabla' = l_{\text{char}} \nabla, \quad p' = \frac{p l_{\text{char}}}{\mu_f u_{\text{char}}}, \quad (2.11)$$

which yields [80]

$$\text{Re} \frac{\partial \mathbf{u}'}{\partial t'} + \text{Re}(\mathbf{u}' \cdot \nabla') \mathbf{u}' - \nabla'^2 \mathbf{u}' = -\nabla' p', \quad (2.12)$$

$$\nabla' \cdot \mathbf{u}' = 0. \quad (2.13)$$

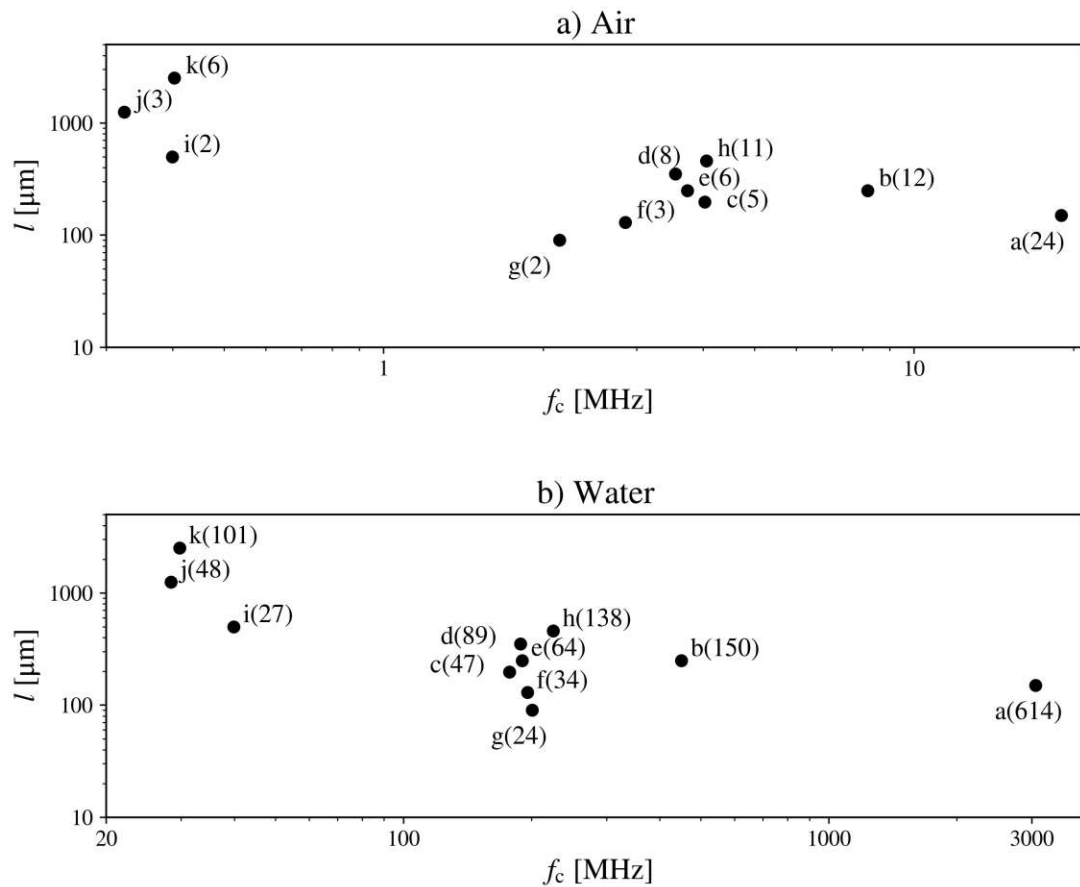


Figure 2.10: Limiting frequency f_c of the different plates in a) air and b) water. In parenthesis, the mode number at which f_c occurs is given.

The terms with prime correspond to the non-dimensional variable without prime in Eq. 2.13. Re stands for the Reynolds number, defined as

$$Re = \frac{\rho_f u_{\text{char}} l_{\text{char}}}{\mu_f}. \quad (2.14)$$

The Reynolds number Re characterizes the ratio of viscous forces to inertial forces. As the characteristic length l_{char} of a structure decreases, the Reynolds number and the ratio between viscous forces and inertial forces in the fluid flow around the structure also decrease, which leads to different regimes of viscous flows. When $Re \ll 1$, the flow is known as creeping flow or Stokes flow and the governing equations are simplified to

$$Re \frac{\partial \mathbf{u}'}{\partial t'} - \nabla'^2 \mathbf{u}' = -\nabla' p', \quad (2.15)$$

$$\nabla' \cdot \mathbf{u}' = 0. \quad (2.16)$$

The transition from Stokes flow to Navier-Stokes flow is defined at $Re = 0.01$ [75]. For $Re > 0.01$, the convective terms in the Navier-Stokes equations may not be neglected and Stokes equations are not applicable [78, 75].

Fig. 2.11 shows the Stokes flow limit of $Re \leq 0.01$ considering different amplitude oscillations with a characteristic velocity u_{char} as a function of the length l in air and in water. In air, considering a characteristic velocity $u_{char} = 10 \mu\text{s}^{-1}$ (represented by a dashed black line in Fig. 2.11) even structures with $l = 5000 \mu\text{m}$ are in the Stokes flow regime. In water, Re is below the 0.01 threshold considering $u_{char} = 10 \mu\text{s}^{-1}$ for structures with characteristic length smaller than $900 \mu\text{m}$. Considering small amplitude oscillations with a characteristic velocity $u_{char} = 1 \mu\text{s}^{-1}$ yields a small Reynolds number $Re \leq 0.01$ both in air and in water for structures whose characteristic length is even as large as $5000 \mu\text{m}$.

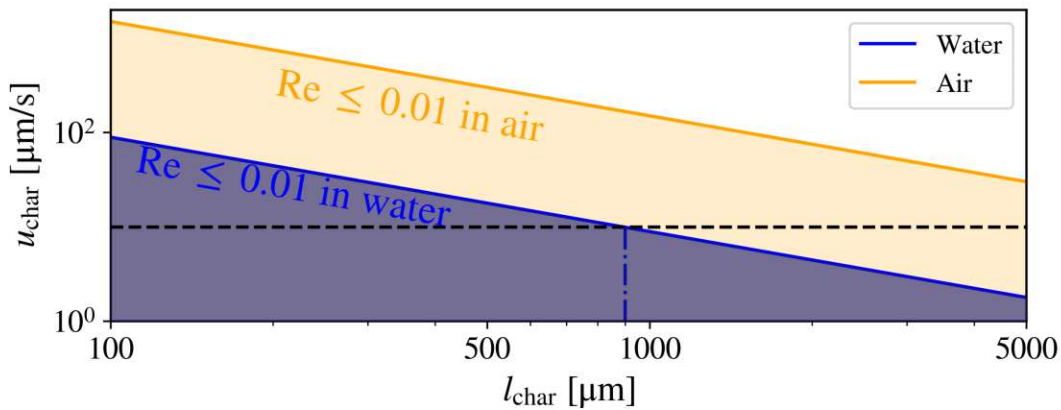


Figure 2.11: Characteristic velocity u_{char} for the limiting Reynolds number of 0.01 in air and water. The black dashed line represents $u_{char} = 10 \mu\text{s}^{-1}$ as a reference value.

Given the different non-dimensional numbers here introduced (Ma, Re and Kn), it is interesting to note that for gases it is possible to write Kn in terms of Re and Ma, given that the three parameters are non-dimensional numbers of the fluid flow and geometry of the micro-plate-resonator. The Knudsen number is defined as a function of the Mach number and Reynolds number according to

$$Kn = \frac{\lambda_{mfp}}{l_{char}} \sqrt{\frac{\pi \gamma_f}{2}} \frac{Ma}{Re}, \quad (2.17)$$

where γ_f is the ratio of the specific heat of the fluid. Fig. 2.12 summarizes the different flow regimes that can occur around micro-plates undergoing small amplitude oscillations of $u_{char} = 1 \mu\text{s}^{-1}$ in air in SATP.

From the dimensional analysis in this section, we conclude that the flow around micro-plates is typically in the continuum regime, the fluid is incompressible and the inertial forces are much smaller than the viscous forces (small Re). Therefore, the Stokes

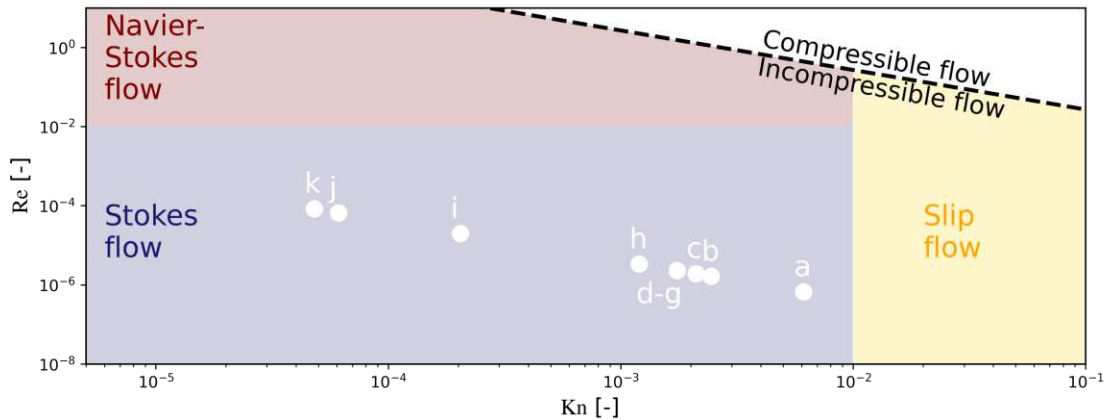


Figure 2.12: Classification of the fluid flow around micro-plates in terms of Re and Kn in air.

equations are the most appropriate governing equations to determine the fluid flow dynamics around micro-plates.

2.3 Mathematical formulation of a micro-plate in a viscous fluid

We consider a micro-plate with width b , length l and thickness h , as shown in Fig. 2.13. The Cartesian coordinate system has x along the plate's length, y along the plate's width, and z along its thickness. The plate undergoes purely out-of-plane displacement $w(x, y)$, while lateral movement in x - and y -directions are negligible. We use the Kirchhoff plate equation for thin plates to determine $w(x, y)$, and represent the three-dimensional resonator by its two-dimensional mid-plane Ω_p according to the Kirchhoff plate theory.

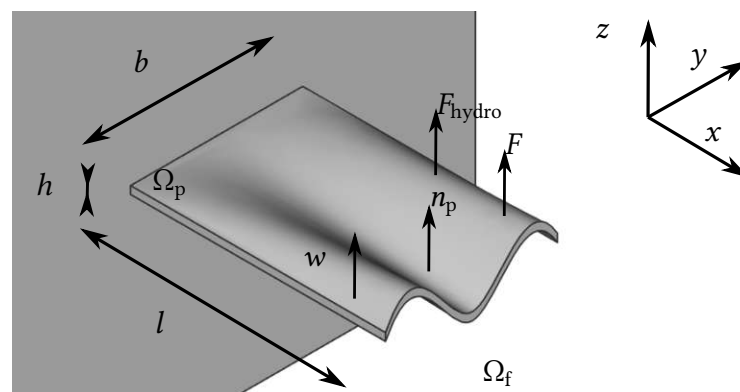


Figure 2.13: Representation of a thin micro-plate immersed in a viscous fluid and subject to an arbitrary load F . The shown transverse displacement $w(x, y)$ of the plate corresponds to a roof tile-shaped vibrational mode.

The plate is fully immersed in a fluid of density ρ_f , dynamic viscosity μ_f and kinematic viscosity ν_f . The fluid acts on the plate's surfaces, which results in a hydrodynamic force F_{hydro} acting on the plate's midplane Ω_p . The micro-plate dynamics in a fluid are determined with the Kirchhoff plate equation with an added hydrodynamic force F_{hydro} yielding

$$\frac{Eh^3}{12(1-\nu^2)} \left(\frac{\partial^4 w(x, y)}{\partial x^4} + 2 \frac{\partial^4 w(x, y)}{\partial x^2 \partial y^2} + \frac{\partial^4 w(x, y)}{\partial y^4} \right) + \rho h \frac{\partial^2 w(x, y, \omega)}{\partial t^2} = F(x, y) + F_{\text{hydro}}(x, y). \quad (2.18)$$

To determine F_{hydro} , it is necessary to find the fluid stress acting on each surface of the plate, which will be explained in Chapter 4. Besides the fluid stress acting on the plate, kinematic conditions also play a role in the fluid-plate interaction problem. The kinematic interface condition for the fluid-plate interaction relates the motion of the plate with the fluid velocity at the plate's surfaces. Since the fluid flow around micro-plates is in the continuum regime, the no-slip and no-penetration boundary conditions are the valid kinematic interface conditions.

The governing Eq. 2.18, with the kinematic boundary conditions along with the Stokes equations, form the mathematical model for the micro-plate fluid interaction problem. Since these equations are linear, their Fourier transforms do not contain coupling terms between different frequencies. We focus on periodic solutions to this system of equations, thus the Fourier transform of the governing equation Eq. 2.18 is used which yields

$$\frac{Eh^3}{12(1-\nu^2)} \left(\frac{\partial^4 \hat{w}(x, y)}{\partial x^4} + 2 \frac{\partial^4 \hat{w}(x, y)}{\partial x^2 \partial y^2} + \frac{\partial^4 \hat{w}(x, y)}{\partial y^4} \right) - \omega^2 \rho h \hat{w} = \hat{F}(x, y) + \hat{F}_{\text{hydro}}(x, y).$$

\hat{w} and \hat{F} refer to the Fourier transform of the respective time-dependent variables. The unsteady Stokes equations in the frequency domain are [80]

$$\begin{aligned} j\omega \hat{\mathbf{u}} - \nu_f \nabla^2 \hat{\mathbf{u}} &= -\frac{1}{\rho_f} \nabla \hat{p}, \\ \nabla \cdot \hat{\mathbf{u}} &= 0, \end{aligned} \quad (2.19)$$

where $\hat{\mathbf{u}}$ and \hat{p} are the Fourier transform of \mathbf{u} and p , respectively.

To determine \hat{F}_{hydro} , it is necessary to find the fluid stress $\hat{\boldsymbol{\sigma}}$ acting on each surface of the plate. A cantilevered plate has five surfaces in contact with the fluid, those are top ($z = +h/2$), bottom ($z = -h/2$), left ($y = -b/2$), right ($y = +b/2$) and free end ($x = l$), denoted respectively by Σ^t , Σ^b , Σ^l , Σ^r and Σ_f as shown in Fig.2.14a.

Since the fluid flow is in the continuum, the resulting fluid force of the plate's surfaces $\hat{\mathbf{F}}_{\text{surf}}$ is the result of the fluid stress $\hat{\boldsymbol{\sigma}}$ as

$$\hat{\mathbf{F}}_{\text{surf}} = \hat{\boldsymbol{\sigma}} \cdot \mathbf{n}_p. \quad (2.20)$$

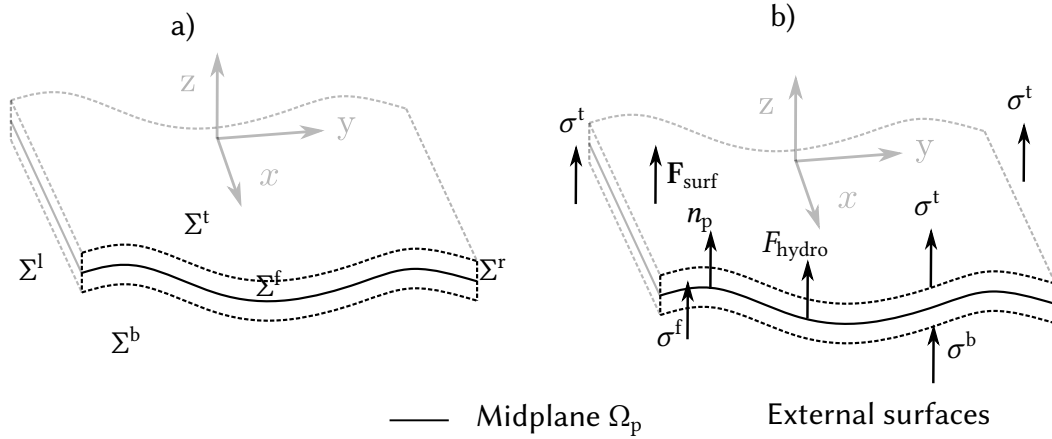


Figure 2.14: Representation of a) the five surfaces in contact with a fluid in a cantilevered plate and b) the fluid stress acting on each surface.

The fluid stress $\hat{\sigma}$ in an incompressible Newtonian fluid is

$$\hat{\sigma} = -\mathbf{I} p + 2\mu_f \hat{\epsilon}, \quad (2.21)$$

where \mathbf{I} is the 3 by 3 identity matrix, and $\hat{\epsilon}$ is the strain rate tensor, defined as

$$\hat{\epsilon} = \frac{1}{2} (\nabla \hat{\mathbf{u}} + \nabla \hat{\mathbf{u}}^T). \quad (2.22)$$

The fluid stress acting on the top, bottom, left, right and free-end surfaces of a micro-plate is denoted respectively, $\hat{\sigma}_t$, $\hat{\sigma}_b$, $\hat{\sigma}_l$, $\hat{\sigma}_r$ and $\hat{\sigma}_f$ respectively as depicted in Fig. 2.14b. Since the plate is thin, the lateral surfaces Σ_l , Σ_r and Σ_f are much smaller than Σ_t and Σ_b , the contribution of the fluid stress on these surfaces may be neglected [10] resulting in $\hat{\mathbf{F}}_{\text{surf}}$ as

$$\hat{\mathbf{F}}_{\text{surf}} = (\hat{\sigma}_t - \hat{\sigma}_b) \cdot \mathbf{n}_p, \quad (2.23)$$

assuming the normal \mathbf{n}_p to be in the positive z -direction.

In thin plate theory, the elongation along the z -direction is negligible, which means surfaces forces are transmitted without any loss of amplitude to the plate's midplane, therefore \hat{F}_{hydro} is simply the projection of F_{surf} in the z -direction as

$$\hat{F}_{\text{hydro}} = \hat{\mathbf{F}}_{\text{surf}} \cdot (0, 0, 1)^T = [(\hat{\sigma}_t - \hat{\sigma}_b) \cdot \mathbf{n}_p] \cdot (0, 0, 1)^T, \quad (2.24)$$

where the T superscript stands for transpose. Furthermore, since small amplitude oscillations are considered, the plate normal \mathbf{n}_p does not alter greatly during one oscillation period and is approximated as $\mathbf{n}_p = (0, 0, 1)^T$, which together with the stress definition in Eq. 2.21 results in

$$\hat{F}_{\text{hydro}} = (\hat{p}^t - \hat{p}^b) + \mu_f \left(\frac{\partial \hat{u}_z^t}{\partial z} - \frac{\partial \hat{u}_z^b}{\partial z} \right), \quad (2.25)$$

where \hat{p}^t and \hat{p}^b is the pressure at the top and bottom plate surfaces, and \hat{u}_z^t and \hat{u}_z^b are the fluid's velocity in z direction at the top and bottom surfaces.

Besides the fluid stress acting on the plate, kinematic conditions also play a role in the fluid-structure interaction problem. The kinematic interface condition for the fluid-plate interaction relates the motion of the plate with the fluid velocity $\hat{\mathbf{u}}$ at the plate's surfaces. Since the fluid flow around micro-plates is in the continuum regime, the no-slip and no-penetration boundary conditions are the valid kinematic interface conditions. With the thin plate assumptions, the plate elongation along the plate's thickness is zero. As a result, at the plate's top surface Σ_t and the plate's bottom surface Σ_b , the plate moves with the same velocity which is equal to $\hat{\mathbf{u}}_p = (0, 0, j\omega\hat{w})$, that is the velocity of the plate's midplane Ω_p . With the no-slip and no-penetration conditions, the fluid velocity at the plate's top and bottom surfaces, $\hat{\mathbf{u}}_f^t$ and $\hat{\mathbf{u}}_f^b$ respectively as depicted in Fig. 2.15, are equal to $\hat{\mathbf{u}}_p$, resulting in

$$\hat{\mathbf{u}}_f^t = \hat{\mathbf{u}}_f^b = (0, 0, j\omega\hat{w})^T. \quad (2.26)$$

which is equal to the fluid velocity at the plate's top surface $\hat{\mathbf{u}}_f^t$. Applying the conti-

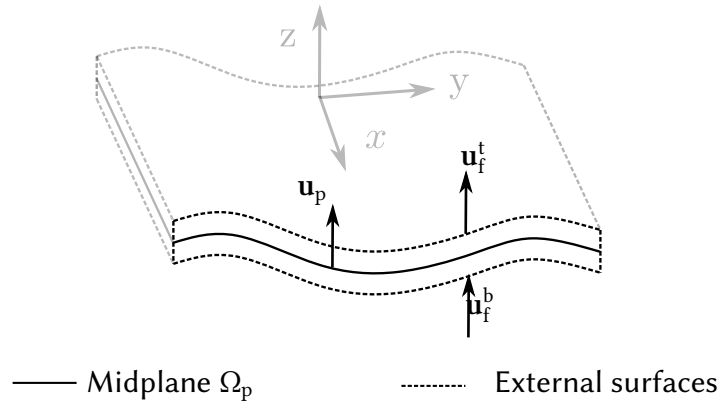


Figure 2.15: Kinematic interface conditions of the fluid flow around a micro-plate.

nity equation (Eq. 2.16) to the plate's top and bottom surfaces with the no-slip and no-penetration boundary conditions (Eq.2.26) yields $\partial\hat{u}_z^t/\partial z = \partial\hat{u}_z^b/\partial z = 0$. Thus, the hydrodynamic force given by Eq. 2.25 becomes

$$\hat{F}_{\text{hydro}} = \hat{p}^t - \hat{p}^b = \Delta\hat{p}. \quad (2.27)$$

$\Delta\hat{p}$ is typically called the pressure jump. Thus, for a micro-plate undergoing purely out-of-plane displacement with small amplitude oscillations, the hydrodynamic force is simply the result of the pressure difference between the top and bottom surfaces.

2.4 Conclusions

Here we presented a dimensional analysis of the micro-flow around micro-plates with typical fluids to define a proper set of governing equations. We conclude that the governing equations to predict the micro-plate dynamics are a) the Kirchhoff-plate equation for the elastic body dynamics and b) the Stokes Equations for fluid dynamics. These equations are coupled through the non-slip and no-penetration boundary conditions and the hydrodynamic force. We defined the set of governing equations for the micro-plate-fluid interaction problem in the frequency domain and determined the hydrodynamic force as a pressure difference between top and bottom plate surfaces. In the next chapters, we develop the semi-numerical method to solve this system of equations.

3 Numerical methods for the plate equation

In this chapter, numerical methods to solve the Kirchhoff plate equation (in the absence of the hydrodynamic force) are introduced and results between different methods are compared in order to determine a suitable numerical method to solve the micro-plate-fluid interaction problem.

3.1 Isotropic and anisotropic material models

In Chapter 2 the Kirchhoff plate equation for isotropic material was introduced. However, silicon is the most common material for MEMS resonators [5], and silicon is an anisotropic material [74]. Hence, a modification to the plate equation is required to account for the material anisotropy. This modification is achieved using a fourth-order elasticity tensor \mathbf{C} and writing the plate equation in Einstein's summing notation with the indices $\alpha, \beta, \gamma,$ and δ to represent x - and y -directions, yielding

$$\frac{h^3}{12} C_{\alpha\beta\gamma\delta} \hat{w}_{,\alpha\beta\gamma\delta} - \omega^2 \rho h \hat{w} = \hat{F}. \quad (3.1)$$

$C_{\alpha\beta\gamma\delta}$ are the elements of the fourth-order elasticity tensor \mathbf{C} and the indices following a comma in the sub-scripted variables represent spatial derivatives in the index direction.

The non-zero values of the fourth-order elasticity tensor and density of silicon are shown in Table 3.1 for a silicon wafer in the standard (100) orientation [74]. Throughout the thesis, when the plate is defined with orthotropic properties, we refer to Table 3.1 for silicon's elastic properties.

Parameter	Value
C_{xxxx}, C_{yyyy} [GPa]	194.5
C_{xxyy}, C_{yyxx} [GPa]	35.7
$C_{xyxy}, C_{xyyx}, C_{yxxy}, C_{yxyx}$ [GPa]	50.9
ρ [kg m ⁻³]	2330

Table 3.1: Material properties of silicon as anisotropic material [74].

For comparisons with previously existing methods for beams, it is preferable to approximate silicon as an isotropic material. For these cases, the fourth-order constitutive tensor $C_{\alpha\beta\gamma\delta}$ for an isotropic material is written from the isotropic values of Young's modulus E and Poisson coefficient ν as

$$C_{\alpha\beta\gamma\delta} = \left[\frac{E (\delta_{\alpha\gamma} \delta_{\beta\delta} + \delta_{\alpha\delta} \delta_{\beta\gamma})}{2(1 + \nu)} + \frac{E\nu}{1 - \nu^2} \delta_{\alpha\beta} \delta_{\gamma\delta} \right], \quad (3.2)$$

where $\delta_{\alpha\gamma}$ is the Kronecker delta. For silicon, the isotropic values are presented in Table 2.2.

From hereon the plate equation is shown using the index notation with the elasticity tensor \mathbf{C} , which allows both for the isotropic and anisotropic formulation. In addition, index notation is compact which makes it easier for the following definitions.

3.2 Boundary conditions

The boundaries of the plate's mid-plane Ω_p are denoted by $\partial\Omega_p$. $\partial\Omega_p$ is, in itself, divided into four regions depending on the boundary conditions applied in such a region. The region of $\partial\Omega_p$ in which the displacement \hat{w} is restricted to g is defined as Γ_c , yielding

$$\hat{w} = g \text{ on } \Gamma_c. \quad (3.3)$$

Regions of the plate's boundaries where the rotation angle is restricted to θ are defined as Γ_θ . At Γ_θ , the boundary condition is written in summing notation as

$$\hat{w}_{,\alpha} n_\alpha^b = \theta \text{ on } \Gamma_\theta. \quad (3.4)$$

n_α^b denotes the component of the unit outward normal at the boundaries $\partial\Omega_p$ as shown in Fig. 3.1. Fig. 3.1 shows a cantilevered plate whose left edge at $x = 0$ is clamped and free at all other edges.

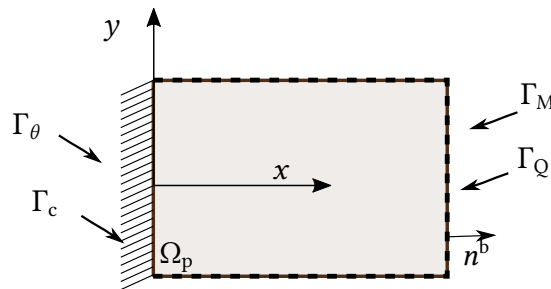


Figure 3.1: The plate's left boundary Γ_c and Γ_θ is clamped and all others are free Γ_M and Γ_Q (dashed line).

When a plate is considered with a clamped edge, both the rotation angle θ and the displacement g are zero at this edge, and $\Gamma_\theta = \Gamma_c$. A cantilevered plate is clamped at one edge and free at the other edges. The free edge boundary conditions are defined as

$$\frac{h^3}{12} C_{\alpha\beta\gamma\delta} \hat{w}_{,\gamma\delta} n_\alpha^b n_\beta^b = M \text{ on } \Gamma_M, \quad (3.5)$$

and

$$\frac{h^3}{12} C_{\alpha\beta\gamma\delta} \hat{w}_{,\beta\gamma\delta} n_\alpha^b = Q_s \text{ on } \Gamma_Q. \quad (3.6)$$

Eqs. 3.5 and 3.6 impose the momentum and shear forces at the edges Γ_M and Γ_Q to be M and Q_s , respectively. Free edge conditions imply that $\Gamma_Q = \Gamma_M$.

3.3 Finite element method for the plate equation

An analytic solution to the strong form of the Kirchhoff PDE (Eq. 3.1) with cantilevered boundary conditions is not known [65], and therefore a numerical technique to solve the plate dynamics is required. A family of methods to numerically solve a PDE is the Galerkin method, in which the equation's weak form is solved instead of the PDE's strong form. The weak form of the Kirchhoff PDE is obtained introducing a Hilbert function space \mathcal{W} , and stating the problem as: Find $\bar{w} \in \mathcal{W}$ such that

$$a(\bar{w}, v) = l(v), \forall v \in \mathcal{W}. \quad (3.7)$$

$a(\bar{w}, v)$ is known as the bilinear form of the PDE, and $l(v)$ the linear form.

The Galerkin method consists in the dimension reduction from the Hilbert function space \mathcal{W} to finite function spaces $\mathcal{W}^h \subset \mathcal{W}$ and $\mathcal{V}^h \subset \mathcal{W}$, and defining the problem as: Find $w^h \in \mathcal{W}^h$ such that

$$a(w^h, v^h) = l(v^h), \forall w^h \in \mathcal{V}^h. \quad (3.8)$$

\mathcal{W}^h is called the test function space, w^h the test function, \mathcal{V}^h is the trial function space, v^h the trial function. If the test and trial function spaces are the same, the resulting bilinear form is symmetric and the method is called a Ritz-Galerkin method [81]. Among the Ritz-Galerkin methods, the finite element method (FEM) is one of the most known. Here we use FEM to determine the plate's dynamics numerically since the solution of the Kirchhoff plate equation with FEM is the object of several studies [82, 83, 84, 85, 65, 86] and good agreement between FEM and analytic solutions were obtained.

In FEM, the most commonly used function space is the function space of the Lagrangian FE shape functions of degree k . A function space is defined considering a partitioning of the plate's mid-plane $\mathcal{P}(\Omega_p)$ in triangular elements E_i , $i = 1, \dots, N_t$. N_t is the total number of triangles of the partitioning, equals to $4N_y N_x$ where N_y and N_x are the number of quadrilateral elements in y - and x -direction, respectively. Each quadrilateral element is divided into four triangles as shown in Fig. 3.2. A structured mesh is considered because of its simplicity, but any unstructured mesh could be used without loss of generality. The union of all internal edges e_i of the partitioning $\mathcal{P}(\Omega_p)$ is denoted by $\tilde{\Gamma}$, and the union of internal edges and external boundaries is denoted by $\Gamma = \tilde{\Gamma} \cup \partial\Omega_p$.

Using the partitioning $\mathcal{P}(\Omega_p)$ a trial function space \mathcal{W}^h is defined as

$$\mathcal{W}^h = \{ \hat{w}^h \in H^2(\Omega_p) : \hat{w}^h|_{E_i} \in P^k(E_i) \forall E_i \in \mathcal{P}(\Omega_p), \hat{w}^h|_{\Gamma_c} = 0 \}, \quad (3.9)$$

and the test function space \mathcal{V}^h is

$$\mathcal{V}^h = \{ v^h \in H^2(\Omega_p) : v^h|_{E_i} \in P^k(E_i) \forall E_i \in \mathcal{P}(\Omega_p), v^h|_{\Gamma_c} = 0 \}. \quad (3.10)$$

$P^k(E_i)$ are the C^0 continuous Lagrangian finite element (FE) shape functions of degree k defined on the element E_i . The Dirichlet boundary condition at Γ_c appears as a direct restriction of the trial function space \mathcal{W}^h .

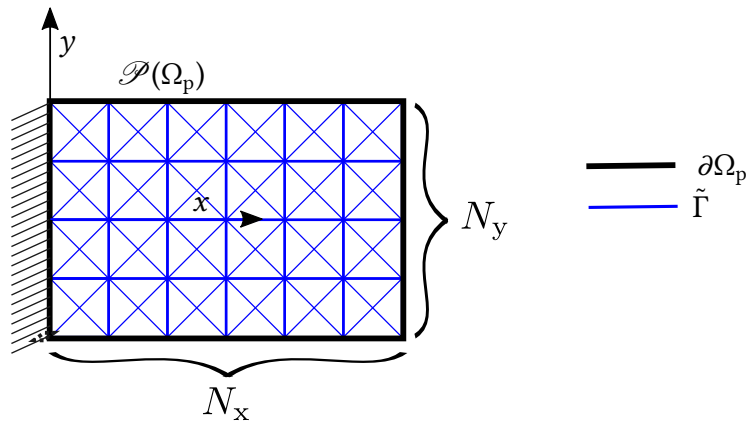


Figure 3.2: Partitioning of the plate's mid surface Ω_p in N_x by N_y quadrilateral elements, each one divided into four triangles. The union of all internal edges is $\tilde{\Gamma}$, and the external are denoted by $\partial\Omega_p$.

C^0 continuity means the functions v^h are continuous, but the derivatives of v^h are discontinuous at the edges Γ . To exemplify the discontinuity of the derivative of the basis functions, let us define a partitioning of the plate's domain in 3 by 3 quadrilateral elements as depicted in 3.3. The non-dimensional axes x^* and y^* are introduced as $x^* = x/l$ and $y^* = y/b$.

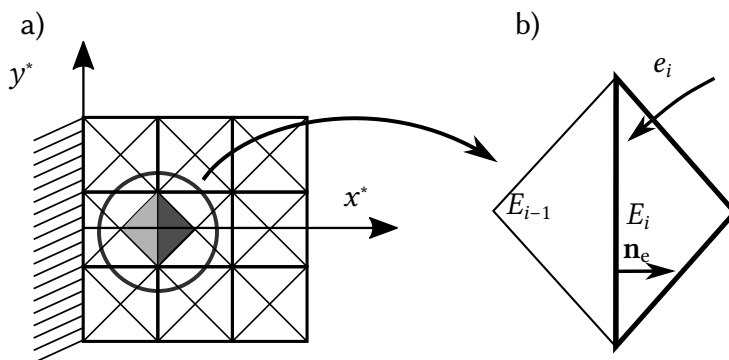


Figure 3.3: a) Example of the partitioning of the plate's mid surface Ω_p in 3 by 3 quadrilateral elements, each one divided in four triangles. b) Single element E_i with the enclosing edges e_i and normal \mathbf{n}_e .

Fig. 3.4 shows examples of the basis functions v^h of the two-dimensional Lagrange FE shape functions with degrees 1, 2 and 3 in this partitioning with 3 x 3 quadrilateral elements. The basis functions are depicted with a maximum at the domain's geometric center, that is $x^* = 0.5$ and $y^* = 0$. Fig. 3.4 shows the test function v_h and the x -derivative of v_h at the position $y^* = 0$. The blue line marks the position of the edges of the element E_i in which the basis function is defined. Note that the function v^h is continuous over the entire plate domain and at the edges e_i . The derivatives of v^h , on the other hand, are discontinuous at the edges of the element E_i on which v^h is defined. Here, these discontinuities occur at $x^* = 0.33333$, $x^* = 0.5$ and $x^* = 0.66666$.

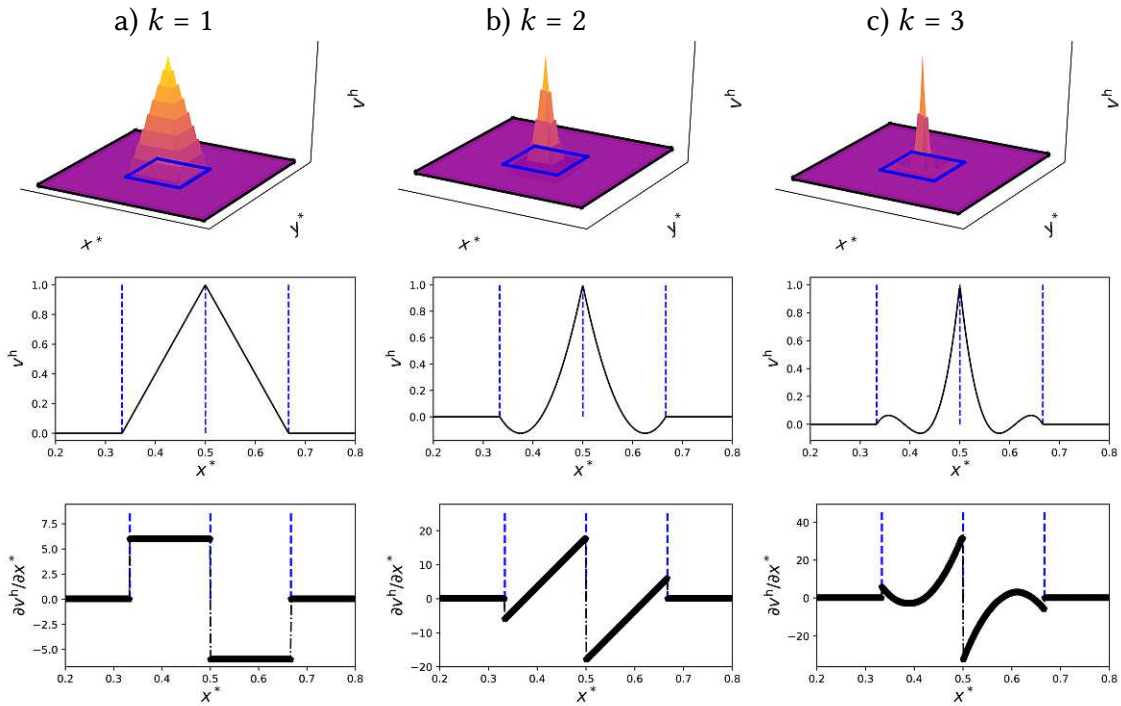


Figure 3.4: Example of Lagrangian polynomial basis functions and the x -derivatives of different degrees k equals to a) 1, b) 2 and c) 3. On the top, the solid blue line represents the edges of the quadrilateral element. On the top, the basis function in two dimensions, on the middle the basis function at $y^* = 0$, and on the bottom the x -derivative of the basis function at $y^* = 0$, where the dashed blue lines represent the location of the triangular element's edges.

To solve the Kirchhoff plate equation, the solution function space in a conformal FEM setting is required to be H^2 [83, 85], i.e., the Sobolev space of functions with square-integrable generalized second derivatives. In essence, C^1 continuity of the basis functions in the solution function space is required, so that no discontinuities in the slope of the displacement \hat{w} exist. C^1 continuity means the first derivatives of the basis functions are continuous. However, C^1 continuous basis functions in two dimensions are very challenging to implement [85, 65].

An alternative to C^1 basis functions are continuous/discontinuous Galerkin methods [85, 87, 88, 89]. Continuous/discontinuous (C/DC) methods combine standard Lagrangian C^0 -continuous basis functions from the defined function spaces \mathcal{V}^h and \mathcal{W}^h with discontinuous methods such as interior penalty (IP) methods [85, 89, 82] or lifting operator (LO) methods [83, 90, 84, 91] to enforce C^1 continuity of the solution.

The weak form of Eq. 3.1 with C/DC methods is obtained considering a single triangular element E_i , and noting that the triangulation of the entire plate domain Ω_p is the sum of all internal elements as $\mathcal{P}(\Omega_p) = \sum_{i=1}^{N_t} E_i$. The local weak form of Eq. 3.1 on the element E_i is: find \hat{w}^h in \mathcal{W}^h such that

$$\int_{E_i} \frac{h^3}{12} C_{\alpha\beta\gamma\delta} \hat{w}_{,\alpha\beta\gamma\delta}^h v^h d\Omega - \int_{E_i} \omega^2 \rho h \hat{w}^h v^h d\Omega = \int_{E_i} \hat{F} v^h d\Omega \quad \forall v^h \in \mathcal{V}^h. \quad (3.11)$$

Here the integral with $d\Omega$ stands for two-dimensional surface integrals. Using Green's theorem, Eq. 3.11 is written in terms of one surface integral and two edge integrals as

$$\int_{E_i} \frac{h^3}{12} C_{\alpha\beta\gamma\delta} \hat{w}_{,\alpha\beta}^h v_{,\gamma\delta}^h d\Omega - \int_{e_i} \frac{h^3}{12} C_{\alpha\beta\gamma\delta} \hat{w}_{,\alpha\beta}^h v_{,\delta}^h n_{\delta}^e n_{\gamma}^e ds + \int_{e_i} \frac{h^3}{12} C_{\alpha\beta\gamma\delta} \hat{w}_{,\alpha\beta\gamma}^h v^h n_{\delta}^e ds - \int_{E_i} \omega^2 \rho h \hat{w}^h v^h d\Omega = \int_E \hat{F} v^h d\Omega \quad \forall v^h \in \mathcal{V}^h, \quad (3.12)$$

where ds is the line integral at the edges e_i around the element E_i . n_{δ}^e stand for the components of the normal vector at the edges e_i . The normal vector \mathbf{n}^e is usually defined in the direction of the element E_i with lower index i to the higher index as shown in Fig. 3.3 from element E_{i-1} to E_i .

Note in Eq. 3.12 that the edge integrals take into account derivatives of the test v_h and trial \hat{w}_h function at the edges e_i . Using the C^0 functions as defined in the function spaces \mathcal{V}^h and \mathcal{W}^h , this poses a challenge since the derivatives of these functions are not continuous at the edges as seen in Fig. 3.4.

To account for discontinuities in v^h and \hat{w}^h , C/DC methods use the average $\langle \cdot \rangle$ and the jump $[[\cdot]]$ operators at the internal edges e_i to measure the discontinuities. For two internal elements E_i and E_{i-1} that share an edge as shown in Fig. 3.3 the average operator of the derivative of the test function v^h in the direction α at the edge e_i is

$$\langle v_{,\alpha}^h \rangle = 1/2 (v_{,\alpha}^{h,i} + v_{,\alpha}^{h,i-1}), \quad (3.13)$$

where the i and $i-1$ superscripts mean evaluation of the derivative at the edge e_i in the elements E^i and E^{i-1} , respectively.

The jump of the derivative of v^h in the normal direction \mathbf{n}_e at the edge e_i is

$$[[v_{,\alpha}^h n_{\alpha}^e]] = v_{,\alpha}^{h,i} n_{\alpha}^e - v_{,\alpha}^{h,i-1} n_{\alpha}^e. \quad (3.14)$$

The jump and average operator at the left edge of an element E_i (as depicted in Fig. 3.3) are represented in Fig. 3.5 for a polynomial function of degree $k = 2$. Since \mathbf{n}_e at the left edge e_i is simply $(1, 0)^T$, the average and jump operator takes into account only the derivative in x -direction.

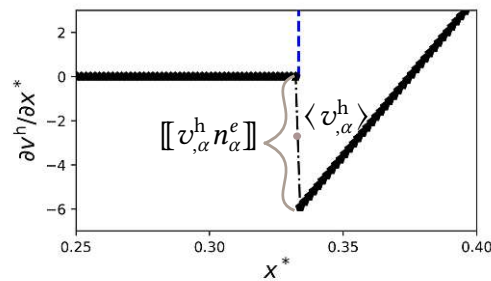


Figure 3.5: Jump and average operators representation at the left edge e_i of element E_i for a test function of degree $k = 2$.

Expanding Eq. 3.12 to consider the entire plate partitioning $\mathcal{P}(\Omega_p) = \sum_{i=1}^{N_i} E_i$ and applying the jump operator at all the internal edges Γ yields

$$\begin{aligned} \int_{\Omega_p} \frac{h^3}{12} C_{\alpha\beta\gamma\delta} \hat{w}_{,\alpha\beta}^h v_{,\gamma\delta}^h d\Omega - \int_{\tilde{\Gamma}} \frac{h^3}{12} \llbracket C_{\alpha\beta\gamma\delta} \hat{w}_{,\alpha\beta}^h v_{,\delta}^h n_\delta^e \rrbracket n_\gamma^e ds + \int_{\tilde{\Gamma}} \frac{h^3}{12} \llbracket C_{\alpha\beta\gamma\delta} \hat{w}_{,\alpha\beta\gamma}^h v^h \rrbracket n_\delta^e ds \\ - \int_{\partial\Omega_p} \frac{h^3}{12} C_{\alpha\beta\gamma\delta} \hat{w}_{,\alpha\beta}^h v_{,\delta}^h n_\gamma^b ds + \int_{\partial\Omega_p} \frac{h^3}{12} C_{\alpha\beta\gamma\delta} \hat{w}_{,\alpha\beta\gamma}^h v^h n_\delta^b ds \\ - \int_{\Omega_p} \omega^2 \rho h \hat{w}^h v^h d\Omega = \int_{\Omega_p} \hat{F} v^h d\Omega \quad \forall v^h \in \mathcal{V}^h \end{aligned} \quad (3.15)$$

where note that $\partial\Omega_p$ are the external edges of the plate domain, and $\tilde{\Gamma}$ are all internal edges of the plate triangulation.

Using the identity

$$\llbracket uv \rrbracket = \llbracket u \rrbracket \{v\} + \llbracket v \rrbracket \{u\}, \quad (3.16)$$

Eq. 3.15 is expanded in terms of individual jump and average operators as

$$\begin{aligned} \int_{\Omega_p} \frac{h^3}{12} C_{\alpha\beta\gamma\delta} \hat{w}_{,\alpha\beta}^h v_{,\gamma\delta}^h d\Omega - \int_{\tilde{\Gamma}} \frac{h^3}{12} \llbracket C_{\alpha\beta\gamma\delta} \hat{w}_{,\alpha\beta}^h \rrbracket \{v_{,\delta}^h n_\gamma^e\} ds - \int_{\tilde{\Gamma}} \frac{h^3}{12} \{C_{\alpha\beta\gamma\delta} \hat{w}_{,\alpha\beta}^h\} \llbracket v_{,\delta}^h n_\gamma^e \rrbracket ds \\ + \int_{\tilde{\Gamma}} \frac{h^3}{12} \llbracket C_{\alpha\beta\gamma\delta} \hat{w}_{,\alpha\beta\gamma}^h \rrbracket \{v^h n_\delta^e\} ds + \int_{\tilde{\Gamma}} \frac{h^3}{12} \{C_{\alpha\beta\gamma\delta} \hat{w}_{,\alpha\beta\gamma}^h\} \llbracket v^h n_\delta^e \rrbracket ds \\ - \int_{\partial\Omega_p} \frac{h^3}{12} C_{\alpha\beta\gamma\delta} \hat{w}_{,\alpha\beta}^h v_{,\delta}^h n_\gamma^b ds + \int_{\partial\Omega_p} \frac{h^3}{12} C_{\alpha\beta\gamma\delta} \hat{w}_{,\alpha\beta\gamma}^h v^h n_\delta^b ds \\ - \int_{\Omega_p} \omega^2 \rho h \hat{w}^h v^h d\Omega = \int_{\Omega_p} \hat{F} v^h d\Omega \quad \forall v^h \in \mathcal{V}^h \end{aligned} \quad (3.17)$$

The solution \hat{w} is continuous in the entire plate domain, and therefore also the numerical approximation \hat{w}^h must be continuous for consistency [82, 85]. As a result, the integrals containing the jump operators with the derivatives of \hat{w}^h (second and fourth terms in Eq. 3.17) are zero. In addition, the test function v^h is C^0 continuous, therefore the jump of v^h is also zero. Eq. 3.17 is simplified to

$$\begin{aligned} \int_{\Omega_p} \frac{h^3}{12} C_{\alpha\beta\gamma\delta} \hat{w}_{,\alpha\beta}^h v_{,\gamma\delta}^h d\Omega - \int_{\tilde{\Gamma}} \frac{h^3}{12} \{C_{\alpha\beta\gamma\delta} \hat{w}_{,\alpha\beta}^h\} \llbracket v_{,\delta}^h n_\gamma^e \rrbracket ds \\ - \int_{\partial\Omega_p} \frac{h^3}{12} C_{\alpha\beta\gamma\delta} \hat{w}_{,\alpha\beta}^h v_{,\delta}^h n_\gamma^b ds + \int_{\partial\Omega_p} \frac{h^3}{12} C_{\alpha\beta\gamma\delta} \hat{w}_{,\alpha\beta\gamma}^h v^h n_\delta^b ds \\ - \int_{\Omega_p} \omega^2 \rho h \hat{w}^h v^h d\Omega = \int_{\Omega_p} \hat{F} v^h d\Omega \quad \forall v^h \in \mathcal{V}^h. \end{aligned} \quad (3.18)$$

The shear force boundary condition defined in Eq. 3.6 is strongly imposed in Eq. 3.18 at Γ_Q . In Γ_c , \hat{v}^h is zero resulting in a zero value for the integral containing $\hat{w}_{,\alpha\beta\gamma}^h$. The

moment boundary condition can also be strongly imposed to Eq. 3.18, resulting in

$$\begin{aligned}
& \int_{\Omega_p} \frac{h^3}{12} C_{\alpha\beta\gamma\delta} \hat{w}_{,\alpha\beta}^h v_{,\gamma\delta}^h d\Omega - \int_{\tilde{\Gamma}} \frac{h^3}{12} \{C_{\alpha\beta\gamma\delta} \hat{w}_{,\alpha\beta}^h\} \llbracket v_{,\delta}^h n_\gamma^e \rrbracket ds \\
& \quad - \int_{\Gamma_c} \frac{h^3}{12} C_{\alpha\beta\gamma\delta} \hat{w}_{,\alpha\beta}^h v_{,\delta}^h n_\gamma^b ds - \int_{\Omega_p} \omega^2 \rho h \hat{w}^h v^h d\Omega \\
& = \int_{\Omega_p} \hat{F} v^h d\Omega + \int_{\Gamma_Q} Q_s v^h ds + \int_{\Gamma_M} M v_\beta^h n_\beta^b ds \quad \forall v^h \in \mathcal{V}^h. \tag{3.19}
\end{aligned}$$

Solution of the Eq. 3.19 requires the implementation of a method to impose C^1 continuity, that is, $\llbracket v_{,\delta}^h n_\delta^e \rrbracket = 0$. Among the different C/DC methods for the Kirchhoff plate equation, we explore here two established methods: the interior penalty (IP) method [82] and the lifting operator (LO) method[83].

3.3.1 Interior Penalty Method

The IP method consists of adding terms to Eq. 3.19 to obtain a symmetric bilinear form and to penalize the jumps $\llbracket v_{,\delta}^h n_\delta^e \rrbracket$ over all the internal edges $\tilde{\Gamma}$. The resulting weak form is

$$\begin{aligned}
& \int_{\Omega_p} \frac{h^3}{12} C_{\alpha\beta\gamma\delta} \hat{w}_{,\alpha\beta}^h v_{,\gamma\delta}^h d\Omega - \int_{\tilde{\Gamma}} \frac{h^3}{12} \{C_{\alpha\beta\gamma\delta} \hat{w}_{,\alpha\beta}^h\} \llbracket v_{,\delta}^h n_\gamma^e \rrbracket ds - \int_{\tilde{\Gamma}} \frac{h^3}{12} \llbracket C_{\alpha\beta\gamma\delta} \hat{w}_{,\alpha\beta}^h \rrbracket \{v_{,\delta}^h n_\gamma^e\} ds \\
& \quad + \int_{\tilde{\Gamma}} \frac{h^3}{12} \frac{\tau_{ip}}{h_E} C_{\alpha\beta\gamma\delta} \llbracket \hat{w}_{,\alpha}^h n_\beta \rrbracket \llbracket v_{,\gamma}^h n_\delta \rrbracket ds + \int_{\Gamma_c} \frac{h^3}{12} \frac{\tau_{ip}}{2h_E} C_{\alpha\beta\gamma\delta} \hat{w}_{,\alpha}^h n_\beta v_{,\gamma}^h n_\delta ds \\
& \quad - \int_{\Gamma_c} \frac{h^3}{12} C_{\alpha\beta\gamma\delta} \hat{w}_{,\alpha\beta}^h v_{,\delta}^h n_\gamma^b ds - \int_{\Omega_p} \omega^2 \rho h \hat{w}^h v^h d\Omega = \int_{\Omega_p} \hat{F} v^h d\Omega \\
& \quad + \int_{\Gamma_Q} Q_s v^h ds + \int_{\Gamma_M} M v_\beta^h n_\beta^b ds \quad \forall v^h \in \mathcal{V}^h \tag{3.20}
\end{aligned}$$

The third term in Eq. 3.20 was added for symmetry purposes. The fourth integral term in Eq. 3.20 is the penalization term, which ensures $\llbracket \hat{w}_{,\alpha}^h n_\alpha \rrbracket \rightarrow 0$ for a suitable τ_{ip} and imposes C^1 continuity of \hat{w}^h and v^h [82]. The slope boundary condition is weakly imposed with the integral of the fifth term on Γ_c . The bilinear form $a(\hat{w}^h, \hat{v}^h)$ of the Kirchhoff PDE with the IP method is the left-hand side (LHS) of Eq. 3.20, and the linear form $a(\hat{v}^h)$ is the right-hand side (RHS) of Eq. 3.20.

The value of τ_{ip} has to be determined empirically such that the method is convergent [85, 82, 92]. The procedure for determining τ_{ip} is discussed in Section 3.4.

3.3.2 Lifting operator

An alternative C/DC method for the Kirchhoff plate equation was proposed based on the lifting operator (LO) [83, 84, 91]. The LO method consists in applying a lifting operation

on the element edges e_i between two elements E_i and E_{i+1} as

$$\int_{E_i+E_{i+1}} s_{\alpha\beta} r_{\alpha\beta} d\Omega = - \int_{e_i} \{s_{\alpha\beta} n_{\alpha}^e\} \llbracket v_{,\beta}^h n_{\beta}^e \rrbracket ds, \quad (3.21)$$

where $s_{\alpha\beta}$ and $r_{\alpha\beta}$ are trial and test functions defined from the function spaces

$$\mathcal{R}^h = \{r_{\alpha\beta} \in L^2(\Omega_p) : r_{\alpha\beta}|_{E_i} \in P^k(E_i) \forall E_i \in \mathcal{P}(\Omega_p)\}, \quad (3.22)$$

and

$$\mathcal{S}^h = \{s_{\alpha\beta} \in L^2(\Omega_p) : s_{\alpha\beta}|_{E_i} \in P^k(E_i) \forall E_i \in \mathcal{P}(\Omega_p)\}, \quad (3.23)$$

respectively.

Introducing the lifting operation in all internal edges of the plate's partitioning yields a weak form as

$$\begin{aligned} & \int_{\Omega_p} \frac{h^3}{12} C_{\alpha\beta\gamma\delta} \hat{w}_{,\alpha\beta}^h v_{,\gamma\delta}^h d\Omega + \int_{\Omega_p} \frac{h^3}{12} C_{\alpha\beta\gamma\delta} \hat{w}_{,\alpha\beta}^h r_{\gamma\delta} (v_{,\gamma}^h n_{\gamma}^e) d\Omega \\ & + \int_{\Omega_p} \frac{h^3}{12} C_{\alpha\beta\gamma\delta} s_{\alpha\beta} (\hat{w}_{,\alpha}^h n_{\alpha}^e) v_{,\gamma\delta}^h d\Omega + \int_{\Omega_p} \tau_{LO} \frac{h^3}{12} C_{\alpha\beta\gamma\delta} s_{\alpha\beta} (\hat{w}_{,\alpha}^h n_{\alpha}^e) r_{\gamma\delta} (v_{,\gamma}^h n_{\gamma}^e) d\Omega \\ & + \int_{E_c} \tau_{LO} \frac{h^3}{12} C_{\alpha\beta\gamma\delta} s_{\alpha\beta} (\hat{w}_{,\alpha}^h n_{\alpha}^e) r_{\gamma\delta} (v_{,\gamma}^h n_{\gamma}^e) d\Omega - \int_{\Omega_p} \omega^2 \rho h \hat{w}^h v^h d\Omega \\ & = \int_{\Omega_p} \hat{F} v^h d\Omega \quad \forall v^h \in \mathcal{V}^h, \end{aligned} \quad (3.24)$$

where E_{θ} stands for the elements at the clamped edges Γ_{θ} . The bilinear form $a(\hat{w}^h, \hat{v}^h)$ of the Kirchhoff PDE with the LO method is the LHS of Eq. 3.24, and the linear form $a(\hat{v}^h)$ is the RHS of Eq. 3.24. For details on the derivation of the LO method, we refer to [83, 84, 91]. The advantage of the LO method is that it is stable for any coefficient $\tau_{LO} > 0$. However, a limitation of the LO method is that the lifting operation requires local projections of $\llbracket v_{,\beta}^h n_{\beta}^e \rrbracket$ in pair-wise elements that share an internal edge, which increases the computation time [84].

3.4 Numerical results

3.4.1 Static simply supported square plate

To check the implementation and convergence of both methods and their time performance, we implement both methods for a plate under conditions whose analytic solution is known. Consider a square plate simply supported on all sides as depicted in Fig. 3.6. Simply supported plate on all edges means only the displacement and momentum boundary conditions as defined by Eqs. 3.3 and 3.5 are imposed.

Material is considered silicon with the properties of isotropic material with values defined in Table 2.2, and the plate has a length $l = 1$ m, width $b = 1$ m and thickness $h = 0.01$ m. The plate is under the action of a static force distribution equals

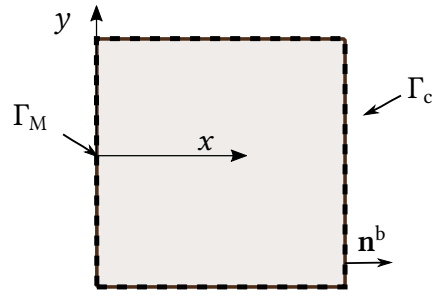


Figure 3.6: Simply supported square plate.

$$F = \sin \frac{\pi x}{l} \sin \frac{\pi y}{b}. \quad (3.25)$$

The analytic static displacement is w_{analytic} is [82]

$$w_{\text{analytic}} = \frac{lb}{\pi^4 E(1 - \nu_p^2) h^3} \sin \frac{\pi x}{l} \sin \frac{\pi y}{b}. \quad (3.26)$$

Fig. 3.7 shows the analytic solution and the numerical results obtained with a 16 x 16 mesh in both methods and with constants $\tau_{\text{IP}} = 100$ and $\tau_{\text{LO}} = 100$. Both methods result in similar displacement w which is similar to the analytic solution.

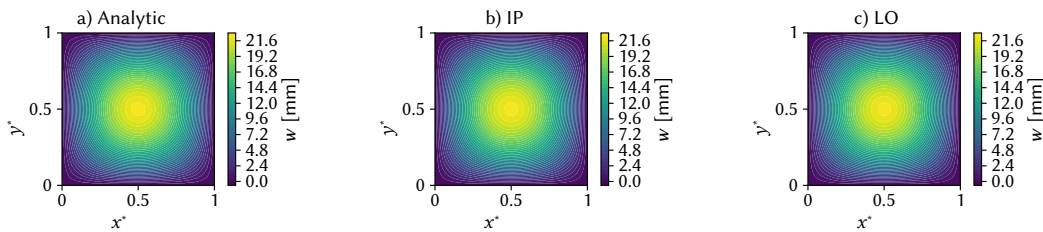


Figure 3.7: Static displacement of the simply supported static plate obtained a) analytically, b) with the IP method and c) with the LO method.

To quantify the error between numerical and analytic solutions, we introduce the error norm $\epsilon_{\text{analytic}}$ as

$$\epsilon_{\text{analytic}} = \|w^h - w_{\text{analytic}}\|_{L^2}, \quad (3.27)$$

where $\|\cdot\|_{L^2}$ denotes the L^2 norm as

$$\|v\|_{L^2} = \int_{\Omega_p} |v|^2 d\Omega. \quad (3.28)$$

For numerical methods, convergence between numerical solutions for consecutively refined FE-meshes is required. $\epsilon_{\text{convergence}}$ is introduced to quantify the convergence of

the method with the number of mesh elements as

$$\epsilon_{\text{convergence}} = \frac{\|\hat{\mathbf{w}}^{i+1} - \hat{\mathbf{w}}^i\|_{L^2}}{\|\hat{\mathbf{w}}^i\|_{L^2}}, \quad (3.29)$$

where $\hat{\mathbf{w}}^{i+1}$ and $\hat{\mathbf{w}}^i$ are solutions obtained with FE-meshes consistent of $2^i \times 2^i$ ($N_x \times N_y$) elements.

Fig. 3.8 shows the error $\epsilon_{\text{analytic}}$ as well as the convergence difference $\epsilon_{\text{convergence}}$ and the computation time with the IP and LO methods. The degree of the polynomial spaces V^h and W^h is two, which results in both $\epsilon_{\text{analytic}}$ and $\epsilon_{\text{convergence}}$ converging with an exponent equals two. While the convergence rates are similar with both methods, the elapsed time of the two methods greatly differs. The simulation time of the LO method grows with the square of N_x , while the IP method's time increases only with $N_x^{0.12}$.

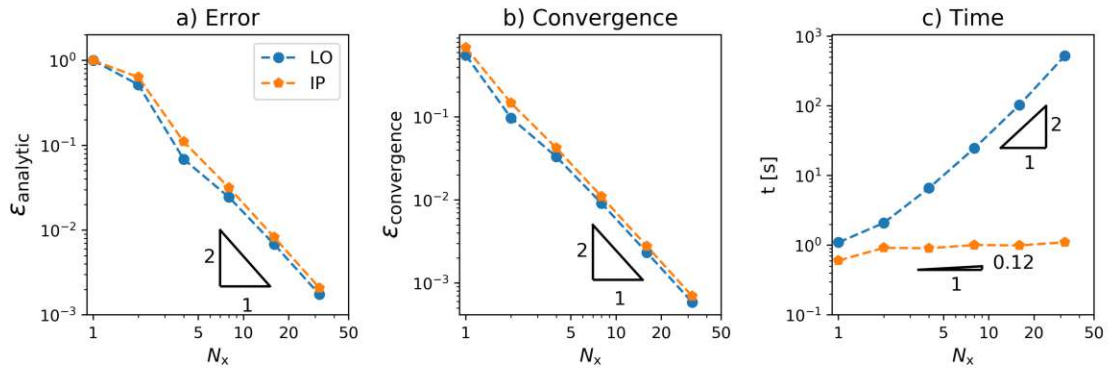


Figure 3.8: a) Error, b) convergence and c) elapsed time of the IP and LO methods for the simply supported static plate. The degree of the polynomial space is 2.

Increasing the degree of the polynomial spaces V^h and W^h to three results in higher convergence rates equal 4 for both methods as seen in Fig. 3.9. These convergence rates of 2 for $k = 2$, and four for $k = 3$ agree with the predictions reported previously [82, 83, 84, 91].

Increasing the polynomial degree k does not alter the slope of the elapsed time for each method, however higher k results in larger elapsed time as seen in Fig. 3.10. Thus, time-wise, the most efficient method is the IP method, which is much faster than the LO method.

In addition, the convergence rate with both methods is independent of the coefficients τ_{IP} and τ_{LO} as seen in Fig. 3.11. Provided τ_{IP} and τ_{LO} are greater than 1, both methods converge with the same convergence rate.

Therefore, for the static plate, both methods converge provided the constants are greater than 1 with a convergence rate equal to 2 for polynomial degree equals 2 and a convergence rate equals 4 for $k = 3$. Notably, the IP method is much faster than the LO method. The elapsed time by the IP method increases with the FE-mesh as $t = N_x^{0.12}$, while the LO method increases with $t = N_x^2$. This difference in time performance occurs because of the additional function space and projections required by the lifting operation, which in the IP method is not necessary.

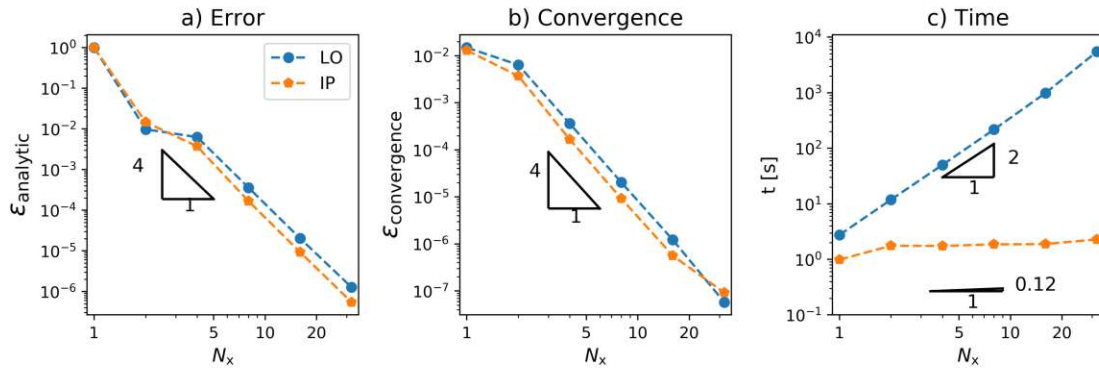


Figure 3.9: a) Error, b) convergence and c) elapsed time of the IP and LO methods for the simply supported static plate. The degree of the polynomial space is 3.

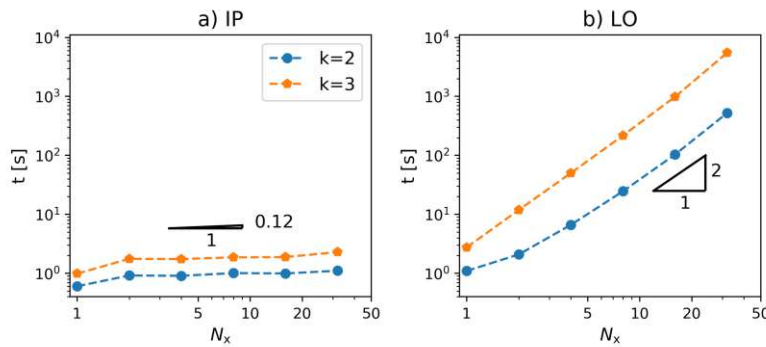


Figure 3.10: Elapsed time for the a) IP and b) LO methods with different values of k .

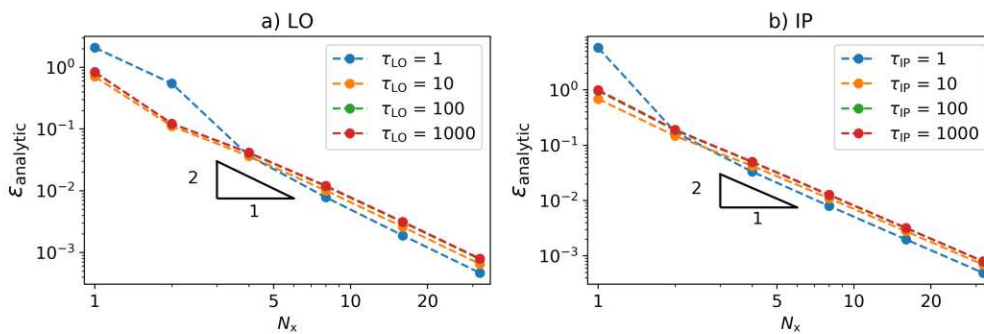


Figure 3.11: Error with the analytic solution for the a) LO method with different τ_{LO} constants and b) IP method with different τ_{IP} constants. The degree of the polynomial space is 2.

3.4.2 Cantilevered plate with a sinusoidal force

With both methods implemented and validated for the static plate, we alter the conditions to the cantilevered plate case with a sinusoidal force \hat{F} and with the inertia term in both formulations. Since the Kirchhoff plate equation has no analytic solutions with the cantilevered boundary conditions, a slender beam is an ideal example since the res-

onance frequencies of a slender plate are approximately the frequencies of the slender beam as determined by Eq. 2.8. Here, a slender plate with $l = 1000 \mu\text{m}$, $b = 125 \mu\text{m}$ and $h = 5 \mu\text{m}$ is considered as depicted in Fig. 3.12. The plate is clamped at its left edge at $x = 0$ and free at all others.

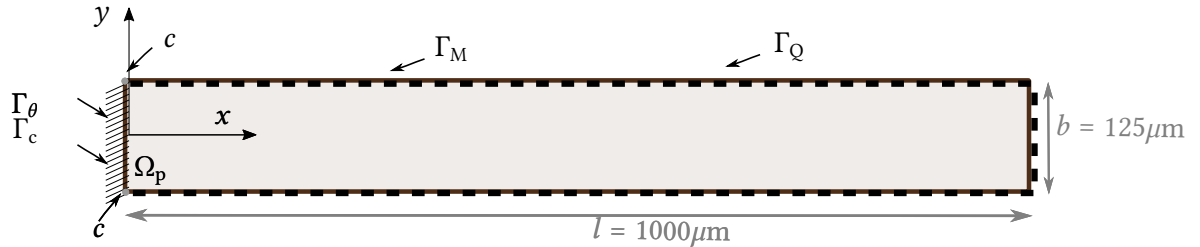


Figure 3.12: Boundaries and dimensions of a cantilevered plate used in the convergence analysis. The plate is clamped at its left edge marked by a solid black line.

Applying a dynamic distributed sinusoidal force $\hat{F} = 1 \text{ Pa}$ results in the spectral displacement of the plate's free corner \hat{w}_t at $x = l$, $y = b/2$ as shown in Fig. 3.13. Numerical results here were obtained with a 64×8 mesh in both methods and with constants $\tau_{\text{IP}} = 100$ and $\tau_{\text{LO}} = 100$. \hat{w}_t obtained with both methods exhibit excellent agreement with each other. Furthermore, the frequencies of maximum \hat{w}_t are similar to the resonance frequencies obtained with the EB theory according to Eq. 2.8.

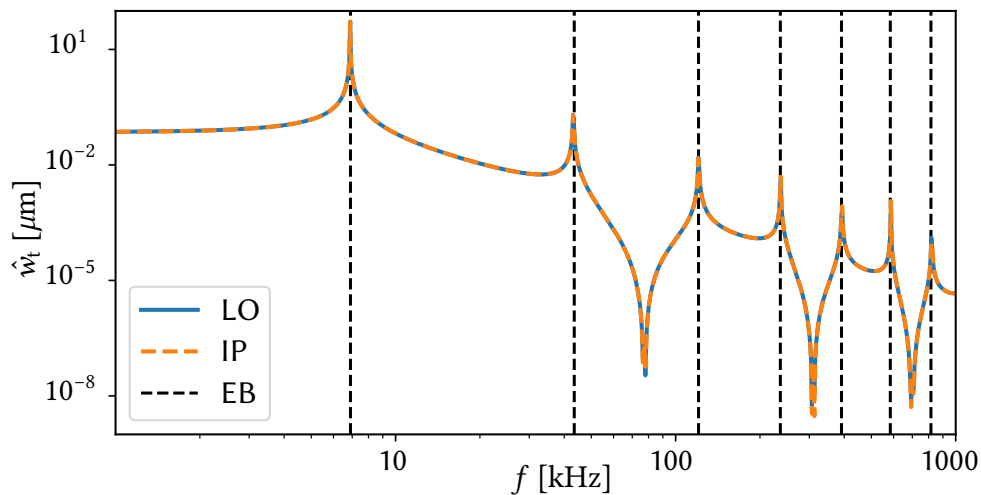


Figure 3.13: Spectral dynamic displacement of the plate's tip \hat{w}_t of a slender beam obtained with the IP and LO methods.

In addition to the validation shown in Fig. 3.13, both methods must be convergent at a wide frequency range (up to units of megahertz regime) so that the methods can be reliably used for the micro-plate-fluid interaction problem. Fig. 3.14 shows $\epsilon_{\text{convergence}}$ with the number of elements N_x at 10 kHz, 100 kHz and 1 MHz for penalty parameters τ_{IP} between 5 and 1000. At the low frequency of $f = 10 \text{ kHz}$ the IP method converges with a mesh with $N_x \leq 64$ elements. For finer meshes, the solution diverges for all values of τ_{IP} ,

and higher τ_{IP} exhibit a higher convergence error $\epsilon_{convergence}$ than solutions with lower τ_{IP} . At the two selected high frequencies, $\epsilon_{convergence}$ converges with a convergence rate equal to 2 independently of τ_{IP} for all meshes with $N_x \geq 32$ elements.

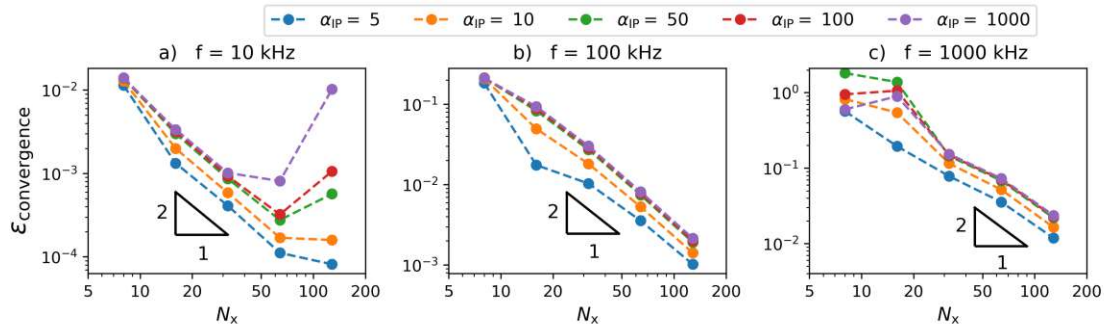


Figure 3.14: Convergence of the IP method at different frequencies.

The LO method exhibits a convergent behavior for the low frequencies $f = 10$ kHz and $f = 100$ kHz. At 10 kHz, the LO method actually diverges for $\tau_{LO} = 1000$. At the high frequency simulation of $f = 1000$ kHz, the LO method diverges for fine meshes with $N_x \geq 64$ with any value of τ_{LO} .

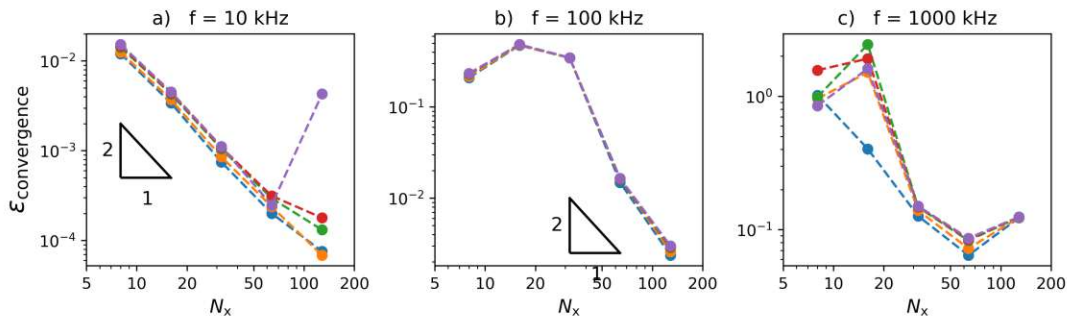


Figure 3.15: Convergence of the LO method at different frequencies.

Furthermore, the LO method takes a greater computation time than the IP method, as shown in Fig. 3.16 where the computation time as a function of the number of mesh elements in x -direction N_x .

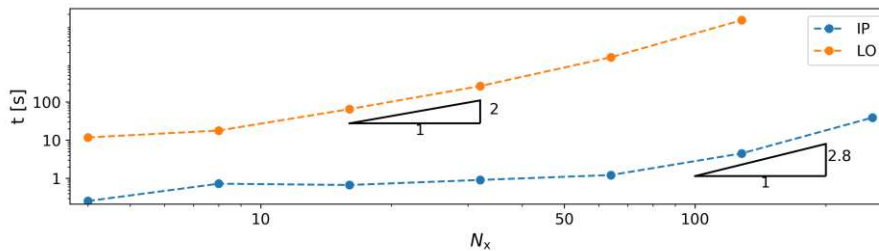


Figure 3.16: Computation time of the IP and LO methods.

3.4.3 Generalized eigenvalue problem

Finally, we consider a wide plate with $l = 1000 \mu\text{m}$, $b = 500 \mu\text{m}$, that is, a plate with aspect ratio $r_a = 2/1$ as depicted in Fig. 3.17. The plate has a thickness of $h = 5 \mu\text{m}$. As an additional step to validate the IP method for the plate equation we compare the vibrational modes of the micro-plate obtained with the IP method and with a FEM software, namely, COMSOL Multiphysics.

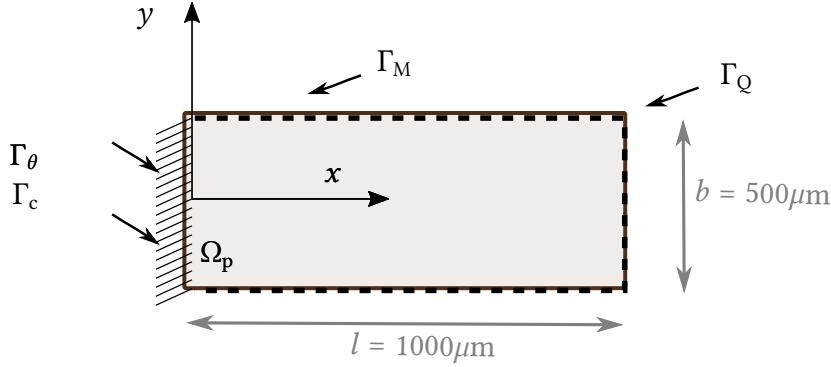


Figure 3.17: Boundaries and dimensions of a cantilevered plate used in the eigenvalue analysis.

The mode shapes with the IP method are obtained from posing the generalized eigenvalue problem as

$$\mathbf{K}\Phi = \lambda^2 \mathbf{M}\Phi, \quad (3.30)$$

where \mathbf{K} is the elasticity matrix, \mathbf{M} is the mass matrix, λ are the eigenvalues and Φ the eigenvectors (or mode shapes). The vacuum resonance frequency of the i -th mode is related to λ through

$$f_i^{\text{vac}} = \frac{\lambda_i}{2\pi}, \quad (3.31)$$

where λ_i is i -th element of λ .

The elasticity matrix \mathbf{K} and the mass matrix \mathbf{M} are obtained from Eq. 3.20 without the driving force term, respectively, as

$$\begin{aligned} \mathbf{K} = & \int_{\Omega_p} \frac{h^3}{12} C_{\alpha\beta\gamma\delta} \hat{w}_{,\alpha\beta}^h v_{,\gamma\delta}^h d\Omega - \int_{\Gamma} \frac{h^3}{12} \{C_{\alpha\beta\gamma\delta} \hat{w}_{,\alpha\beta}^h\} \llbracket [v_{,\delta}^h n_\gamma^e] \rrbracket ds - \int_{\Gamma} \frac{h^3}{12} \llbracket [C_{\alpha\beta\gamma\delta} \hat{w}_{,\alpha\beta}^h] \rrbracket \{[v_{,\delta}^h n_\gamma^e]\} ds \\ & + \int_{\Gamma} \frac{h^3}{12} \frac{\tau_{\text{ip}}}{h_E} C_{\alpha\beta\gamma\delta} \llbracket [\hat{w}_{,\alpha}^h n_\beta] \rrbracket \llbracket [v_{,\gamma}^h n_\delta] \rrbracket ds + \int_{\Gamma_c} \frac{h^3}{12} \frac{\tau_{\text{ip}}}{2h_E} C_{\alpha\beta\gamma\delta} \hat{w}_{,\alpha}^h n_\beta v_{,\gamma}^h n_\delta d\Gamma \end{aligned} \quad (3.32)$$

and

$$\mathbf{M} = \int_{\Omega_p} \rho h \hat{w}^h v^h d\Omega, \quad (3.33)$$

for all test and trial functions.

Excellent agreement was obtained between the resonance frequencies f_{vac} obtained with the IP method and a numerical simulation performed in FEM software, COMSOL

Multiphysics, as seen in Fig. 3.18. A difference smaller than 0.3 % is seen up to the tenth vibrational mode.

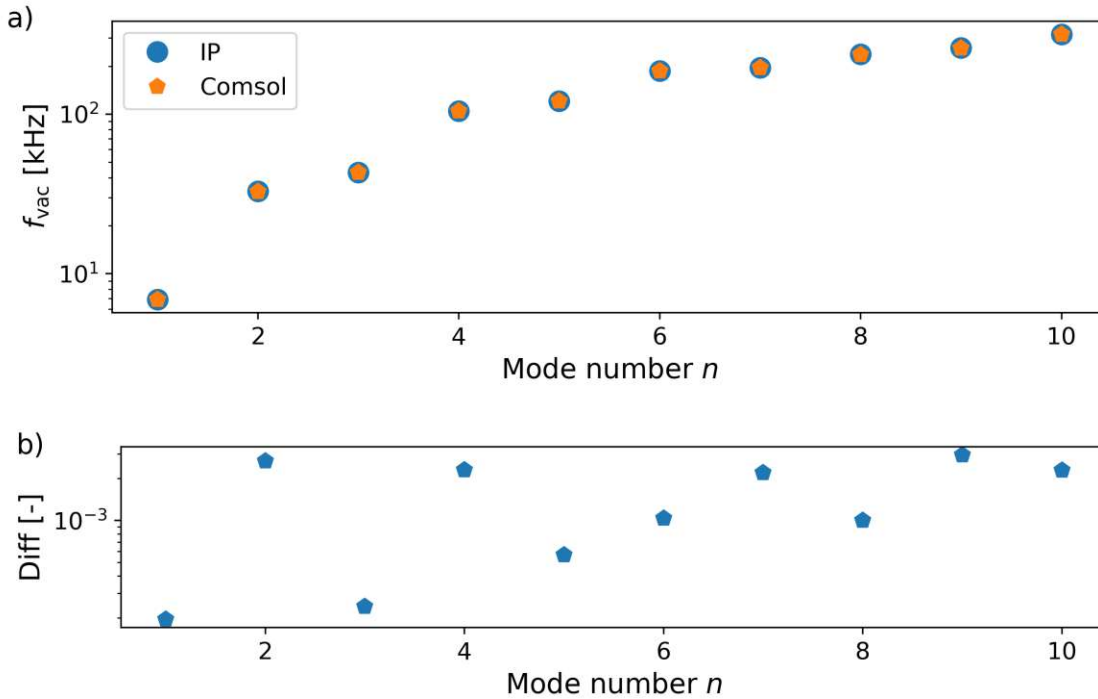


Figure 3.18: a) Resonance frequencies and b) difference between resonance frequencies obtained with the IP method and COMSOL multiphysics software.

Furthermore, the vibrational modes obtained with both methods also show excellent agreement, as seen in Fig. 3.19 for this micro-plate’s first ten vibrational modes.

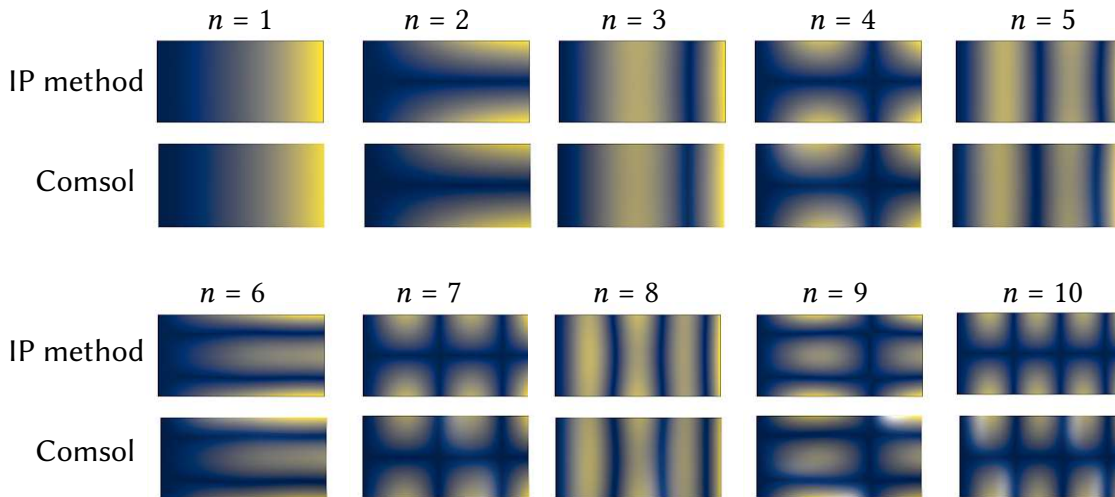


Figure 3.19: Ten lowest vibrational modes of a cantilevered wide plate obtained with the IP method and with COMSOL Multiphysics.

3.5 Conclusions

Here we introduced the mathematical formulation to solve the Kirchhoff plate equation without the hydrodynamic force with FEM. Due to the fourth-order spatial derivatives of the Kirchhoff plate equation, C/DC methods such as the IP and LO methods must be implemented. Both methods exhibit similar convergence rates and give similar results for the spectral displacement of a plate. However, the LO method consumes much longer for an equal number of elements, given the projections between different functions and vector spaces required by the lifting operation. A drawback of the IP method is the requirement to determine the parameter τ_{IP} for stability, which we define from the analysis in this chapter as equal to 5 for stable convergence behavior. An excellent agreement between conventional FEM software and the IP method was obtained for a wide micro-plate's vibrational modes and resonance frequencies. For these reasons, the IP method will be used throughout this thesis with $\tau_{IP} = 5$.

4 Hydrodynamic forces on a micro-plate

The pressure difference $\Delta\hat{p}$ as a function of the plate's displacement \hat{w}_t is to be determined from the unsteady Stokes equations and the no-slip and no-penetration boundary conditions as discussed in Chapter 2. There exist different methods which allow for determining $\Delta\hat{p}$, one of which is using the boundary integral equation method (BIEM). A key feature of BIEM is that $\Delta\hat{p}$ is calculated using a fundamental solution to the unsteady Stokes equations without the necessity for solving the unsteady Stokes equations in the entire fluid domain Ω_f . Thus, multi-scale issues which occur in monolithic methods such as in FEM or in Finite Volumes are avoided.

4.1 Boundary integral equation method

The unsteady Stokes equations have different fundamental solutions, e.g., the Stokeslet in two or three dimensions [93, 94] and the fundamental solution to the stream-function formulation of the unsteady Stokes equations in two dimensions. One advantage of the latter fundamental solution is that analytical solutions to the arising boundary integrals are known [95], thus making the method very efficient. With a two-dimensional fluid flow approximation, the fluid flow is confined in a plane, parallel to the y - z plane, as shown in Fig. 4.1a. Thus the fluid moves only in y - and z -directions, with a zero velocity in x -direction.

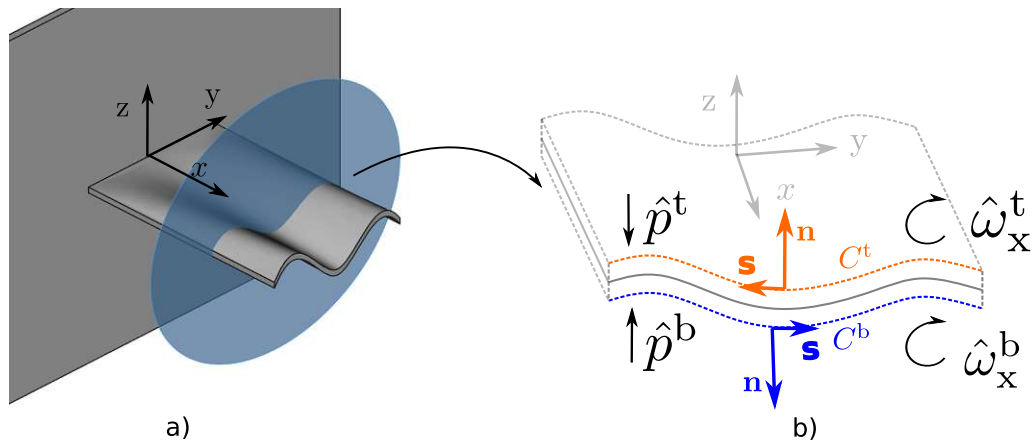


Figure 4.1: a) The fluid flow is confined to a plane (in blue), which is parallel to the $y - z$ plane. b) Pressure and vorticity act both on the top and bottom surfaces of the plate. \mathbf{n} and \mathbf{s} stand for normal and transverse directions at each surface.

The exact extent to which three-dimensional flow affects the beam's and the plate's dynamics in fluids is yet an unsolved question. Comparison to purely numerical methods [63, 64] shows that a two-dimensional flow formulation accurately predicts the $\Delta\hat{p}$ acting on the plate everywhere except near the plate's the completely free edge at $x^c = l$ [64]. In this end region (near $x^c = l$), the two-dimensional fluid model is expected to overestimate $\Delta\hat{p}$ because the fluid is forced to move farther in the direction of the side edges of the plates ($y = \pm b/2$) instead of moving over the completely free

edge of the plate ($x^c = l$). As a consequence, the use of two-dimensional fluid flow approximation underestimates both the plate's resonance frequency and the Q-factor in comparison to methods that assume a three-dimensional fluid flow, such as purely numerical methods.

Here, the viscous flow is modeled with the two-dimensional fundamental solution to the stream-function formulation. This formulation makes the present method very efficient. However, it imposes two main limitations to the method's applicability. The plate's aspect ratio r_a must be larger than 2 so that the fluid flow over the free edge at $x^c = l$ of the plate does not dominate the fluid flow. In Chapter 10 of the present thesis, a formulation that takes into account the three-dimensional flow is proposed and implemented to establish the limit between two-dimensional and three-dimensional fluid flow.

To solve the micro-plate fluid interaction problem with the boundary integral method using the two-dimensional fundamental solution, the stream-function formulation in vector notation in the frequency domain is introduced. The fluid velocity along the x -axis is assumed to be negligible $\hat{\mathbf{u}}^T = (0, \hat{u}_y, \hat{u}_z)$. The vorticity vector $\hat{\boldsymbol{\omega}}$ is given by

$$\hat{\boldsymbol{\omega}} = \nabla \times \hat{\mathbf{u}}, \quad (4.1)$$

and the vector potential $\hat{\boldsymbol{\psi}}$

$$\hat{\mathbf{u}} = \nabla \times \hat{\boldsymbol{\psi}}. \quad (4.2)$$

Using the definition from Eq. 4.2 in Eq. 4.1 leads to

$$\hat{\boldsymbol{\omega}} = -\nabla^2 \hat{\boldsymbol{\psi}}. \quad (4.3)$$

Taking the curl of the Stokes equations Eq. 2.19 and writing the vorticity $\hat{\boldsymbol{\omega}}$ in terms of the vector potential $\hat{\boldsymbol{\psi}}$ yields

$$\nabla^4 \hat{\boldsymbol{\psi}} - \frac{j\omega}{\nu_f} \nabla^2 \hat{\boldsymbol{\psi}} = (0, 0, 0)^T. \quad (4.4)$$

In the 2D fluid formulation, since the velocity in x -direction and fluid velocity $\hat{\mathbf{u}}$ variations in x -direction are neglected, the vorticity has only one non-zero component, $\hat{\boldsymbol{\omega}}^T = (\hat{\omega}_x, 0, 0)$, as well as the stream vector $\hat{\boldsymbol{\psi}}^T = (\hat{\psi}_x, 0, 0)$. $\hat{\psi}_x$ is the stream-function for the two-dimensional flow field. The fundamental solution $\hat{\Psi}$ to the x -component of Eq. 4.4 is defined as [95]

$$\hat{\Psi} = \frac{1}{2\pi} \frac{\nu_f^2}{\omega^2} \left\{ \log \left(\sqrt{(y - y')^2 + (z - z')^2} \right) + K_0 \left(j\omega \sqrt{(y - y')^2 + (z - z')^2} \right) \right\}, \quad (4.5)$$

where K_0 is the modified Bessel function of the third kind and order zero. y' and z' are coordinate axes with coincident orientation to y and z , respectively.

The fundamental solution Ψ is used to describe the fluid flow based on the fluid stresses acting on the plate's surfaces. Consider a plate's cross-section C positioned at a position $x = x^c$, whose lower edge is defined as C^b and top edge as C^t as shown in Fig. 4.1b. With the application of the Green's theorem at C , the stream function $\hat{\psi}_x$ at x^c is given by [95]

$$\begin{aligned} \hat{\psi}_x(x^c, y', z') = & \int_{C^b} \frac{1}{\mu_f} \hat{p}^b(x^c, y) \frac{\partial \hat{\Psi}}{\partial s} + \hat{\omega}_x^b(x^c, y) \frac{\partial \hat{\Psi}}{\partial n} ds \\ & + \int_{C^t} \frac{1}{\mu_f} \hat{p}^t(x^c, y) \frac{\partial \hat{\Psi}}{\partial s} + \hat{\omega}_x^t(x^c, y) \frac{\partial \hat{\Psi}}{\partial n} ds, \end{aligned} \quad (4.6)$$

where $\hat{\omega}_x^b$ and $\hat{\omega}_x^t$ stand for the x-component of the vorticity vector at the plate's lower edge and top edge, respectively. Similarly, \hat{p}^t and \hat{p}^b are the pressures on the top and bottom edges, respectively. n is the derivative in the direction of the edge normal and the derivative with respect to s is the tangential derivative along the plate's width. As depicted in 4.1b, n and s exhibit opposite directions in C^t and C^b , in essence on the top surface $n = z$ and $s = -y$, and on the bottom $n = -z$ and $s = y$. Therefore, Eq. 4.6 is rewritten as

$$\begin{aligned} \hat{\psi}_x(x^c, y', z') = & \int_{C^b} \frac{1}{\mu_f} \hat{p}^b(x^c, y) \frac{\partial \hat{\Psi}}{\partial y} - \hat{\omega}_x^b(x^c, y) \frac{\partial \hat{\Psi}}{\partial z} dy \\ & + \int_{C^t} -\frac{1}{\mu_f} \hat{p}^t(x^c, y) \frac{\partial \hat{\Psi}}{\partial y} + \hat{\omega}_x^t(x^c, y) \frac{\partial \hat{\Psi}}{\partial z} dy. \end{aligned} \quad (4.7)$$

Given that the plate is a thin structure, one may use a slender body formulation to define the fundamental solution Ψ in the integral equation in Eq. 4.7 at $z = 0$ for the pressure and vorticity defined on the top or bottom surfaces (rather than defining Ψ at $z = \pm h/2$), which allows rewriting Eq. 4.7 in terms of the pressure jump $\nabla \hat{p}$ and vorticity jump $\nabla \hat{\omega}_x = \hat{\omega}_x^t - \hat{\omega}_x^b$ as

$$\hat{\psi}_x(x^c, y', z') = \int_{-b/2}^{b/2} \nabla \hat{\omega}_x(x^c, y) \frac{\partial \hat{\Psi}}{\partial z} \Big|_{z=0} - \frac{1}{\mu_f} \Delta \hat{p}(x^c, y) \frac{\partial \hat{\Psi}}{\partial y} \Big|_{z=0} dy. \quad (4.8)$$

Applying Eq. 4.8 at the plate's mid-plane at $z' = 0$, and noting that $\frac{\partial \hat{\Psi}}{\partial z} \Big|_{z=0} = 0$ [95] yields

$$\hat{\psi}_x(x^c, y', 0) = -\frac{1}{\mu_f} \int_{-b/2}^{b/2} \Delta \hat{p}(x^c, y) \frac{\partial \hat{\Psi}}{\partial y} \Big|_{z=0} dy. \quad (4.9)$$

Differentiation of Eq. 4.9 with respect to y' renders a relation between $\Delta \hat{p}$ with \hat{u}_z at the plate's mid-plane $z' = 0$ as

$$\hat{u}_z(x^c, y', 0) = \frac{1}{\mu_f} \int_{-b/2}^{b/2} \Delta \hat{p}(x^c, y) \frac{\partial^2 \hat{\Psi}}{\partial y \partial y'} \Big|_{z=0} dy. \quad (4.10)$$

Given that the plate's velocity at the mid-plane is $\hat{u}_z(x^c, y', 0) = j\omega\hat{w}(x^c, y')$, a relation between $\Delta\hat{p}$ and the plate's transverse displacement \hat{w} arises as

$$\int_{-b/2}^{b/2} \Delta\hat{p}(x^c, y) \frac{\partial^2 \hat{\Psi}}{\partial y \partial y'} \Big|_{\substack{z=0 \\ z'=0}} dy = \mu_f j \omega \hat{w}(x^c, y'). \quad (4.11)$$

Note that the function $\partial^2 \hat{\Psi} / \partial y \partial y'$ relates the pressure difference at a point x, y with the displacement at another point x, y' in the same cross-section at a position x .

Eq. 4.11 is known as a Fredholm integral equation since the unknown pressure jump $\Delta\hat{p}$ is inside the integral. One efficient method to numerically evaluate Eq. 4.11 is to assume $\Delta\hat{p}$ to be piece-wise constant in a certain discretization scheme. This is an appropriate strategy given if the variation of $\Delta\hat{p}$ between two grid points of the discretization scheme is much smaller than the variation of $\partial^2 \hat{\Psi} / \partial y \partial y'$. The numerical integration of the LHS of Eq. 4.11 becomes then a sum of \mathcal{M}_y integrals as

$$\sum_{i=1}^{\mathcal{M}_y} \Delta\hat{p}(x^c, y_i) \int_{y_i^{(l)}}^{y_{i+1}^{(l)}} \frac{\partial^2 \hat{\Psi}}{\partial y \partial y'} \Big|_{\substack{z=0 \\ z'=0}} dy = \mu_f j \omega \hat{w}(x^c, y'_j) \quad (4.12)$$

where the pressure difference $\Delta\hat{p}(x^c, y_i)$ and the displacement $\hat{w}(x^c, y'_j)$ are discretized in y -direction according to the discretization scheme, and $y_i^{(l)}$ and $y_{i+1}^{(l)}$ are the limits of integration around the point y_i .

One possible discretization scheme to determine $\Delta\hat{p}$ is the uniform discretization scheme. With the uniform discretization scheme, the plate's width is divided into M_y segments, each with length $\Delta y = b/M_y$. The quadrature discretization points y_i is

$$y_i = -\frac{b}{2} + \frac{2i-1}{2} \Delta y, \quad (4.13)$$

for $i = 1 \dots M_y$, and the limits $y_j^{(l)}$ are

$$y_j^{(l)} = -\frac{b}{2} + j \Delta y, \quad (4.14)$$

for $j = 0 \dots M_y$. The uniform discretization scheme is represented in Fig. 4.2.

Assuming $\Delta\hat{p}$ to be piece-wise constant allows for using the analytical evaluation of each integral in Eq. 4.12 around y_i as [95]

$$\int_{y_i^{(l)}}^{y_{i+1}^{(l)}} \frac{\partial^2 \Psi}{\partial y \partial y'} \Big|_{\substack{z=0 \\ z'=0}} dy = \frac{\sqrt{V_f}}{j2\pi\sqrt{\omega}} \left[\mathcal{F} \left(\sqrt{\frac{\omega}{V_f}} (y_{i+1}^{(l)} - y'_j) \right) - \mathcal{F} \left(\sqrt{\frac{\omega}{V_f}} (y_i^{(l)} - y'_j) \right) \right]. \quad (4.15)$$

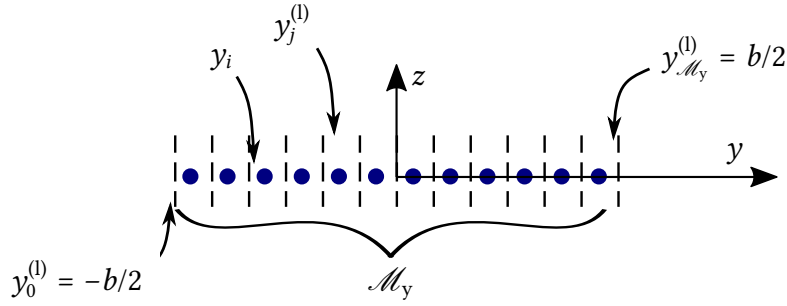


Figure 4.2: Quadrature points y_i (blue dots) and limiting points $y_j^{(l)}$ (dashed lines) in the uniform discretization scheme.

Evaluation of Eq. 4.15 depends on the position y'_j as well as on the limits of integration $y_{i+1}^{(l)}$ and $y_i^{(l)}$. The function \mathcal{F} is defined as

$$\mathcal{F}(g) = \frac{1}{g} + \text{Ker}(g) + j\text{Kei}(g) \quad \text{for } g > 0, \quad (4.16)$$

$$\mathcal{F}(g) = \frac{1}{g} - \text{Ker}(-g) - j\text{Kei}(-g) \quad \text{for } g < 0, \quad (4.17)$$

where Ker and Kei are real and imaginary Kelvin Functions, respectively.

Eq. 4.12 is written as a matrix-vector product,

$$\mathbf{A}\Delta\hat{\mathbf{p}} = \mu_{\text{fj}}\omega\hat{\mathbf{w}}. \quad (4.18)$$

The matrix elements A_{ij} are given by the RHS of Eq. 4.15 as

$$A_{ij} = \frac{\sqrt{v_{\text{f}}}}{j2\pi\sqrt{\omega}} \left[\mathcal{F} \left(\sqrt{\frac{\omega}{v_{\text{f}}}}(y_{i+1}^{(l)} - y'_j) \right) - \mathcal{F} \left(\sqrt{\frac{\omega}{v_{\text{f}}}}(y_i^{(l)} - y'_j) \right) \right]. \quad (4.19)$$

$\Delta\hat{\mathbf{p}}$ and $\hat{\mathbf{w}}$ are the pressure difference and displacement vectors evaluated at all points y_j at the same cross-section at a fixed x^c . Multiplying Eq. 4.18 with the inverse matrix \mathbf{A}^{-1} , a matrix-vector product for the pressure difference $\Delta\hat{\mathbf{p}}$ is obtained as

$$\Delta\hat{\mathbf{p}} = \mu_{\text{fj}}\omega\mathbf{A}^{-1}\hat{\mathbf{w}}. \quad (4.20)$$

4.2 Hydrodynamic force due to different vibrational modes

It is crucial to understand how $\Delta\hat{\mathbf{p}}$ behaves for the different vibrational modes of a plate. Using the wide plate introduced in Section 3.4.3 whose vibrational modes and resonance frequencies were previously determined, the pressure jump $\Delta\hat{\mathbf{p}}$ is calculated using Eq. 4.20 for the plate's different vibrational modes. As a fluid, air is used at SATP (properties given in Table 2.3). We select air for this example because the resonance frequencies in the air are similar to the frequencies in the vacuum. Hence, one may directly evaluate the pressure jump $\Delta\hat{\mathbf{p}}$ at the vacuum resonance frequency as a representative

example. In liquids, the resonance frequency in the fluid is different than the vacuum's resonance frequency due to the high added-mass effect.

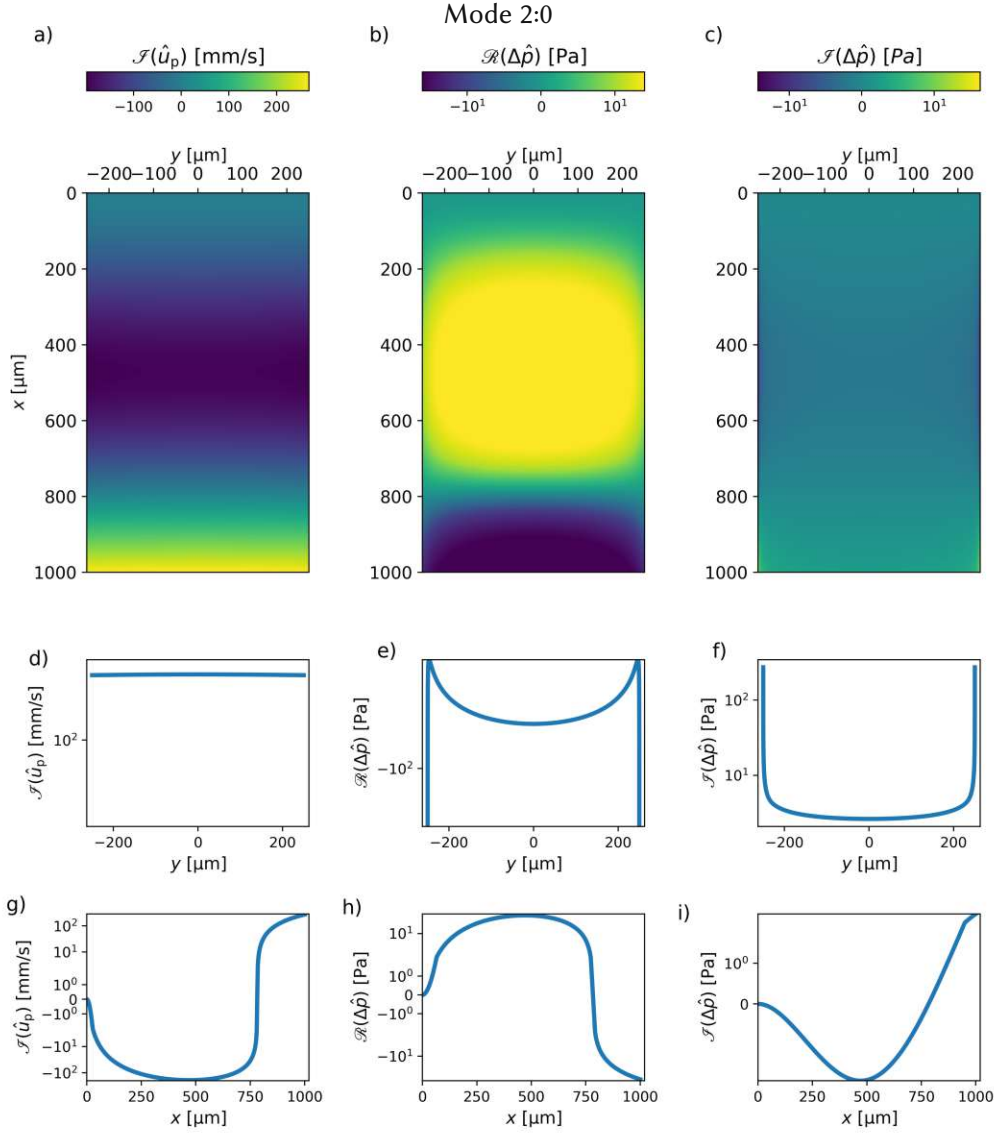


Figure 4.3: Imaginary component of the plate's velocity $\mathcal{I} u_p$, real component of the pressure jump $\mathcal{R}(\Delta\hat{p})$ and imaginary component of the pressure jump $\mathcal{I}(\Delta\hat{p})$ when the plate vibrates with the third vibrational mode. In a), b) and c) these quantities are shown over the entire plate domain. In d), e), and f), they are shown across the y -direction at the free edge $x^c = l$. In g), h), and i) they are shown along the x -direction at $y = 0$.

Fig. 4.3 shows the imaginary component of the plate's velocity $\mathcal{I} u_p$ (the velocity has only imaginary component, given that the mode shape is real-valued), the real component of the pressure jump $\mathcal{R}(\Delta\hat{p})$ and the imaginary component of the pressure jump $\mathcal{I}(\Delta\hat{p})$. Note that regions of the plate with high velocity also exhibit high $\mathcal{R}(\Delta\hat{p})$ as clear in the wide yellow region in Fig. 4.3b. More importantly, note the high amplitude of both $\mathcal{R}(\Delta\hat{p})$ and $\mathcal{I}(\Delta\hat{p})$ towards the plate's side edges $y = \pm b/2$ shown in Fig. 4.3.

This agrees with previous observations for ribbons moving with a uniform velocity that the pressure jump is unbounded at the edges and exhibits an inverse square-root singularity towards the side edges [95]. Note that in x -direction this singularity does not occur as a result of the two-dimensional fluid flow approximation.

The pressure jump singularity also occurs when the plate moves with other vibrational modes than the conventional Euler-Bernoulli like modes. For instance, Fig. 4.4 shows the velocity and pressure jump when the vibrational mode is a torsional-like mode, here the tenth mode as shown in Fig. 3.19. From Figs. 4.4e and 4.4f, it is evident that the pressure jump singularity towards the side edges of the plate is present also for the torsional-like modes.

In Fig. 4.5 also the pressure jump for the first roof tile-shaped mode of the micro-plate is shown, i.e. the sixth mode in Fig. 3.19. Note that, because of the mode shape, the components of the pressure jump $\mathcal{I}(\Delta\hat{p})$ and $\mathcal{R}(\Delta\hat{p})$ exhibit a great variation along the plate's width direction.

4.3 Integration of the hydrodynamic force

From the previous chapters, determine that the governing equation for the micro-plate-fluid interaction problem is

$$\frac{h^3}{12} C_{\alpha\beta\gamma\delta} \hat{w}_{,\alpha\beta\gamma\delta} - \omega^2 \rho h \hat{w} = \hat{F} + \Delta\hat{p}. \quad (4.21)$$

Solving Eq. 4.21 involves multiplying it with the test function $v^h \in \mathcal{V}^h$, resulting in a weak form of the type: find \hat{w}^h in \mathcal{W}^h such that

$$\begin{aligned} \int_{\Omega_p} \frac{h^3}{12} C_{\alpha\beta\gamma\delta} \hat{w}_{,\alpha\beta\gamma\delta}^h v^h d\Omega - \int_{\Omega_p} \omega^2 \rho h \hat{w}^h v^h d\Omega \\ = \int_{\Omega_p} \hat{F} v^h d\Omega + \int_{\Omega_p} \Delta\hat{p} v^h d\Omega, \quad \forall v^h \in \mathcal{V}^h. \end{aligned} \quad (4.22)$$

Upon investigation of Eq. 4.22, it is evident that a numerical procedure to evaluate the last integral term in Eq. 4.22 using the pressure difference definition in Eq. 4.11 must be defined. To determine the appropriate quadrature scheme, let us numerically determine the resulting force $F_{\text{resultant}}$ of the pressure jump as

$$F_{\text{resultant}} = \int_{\Omega_p} \Delta\hat{p} d\Omega. \quad (4.23)$$

Since $\Delta\hat{p}$ varies more than the test functions v^h , a suitable numerical scheme for evaluating Eq. 4.23 is also suitable for evaluating the last integral term in Eq. 4.22.

Since a two-dimensional formulation for the fluid dynamics is implemented, the pressure difference $\Delta\hat{p}(x^c, y)$ depends only on the displacements $\hat{w}(x^c, y)$ on the same position x^c . Therefore, integration of the pressure difference $\Delta\hat{p}$ in Eq. 4.23 is written as

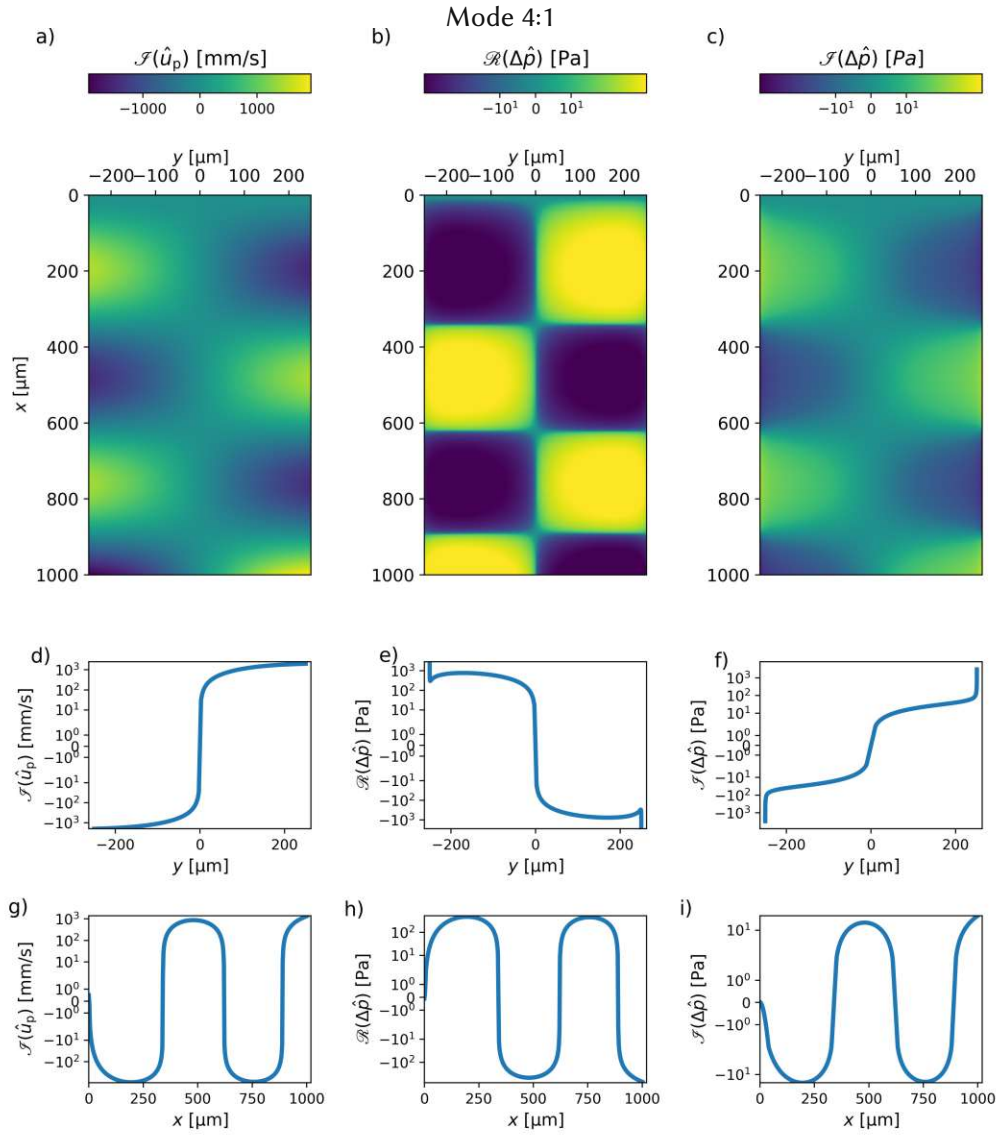


Figure 4.4: Imaginary component of the plate's velocity $\mathcal{I}u_p$, real component of the pressure jump $\mathcal{R}(\Delta\hat{p})$ and imaginary component of the pressure jump $\mathcal{I}(\Delta\hat{p})$ when the plate vibrates with the tenth vibrational mode. In a), b) and c) these quantities are shown over the entire plate domain. In d), e), and f), they are shown across the y -direction at the free edge $x^c = l$. In g), h), and i) they are shown along the x -direction at $y = -b/4$.

successive integration in y and x -direction as

$$\int_{\Omega_p} \Delta\hat{p}(x^c, y) d\Omega = \int_0^l \int_{-b/2}^{b/2} \Delta\hat{p}(x^c, y) dy dx, \quad (4.24)$$

and two different quadrature schemes in x and y direction can be used.

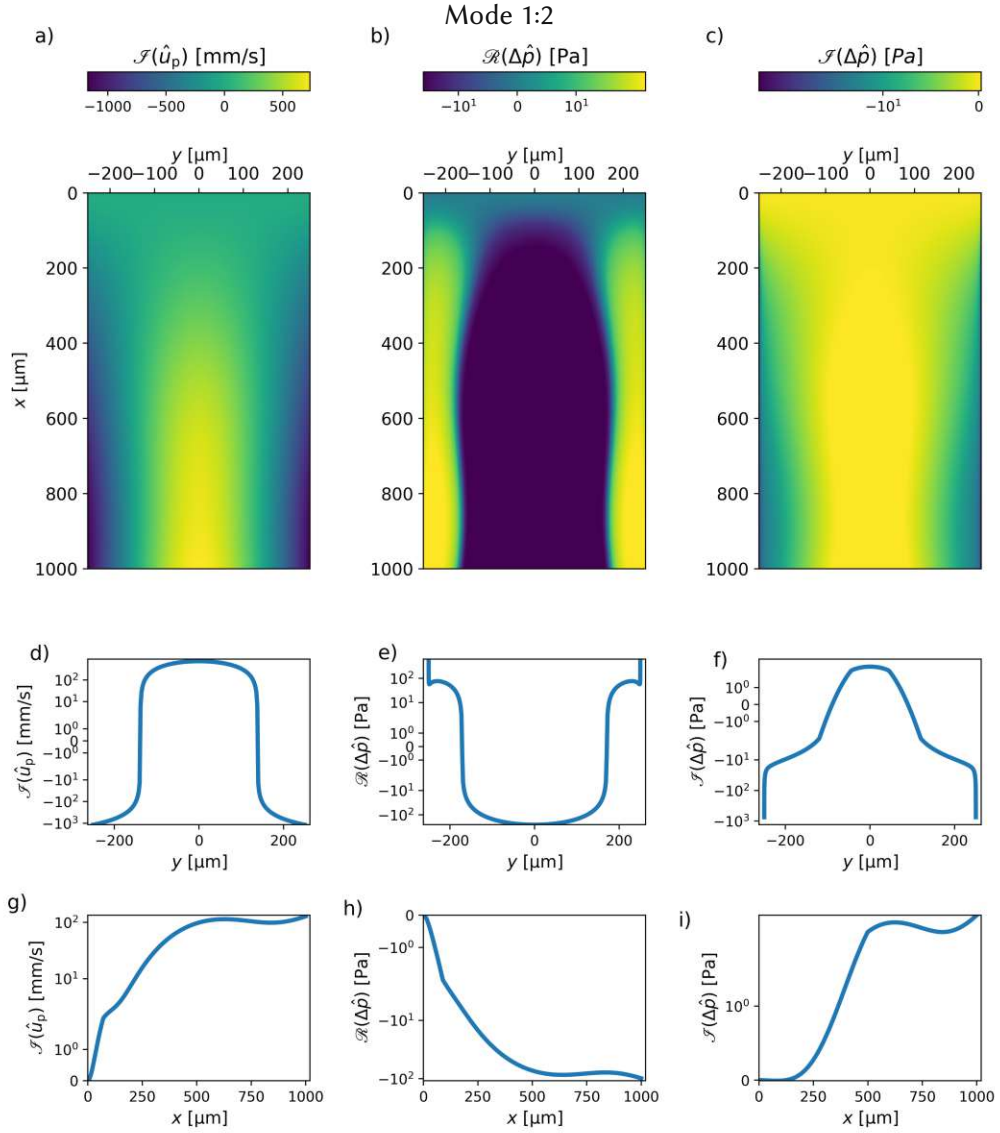


Figure 4.5: Imaginary component of the plate's velocity $\mathcal{I} u_p$, real component of the pressure jump $\mathcal{R}(\Delta\hat{p})$ and imaginary component of the pressure jump $\mathcal{I}(\Delta\hat{p})$ when the plate vibrates with the sixth vibrational mode. In a), b) and c) these quantities are shown over the entire plate domain. In d), e), and f), they are shown across the y -direction at the free edge $x^c = l$. In g), h), and i) they are shown along the x -direction at $y = 0$.

4.3.1 Numerical integration in y -direction

With the uniform discretization scheme, the mid-point integration scheme is used to numerically determine the integration of $\Delta\hat{p}$ in y -direction at a fixed position $x^c = l$ as

$$I_y = \int_{-b/2}^{b/2} \Delta\hat{p}(x^c = l, y) dy = \sum_{i=1}^{M_y} \Delta\hat{p}(x^c = l, y_i) \Delta y. \quad (4.25)$$

An appropriate choice of quadrature scheme for a function that exhibits an inverse square root singularity is the Chebyshev-Gauss quadrature [96, 95]. In y -direction, the Chebyshev-Gauss quadrature points are distributed over the plate's width as

$$y_i = \frac{b}{2} \cos\left(\frac{2i-1}{2\mathcal{M}_y} \pi\right), \quad (4.26)$$

where \mathcal{M}_y is the number of grid points in the y -direction and $i = 1 \dots \mathcal{M}_y$. The limits $y_j^{(l)}$ are the mid-points between y_j for $j = 1 \dots \mathcal{M}_y - 1$, with the endpoints $y_0^{(l)} = -b/2$ and $y_{\mathcal{M}_y}^{(l)} = b/2$ as depicted in Fig. 4.6.

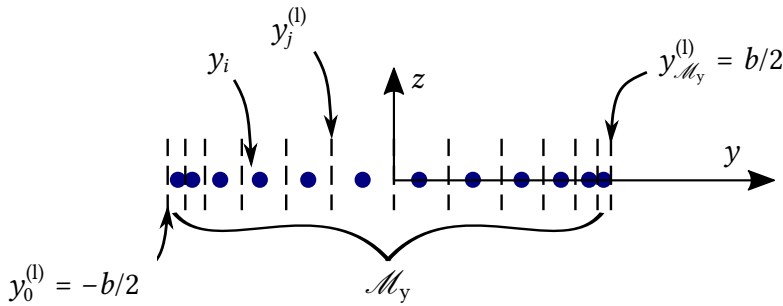


Figure 4.6: Quadrature points y_i (blue dots) and limiting points $y_j^{(l)}$ (dashed lines) in the Chebyshev-Gauss quadrature.

To evaluate the y -integration of $\Delta\hat{p}(x^c, y)$ note that the integration of a polynomial function f divided by the inverse square root singularity with Chebyshev-Gauss quadrature is given by

$$\int_{-b/2}^{b/2} \frac{f(y)}{\sqrt{(b/2)^2 - y^2}} dy = \frac{\pi}{n} \sum_{j=1}^n f(y_j), \quad (4.27)$$

where $f(y_j)$ are the function's value at the discrete points defined in Eq. 4.26. The definition in 4.27 is exact when the degree of the polynomial function f is $n-1$. This definition is used to numerically evaluate I_y as

$$I_y = \frac{\pi}{\mathcal{M}_y} \sum_{i=1}^{\mathcal{M}_y} \Delta\hat{p}(l, y_i) \sqrt{(b/2)^2 - y_i^2}. \quad (4.28)$$

To quantify the convergence of the numerical integration we define ϵ_y

$$\epsilon_y = \frac{|I_y^{\mathcal{M}_y^{i+1}} - I_y^{\mathcal{M}_y^i}|}{|I_y^{\mathcal{M}_y^i}|}, \quad (4.29)$$

where $I_y^{\mathcal{M}_y^{i+1}}$ and $I_y^{\mathcal{M}_y^i}$ are solutions obtained with quadrature schemes with \mathcal{M}_y^{i+1} and \mathcal{M}_y^i points, respectively. Also, $\mathcal{M}_y^{i+1} = 2\mathcal{M}_y^i$.

Considering once again the third vibrational mode of the plate defined in Section 3.4.3, note in Fig. 4.7a that $|I_y|$ converges to a value of $1.93 \cdot 10^{-2}$ with $\mathcal{M}_y = 1024$ points with

the mid-point quadrature scheme. The mid-point scheme exhibits an average convergence rate equal to 1, as shown in Fig. 4.7b. The Chebyshev-Gauss quadrature provides a much smaller ϵ_y for fine fluid grids with $\mathcal{M}_y \geq 128$. For finer fluid grids with $\mathcal{M}_y \geq 256$, convergence rates equal to one are obtained with both methods. Therefore, for the Euler-Bernoulli like modes, the Chebyshev-Gauss quadrature is a more suitable quadrature scheme to integrate the pressure jump given the much smaller values of ϵ_y achieved.

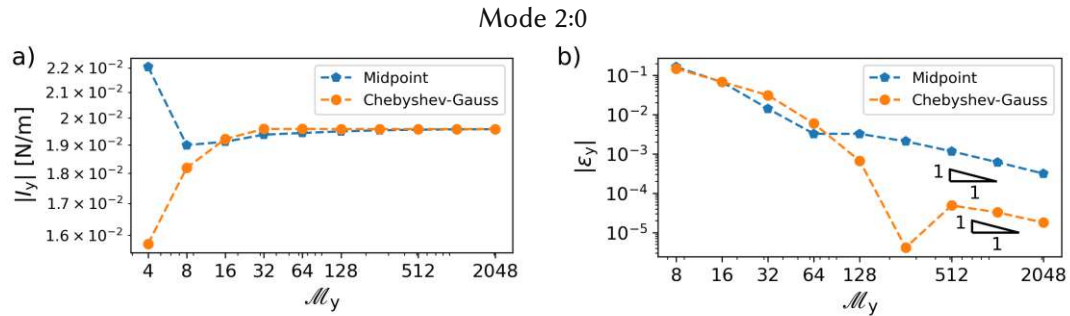


Figure 4.7: a) Result and b) convergence of the integral of the pressure jump in y-direction I_y with the Chebyshev-Gauss and mid-point quadrature rules for the mode 2:0 of the example plate.

For the mode 4:1, also I_y obtained with both quadrature techniques converges as seen in Fig. 4.9. The mid-point quadrature scheme exhibits smaller ϵ_y up to $\mathcal{M}_y = 512$. For finer fluid grids, however, the mid-point rule converges with a convergence rate equal to one, while the Chebyshev-Gauss quadrature converges with a convergence rate equal to three, reaching a value of 10^{-5} for $\mathcal{M}_y = 1024$.

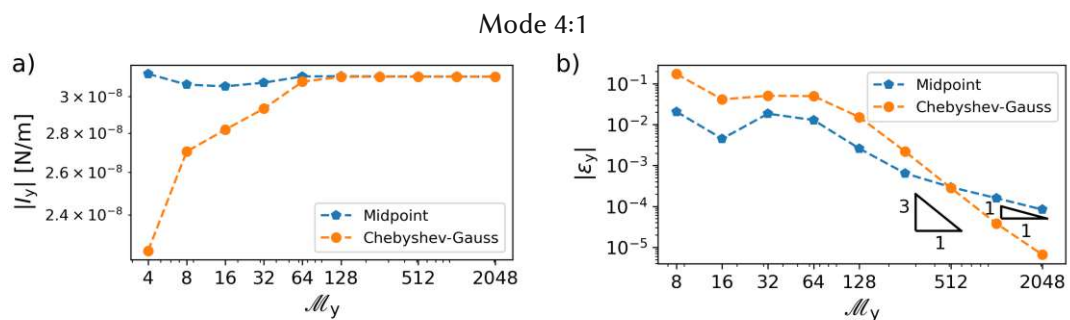


Figure 4.8: a) Result and b) convergence of the integral of the pressure jump in y-direction I_y with the Chebyshev-Gauss and mid-point quadrature rules for the mode 4:1 of the example plate.

For the first roof tile shaped mode, the convergence rate with the Chebyshev-Gauss quadrature is equals two, while the mid-point rule exhibits a convergence rate of one as seen in Fig. 4.9.

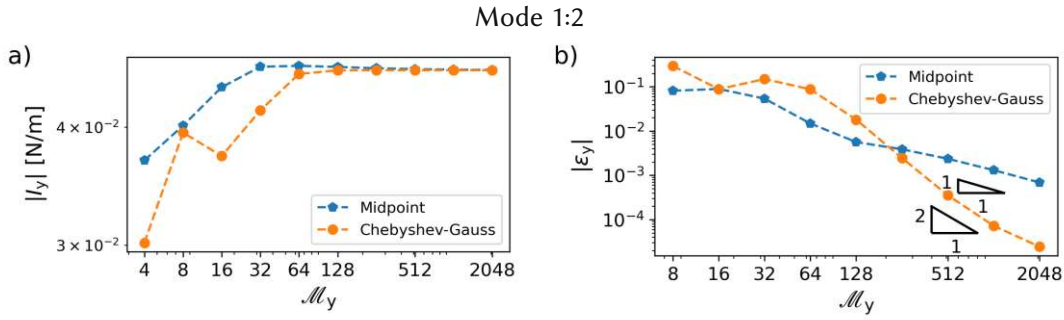


Figure 4.9: a) Result and b) convergence of the integral of the pressure jump in y -direction I_y with the Chebyshev-Gauss and mid-point quadrature rules for the mode 1:2 of the example plate.

Therefore, for all modes, the Chebyshev-Gauss quadrature exhibits a higher convergence rate than the mid-point rule, and the convergence rate depends on the vibrational mode and frequency, while for the mid-point rule discretization, it is equal to one.

4.3.2 Numerical integration in x -direction

From Figs. 4.3, 4.4 and 4.5, it is clear that in x -direction, $\Delta \hat{p}$ does not vary as greatly as in y -direction. In fact, there is no singularity at the edge $x^c = l$ due to the two-dimensional fluid flow formulation. In addition to the mid-point quadrature rule, here we introduce the 1/3 Simpson's rule. With the 1/3 Simpson's rule, the quadrature points are

$$x_i = i\Delta x, \quad (4.30)$$

for $i = 0 \dots M_x$ and $\Delta x = l/M_x$. Evaluation of the pressure jump at a fixed position y with the 1/3 Simpson's rule is

$$I_x = \int_0^l \Delta \hat{p}(x^c, y) dx = \sum_{i=0}^{M_x} \Delta \hat{p}(x_i, y) q_i \Delta x, \quad (4.31)$$

where q_i are the 1/3 Simpson's rule weighting constants. $q_0 = 1$, $q_{M_x} = 1$, when i is even $q_i = 2$ and if i is odd $q_i = 4$. To quantify the convergence of the numerical integration we define ϵ_x

$$\epsilon_x = \frac{|I_x^{M_x^{i+1}} - I_x^{M_x^i}|}{|I_x^{M_x^i}|}. \quad (4.32)$$

In x -direction the convergence rate is independent of the vibrational mode and frequency as seen in Fig. 4.10. The 1/3 Simpson's rule exhibits a convergence rate equal to 4, while the mid-point rule converges with a rate equal to two.

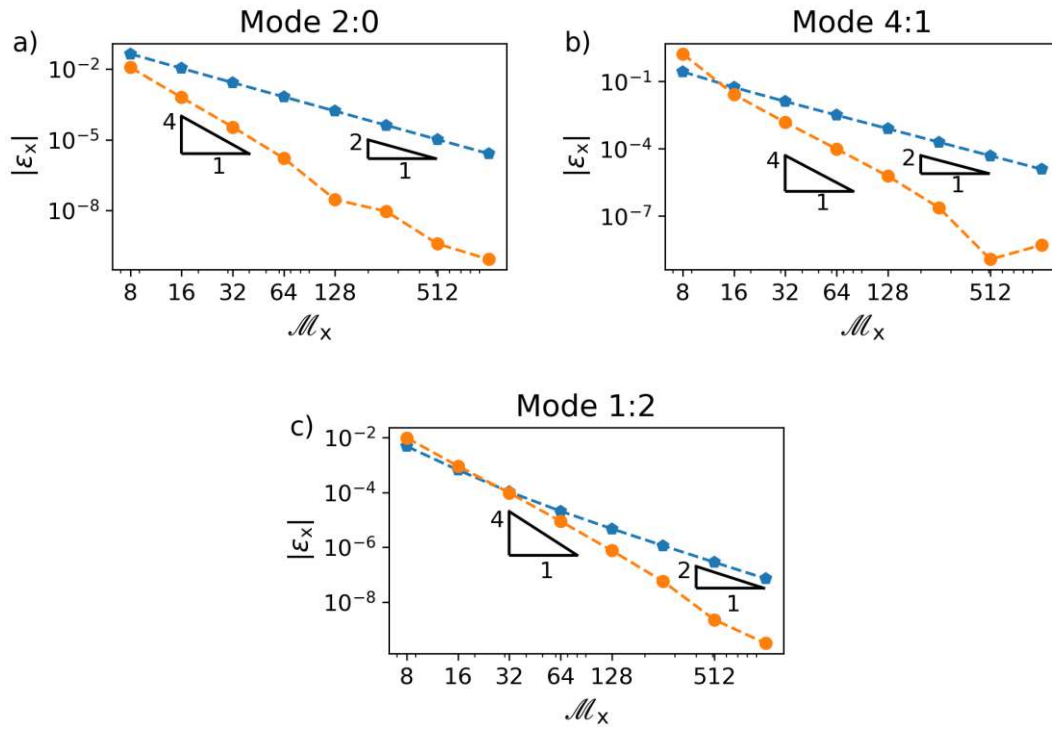


Figure 4.10: Convergence of the integral of the pressure jump in x-direction I_x with the 1/3 Simpsons and mid-point quadrature rules.

4.3.3 Convergence of the two-dimensional integration

In the previous sections, the convergence of the numerical integration was analyzed in each direction separately. Using the Chebyshev-Gauss quadrature in y -direction and the 1/3 Simpsons rule in x -direction, the two-dimensional integral of the pressure jump is given by

$$F_{\text{resultant}} = \int_{\Omega_p} \Delta \hat{p}(x^c, y) d\Omega = \sum_{i=0}^{\mathcal{M}_x} q_i \sum_{j=0}^{\mathcal{M}_y} \frac{\pi}{\mathcal{M}_y} \Delta \hat{p}(x_i, y_j) \sqrt{(b/2)^2 - y_j^2}. \quad (4.33)$$

To quantify the convergence of the two-dimensional numerical integration we define $\epsilon_{\text{resultant}}$

$$\epsilon_{\text{resultant}} = \frac{|F_{\text{resultant}}^{\mathcal{M}_t^{i+1}} - F_{\text{resultant}}^{\mathcal{M}_t^i}|}{|I_x^{\mathcal{M}_t^i}|}, \quad (4.34)$$

where \mathcal{M}_t is the total number of points, which is equal to $\mathcal{M}_x \mathcal{M}_y$.

Fig. 4.11 shows $\epsilon_{\text{resultant}}$ for the three recurrent vibrational modes of the example plate. Different combinations of the number of points in x and y directions are investigated, those are $\mathcal{M}_y = 0.5 \mathcal{M}_x$, $\mathcal{M}_y = \mathcal{M}_x$, $\mathcal{M}_y = 2 \mathcal{M}_x$, $\mathcal{M}_y = 4 \mathcal{M}_x$, $\mathcal{M}_y = 8 \mathcal{M}_x$ and $\mathcal{M}_y = 16 \mathcal{M}_x$. For the three modes, the fluid grid consistent of $\mathcal{M}_y = 0.5 \mathcal{M}_x$ requires the highest total number of grid points \mathcal{M}_t for reaching a reference value of $\epsilon_{\text{resultant}} =$

10^{-3} (in comparison to the other fluid grids). For the three modes, either the fluid grid with $\mathcal{M}_y = 8\mathcal{M}_x$ or $\mathcal{M}_y = 16\mathcal{M}_x$ achieved the reference value of $\epsilon_{\text{resultant}} = 10^{-3}$ with the smallest \mathcal{M}_t .

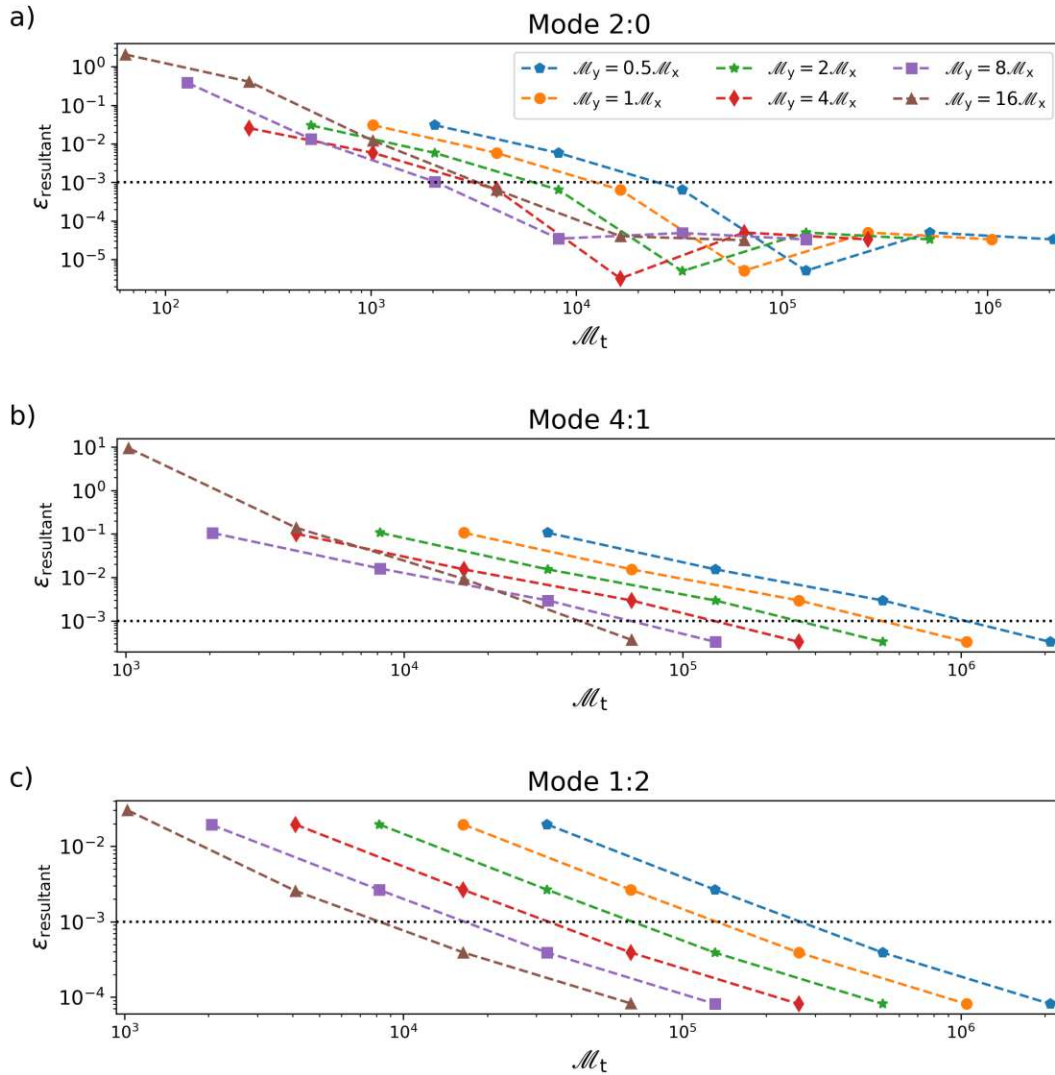


Figure 4.11: Convergence of the integral of the pressure jump in two dimensions with different combinations of \mathcal{M}_x and \mathcal{M}_y . The reference value of $\epsilon_{\text{resultant}} = 10^{-3}$ is shown as a dotted line.

4.4 Conclusions

Here the hydrodynamic force acting on the mid-plane Ω_p of the micro-plate is determined using a boundary integral equation method considering a two-dimensional fluid flow. The pressure jump was calculated for a micro-plate vibrating in different mode shapes in air, and in all cases an inverse square root singularity towards the plate's

side edges was present. Different numerical quadrature schemes were investigated for integrating the resulting hydrodynamic force in y and x directions. In y -direction a Chebyshev-Gauss quadrature exhibited better results with a convergence rate that varies between 1 and 3, depending on the vibrational mode and resonance frequency. In x -direction, the hydrodynamic force does not exhibit the same singularity that occurs in y -direction, and as a result, the 1/3 Simpson's rule exhibits a high convergence rate (equals four). The two-dimensional integration analysis showed that the fluid grid consistent of $\mathcal{M}_y = 8 \cdot \mathcal{M}_x$ or $\mathcal{M}_y = 16 \cdot \mathcal{M}_x$ exhibited convergence to a reference value with fewer grid points than other grid combinations.

5 A semi-numerical method for micro-plates in viscous fluids

Results of this chapter were partially published in [70].

In the previous chapters, we determine the governing PDE for the micro-plate-fluid interaction problem to be

$$\frac{h^3}{12} C_{\alpha\beta\gamma\delta} \hat{w}_{,\alpha\beta\gamma\delta} - \omega^2 \rho h \hat{w} = \hat{F} + \Delta \hat{p}. \quad (5.1)$$

where $\Delta \hat{p}$ is to be determined from the Stokes equations and the no-slip and no-penetration boundary conditions with the boundary integral method as discussed in Chapter 4. Solution of Eq. 5.1 is achieved by multiplying it with the test function $v^h \in \mathcal{V}^h$, resulting in

$$\int_{\Omega_p} \frac{h^3}{12} C_{\alpha\beta\gamma\delta} \hat{w}_{,\alpha\beta\gamma\delta} v^h d\Omega - \int_{\Omega_p} \omega^2 \rho h \hat{w} v^h d\Omega = \int_{\Omega_p} \hat{F} v^h d\Omega + \int_{\Omega_p} \Delta \hat{p} v^h d\Omega, \quad \forall v^h \in \mathcal{V}^h. \quad (5.2)$$

Eq. 5.2 is solved with a FEM, namely the IP method, whose details were discussed in Chapter 3. The resulting weak form of the governing equation for the micro-plate fluid interaction problem with the IP method considering cantilevered boundary conditions is: find \hat{w}^h in \mathcal{W}^h such that

$$\begin{aligned} \int_{\Omega_p} \frac{h^3}{12} C_{\alpha\beta\gamma\delta} \hat{w}_{,\alpha\beta} v_{,\gamma\delta}^h d\Omega - \int_{\bar{\Gamma}} \frac{h^3}{12} \{C_{\alpha\beta\gamma\delta} \hat{w}_{,\alpha\beta}\} \llbracket v_{,\delta}^h n_\gamma^e \rrbracket ds - \int_{\bar{\Gamma}} \frac{h^3}{12} \llbracket C_{\alpha\beta\gamma\delta} \hat{w}_{,\alpha\beta} \rrbracket \{v_{,\delta}^h n_\gamma^e\} ds \\ + \int_{\bar{\Gamma}} \frac{h^3}{12} \frac{\tau_{ip}}{h_E} C_{\alpha\beta\gamma\delta} \llbracket \hat{w}_{,\alpha} n_\beta \rrbracket \llbracket v_{,\gamma}^h n_\delta \rrbracket ds + \int_{\Gamma_c} \frac{h^3}{12} \frac{\tau_{ip}}{2h_E} C_{\alpha\beta\gamma\delta} \hat{w}_{,\alpha} n_\beta v_{,\gamma}^h n_\delta ds \\ - \int_{\Gamma_c} \frac{h^3}{12} C_{\alpha\beta\gamma\delta} \hat{w}_{,\alpha\beta} v_{,\delta}^h n_\gamma^b ds - \int_{\Omega_p} \omega^2 \rho h \hat{w} v^h d\Omega \\ = \int_{\Omega_p} \hat{F} v^h d\Omega + \int_{\Omega_p} \Delta \hat{p} v^h d\Omega, \quad \forall v^h \in \mathcal{V}^h. \quad (5.3) \end{aligned}$$

Eq. 5.3 is similar to the plate equation in vacuum Eq. 3.20 with the addition of the projection of the pressure jump $\Delta \hat{p}$. The projection of $\Delta \hat{p}$ to the basis functions v^h is obtained by applying the Chebyshev-Gauss quadrature in the y -direction and the Simpson's one-third rule (as discussed in the Chapter 4), yielding

$$\int_{\Omega_p} \Delta \hat{p}(x, y) v^h d\Omega = \mu \epsilon j \omega \frac{\pi}{\mathcal{M}_y} \sum_{k=0}^{\mathcal{M}_x} q_k \sum_{j=1}^{\mathcal{M}_y} \sum_{i=1}^{\mathcal{M}_y} A_{ij}^{-1} \hat{w}^h(x_k, y_i) v^h(x_k, y_j) \sqrt{(b/2)^2 - y_j^2}. \quad (5.4)$$

Eq. 5.4 reveals that the projection of the pressure jump corresponds to a weighted projection of the inverse of matrix \mathbf{A}^{-1} into the function space \mathcal{W}^h . Fig. 5.1 shows the fluid grid resultant of the Chebyshev-Gauss and Simpson's one-third rule quadrature schemes. The fluid grid consists of \mathcal{M}_x points in x -direction and \mathcal{M}_y points in y -direction

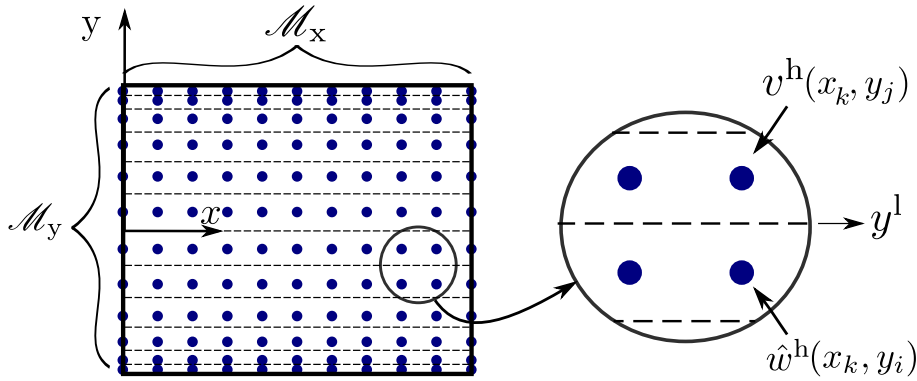


Figure 5.1: Representation of the fluid grid defined with \mathcal{M}_x points in x -direction and \mathcal{M}_y points in y -direction.

With the projection of $\Delta \hat{p}(x, y)$ into \mathcal{V}^h as defined in Eq. 5.4, the weak form of the equation of motion of the plate in a viscous fluid is: find \hat{w}^h in \mathcal{W}^h such that

$$\begin{aligned}
 & \int_{\Omega_p} \frac{h^3}{12} C_{\alpha\beta\gamma\delta} \hat{w}_{,\alpha\beta}^h v_{,\gamma\delta}^h d\Omega - \int_{\Gamma} \frac{h^3}{12} \{C_{\alpha\beta\gamma\delta} \hat{w}_{,\alpha\beta}^h\} \llbracket v_{,\delta}^h n_\gamma^e \rrbracket ds - \int_{\Gamma} \frac{h^3}{12} \llbracket C_{\alpha\beta\gamma\delta} \hat{w}_{,\alpha\beta}^h \rrbracket \{v_{,\delta}^h n_\gamma^e\} ds \\
 & + \int_{\Gamma} \frac{h^3}{12} \frac{\tau_{ip}}{h_E} C_{\alpha\beta\gamma\delta} \llbracket \hat{w}_{,\alpha}^h n_\beta \rrbracket \llbracket v_{,\gamma}^h n_\delta \rrbracket ds + \int_{\Gamma_c} \frac{h^3}{12} \frac{\tau_{ip}}{2h_E} C_{\alpha\beta\gamma\delta} \hat{w}_{,\alpha}^h n_\beta v_{,\gamma}^h n_\delta ds \\
 & - \int_{\Gamma_c} \frac{h^3}{12} C_{\alpha\beta\gamma\delta} \hat{w}_{,\alpha\beta}^h v_{,\delta}^h n_\gamma^b ds - \int_{\Omega_p} \omega^2 \rho h \hat{w}^h v^h d\Omega \\
 & - \mu_f j \omega \frac{\pi}{\mathcal{M}_y} \sum_{k=0}^{\mathcal{M}_x} q_k \sum_{j=1}^{\mathcal{M}_y} \sum_{i=1}^{\mathcal{M}_y} A_{ij}^{-1} \hat{w}^h(x_k, y_i) v^h(x_k, y_j) \sqrt{(b/2)^2 - y_j^2} \\
 & = \int_{\Omega_p} \hat{F} v^h d\Omega, \forall v^h \in \mathcal{V}^h. \quad (5.5)
 \end{aligned}$$

Therefore, the proposed method is resumed to a single equation to determine the plate dynamics accounting for the viscous forces of an incompressible fluid in an unbounded domain around a micro-plate undergoing purely out-of-plane displacement. The elements A_{ij}^{-1} of the inverse of the A matrix are obtained from Eq. 4.19 considering the Chebyshev-Gauss quadrature scheme.

5.1 Convergence

The proposed method must be convergent with the number of elements of the FE-mesh (represented by N_x) as well as with the fluid grid discretization (represented by \mathcal{M}_x). Here, the convergence of the method is analyzed in air and water at SATP as representing fluids for gases and liquids. For the convergence analysis, we consider a wide plate with $l = 1000 \mu\text{m}$, $b = 500 \mu\text{m}$, that is, a plate with aspect ratio $r_a = 2$ as depicted in Fig. 3.17. The plate has thickness $h = 5 \mu\text{m}$ and is comprised of Silicon with orthotropic properties as given in Table 3.1.

5.1.1 Convergence with the FE-mesh

The finite element mesh consists of N_x elements in x -direction and $N_y = 64/r_a$ elements in y -direction so that the internal angles of the mesh are similar and the numerical error stemming from different internal angles is minimized. The convergence is analyzed with $\epsilon_{\text{convergence}}$ as defined in Eq. 3.29 between consecutively refined FE-meshes. The fluid grid is the same in all simulations with 32×256 points, which follows a ratio of 8 points in the y -direction for each point in the x -direction.

Fig. 5.2 shows $\epsilon_{\text{convergence}}$ at 10 kHz, 100 kHz and 1000 kHz with the number of FE-mesh elements in x -direction N_x in air. At 10 kHz, the proposed method converges with a convergence rate equal to 1.8 for an FE-mesh discretized up to $N_x = 64$ elements. For $N_x > 64$, solution \hat{w} diverges, similarly to the IP method convergence results at 10 kHz in vacuum shown in Fig. 3.14. Thus at 10 kHz the convergence/divergence behavior of the complete method is dominated by the convergence/divergence of the IP method. At 100 kHz and 1 MHz, the method converges with a rate equal to 1.8 as well. The convergence rate of the proposed method is at all frequencies equal to 1.8 in air, which is slightly smaller than the convergence rate of the IP method (equals 2) at Fig. 3.14.

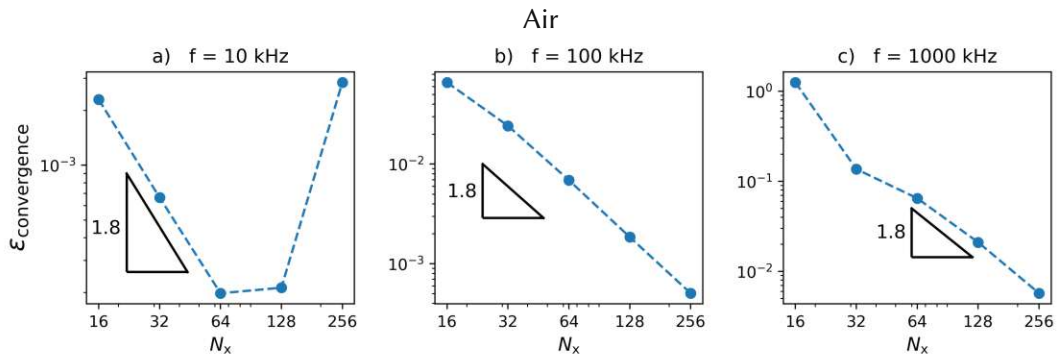


Figure 5.2: In air, convergence as a function of the number of elements N_x in the FE-mesh of the plate with $r_a = 2$ at (a) 10 kHz, (b) 100 kHz and (c) 1 MHz.

In water, at a low frequency, a similar convergence rate of 1.8 is obtained. At 1 MHz a slightly higher convergence rate equal to 2.3 is achieved. From the convergence results shown in this section, we show that the proposed method is convergent in a gas (air) and in a liquid (water) with a minimum convergence rate of 1.8. The only exception is the low frequency (10 kHz) case with a very fine mesh ($N_x \geq 64$), for which case the method diverges due to the IP method.

5.1.2 Convergence with the fluid grid

To investigate the method's convergence with the fluid grid, we define ϵ_{fg} to quantify the convergence of the method with the number of fluid grid points as

$$\epsilon_{\text{fg}} = \frac{\|\hat{w}^{i+1} - \hat{w}^i\|_{L^2}}{\|\hat{w}^i\|_{L^2}}, \quad (5.6)$$

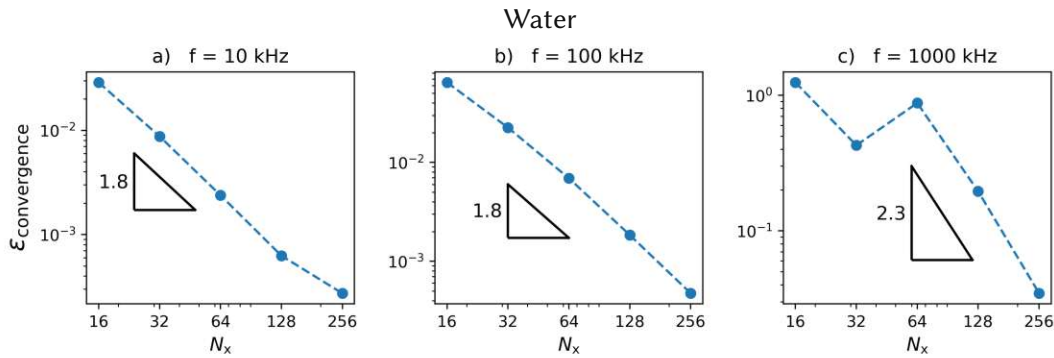


Figure 5.3: In water, convergence as a function of the number of elements N_x in the FE-mesh of the plate with $r_a = 2$ at (a) 10 kHz, (b) 100 kHz and (c) 1 MHz.

where \hat{w}^{i+1} and \hat{w}^i are solutions obtained with FE-meshes consistent of $2^i \times 8 \cdot 2^i$ ($\mathcal{M}_x \times \mathcal{M}_y$) elements. The FE-mesh is constant with 64×32 elements.

Fig. 5.4 shows ϵ_{fg} at 10 kHz, 100 kHz and 1000 kHz with the number of fluid grid points in x -direction \mathcal{M}_x in air. At all frequencies, the method converges. At low frequency, 10 kHz, the proposed method converges with a convergence rate equal to 0.9, while at 1 MHz a convergence rate equals to 2.8 is achieved.

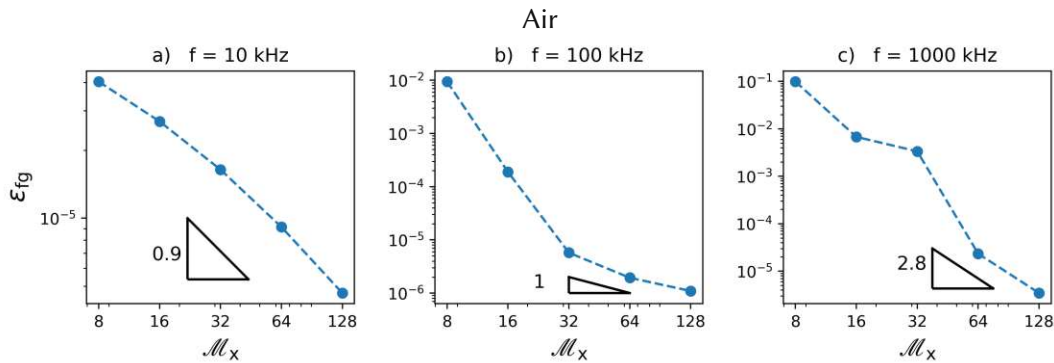


Figure 5.4: In air, convergence as a function of the number of points \mathcal{M}_x in the fluid grid of the plate with $r_a = 2$ at (a) 10 kHz, (b) 100 kHz and (c) 1 MHz.

In water, the method exhibits a low convergence rate at low frequency and a high convergence rate achieving the value of 4 at 1 MHz. In addition, note that the amplitude of ϵ_{fg} at the order of 10^{-4} at 10 kHz for \mathcal{M}_x both in air and in water, meaning increasing the number of points further would only slightly change the resulting displacement field. At high frequencies, ϵ_{fg} is higher, thus a finer fluid grid would be required for similarly small errors.

5.2 Validation with semi-analytic methods

A key semi-analytic method for MEMS in fluids is the method proposed by Sader for beams in incompressible viscous fluids [31]. Here, we use Sader's method as a bench-

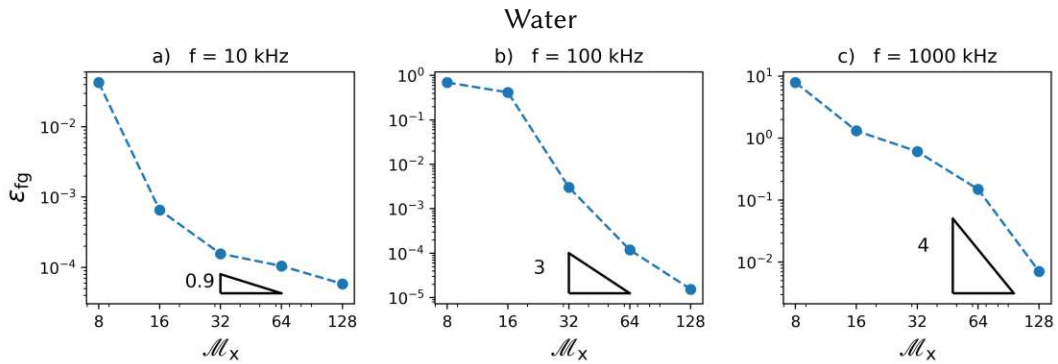


Figure 5.5: In water, convergence as a function of the number of points \mathcal{M}_x in the fluid grid of the plate with $r_a = 2$ at (a) 10 kHz, (b) 100 kHz and (c) 1 MHz.

mark to compare the spectral displacement obtained with the proposed method for slender plates (beams).

5.2.1 Spectral displacement

Here, a slender plate with an aspect ratio $r_a = 8$ with $l = 1000 \mu\text{m}$, $b = 125 \mu\text{m}$ and $h = 5 \mu\text{m}$ is considered as depicted in Fig. 5.6. A uniform force equals $\hat{F} = 1 \text{ Pa}$ is applied to the entire plate's top surface, and the plate's displacement is evaluated at its free corner at $x = l$, $y = b/2$ (see Fig. 5.6).

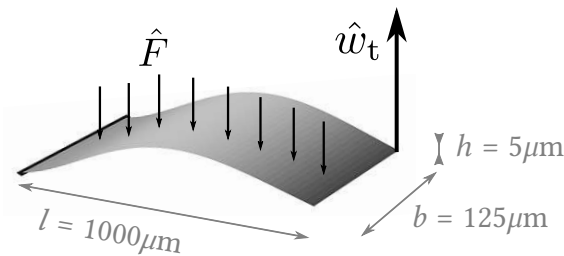


Figure 5.6: Dimensions of a cantilevered plate used in the validation analysis. The plate is excited by an uniform distributed force \hat{F} .

Fig. 5.7 shows the absolute displacement spectrum \hat{w}_t of the slender plate in air and in water. The considered frequency band ranges from 1 kHz to 700 kHz with 350 discretization steps. The FE-mesh consists of 64×8 elements and the fluid grid of 32×256 points. The proposed method exhibits excellent agreement with Sader's method both in air and water.

In air, the resonance frequencies obtained with the proposed method also agree with the prediction using the inviscid method by Chu et al. [45], which is a further proof of the validity of the method. In water, a small difference is noted between the fluid resonance frequency f^f obtained with Chu's method and the others. Chu's method overestimates the resonance frequencies because it neglects the effect of the fluidic damping acting

on the plate. Sader's method and the present method, on the other hand, agree well over the entire frequency range analysed.

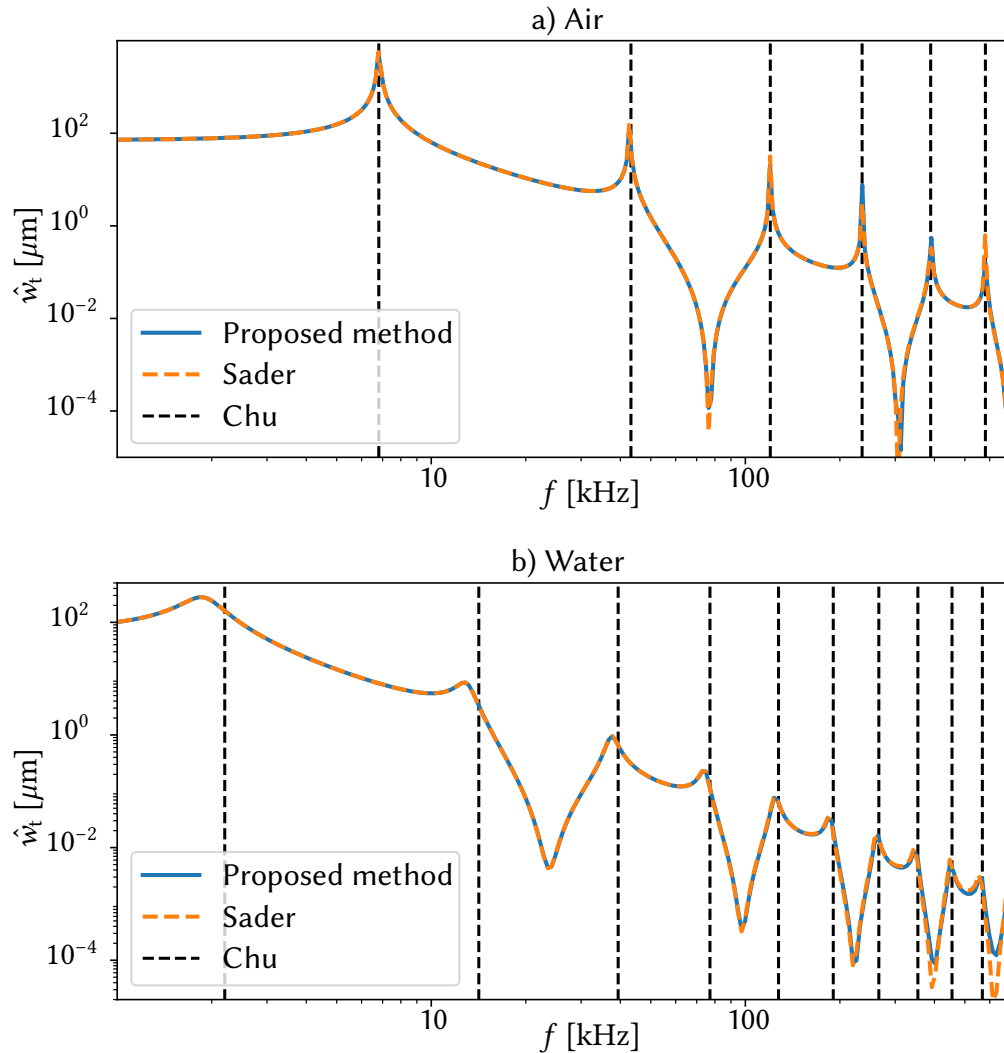


Figure 5.7: Spectral dynamic displacement of the slender plate's tip \hat{w}_t in a) air and in b) water. Results obtained with the proposed method, Sader's method [31] and the inviscid method by Chu et al. [45].

5.2.2 Quality factor

The quality factor of each vibrational mode is obtained from the displacement spectrum \hat{w}_t . In the vicinity of a resonance frequency, the immersed plate is approximated as lumped element model (LEM) composed of a linear spring-damper-mass system in which the hydrodynamics force (due to the pressure jump $\Delta\hat{p}$) appears as a linear damping term with damping coefficient γ and an additional mass Δm as depicted in Fig. 5.8.

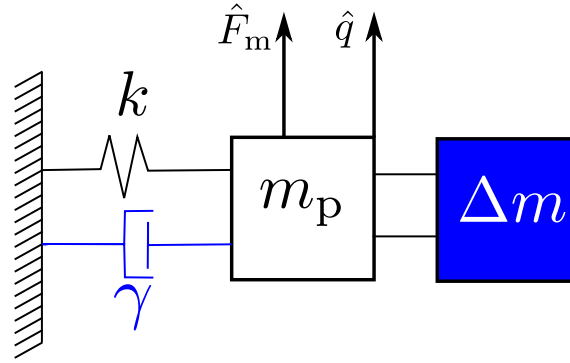


Figure 5.8: Lumped element model of the micro-plate in a viscous fluid. The fluid acts a linear damping term with damping coefficient γ and an additional mass Δm .

The equation of motion for the micro-plate-fluid problem with the LEM is given by the damped harmonic oscillator equation with one degree-of-freedom as

$$m_p \frac{\partial^2 q}{\partial t^2} + \Delta m \frac{\partial^2 q}{\partial t^2} + \gamma \frac{\partial q}{\partial t} + kq = F_m. \quad (5.7)$$

Here, q is the time-dependent displacement of the plate at an arbitrarily defined position, F_m is an effective external drive force, m_p is the plate mass and k the modal stiffness. We define the damped angular resonance frequency as $\omega_d = \sqrt{k/m}$, where m is the total modal mass $m_t = m_p + \Delta m$. From the damped angular resonance frequency, we define the damped fluid resonance frequency f_d as $f_d = \omega_d/(2\pi)$. The Fourier transform of Eq. 5.7 yields

$$-\omega^2 \hat{q} + j\omega \frac{\gamma}{m} \hat{q} + \omega_d^2 \hat{q} = \hat{F}_p. \quad (5.8)$$

The Q-factor Q of a vibrational mode and its modal damping coefficient γ are inversely proportional [62] as

$$Q = \frac{m_t \omega_d}{\gamma}. \quad (5.9)$$

This definition of Q based on the DHO equation renders similar results to the Q-factor definition based on dissipated energy in Eq. 1.2.

From the previous equations, we define a fit spectral response function \hat{q}_{dho} as

$$\hat{q}_{\text{DHO}}(a, Q, \omega_d) = \frac{a \hat{F}_p}{-\omega^2 + j\omega \omega_d / Q + \omega_d^2}. \quad (5.10)$$

In Eq. 5.10, a is an amplitude fitting parameter. To evaluate Q and f_d , we fit the spectral response function q_{DHO} around each damped resonance frequency.

The spectrum displacement \hat{w}_t (and by consequence, Q and f_d) slightly vary with the fluid grid discretization for each mode until convergence is achieved. Fig. 5.9 shows the spectrum displacement \hat{w}_t , the Q-factor and f_d for the first three vibrational modes as

a function of the fluid grid. For the three vibrational modes, at least a fluid grid with $\mathcal{M}_x = 8$ is required (8 x 64 fluid grid).

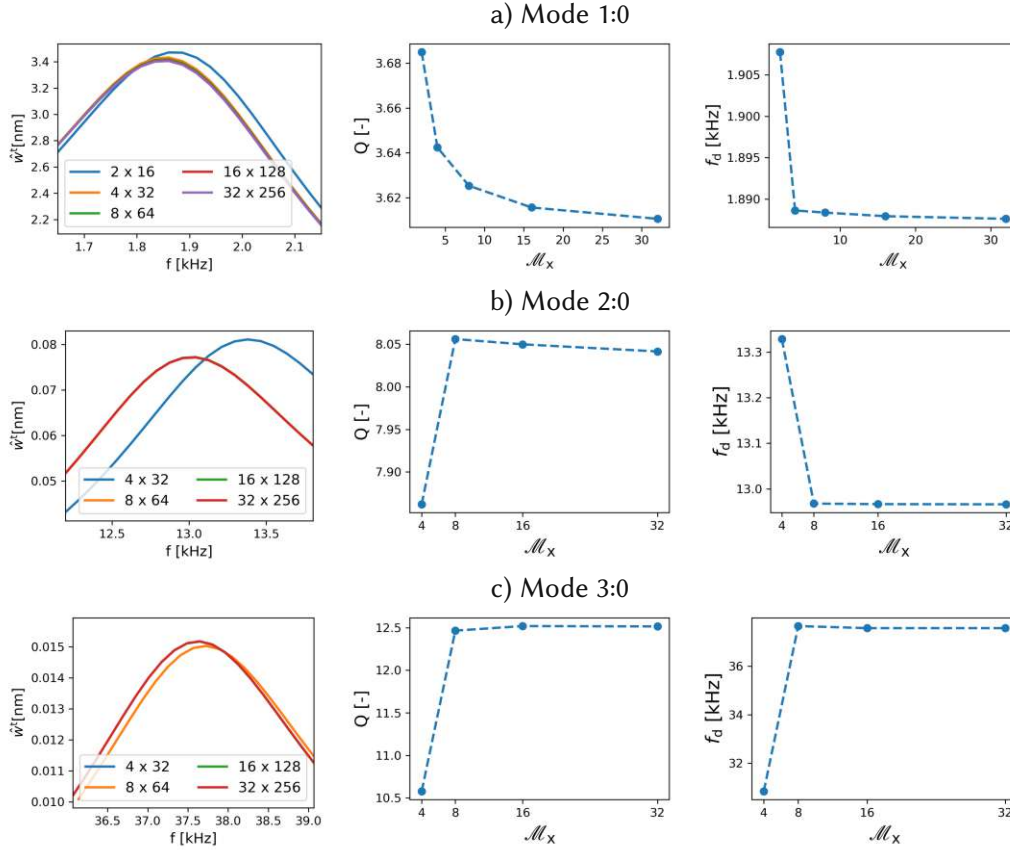


Figure 5.9: Spectrum displacement \hat{w}_t , Q-factor and f_d for the a) 1:0, b) 2:0 and c) 3:0 vibrational modes as a function of the fluid grid in water.

To quantify the convergence of the quality factor we introduce

$$\epsilon_Q^i = \frac{|Q^i - Q^{i-1}|}{\max(Q_n^i, Q_n^{i-1})} \quad (5.11)$$

where Q^i and Q^{i-1} are quality factors obtained with two consecutively refined fluid grids for the same vibrating mode. Fig. 5.10 shows ϵ_Q for all modes of the plates with aspect ratio $r_a = 8$. The Q-factor of lower-order modes converges with a coarser fluid grid than the Q-factor of higher-order modes. For instance, the 1:0 mode converges for $\mathcal{M}_x \geq 8$, while the 5:0 mode converges with $\mathcal{M}_x \geq 32$. The Q-factor is considered converged when the difference between the Q-factors obtained with two consecutively refined fluid grids is smaller than 1% ($\epsilon_Q \leq 0.01$).

Fig. 5.11 shows the converged quality factors of the EB modes in water. In addition to the present method's prediction, Q obtained with Sader's method [31] for flexural modes is shown. The quality factors Q of flexural modes agree within 0.5% to those obtained with Sader's method up to the sixth mode which is here shown.

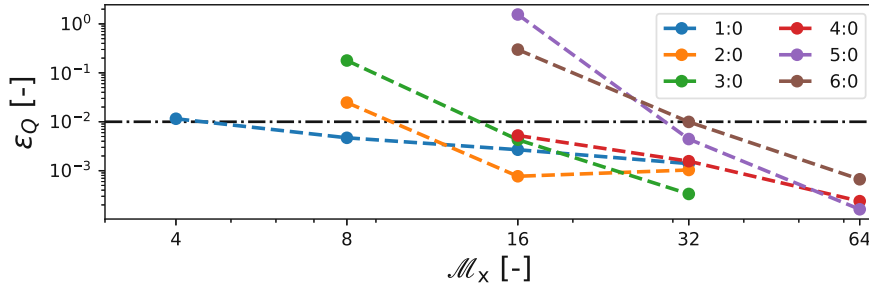


Figure 5.10: Convergence of quality factor ϵ_Q for the slender beam in water. The dotted black line stands for $\epsilon_Q = 0.01$, the value at which we consider that the Q-factor for this mode converged.

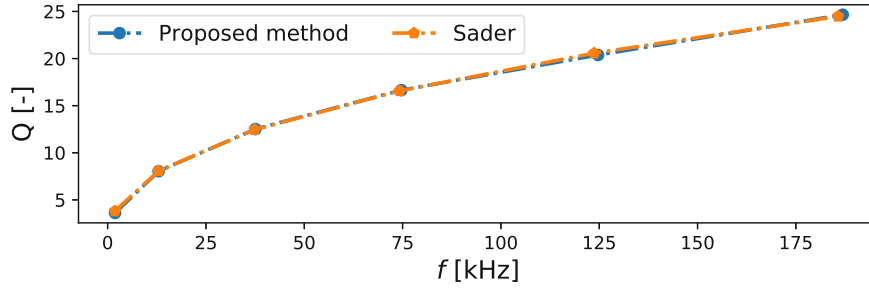


Figure 5.11: Quality factor of the vibrational modes of the plate with $r_a = 8$ in water obtained with the proposed method and Sader's method.

5.2.3 Added-mass effect

In addition to the Q-factor, for MEMS resonators it is essential to quantify the added mass effect caused by the fluid. This is achieved with the fluid-added-mass-per-plate-mass-ratio \mathcal{M} , defined as

$$\mathcal{M} = \frac{\Delta m}{m_{\text{plate}}} = \frac{f_n^2}{f_d^2} - 1. \quad (5.12)$$

\mathcal{M} quantifies the added mass effect, characterized by the reduction of the resonance frequency of a resonator in vacuum f_n to its damped resonance frequency in a fluid f_d [35]. When $f_d \approx f_n$ the added mass is negligible and $\mathcal{M} \approx 0$.

Similarly to the quality factor convergence, we quantify the convergence of the resonance frequency with

$$\epsilon_f^i = \frac{|f_d^i - f_d^{i-1}|}{\max(f_d^i, f_d^{i-1})}, \quad (5.13)$$

where f_d^i and f_d^{i-1} are resonance frequencies obtained with two consecutively refined fluid grids for the same vibrating mode. Fig. 5.12 shows the convergence of the resonance frequency of the slender plates. We consider convergence when $\epsilon(f_d) \leq 0.001$. f_d varies less with the fluid grid than the Q-factor. For this reason, $\epsilon(f_d) \leq 0.001$ is fulfilled with coarser fluid grids than required for the Q-factor convergence.

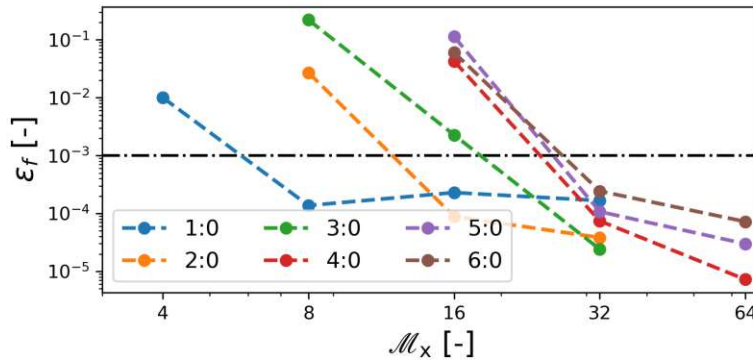


Figure 5.12: Convergence of the damped resonance frequency ϵ_f for the slender beam in water. The dotted black line stands for $\epsilon_f = 0.001$, the value at which we consider that the resonance frequency for this mode converged

Fig. 5.13 shows \mathcal{M} of the slender plate up to 200 kHz. The proposed method slightly under-predicts \mathcal{M} in comparison to Sader's method, but differences are smaller than 5%. These differences are due to differences in the resonance frequencies (both in vacuum and in a fluid) which arise when using Euler-Bernoulli slender beam theory or Kirchhoff plate theory. Since the plate here considered has an aspect ratio of 8, small differences in f_n and f_d are expected, which are seen in the added-mass effect.

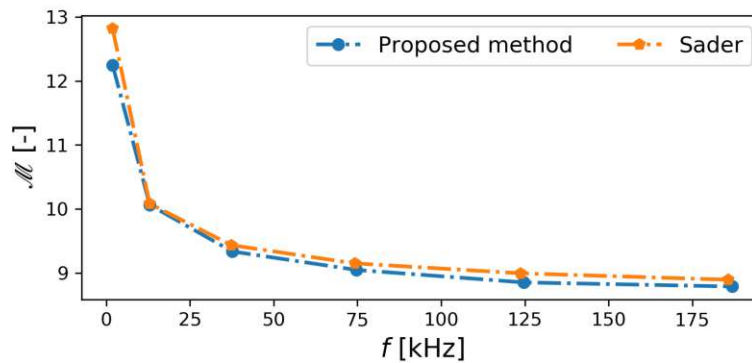


Figure 5.13: Added-mass of the vibrational modes of the plate with $r_a = 8$ in water.

5.3 Validation with purely numerical results

An important assumption in the present method is the two-dimensional fluid flow approximation, as discussed in detail in Section 4.1. Here the Q-factor and \mathcal{M} calculated with the present method and with a purely numerical method [35] which assumes three-dimensional fluid flow are compared. The silicon micro-plate has length equals 197 μm , width equals 29 μm ($r_a \approx 6.5$), and the thickness is 2 μm .

The Q-factor and \mathcal{M} of the first six flexural modes of this slender plate in water are shown in Fig. 5.14. Q-factor with the purely numerical method agrees with the present method's prediction within 10% for the low order modes ($n_x \leq 4$). For higher n_x , the difference in Q-factors increases, reaching 20% difference for the 6:0 mode. There are minimal differences in \mathcal{M} (smaller than 5%) with the two methods up to the sixth flexural mode. Results shown in Fig. 5.14 agree with previous findings of studies that used purely numerical methods [35, 19, 64, 63] that the two-dimensional fluid flow approximation results in an underestimated resonance frequency, which in turns yields an overestimated added mass, as well as under-estimated Q-factor.

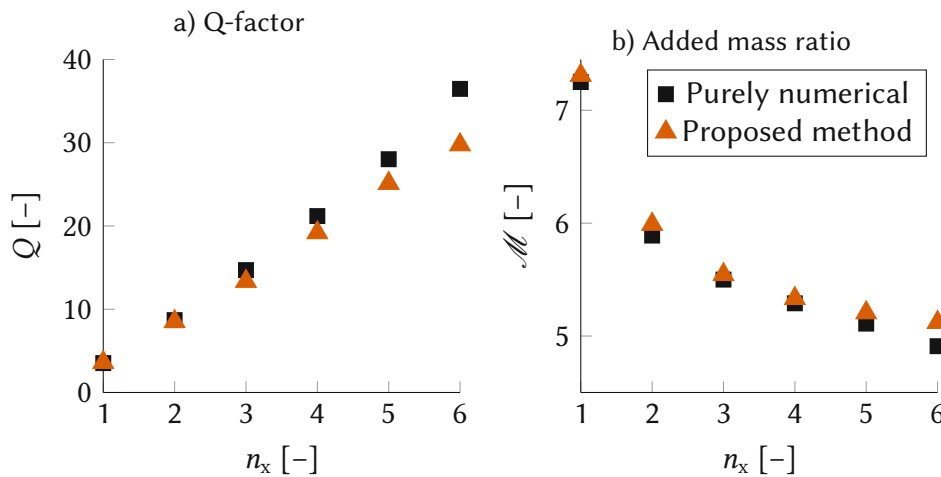


Figure 5.14: a) Q-factor Q and b) fluid-added-mass-per-plate-mass-ratio \mathcal{M} of flexural modes of a slender plate predicted by a purely numerical method [35] and with the present method.

5.4 Validation with experimental results

To validate the proposed semi-numerical method we resort to published experimental data on the Q-factor of micro-plates in a viscous fluid. Here a silicon micro-plate which is 500 μm long, 300 μm wide ($r_a \approx 1.66$) and 11.5 μm thick is investigated [66]. The fluid used in the experiments is isopropanol with $\mu_f = 2.1062$ mPa·s and density $\rho_f = 781.2$ kg/m³. Silicon is here considered as an orthotropic material with properties given in Table 3.1.

Fig. 5.15 shows the Q-factor of the reported vibrational modes obtained experimentally and calculated with the present method. Results include not only roof tile-shaped modes but also other low-order modes [66]. Convergence of the Q-factor and damped resonance frequency with the fluid grid is shown in B.1. Excellent agreement between simulated and experimental Q-factors is found. Notably, we observe exceptional agreement with all vibrational modes up to the 1:2 mode at 750 kHz. For the three higher frequency vibrational modes, the prediction and experimental Q-factors differ by less

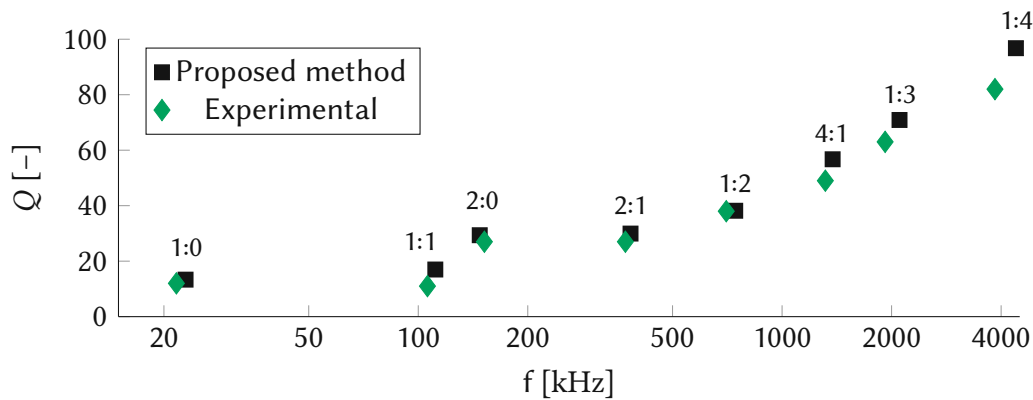


Figure 5.15: Quality factor Q of different vibrational modes of a wide micro-plate in isopropanol.

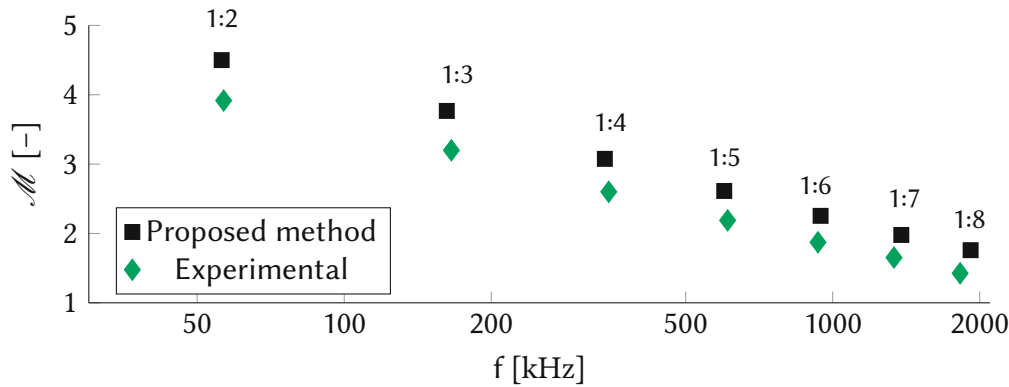


Figure 5.16: Added mass ratio \mathcal{M} of roof tile-shaped modes of a rectangular micro-plate in isopropanol.

than 10%¹, which is a smaller difference than the errors reported using purely numerical methods [35, 19].

Additional studies focused exclusively on the roof tile-shaped modes, for example, a micro-plate with $l = 2524 \mu\text{m}$, $b = 1274 \mu\text{m}$ ($r_a \approx 2$), and $h = 22 \mu\text{m}$ in isopropanol [30, 66]. The experimental fluid-added-mass-per-plate-mass-ratio \mathcal{M} of the roof tile-shaped modes up to 2 MHz are shown in Fig. 5.16. The present method slightly over-predicts \mathcal{M} for all roof tile-shaped modes by $15 \pm 2\%$, while the damped resonance frequencies show very good agreement.

The Q-factors of the roof tile-shaped modes of the same plate are shown in Fig. 5.17. Excellent agreement between the present method's prediction and experimental data is found. Predicted Q-factors are within the experimental errors for most of the evaluated modes, being the only exceptions the 1:4 and 1:5 modes, for which the present method under-predicts the Q-factors by 10%². Fig. 5.17 shows also the Q-factor obtained with

¹Compressibility is not the reason for this 10% difference, since even for the 1:4 mode at 4.12 MHz the acoustic wavelength ($276 \mu\text{m}$) is larger than the flexural wavelength of the 1:4 mode ($151 \mu\text{m}$).

²Note that isopropanol is incompressible even for the 1:8 mode because the acoustic wavelength at 1.92 MHz is $592 \mu\text{m}$, which is much larger than the flexural wavelength of the (1,8) mode that is $320 \mu\text{m}$

a purely numerical method from Ruiz Diez et al. [42]. In [42], the Q-factor is obtained by assuming the vibrational mode in the fluid to be the same as the plate's vibrational mode in vacuum, which is obtained numerically. The dynamics of the plate-fluid domains are solved in the time domain in a single cross-section of the plate assuming a two-dimensional incompressible fluid flow. The damping factor and added mass coefficients are determined from the fluid stress on the top and bottom sides of the plate and the Q-factor is then obtained from Eq. 5.9. With the purely numerical method, good agreement in the Q-factor is found only for the 1:2 mode. For the 1:3 mode, Q is over-predicted, whereas for the higher order roof tile-shaped modes 1:4 to 1:8 Q is under-predicted. For instance, the Q-factor of the 1:8 mode is underestimated by 50.2% with the purely numerical method. Moreover, the purely numerical method under-predicts the resonance frequencies of all roof tile-shaped modes. These differences are likely due to differences in the vibrational modes in vacuum and in liquids (which this particular purely numerical method assumes to be the same), or to not enough discretization near the plate's side edges, where the pressure jump tends to infinite. Results in Fig. 5.17 evidence that the proposed method surpasses the accuracy of purely numerical methods in the estimation of both resonance frequencies and Q-factors of micro-plates in viscous fluids.

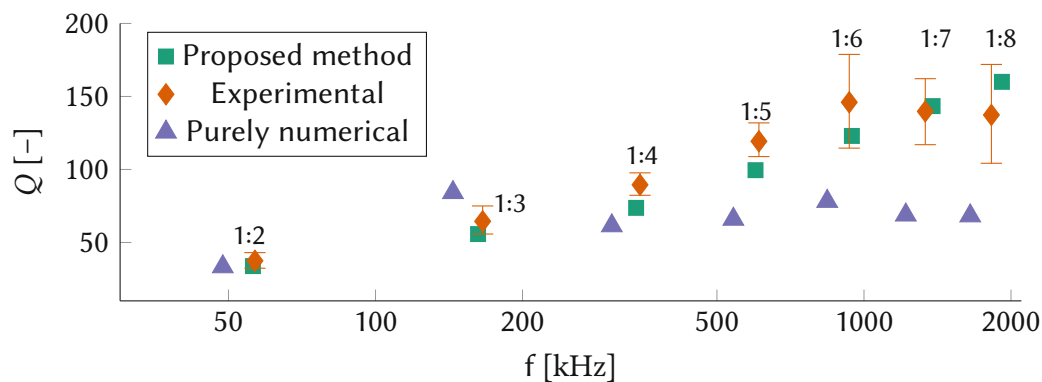


Figure 5.17: Q-factor of the roof tile-shaped modes of a rectangular micro-plate in isopropanol. Experimental and purely numerical results are obtained from Ruiz Diez et al. [42].

5.5 Conclusions

In this chapter, the semi-numerical method for determining the dynamics of micro-plates immersed in incompressible viscous fluids was defined. The proposed method converges at all frequencies tested in water and in air with a minimum convergence rate equal to 1.8. For a plate with $r_a = 8$, the difference in Q-factor prediction between the proposed method and semi-analytical models [31] was minimal, showing the proposed

The acoustic wavelength is calculated considering the speed of sound of isopropanol as 1139 m s^{-1} [66]. The flexural wavelength is calculated using a two-dimensional Fourier transform.

method's accuracy. What is more, excellent agreement to experimental data of micro-plates in liquids (Figs 5.15 to 5.17) was obtained both for the Q-factor as well as for the added-mass \mathcal{M} . These results ensure that the proposed method accurately predicts the Q-factor and the fluid-added-mass-per-plate-mass-ratio \mathcal{M} of different vibrational modes of micro-plates in viscous fluids.

Part II

Numerical and experimental results

6 Viscous losses in the beam-plate transition

Results of this chapter were partially published in [71].

With the convergence and validation of the proposed method shown, it is possible to investigate different effects in the micro-plate-fluid structure interaction. The first question that requires attention is how the viscous losses vary as the elastic structure ranges from a slender beam to a wide plate in different fluids. For that purpose, we consider plates with $l = 800 \mu\text{m}$, $h = 5 \mu\text{m}$, and whose widths spawn from $b = 12.5 \mu\text{m}$ to $b = 400 \mu\text{m}$. Hence, the structures range from a narrow beam with aspect ratio $r_a = 64/1$ to a wide plate with $r_a = 64/32$, as depicted in Fig. 6.1. With this selection of geometries, we obtain a broad perspective of the beam-plate transition.



Figure 6.1: Example of plates with different aspect ratios a) $r_a = 64/1$, b) $r_a = 64/12$, c) $r_a = 64/20$ and d) $r_a = 64/32$ which are here investigated.

The beam-plate transition is here investigated in air and in water as representative fluids for gases and liquids, respectively. The properties of air and water are considered at SATP as given in Table 2.3.

6.1 Air

6.1.1 Displacement spectrum

The structure's displacement spectrum is calculated considering an excitation of 1 mN applied to the plate's free corner $x = l$, $y = b/2$. The structure's displacement is analyzed once more at the plate's free corner at $x = l$, $y = b/2$, as shown in Fig. 6.2. The free-corner displacement \hat{w}_t is ideal for such analysis since all vibrational modes exhibit a significant displacement at the free corner.

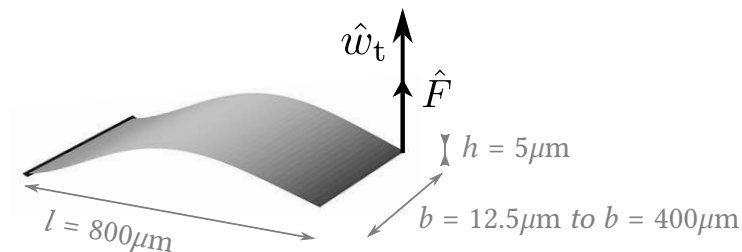


Figure 6.2: Dimensions of the cantilevered plates used in the beam-plate transition analysis.

In air, a frequency range from 1 kHz to 1 MHz is defined with a 1 kHz discretization step. Fig. 6.3 shows the spectral displacement \hat{w}_t of the slender beam with $b = 12.5 \mu\text{m}$ and the wide plate with $b = 400 \mu\text{m}$. In the 1 MHz frequency range, the slender beam exhibits only six resonance frequencies which refer to the lowest six EB modes (from 1:0 to 6:0 according to Leissa's notation). The wide micro-plate (with $b = 400 \mu\text{m}$) exhibits also six EB-modes in the same frequency range. But, additionally, the micro-plate exhibits five torsional modes, two roof tile-shaped modes and four higher-order plate modes.

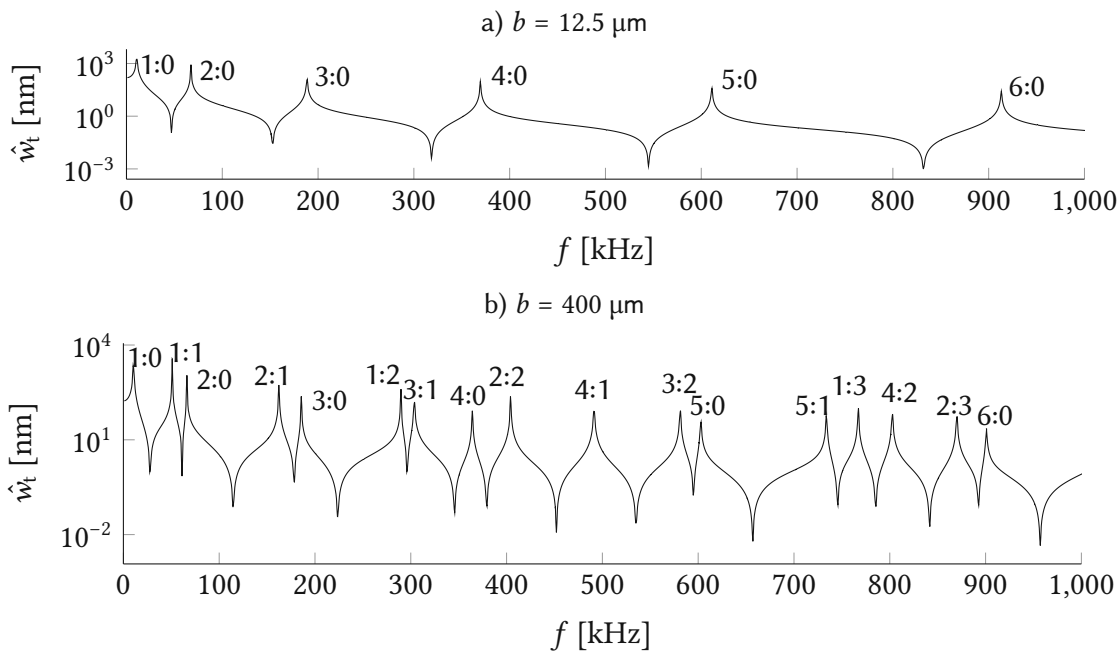


Figure 6.3: Displacement spectrum of the a) slender beam with $b = 12.5 \mu\text{m}$ and b) wide plate with $b = 400 \mu\text{m}$ in air.

The vibrational modes of the plate with $r_a = 64/32$ in air are shown in Fig. 6.4. In order for better visualization of the different vibrational modes occurring in plates, here and throughout this thesis EB modes are depicted in a green background (or with green markers), torsional modes in violet, roof tile-shaped (RTS) modes in blue and higher-order plate (HOP) modes in a red background.

Fig. 6.5 shows the absolute displacement spectrum $|\hat{w}_t|$ of the plates with width ranging from $12.5 \mu\text{m}$ to $400 \mu\text{m}$ due to a force of 1 mN applied to one of the plate's free corner in air. As the plate becomes wider (increasing b), more non-EB vibrational modes occur in the frequency range up to 1000 kHz while the number of EB modes remains the same. The damped resonance frequencies f_d of the EB vibrational modes are identified with a green dashed line, violet lines identify the torsional modes, blue the RTS modes and red lines the HOP modes.

In air, the damped resonance frequencies f_d of EB modes remain unaltered through the beam-plate transition, while for all non-EB modes, f_d reduces as the plate's width increases. f_d of the EB modes is independent of the plate's width because the added-

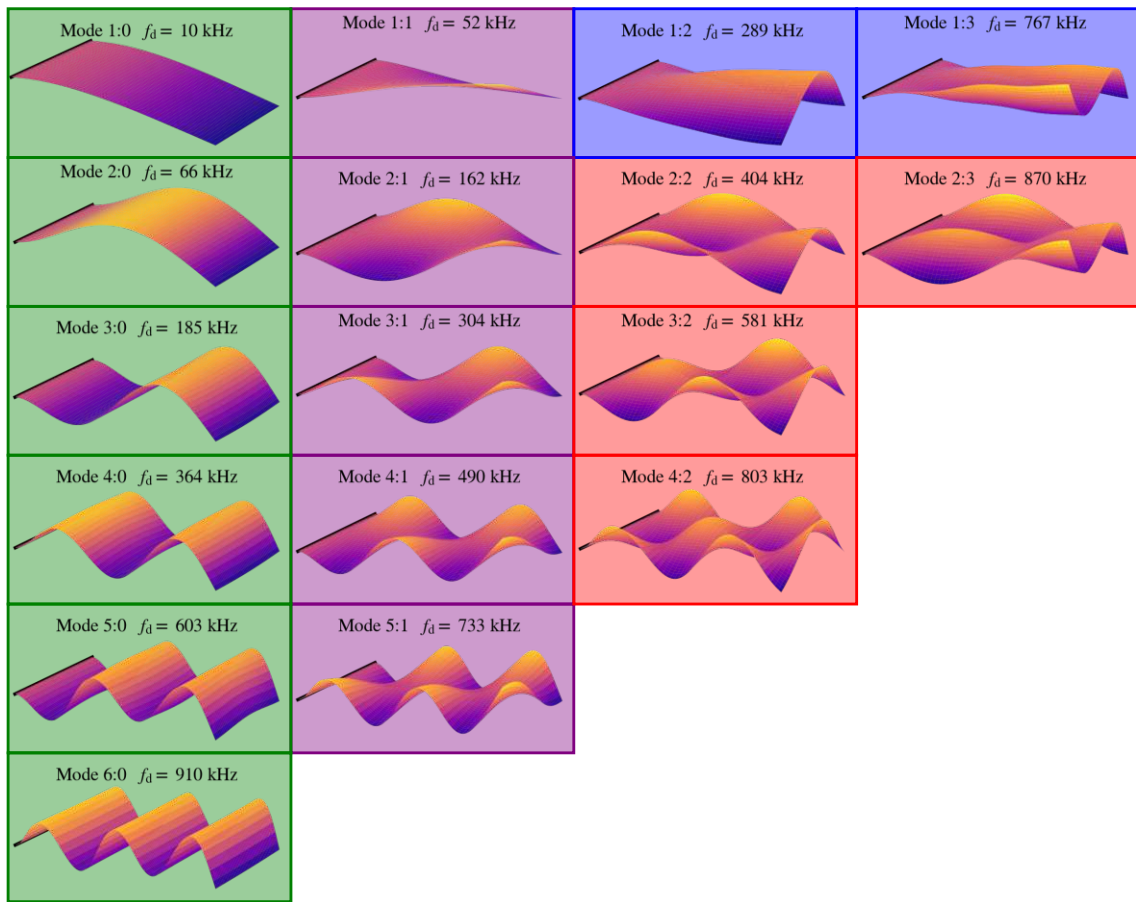


Figure 6.4: Vibrational modes of the plate with $b = 400 \mu\text{m}$ in air. Green background identifies the EB modes, a violet background the torsional modes, blue the RTS modes and red the HOP modes.

mass effect in air is negligible, which means $f_d \approx f_{\text{vac}}$. The vacuum resonance frequencies f_{vac} of the out-of-plane bending modes of beams are independent of the beam's width according to Euler Bernoulli's theory. Table 6.1 shows the vacuum resonance frequencies of the modes 1:0 to 6:0 of the plates with widths ranging from $b=12.5 \mu\text{m}$ to $b=400 \mu\text{m}$. f_{vac} are obtained from an eigenvalue analysis of the Kirchhoff plate equation, essentially Eq. 3.1 without the right-hand-side terms for orthotropic silicon.

Table 6.1: Average vacuum resonance frequencies and standard deviation of the beam-like modes 1:0 to 6:0 of the plates with aspect ratio from $r = 64/1$ to $r = 64/32$.

Mode	1:0	2:0	3:0	4:0	5:0	6:0
f_{vac} [kHz]	10.2 ± 0.1	66.3 ± 0.1	185.5 ± 0.1	364.9 ± 0.1	603.6 ± 0.1	910.8 ± 0.2

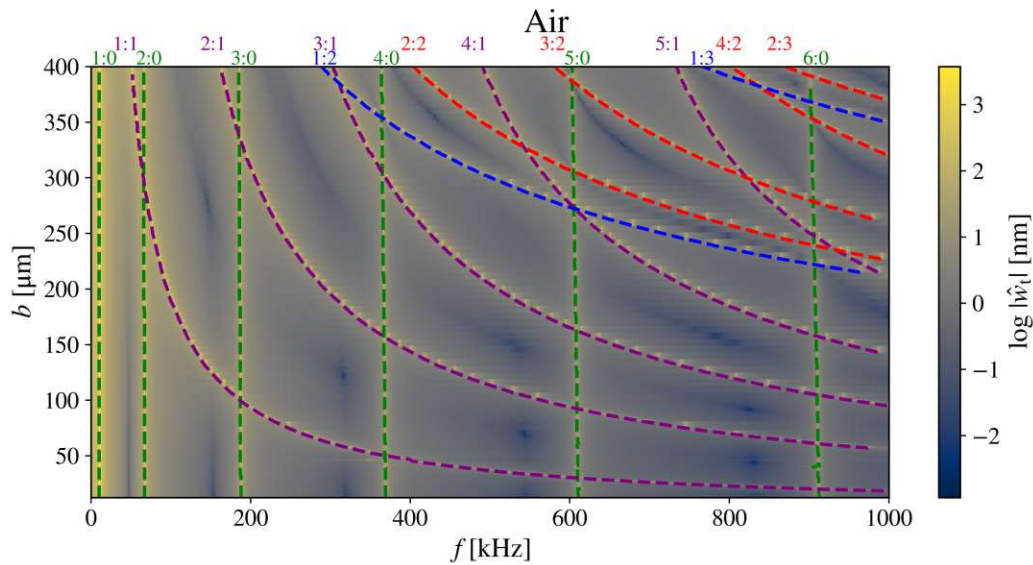


Figure 6.5: Absolute displacement spectrum \hat{w}_t of plates with different widths in air. On the y-axis, the width b ranges from 12.5 μm to 400 μm , and on the x-axis the frequency range up to 100 kHz. The colormap refers to the logarithmic value of the absolute displacement, where bright yellow represents maximum displacement and are associated with a resonance frequency and vibrational mode. Green dashed lines identify the resonance frequencies of EB modes, violet lines represent torsional modes, blue lines the RTS modes and red lines the HOP modes.

6.1.2 Q-factor

The Q-factor of each vibrational mode of the different micro-plates are determined using the LEM as introduced in Section 5.2.2. Fig. 6.6 shows the Q-factor of the two limiting structures here analyzed in air: that is the slender beam with $b = 12.5 \mu\text{m}$ and the plate with $b = 400 \mu\text{m}$, respectively. The convergence for both plates, as well as the following plates whose data are shown in this section, for f_d and Q , are shown in the Appendix B.

For the slender beam, there are only EB-like modes in the 1 MHz frequency range and the highest Q-factor in the 1 MHz frequency range is the 6:0 mode's Q-factor equals 1264 for a frequency of $f_d = 913 \text{ kHz}$. For the wide plate, the highest Q-factor in the same frequency range is the 2:3 mode's $Q_{\text{plate}}^{2:3}$ equals to 2820, which is more than twice the highest Q achieved with the beam ($Q_{\text{beam}}^{6:0} = 1264$). Fig. 6.7 shows the Q-factor of the EB and torsional modes as the structure is altered from a slender beam with $b = 12.5 \mu\text{m}$ to a plate with $b = 400 \mu\text{m}$ in air.

In Fig. 6.7, data referring to EB modes are shown in green, with torsional modes in violet. Note that EB modes exhibit an increase in Q with the plate's width b , followed by a decrease in Q . For the 1:0 mode, Q increases with the plate's width until a maximum of $Q = 142$ is achieved. These results for the EB modes agree with Sader's methods predictions, which are shown in Fig. 6.6 in black. The Q-factor of the 4:0 mode differs between the proposed method's and Sader's prediction at $b = 300 \mu\text{m}$. This occurs because for this geometry, modes 4:0 and 1:2 have a similar resonance frequency f_d (see Fig. 6.5 for how f_d alters with b). This effect can not be predicted by Sader's method.

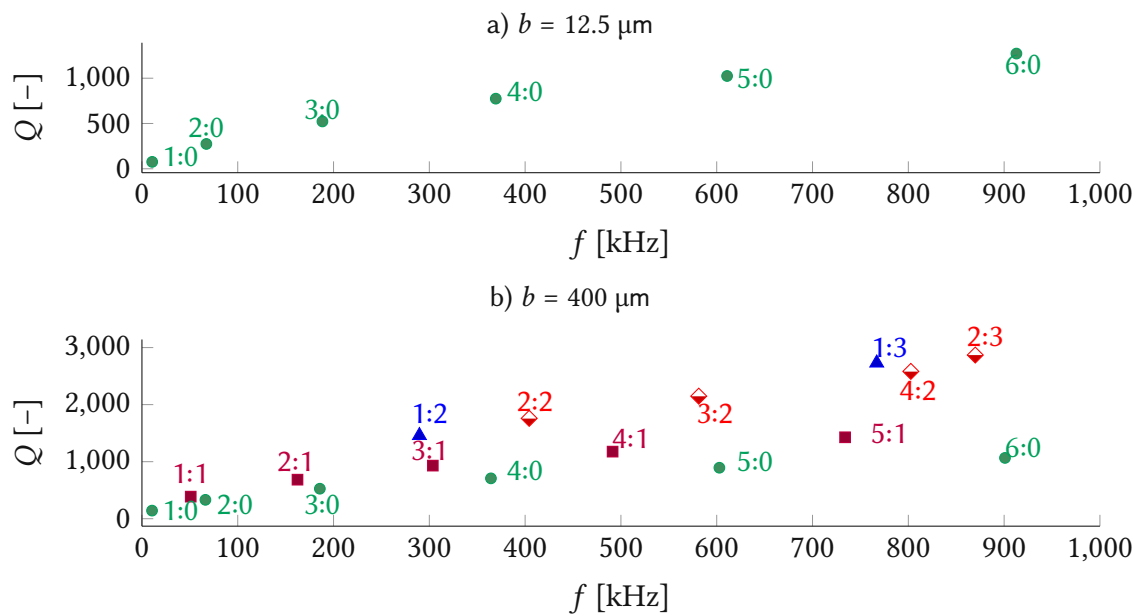


Figure 6.6: Q-factor of the a) slender beam with $b = 12.5 \mu\text{m}$ and b) wide plate with $b = 400 \mu\text{m}$ in air.

For the torsional modes in air, the Q-factor always decreases as the plate's width b is increased.

6.2 Water

6.2.1 Displacement spectrum

Altering the fluid from air to water results in the displacement spectrum \hat{w}_t as shown in Fig. 6.8 where the width of the plates ranges from $12.5 \mu\text{m}$ to $400 \mu\text{m}$. In water, a frequency range from 1 kHz to 500 kHz is defined with a 1 kHz discretization step so that a similar total number of vibrational modes is analyzed in air and in water.

Note that, in water, the resonance frequencies of the EB modes decrease as the plate's width increases. This is different from the results in air since in air f_d^{EB} is independent of b . In water, as the plate becomes wider, more EB vibrational modes fall into the frequency range up to 500 kHz. While the slender beam has only six EB modes in this frequency range, the wide plate exhibits nine. The vibrational modes of the plate which occur in the 500 kHz frequency range are shown in Fig. 6.9. This difference in the f_d dependency with b in air and water is due to the greatly different densities of both fluids, which lead to different added-mass effects in each fluid.

6.2.2 Q-factor

Fig. 6.10 shows the Q-factor of the EB and torsional modes of the micro-plates in water. For all modes, the Q-factor increases as the plate's width b is increased. For instance,

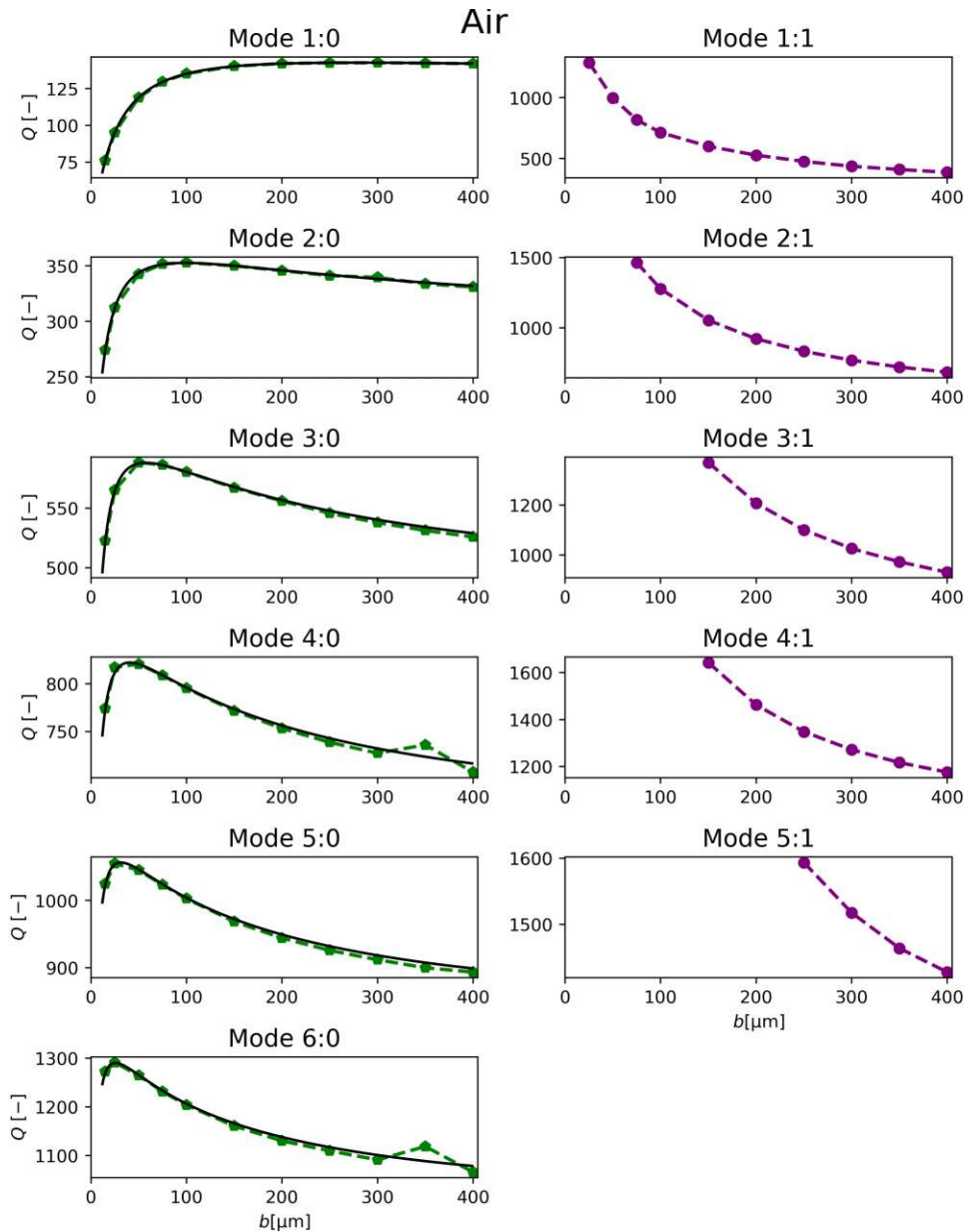


Figure 6.7: Quality factor of EB and torsional modes as the structure is altered from a slender beam with $b = 12.5 \mu\text{m}$ to a plate with $b = 400 \mu\text{m}$ in air. For EB modes, Sader's predictions for the Q-factors are shown in black.

the 2:0 mode exhibits a Q-factor equal to 5 for a beam with $b = 50 \mu\text{m}$, and a Q-factor of 20 for the wide plate with $b = 400 \mu\text{m}$, representing a four-fold increase in Q for a same EB vibrational mode. Also, torsional modes exhibit an increase in Q-factor with b , although less accentuated than EB modes, e.g. the Q-factor of the 2:1 mode increases from 17 for $b = 100 \mu\text{m}$ to $Q=21$ when the micro-plate is $400 \mu\text{m}$ wide.

Fig. 6.11 highlights how an opposite trend of Q-factor in the beam-plate transition occurs in the air and in water for the same vibrational modes. In air, Q decreases for an

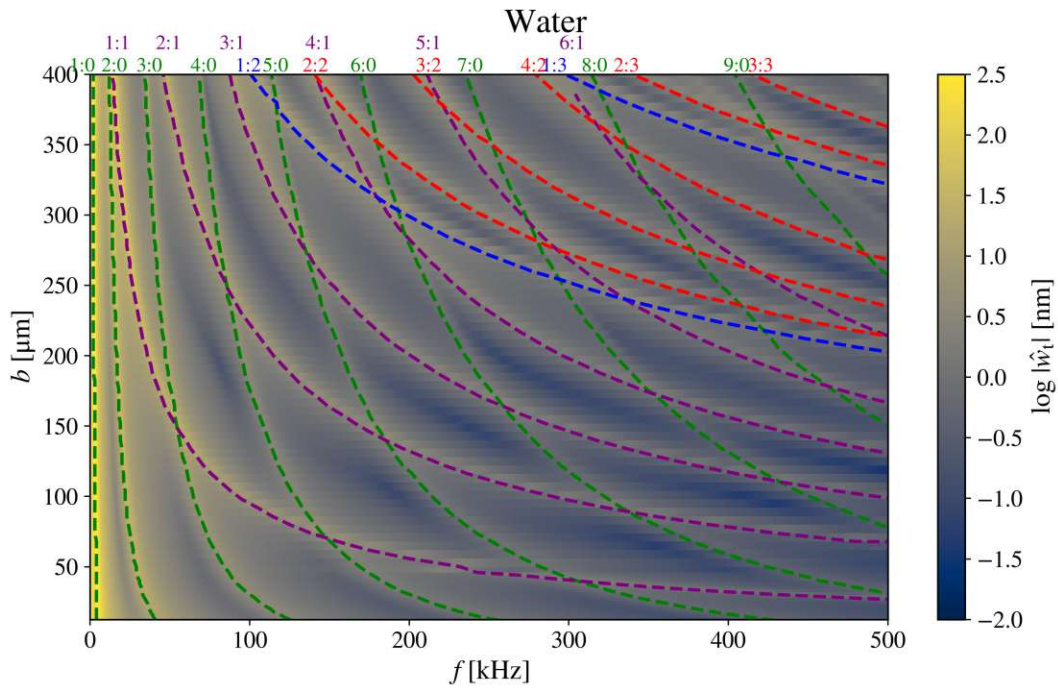


Figure 6.8: Absolute displacement spectrum \hat{w}_t of plates with different widths in water. On the y-axis, the width b ranges from 12.5 μm to 400 μm , and on the x-axis the frequency range up to 100 kHz. The colormap refers to the logarithmic value of the absolute displacement, where bright yellow represents maximum displacement and are associated with a resonance frequency and vibrational mode. Green dashed lines identify the resonance frequencies of EB modes, violet lines represent torsional modes, blue lines the RTS modes and red lines the HOP modes.

increasing width b (except for the very narrow beam with $b \leq 50 \mu\text{m}$ in the EB modes as shown in Fig. 6.7), while in water the opposite occurs and Q increases with the plate's width.

6.3 Added-mass effect and the damping coefficient

The reason why the Q -factor of the EB modes and torsional modes decrease in air and increase in water for wider plates is better understood by identifying that the Q -factor Q of a vibrational mode is affected by changes to the total modal mass $m_t = m_p + \Delta m$, the damped frequency f_d and the damping coefficient γ through

$$Q = \frac{(m_p + \Delta m)2\pi f_d}{\gamma}. \quad (6.1)$$

Interestingly, both in air and in water, γ increases with b in torsional and in EB modes. In the air, the increase in γ results in a decrease in Q with b for $b > 50 \mu\text{m}$. For $b > 50 \mu\text{m}$, γ increases with an exponent equal to or larger than 1 with b , whereas the plate's mass increases with an exponent equal 1 (the added-mass effect is negligible in

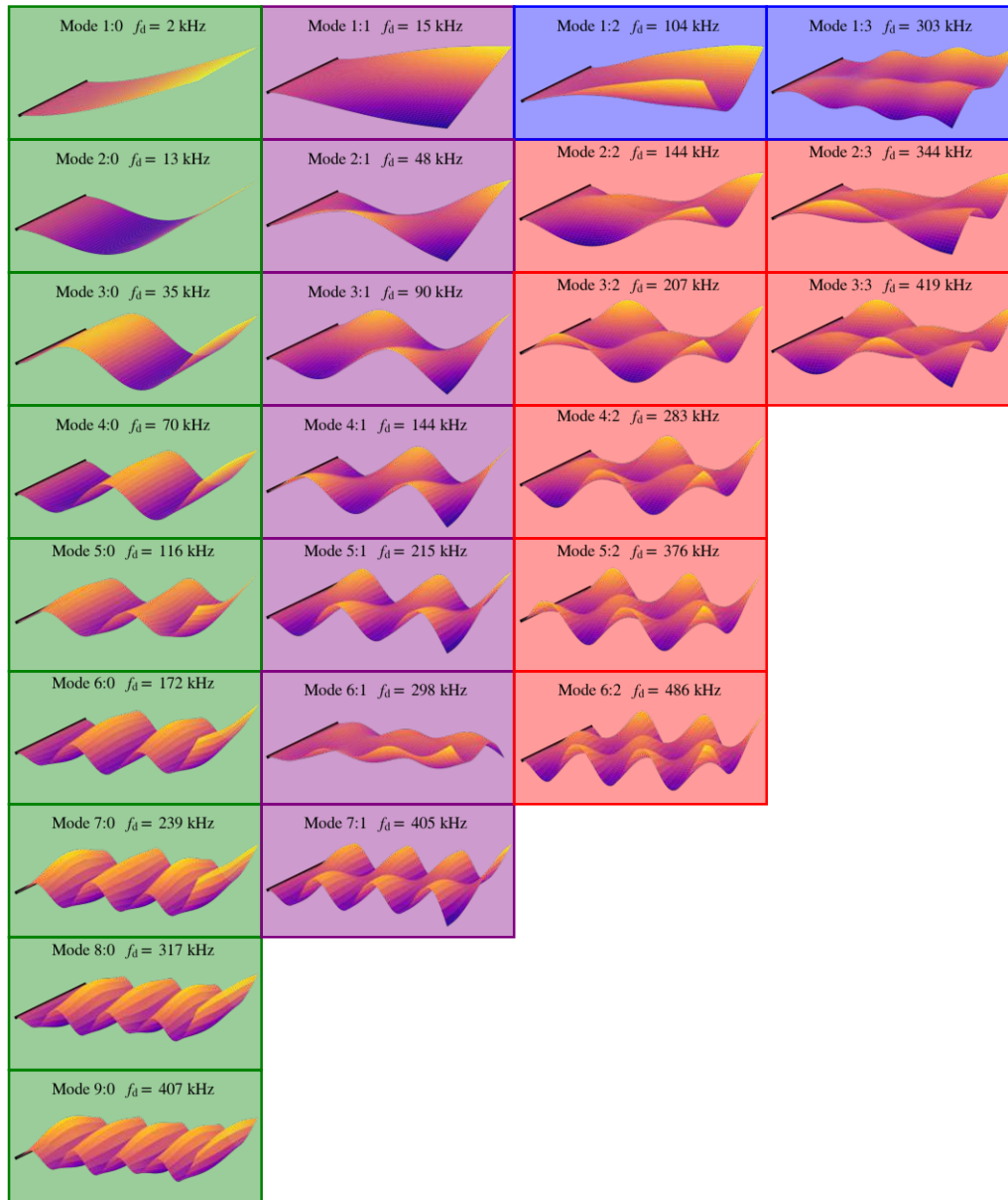


Figure 6.9: Vibrational modes of the plate with $b = 400 \mu\text{m}$ in water. Green background identifies the EB modes, a violet background the torsional modes, blue the RTS modes and red the HOP modes.

air, therefore $\Delta m \approx 0$). Since f_d is constant (with b) for the EB modes, and decreases with b for the torsional modes, this leads to a Q-factor that decreases with b in air for $b \geq 50 \mu\text{m}$. In the very slender beam scenarios with $b < 50 \mu\text{m}$, γ increases with an exponent smaller than 1, resulting in an increasing Q-factor for the EB modes.

In water, the added-mass effect is not negligible and strongly impacts the Q-factor. Fig. 6.13 shows the fluid-added-mass-per-plate-mass-ratio \mathcal{M} of the plates with an aspect ratio between 64/4 and 64/32 in water as a function of the modes' damped resonance frequencies f_d . Similar modes of the different plates are connected with a dashed

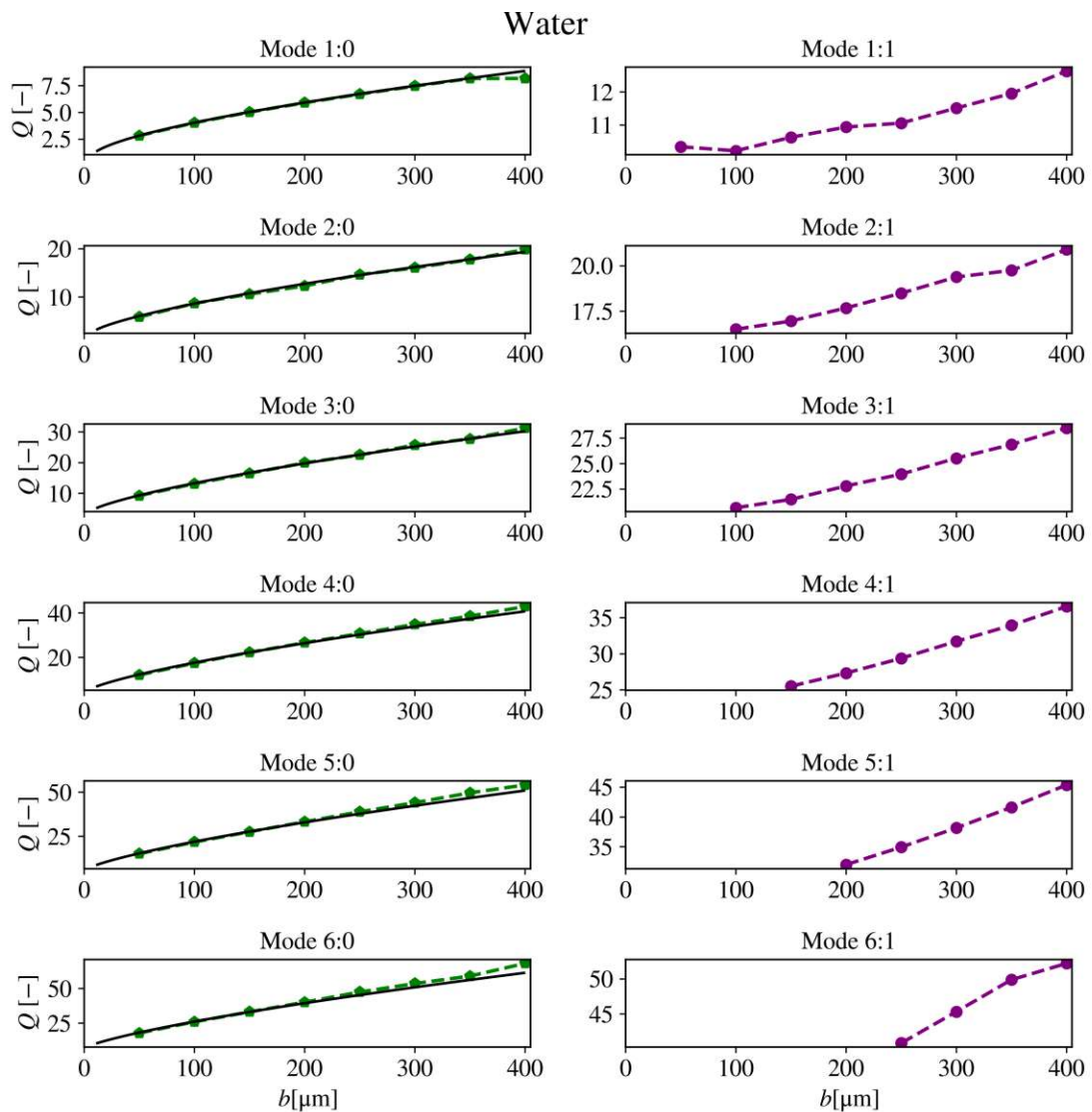


Figure 6.10: Quality factor of EB and torsional modes as the structure is altered from a slender beam with $b = 12.5 \mu\text{m}$ to a plate with $b = 400 \mu\text{m}$ in water. For EB modes, Sader's predictions for the Q -factors are shown in black.

black line. The wider the plate, the greater the \mathcal{M} for the same vibrational mode. Hence, for all modes, slender beams exhibit a lower \mathcal{M} and higher f_d , and wide plates exhibit the opposite, higher added-mass and lower damped resonance frequency. For EB modes, the added-mass effect of wide plates is very strong, achieving values as high as \mathcal{M} , meaning the fluid-added-mass Δm is 30 times the plate's mass m_p .

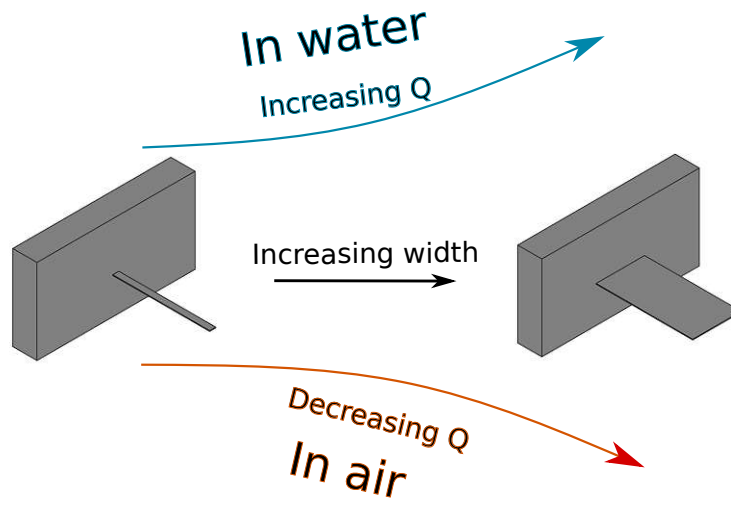


Figure 6.11: Illustration of the beam-plate transition effect on the Q-factor in air and in water.

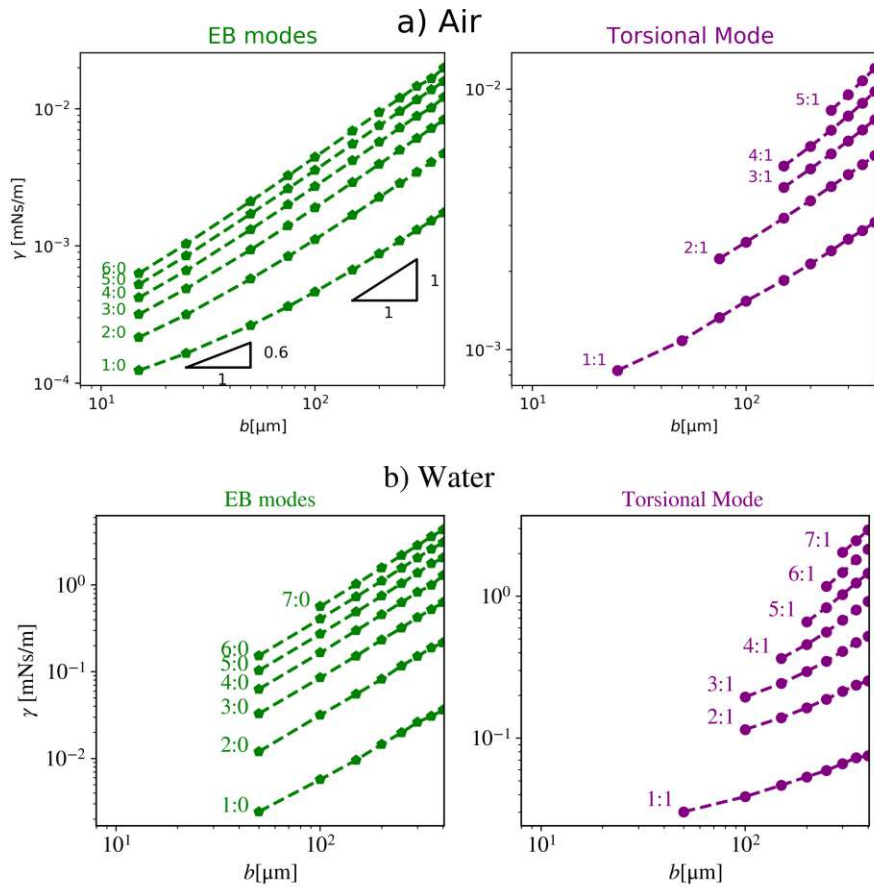


Figure 6.12: Damping coefficient of the EB and torsional modes in a) air and b) water.

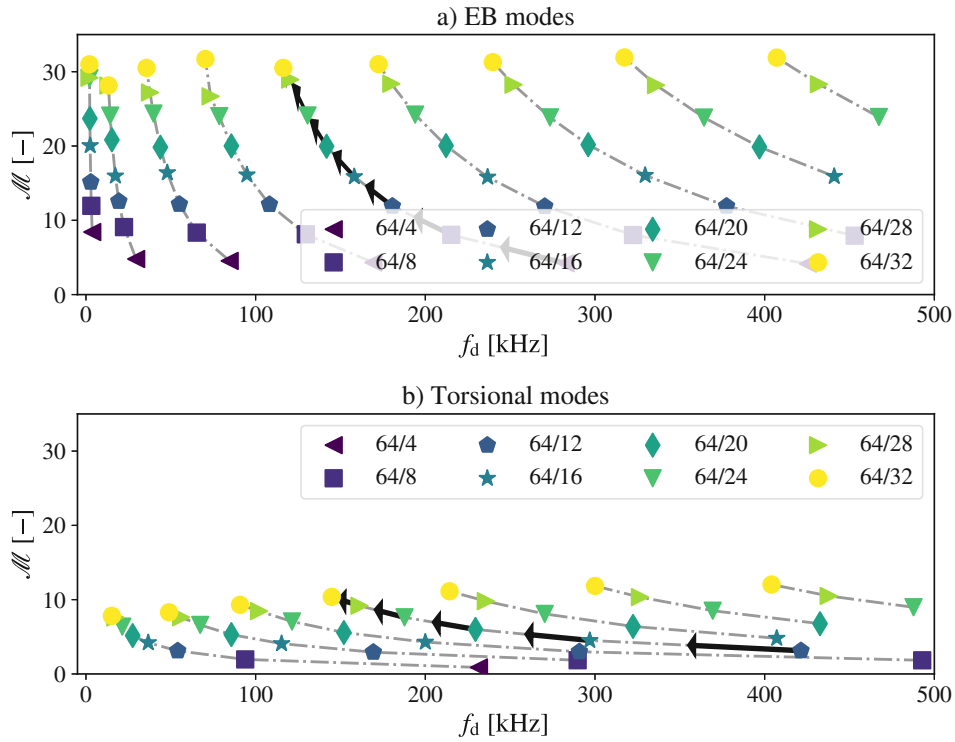


Figure 6.13: Fluid-added-mass-per-plate-mass-ratio \mathcal{M} of the a) EB and b) torsional modes of micro-plates. The legend refers to the plate's aspect ratios r . A gray dashed black line connects the same vibrational mode of the different plates. The arrows indicate the increasing width direction.

6.4 Fluid flow, kinetic energy and viscous dissipation

The fluid-added-mass and fluidic damping coefficient were until the previous sections seen as simple passive elements in the LEM. However, both effects can be traced back to the fluid flow around the different structures and vibrational modes. The present proposed method allows also for determining the velocity field, kinetic energy and viscous dissipation associated with each vibrational mode to further comprehend the micro-plate-fluid problem.

With the 2D fluid flow formulation, the fluid velocity in z and in y directions are determined in any position in the fluid domain taking partial derivatives of the stream-function $\hat{\psi}_x$ definition in Eq. 4.8, which yields

$$\hat{u}_z(x^c, y', z') = \int_{-b/2}^{b/2} \frac{1}{\mu_f} \Delta \hat{p}(x^c, y) \frac{\partial^2 \hat{\psi}}{\partial y \partial y'} \Big|_{z=0} dy, \quad (6.2)$$

and

$$\hat{u}_y(x^c, y', z') = - \int_{-b/2}^{b/2} \frac{1}{\mu_f} \Delta \hat{p}(x^c, y) \frac{\partial^2 \hat{\psi}}{\partial y \partial z'} \Big|_{z=0} dy. \quad (6.3)$$

Eqs. 6.2 and 6.3 can be evaluated numerically using the analytic form for $\hat{\Psi}$ given in Eq. 4.5.

For the fluid flow analysis, we determine the fluid flow surrounding the free edge ($x^c = l$) of the micro-plate as depicted in Fig. 6.14. The plate's displacement is normalized so that the free corner's displacement is $\hat{u}_t = 1 \mu\text{m s}^{-1}$.

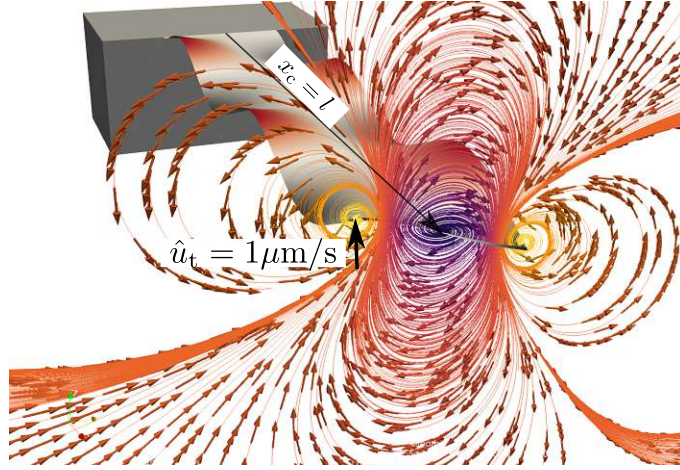


Figure 6.14: Fluid flow representation around the free edge of a micro-plate vibrating in the 5:1 mode. The plate's displacement is normalized so that the free corner's displacement is $\hat{u}_t = 1 \mu\text{m s}^{-1}$.

The fluid flow is divided in in-phase fluid flow $\hat{\mathbf{u}}_{\text{IP}}$ which stands for the fluid flow velocity in-phase with the plate velocity, and out-of-phase fluid flow $\hat{\mathbf{u}}_{\text{OP}}$, for the out-of-phase fluid velocity component with the plate velocity. Fig. 6.15 shows both in-phase and out-of-phase components of the fluid flow surrounding the free edge ($x^c = l$) of plates with different widths. Note in Fig. 6.15 that $\hat{\mathbf{u}}_{\text{IP}}$ and $\hat{\mathbf{u}}_{\text{OP}}$ fulfill the no-slip and no-penetration boundary conditions at the plate's surfaces, given that $\hat{\mathbf{u}}_{\text{IP}}$ has a value of $1 \mu\text{m s}^{-1}$ with only z -component for $-b/2 \geq y \geq b/2$. As the plate moves in positive z -direction, two circulation zones appear in $\hat{\mathbf{u}}_{\text{IP}}$ at $y \approx \pm(b/2 + 10 \mu\text{m})$. As the plate's width is increased, the amplitude of $\hat{\mathbf{u}}_{\text{IP}}$ in these circulation region increase, and at $b = 400 \mu\text{m}$ $\hat{\mathbf{u}}_{\text{IP}}$ is even higher than the plate's velocity around these circulation regions. $\hat{\mathbf{u}}_{\text{OP}}$ exhibits a circulation zone at $y \approx \pm(b/2 + 40 \mu\text{m})$ with opposite orientation to the circulation zone of $\hat{\mathbf{u}}_{\text{IP}}$. For instance, in the positive y -direction, while $\hat{\mathbf{u}}_{\text{IP}}$ moves in a clockwise direction, $\hat{\mathbf{u}}_{\text{OP}}$ moves in an anticlockwise direction. $\hat{\mathbf{u}}_{\text{OP}}$ also increases amplitude with an increase in the plate's width b .

The Q-factor of each mode is evaluated from the dissipated energy E_{D} in the fluid per oscillation cycle as described with Eq. 1.2. To evaluate E_{D} , we introduce the fluid's kinetic energy E_{f} , and note that the rate of change of the fluid kinetic energy in the fluid dE_{f}/dt is

$$dE_{\text{f}}/dt = \int_{S_{\text{p}}} \mathbf{u} \cdot (\mathbf{n}_{\text{p}}^{\text{T}} \cdot \boldsymbol{\sigma}) dS - 2\mu_{\text{f}} \int_{\Omega_{\text{f}}} \boldsymbol{\epsilon} \cdot \boldsymbol{\epsilon} d\Omega_{\text{f}}. \quad (6.4)$$

S_{p} is the union of the plate's top and bottom surfaces. The second term in Eq. 6.4 is the power with which the plate acts on the fluid, and the third term refers to the power

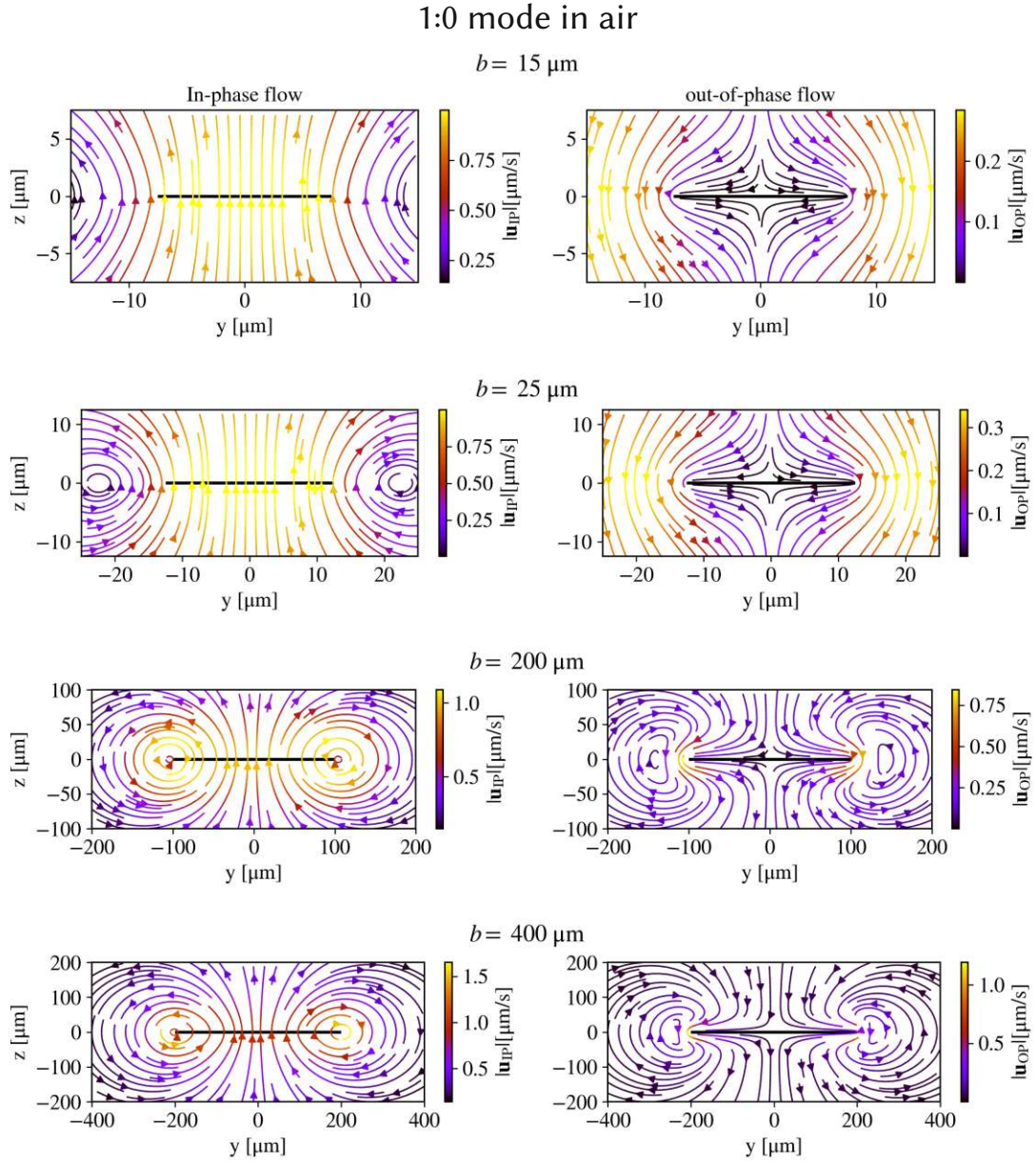


Figure 6.15: Fluid flow for the 1:0 mode around plates with different widths in air. The in-phase flow is shown on the left, and the out-of-phase on the right. The plate is represented by a black solid line.

dissipated by the fluid. Eq. 6.4 is rewritten using the pressure difference between top and bottom plate surfaces (and the normal vectors on both surfaces) in the time-domain as

$$\frac{dE_f}{dt} = \int_{\Omega_p} \frac{\partial w}{\partial t} \Delta p d\Omega_p - 2\mu_f \int_{\Omega_f} \boldsymbol{\epsilon} \cdot \boldsymbol{\epsilon} d\Omega_f. \quad (6.5)$$

Over one oscillation period T at a fixed frequency f ($T = 1/2\pi f$), all the energy that the plate transfers to the fluid is dissipated, and the net difference in kinetic energy in

the fluid is zero. Hence, the energy dissipated by the fluid in one cycle of oscillation E_D is

$$E_D = \int_0^T \int_{\Omega_p} \frac{\partial w}{\partial t} d\Omega_p dt = 2\mu_f \int_0^T \int_{\Omega_f} \boldsymbol{\epsilon} \cdot \boldsymbol{\epsilon} d\Omega_f dt. \quad (6.6)$$

E_D is evaluated using the Fourier-transforms of the time-dependent quantities as

$$E_D = \frac{\pi}{2\pi f} \int_{\Omega_p} \mathcal{R}(j\omega \hat{w} \Delta \hat{p}^*) d\Omega_p = \frac{2\pi\mu_f}{2\pi f} \int_{\Omega_f} \mathcal{R}(\hat{\boldsymbol{\epsilon}} \cdot \hat{\boldsymbol{\epsilon}}^*) d\Omega_f, \quad (6.7)$$

where the $*$ superscript means the complex conjugate and \mathcal{R} is the real operator.

From Eq. 6.7 a energy dissipation density Σ_D is introduced as

$$\Sigma_D = \frac{\mu_f}{f_d} \mathcal{R}(\boldsymbol{\epsilon} \cdot \boldsymbol{\epsilon}^*). \quad (6.8)$$

The integral of Σ_D over the entire fluid domain is the dissipated energy per cycle E_D , which is inversely proportional to Q . Note that $\boldsymbol{\epsilon}$, the strain rate tensor, is complex, which means both the in-phase and out-of-phase flow components dissipate energy. The non-zero components of $\boldsymbol{\epsilon}$ are calculated taking the partial derivatives of the stream function definition in Eq. 4.6 as

$$\epsilon_{yy}(x^c, y, z) = \frac{\partial u_y(x^c, y, z)}{\partial y} = -\frac{1}{\mu_f} \int_{-b/2}^{b/2} \Delta p(x^c, y') \frac{\partial^3 \Psi}{\partial y' \partial z \partial y} dy', \quad (6.9)$$

$$\epsilon_{zz}(x^c, y, z) = \frac{\partial u_z(x^c, y, z)}{\partial z} = \frac{1}{\mu_f} \int_{-b/2}^{b/2} \Delta p(x^c, y') \frac{\partial^3 \Psi}{\partial y' \partial y \partial z} dy', \quad (6.10)$$

$$\epsilon_{zy}(x^c, y, z) = \frac{1}{2} \left(\frac{\partial u_y(x^c, y, z)}{\partial z} + \frac{\partial u_z(x^c, y, z)}{\partial y} \right) \quad (6.11)$$

$$= \frac{1}{\mu_f} \int_{-b/2}^{b/2} \Delta p(x^c, y') \left[\frac{\partial^3 \Psi}{\partial y' \partial y \partial y} - \frac{\partial^3 \Psi}{\partial y' \partial z \partial z} \right] dy', \quad (6.12)$$

and $\epsilon_{yz} = \epsilon_{zy}$. The other terms of $\boldsymbol{\epsilon}$ are zero as a result of the 2D fluid flow approximation. The fluid kinetic energy density $\Sigma_{k,\text{fluid}}$ in the fluid flow is defined as

$$\Sigma_{k,\text{fluid}} = \frac{1}{2} \rho_f \hat{\mathbf{u}} \cdot \hat{\mathbf{u}}. \quad (6.13)$$

In addition, we define also the kinetic energy density in the micro-plate, which is simply

$$\Sigma_{k,\text{plate}} = \frac{1}{2} \rho \omega^2 \hat{w}^2. \quad (6.14)$$

The kinetic and dissipated energy densities (Σ_k and Σ_D) for the 2:0 mode in air around plates with different widths are shown in Fig. 6.16. The majority of the energy dissipation occurs at the plate's side edges $y = \pm b/2$, where Σ_D reaches its maximum. In the central region of the plate ($y = 0$), Σ_D is small and the energy dissipation for the EB

modes is negligible. Due to the small density of air, E_k in the plate domain is much larger than the fluid's $E_{k,\text{fluid}}$.

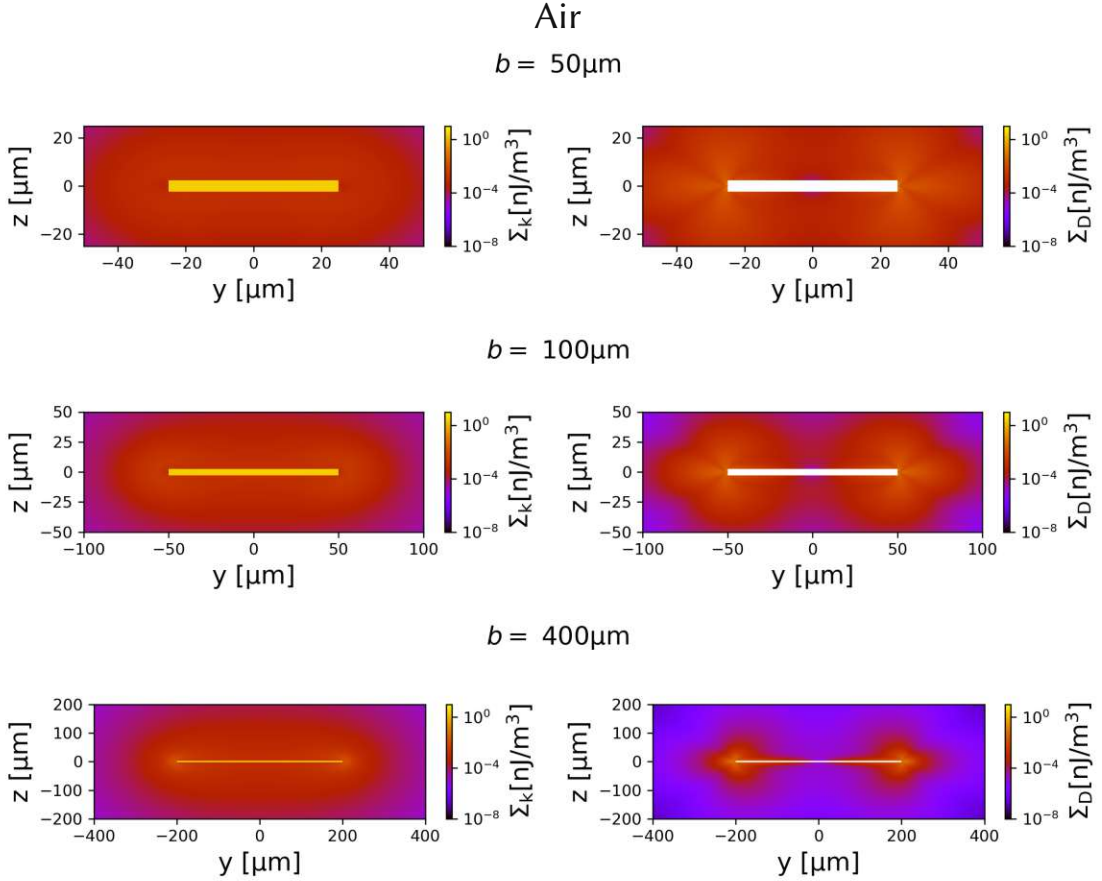


Figure 6.16: Kinetic and dissipated energy densities for the 2:0 mode around plates with different widths in air.

It is possible to further investigate the variation of the Q-factor for the EB mode in the beam-plate transition by integrating the dissipation energy density Σ_D and the kinetic energy densities $\Sigma_{k,\text{fluid}}$ and $\Sigma_{k,\text{plate}}$ in a cross-section for the plates with different widths which results in the energy dissipation per length χ_D , $\chi_{k,\text{fluid}}$ and $\chi_{k,\text{plate}}$, respectively.

Fig. 6.16 shows χ_D , $\chi_{k,\text{fluid}}$ and $\chi_{k,\text{plate}}$ for the 2:0 mode. χ_D increases with b , therefore a wider plate dissipates more energy at each cross-section. The plate's kinetic energy $\chi_{k,\text{plate}}$ increases linearly with b and is much greater than the air's kinetic energy $\chi_{k,\text{fluid}}$. The ratio $\chi_D/\chi_{k,\text{plate}}$ in Fig. 6.17 increases as b is increased, until $b = 100\mu\text{m}$. For wider structures, the ratio $\chi_D/\chi_{k,\text{plate}}$ decreases, yielding the Q-factor reduction seen in Fig. 6.7 in air.

In water, the added mass effect is larger and this is noticeable in $\Sigma_{k,\text{plate}}$ shown in Fig. 6.18 for the mode 2:0 in water. In water, $\Sigma_{k,\text{plate}}$ and $\Sigma_{k,\text{fluid}}$ are the same order of magnitude in a wide region near the plate. The ratio between fluid and plate density is only 2.3, therefore the kinetic energy in the fluid is here significant.

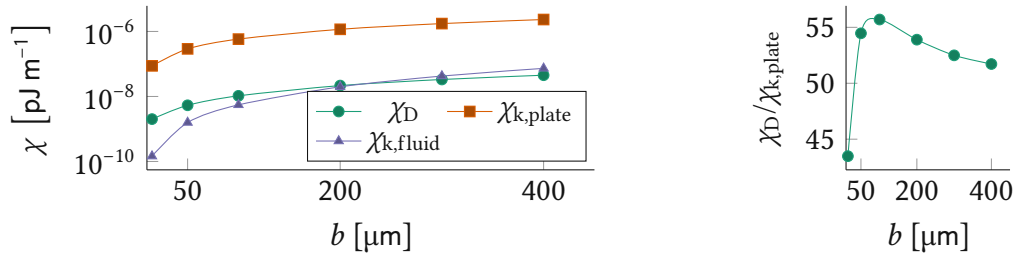


Figure 6.17: On the left, the dissipated energy per unit length χ_D , fluid kinetic energy per unit length $\chi_{k,\text{fluid}}$ and plate kinetic energy per unit length $\chi_{k,\text{plate}}$ the 2:0 mode in air. On the right, is the ratio between dissipated energy by the fluid and stored kinetic energy in the plate's cross-section.

Fig. 6.19 shows χ_D , $\chi_{k,\text{fluid}}$ and $\chi_{k,\text{plate}}$ for the 2:0 mode in water. In water, $\chi_{k,\text{fluid}}$ is much larger than $\chi_{k,\text{plate}}$, meaning there is more kinetic energy stored in the fluid than in the plate. Furthermore, $\chi_{k,\text{fluid}}$ is smaller than χ_D for slender beams, but becomes larger than χ_D as the plate becomes larger. Essentially, with an increase in b , the fluid stores more energy, resulting in an increased $\chi_D/(\chi_{k,\text{plate}} + \chi_{k,\text{fluid}})$ ratio, and as a result, leading to an increase in Q-factor.

6.5 Oscillatory Reynolds number

The oscillatory Reynolds number β is a non-dimensional parameter that appears in several fluid dynamics phenomena[97, 98] and is commonly used for comparison between different structures in fluids[31, 54]. For the fluid-plate interaction problem, β is[70, 44]

$$\beta = \frac{b^2 2\pi f_d}{\nu_f}, \quad (6.15)$$

where the plate's width b is considered the problem's characteristic length. Note that in the present formulation, the square root of β appears in the second term of the fundamental solution ψ in Eq. 4.5.

Figs. 6.20a and 6.20b show the Q-factor and the damping coefficient γ , respectively, of the EB modes of the plates with $r = 64/4$ to $r = 32/64$ as a function of β in water. Interestingly, both the Q-factor and the damping coefficient γ fall into a well-behaved exponential curve increasing with β . Q grows exponentially with an exponent equals 0.47, and γ with an exponent equals 0.53. The fluid-added-mass-per-plate-mass-ratio \mathcal{M} , on the other hand, does not fall into a single exponential curve. However, retrieving the modal mass m from the fluid-added-mass-per-plate-mass-ratio \mathcal{M} and multiplying it with ω_d returns once more an exponential curve (Fig. 6.20c). In fact, note that Q , γ and $m \omega_d$ are related according to Eq. 5.9, and the same is true for the exponential fits presented in Fig. 6.20.

Results in Fig. 6.20 show that even though the hydrodynamic force (pressure jump Δp) is a non-linear force, the resulting Q-factor of beam-like modes follows a well-

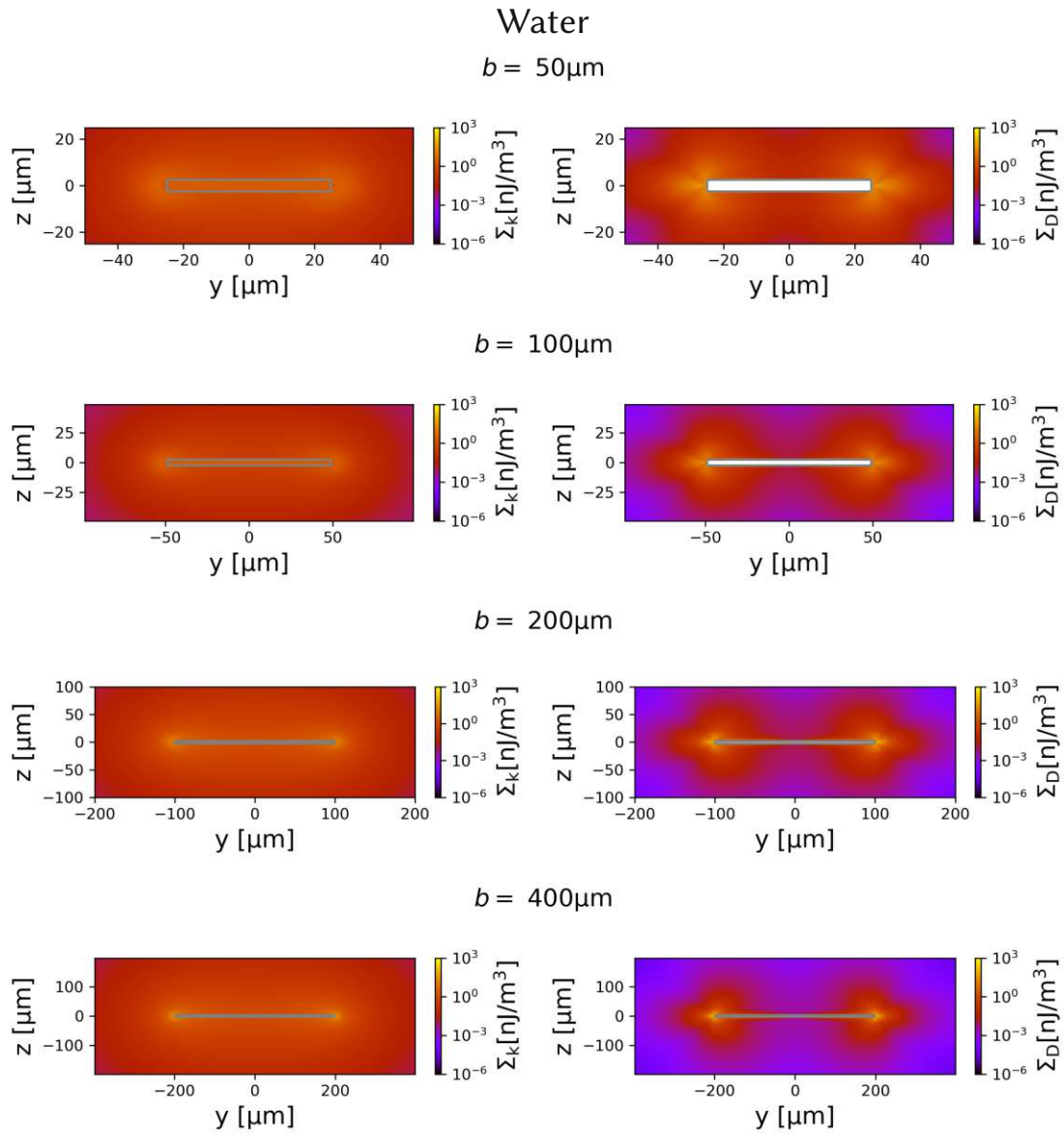


Figure 6.18: Energy density for the 2:0 mode around plates with different widths. The in-phase flow is shown on the left, and the out-of-phase on the right. The plate is represented by a black solid line.

behaved path in the Q vs β graph in water. In air, on the other hand, a similar exponential fit to the Q -factor of the EB modes is not possible as seen in Fig. 6.21.

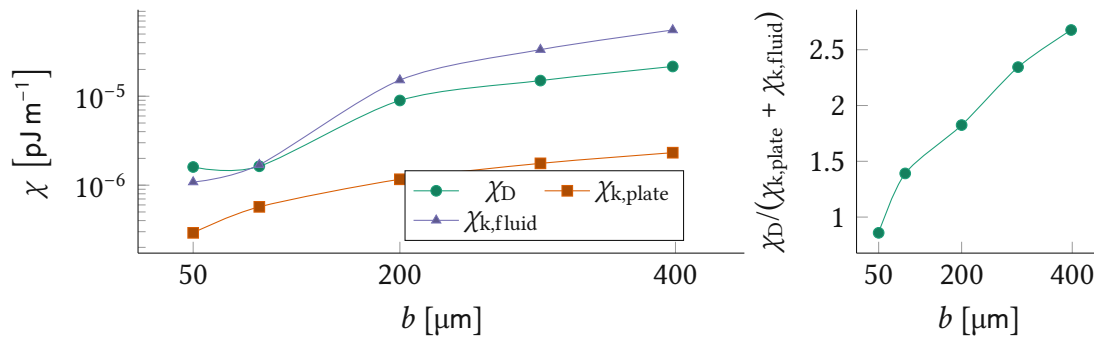


Figure 6.19: On the left, the dissipated energy per unit length χ_D , fluid kinetic energy per unit length $\chi_{k,fluid}$ and plate kinetic energy per unit length $\chi_{k,plate}$ the 2:0 mode in water. On the right, is the ratio between dissipated energy by the fluid and stored kinetic energy in the plate.

6.6 Conclusions

In this chapter, the beam-plate transition in air and in water was investigated. In air, the Q-factor of EB modes increases initially as the plate's width increases and then decreases for wider plates. In the air, torsional modes exhibited a decrease in Q as b increased. In water, Q for both the EB and torsional modes increases for wider plates. An investigation using a lumped element model reveals the importance of the added-mass effect, which effectively increases the Q-factor of modes in water by increasing the kinetic energy stored in the fluid. In air, due to its small density, the added-mass effect is negligible and the Q-factor decreases for wider plates. In the fluid flow in a cross-section, it is easy to see the difference in the kinetic energy stored in the fluid in air and in water.

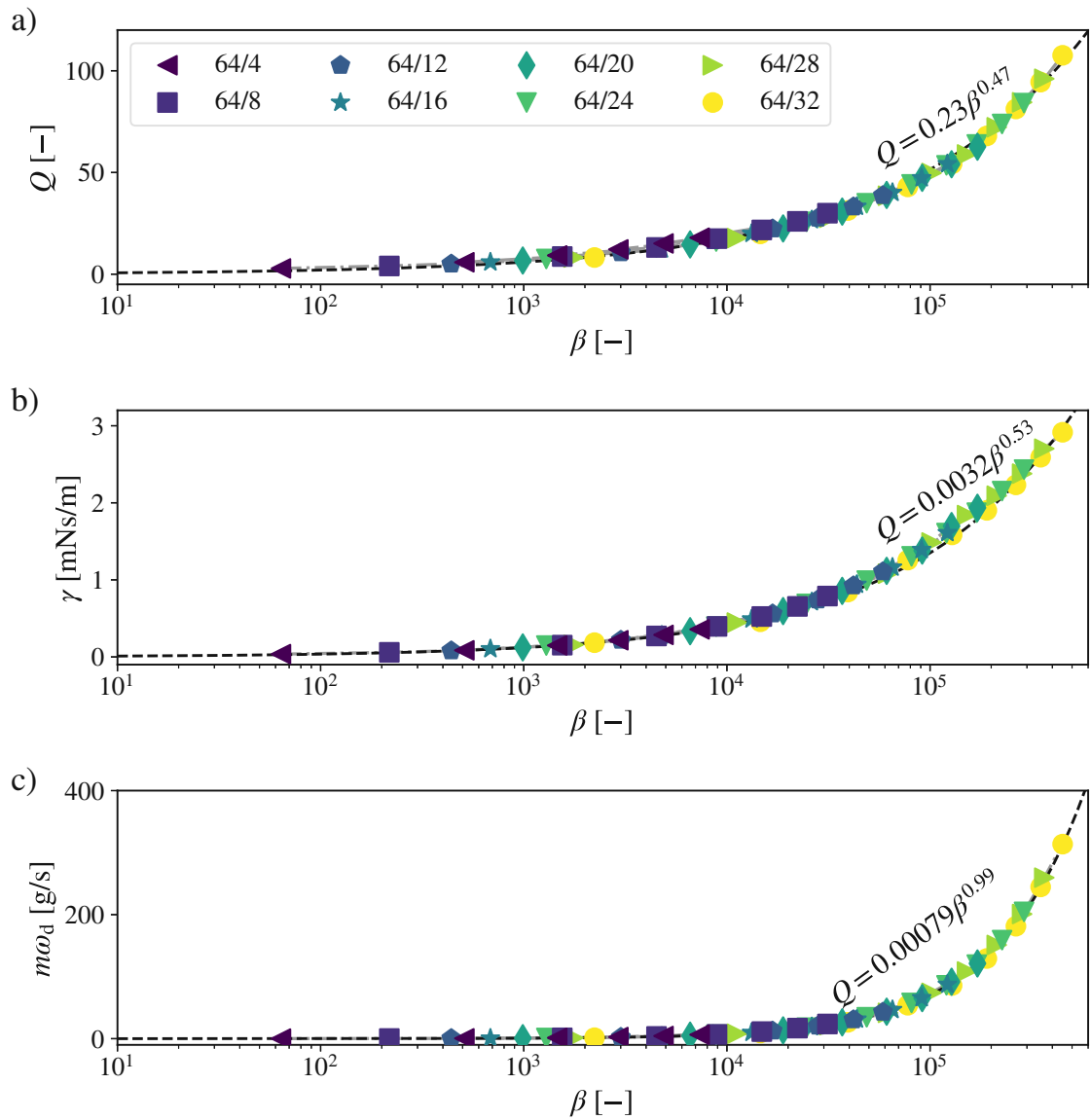


Figure 6.20: a) Q , b) γ and d) $m\omega_d$ of the EB modes as a function of the oscillatory Reynolds number β . The dashed lines are exponential approximations. The labels in a) refer to the plate's aspect ratio.

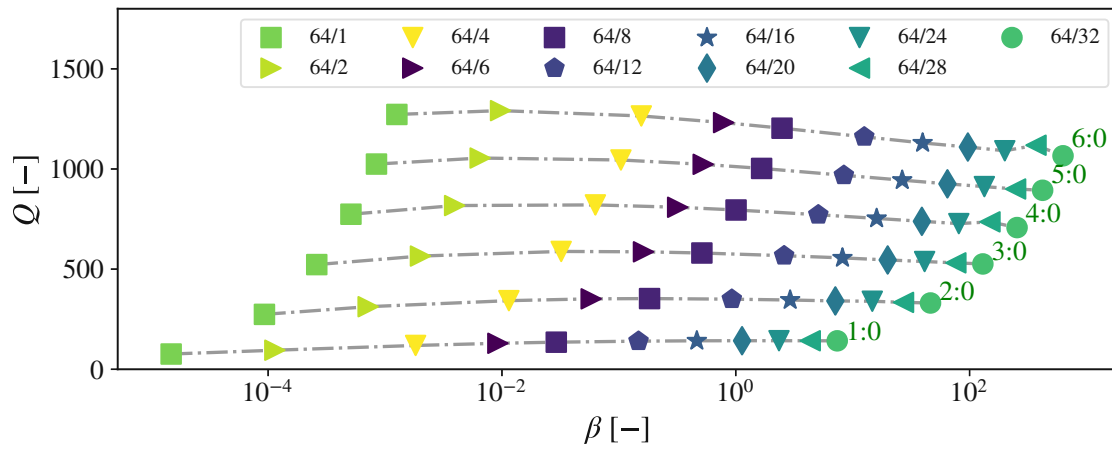


Figure 6.21: Q-factor of the EB modes as a function of the oscillatory Reynolds number β in air. The labels in a) refer to the plate's aspect ratio.

7 Gas-Liquid modal Q-factor inversion

Results of this chapter were partially published in [72].

In the previous chapter, only the EB and the torsional modes were the objects of study in the beam-plate transition range. Here, we determine the Q-factor of all the plate's vibrational modes (EB, torsional, roof tile-shaped modes and higher-order plate modes) in different fluids. Gases and liquids are found in opposite regions in a density-viscosity diagram as shown in Fig. 7.1. Liquids have high density and viscosity, whereas gases exhibit low density and viscosity. A micro-plate immersed in gases and liquids is subject to an effect we define as the gas-liquid modal Q-factor inversion (GL-Q-inversion).

7.1 Galerkin mode decomposition (GMD)

For the single plate case (in which the geometry is not altered, but only the fluid or frequency), the Galerkin mode decomposition (GMD) is a more suited method to solve the governing equations. GMD is advantageous in comparison to FEM for a single structure because the resulting matrices are smaller. In essence, with GMD the size of the matrices is defined by the number of modes to be used as function space, which is usually smaller than the number of basis functions used in FEM.

The Galerkin mode decomposition consists in using the modal basis function space in the dimension reduction from the Hilbert function space \mathcal{W} to finite function spaces $\mathcal{W}^{\text{md}} \subset \mathcal{W}$ and $\mathcal{V}^{\text{md}} \subset \mathcal{W}$, and defining the problem as: Find $w^{\text{md}} \in \mathcal{W}^{\text{md}}$ such that

$$a(w^{\text{md}}, \hat{v}^{\text{md}}) = l(\hat{v}^{\text{md}}), \forall w^{\text{md}} \in \mathcal{W}^{\text{md}}. \quad (7.1)$$

The trial and test function spaces, \mathcal{V}^{md} and \mathcal{W}^{md} respectively, for the GMD is the function space of a finite number N^{md} of free vibrational modes Φ of the plate in vacuum. The trial function space \mathcal{V}^{md} is defined as

$$\mathcal{V}^{\text{md}} = \{ \hat{v}^{\text{md}} \in H^2(\Omega_p) : \hat{v}^{\text{md}} \in \Phi, \hat{v}^{\text{md}}|_{\Gamma_c} = 0 \}, \quad (7.2)$$

and the test function space \mathcal{W}^{md} is

$$\mathcal{W}^{\text{md}} = \{ \hat{w}^{\text{md}} \in H^2(\Omega_p) : \hat{w}^{\text{md}} \in \Phi, \hat{w}^{\text{md}}|_{\Gamma_c} = 0 \}, \quad (7.3)$$

A possible choice for Φ is the set of complex eigenmodes that are the solution to the generalized eigenvalue problem of the governing PDE, that is the non-linear eigenvalue problem which stems from Eq. (5.1) without a driving force P_d . However, both the analytic and numeric solutions to such a non-linear eigenvalue problem with a non-local hydrodynamic force P^h are complicated to determine. An alternative to the complex eigenmodes is the set of free vibrational modes Φ of the plate in vacuum (in absence of fluid) which can be obtained from the generalized eigenvalue problem for the Kirchhoff

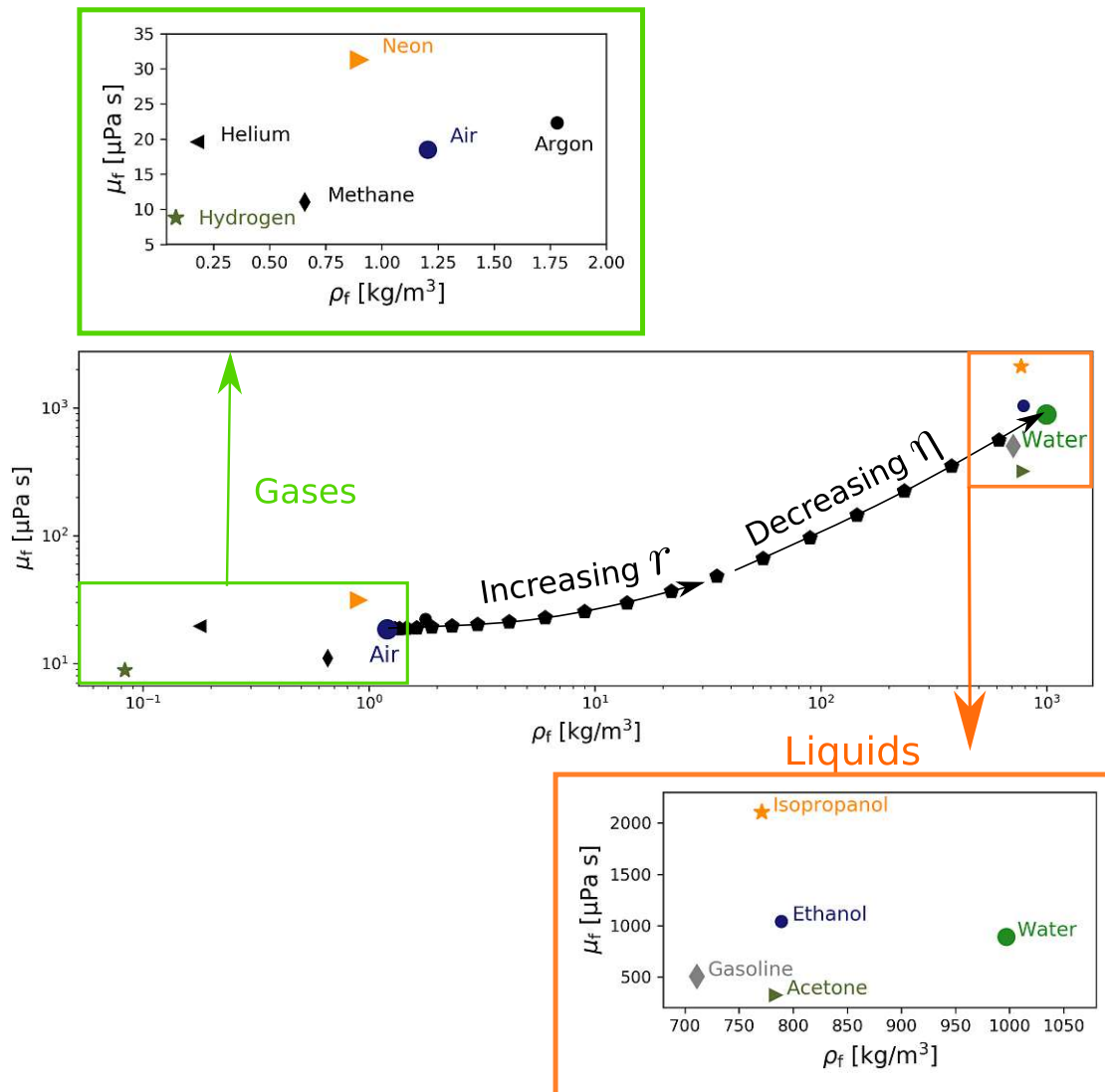


Figure 7.1: Density and viscosity of different gases and liquids. Among the gases: hydrogen, air and neon are highlighted in a linear plot on the top left. Among the liquids: water, acetone, gasoline and isopropanol are highlighted in a linear plot on the bottom right. The solid black line connects air and water in a continuously changing fluid. r and η are quantities introduced in this chapter to quantify the fluid's properties.

plate equation. The set of free vibrational modes has been successfully used previously to solve for the dynamics of fluid-structure interaction problems [31, 99, 100, 60].

Φ is the eigenvector set from the generalized eigenvalue problem defined in Eq. (3.30), determined once more with the IP method as described in Section 3.4.3. The eigenvectors stemming from Eq. (3.30) are L^2 normalized as

$$\rho h \int_{\Omega_p} \Phi_i \Phi_i d\Omega = 1. \quad (7.4)$$

The governing PDE of the micro-plate fluid interaction Eq. (5.1) solved with GMD is then: Find $w^{\text{md}} \in \mathcal{W}^{\text{md}}$ such that

$$\begin{aligned} & \int_{\Omega_p} \frac{h^3}{12} C_{\alpha\beta\gamma\delta} \hat{w}_{\text{md},\alpha\beta} v_{\text{md},\gamma\delta} d\Omega d\Omega - \int_{\Omega_p} \omega^2 \rho h \hat{w}^{\text{md}} \hat{v}^{\text{md}} d\Omega \\ & - \mu_{\text{fj}} \omega \frac{\pi}{\mathcal{M}_y} \sum_{k=0}^{\mathcal{M}_x} q_k \sum_{j=1}^{\mathcal{M}_y} \sum_{i=1}^{\mathcal{M}_y} A_{ij}^{-1} \hat{w}^{\text{md}}(x_k, y_i) \hat{v}^{\text{md}}(x_k, y_j) \sqrt{(b/2)^2 - y_j^2} \\ & = \int_{\Omega_p} \hat{F} \hat{v}^{\text{md}} d\Omega, \forall \hat{v}^{\text{md}} \in \mathcal{V}^{\text{md}}. \end{aligned} \quad (7.5)$$

The last integral in 7.5 is once more evaluated in the y -direction with a Chebyshev-Gauss quadrature with \mathcal{M}_y elements, and in x -direction the 1/3 Simpsons' rule with \mathcal{M}_x elements suffices. The quadrature points in x and y directions are represented in Fig. 5.1.

7.2 Convergence and validation

For the analysis we use a micro-plate with $l = 500 \mu\text{m}$, $b = 250 \mu\text{m}$ and $h = 5 \mu\text{m}$ composed of silicon with orthotropic properties. A plate with aspect ratio $r_a = 2$ is ideal for the analysis of micro-plates in gases and liquids because it exhibits different types of vibrational modes in a relatively low frequency range. For instance, among the lowest twenty vibrational modes of the micro-plate in vacuum (shown in Fig. 7.2 with their resonance frequencies) there are six EB modes, six torsional modes, two RTS and six HOP modes. In this chapter, when referring to RTS and HOP modes, the term HOP modes will be employed as a reference for both types of modes together. HOP modes are essentially the non-beam modes (neither torsional nor EB modes).

There are two parameters on which the convergence of the proposed method must be shown: with the number of vibrational modes N^{md} that form the basis for the GMD and with the fluid grid discretization \mathcal{M}_x by \mathcal{M}_y . To quantify the convergence of the method with N^{md} we define

$$\epsilon^{\text{md}} = \|\hat{w}^{i+1} - \hat{w}^i\|_{L^2}, \quad (7.6)$$

where \hat{w}^{i+1} and \hat{w}^i are solutions obtained $N^{\text{md}} = 5(i + 1)$ and $N^{\text{md}} = 5$. The convergence with the fluid grid is shown using $\epsilon_{\text{convergence}}$ as defined in Eq. 3.29.

The convergence of the method is analysed in air and water as representing fluids for gases and liquids. In both fluids, ϵ_{modes} reduces as N^{md} increases, reaching a value of $0.9 \cdot 10^{-3}$ in water, and of $0.8 \cdot 10^{-4}$ in air as shown in Fig. 7.3.

Fig. 7.4 shows $\epsilon_{\text{convergence}}$ as a function of the fluid grid discretization $\mathcal{N}_x \times \mathcal{N}_y$. Both in air and water at 500 kHz the method converges with similar $\epsilon_{\text{convergence}}$ reaching a value of 10^{-6} for a fluid grid with 384×384 points.

For validating the GMD method, we resort to a comparison to the FEM method described in Chapter 5. Fig. 7.5 shows the absolute spectrum displacement \hat{w}_t of the plate's free-corner ($x = l$, $y = b/2$) in air and in water obtained with GMD and FEM. The

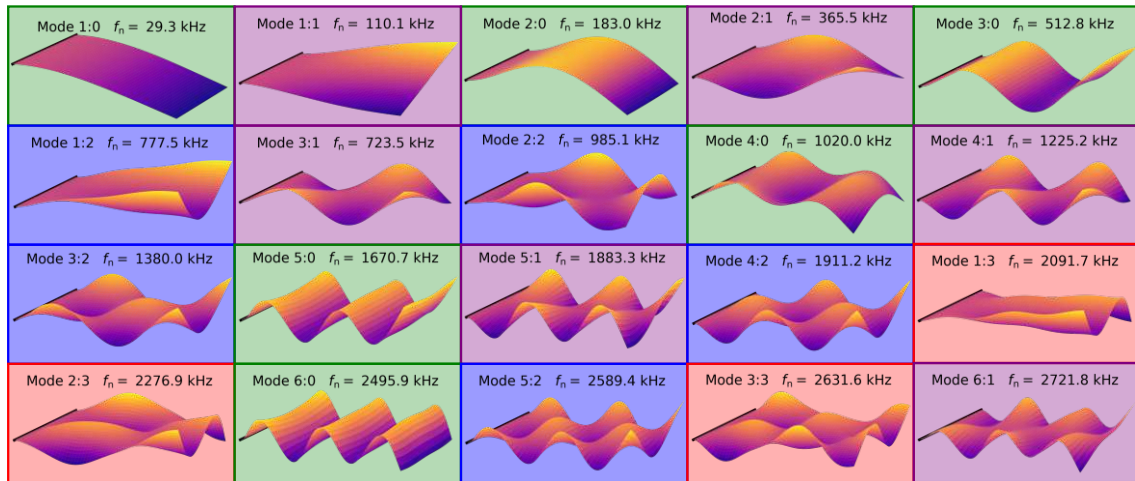


Figure 7.2: Twenty lowest-order vibrational modes of a cantilevered silicon micro-plate clamped at its left edge and free on all others. EB modes are shown with green background, torsional with purple, HOP modes with $n_y = 2$ in blue and HOP with $n_y = 3$ in red background.

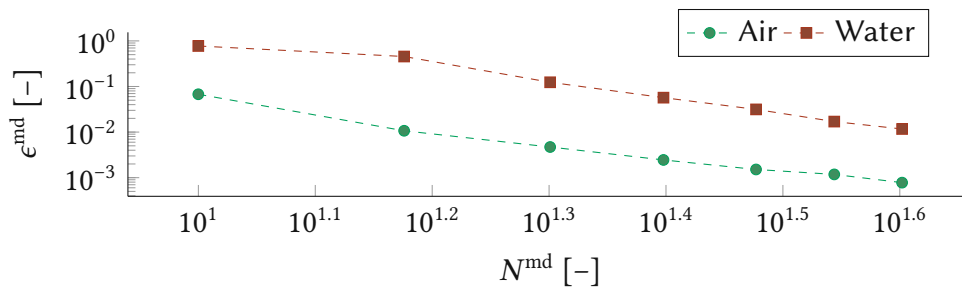


Figure 7.3: Convergence of the GMD method in air and in water with the number of modes.

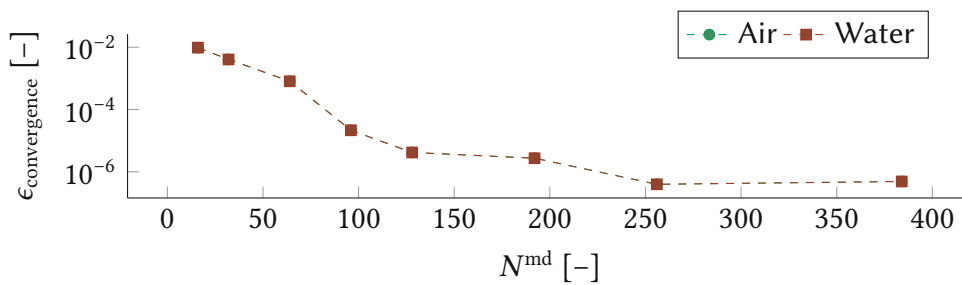


Figure 7.4: Convergence of the present method for a micro-plate in air and in water with the fluid grid $\mathcal{N}_x \times \mathcal{N}_y$.

two methods exhibit excellent agreement in the entire frequency range up to 1 MHz in both fluids.

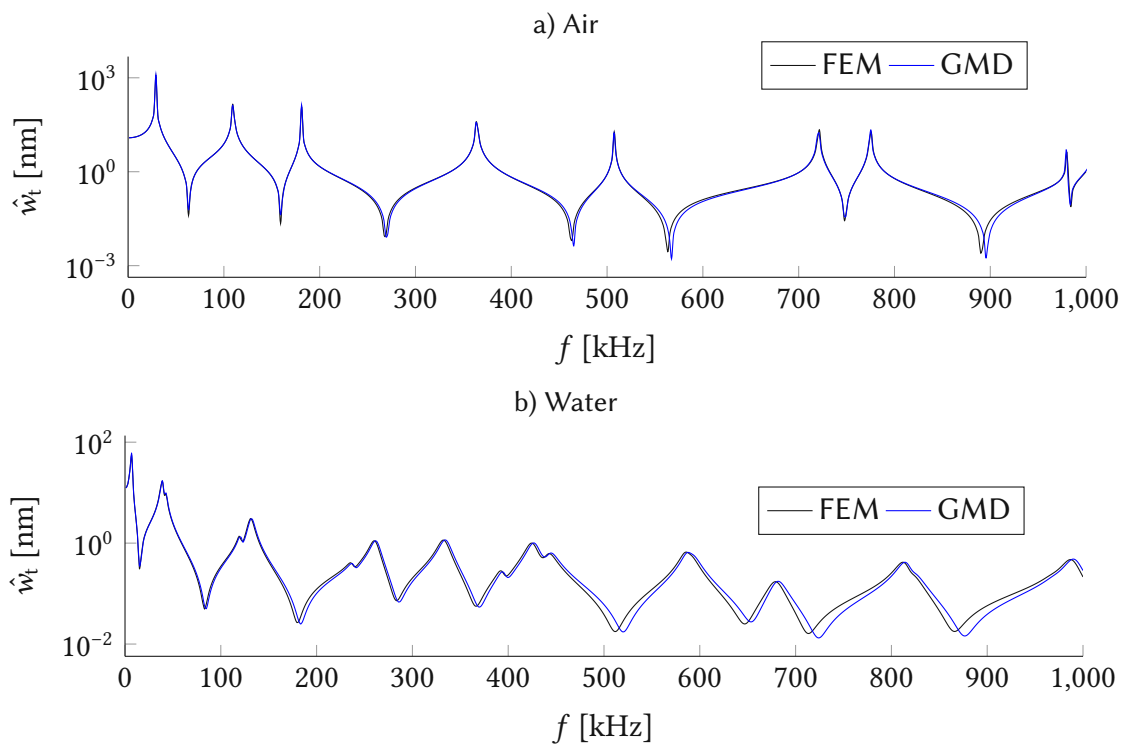


Figure 7.5: Spectral displacement of the plate with GMD and FEM in a) air and b) water.

7.3 Q-factor in gases

For the investigation of the HOP and RTS vibrational modes of micro-plates in gases, as gases of interest we select hydrogen, air and neon because these provide a wide range of viscosities and densities as shown in Fig. 7.1. Table A.1 shows the viscosity and density of the selected gases at SATP conditions.

The absolute spectral displacement of the free-corner of the plate $|\hat{w}_t|$ is shown in Fig. 7.6 in the different gases in a frequency range between 1 kHz and 3 MHz. In the 3 MHz frequency range, there are nineteen maxima in the displacement spectrum which refer to fourteen damped resonance frequencies f_d and vibrational modes. The vibrational modes are indicated with the $n_x : n_y$ notation and are similar to the vibrational modes in vacuum shown in Fig. 7.2. Since all gases have low density, the damped resonance frequency f_d of each mode investigated is similar to the vacuum resonance frequency f_n (gray dashed lines in Fig. 7.6).

The Q-factors of the micro-plate in hydrogen, air and neon are shown in Fig. 7.7. In air and neon, the micro-plate exhibits similar Q-factors, while in hydrogen the micro-plate exhibits much higher Q-factors due to hydrogen's smaller absolute viscosity μ_f . In the three gases, for modes with a same number of nodal lines along the plate's length n_y , Q and f_d increase with n_x . For instance, the Q-factor and f_d of mode 3:0 are higher than Q and f_d of mode 2:0 and so forth. The increase of Q and f_d with n_x has been seen previously for EB and torsional modes of slender beams [31, 35]. Here, also Q and f_d of HOP modes increase with n_x in gases.

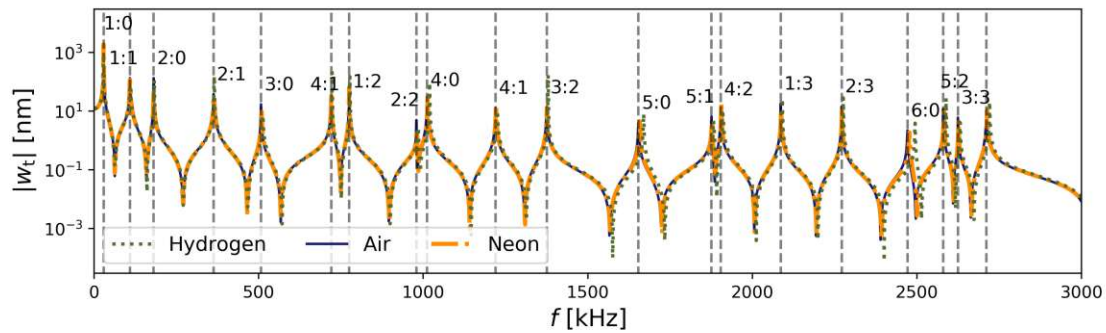


Figure 7.6: Displacement spectrum of a micro-plate in air, neon and hydrogen. Gray dashed lines represent the resonance frequencies in vacuum. The labels on each dashed line represent the vibrational mode of each resonance frequency according to Leissa's notation.

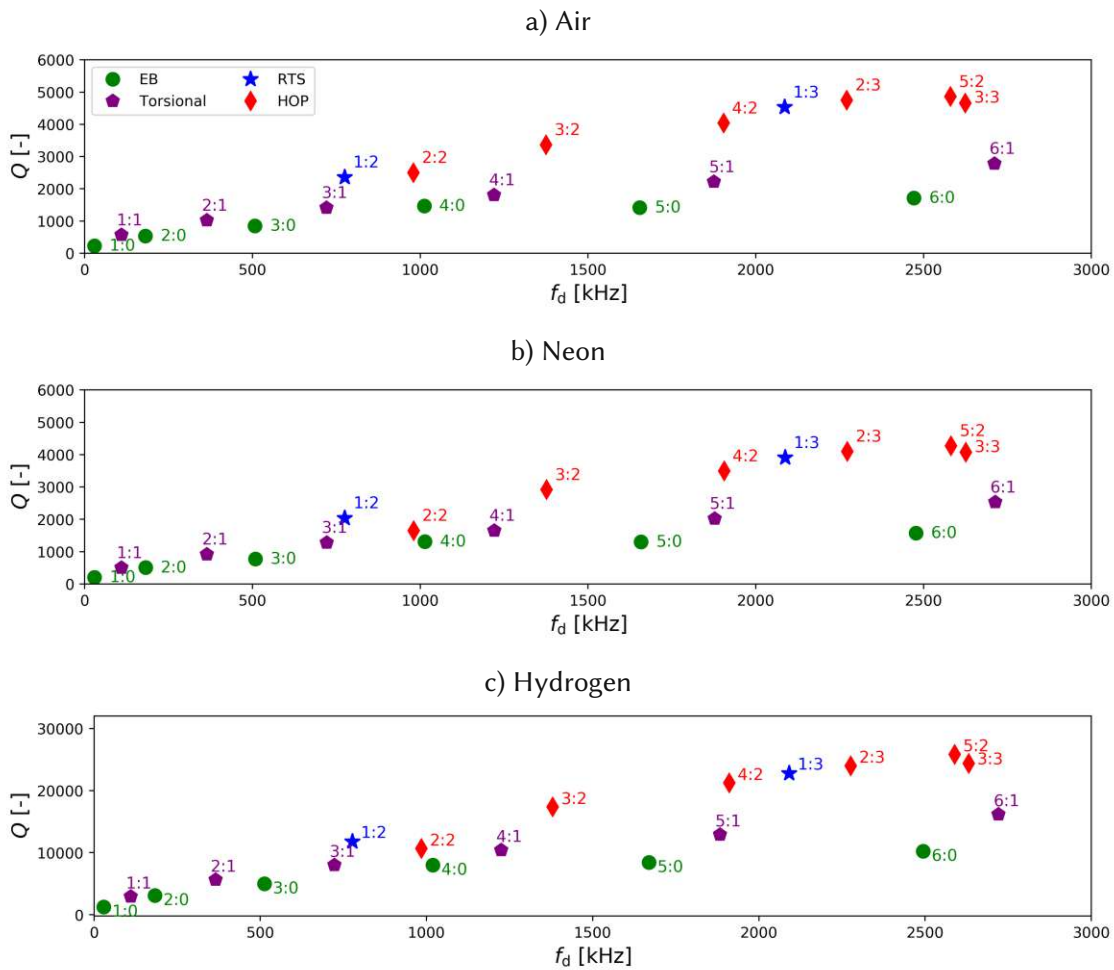


Figure 7.7: Q-factor of the micro-plate in a) air, b) neon and c) hydrogen vibrating in EB, torsional, RTS and HOP modes. The colors used in the marks here are the same as in the respective vibrational mode in Fig. 7.2.

More interestingly, EB modes exhibit the lowest Q-factors when comparing modes with similar damped resonance frequencies f_d . For example, in air, the Q-factor of mode 6:0 ($Q^{6:0}$) is 1715, lower than mode's 6:1 Q-factor ($Q^{6:1}$) which is 2720, which is, in turn, lower than the 5:2's Q-factor of 4860. Torsional modes exhibit higher Q-factors than EB-modes ($Q^{\text{torsional}} > Q^{\text{EB}}$), but lower than RTS and HOP modes. HOP modes and RTS modes exhibit similar Q-factors ($Q^{\text{HOP}} \approx Q^{\text{RTS}}$). In summary, in gases, the Q-factors of the plate vibrational modes follow the pattern $Q^{\text{HOP,RTS}} > Q^{\text{torsional}} > Q^{\text{EB}}$ comparing modes with similar damped resonance frequencies f_d .

7.4 Q-factor in liquids

For the analysis in liquids, we investigate the same micro-plate in isopropanol, ethanol and acetone. This choice of fluids provides a broad range of viscosity as shown in Fig. 7.1 while maintaining comparable densities. Table A.1 shows the liquids' properties at SATP conditions.

Fig. 7.8 shows the plate's displacement \hat{w}_t in the 1.5 MHz frequency range in different liquids. The 1.5 MHz limit is selected because there occur a significant number of vibrational modes and acoustic losses are negligible [30] in this frequency range. The damped resonance frequency f_d of each mode changes for each liquid depending on the liquid's density (in a much more significant way than in gases). Mode 4:2 has a damped resonance frequency of 905 kHz in either liquid, which is much lower than 1911 kHz resonance frequency in vacuum. In the 1.5 MHz frequency range, there are twenty-three maxima in the displacement, 8 EB modes, 7 torsional modes, 6 HOP modes and 2 RTS modes.

In comparison to the spectrum in gases, the maximums in displacement in liquids are less sharp due to the higher viscosity of liquids, which results in smaller Q-factors as shown in Fig. 7.9. In isopropanol, the vibrational modes exhibit the lowest Q-factors, due to isopropanol's largest absolute viscosity μ_f , while in acetone the highest Q-factors are achieved due to acetone's smaller viscosity. All liquids here analyzed have similar densities, and for this reason, damped resonance frequencies are similar.

What is more interesting, in liquids the Q-factor of EB modes is higher than those of non-EB modes at similar f_d . For example, in acetone the Q-factor of mode 7:0 ($Q^{7:0}$) is 112, being higher than mode's 4:2 Q-factor ($Q^{4:2}$) which is 71. In liquids, torsional modes exhibit lower Q-factors than EB-modes ($Q^{\text{torsional}} < Q^{\text{EB}}$), but are higher than those of RTS and HOP modes. Hence, in liquids, the Q-factors of the plate vibrational modes follow the pattern $Q^{\text{HOP,RTS}} < Q^{\text{torsional}} < Q^{\text{EB}}$ comparing modes with similar damped resonance frequencies f_d . This trend is exactly the opposite of the Q-factor pattern seen in gases.

This inversion is more clearly seen in Fig. 7.10, where the Q-factor of the vibrational modes in air and water categorized in EB modes (left), torsional modes (center) and high-order plate modes (right) are shown. Notice that in air, Q increases from left to right (i.e. from EB modes to high-order plate modes), so $Q_{\text{air}}^{\text{HOP,RTS}} > Q_{\text{air}}^{\text{torsional}} > Q_{\text{air}}^{\text{EB}}$. In water, the opposite happens, and Q decreases from EB modes to high-order plate modes ($Q_{\text{water}}^{\text{HOP,RTS}} < Q_{\text{water}}^{\text{torsional}} < Q_{\text{water}}^{\text{EB}}$). To name this phenomenon of the change in Q-factor trend

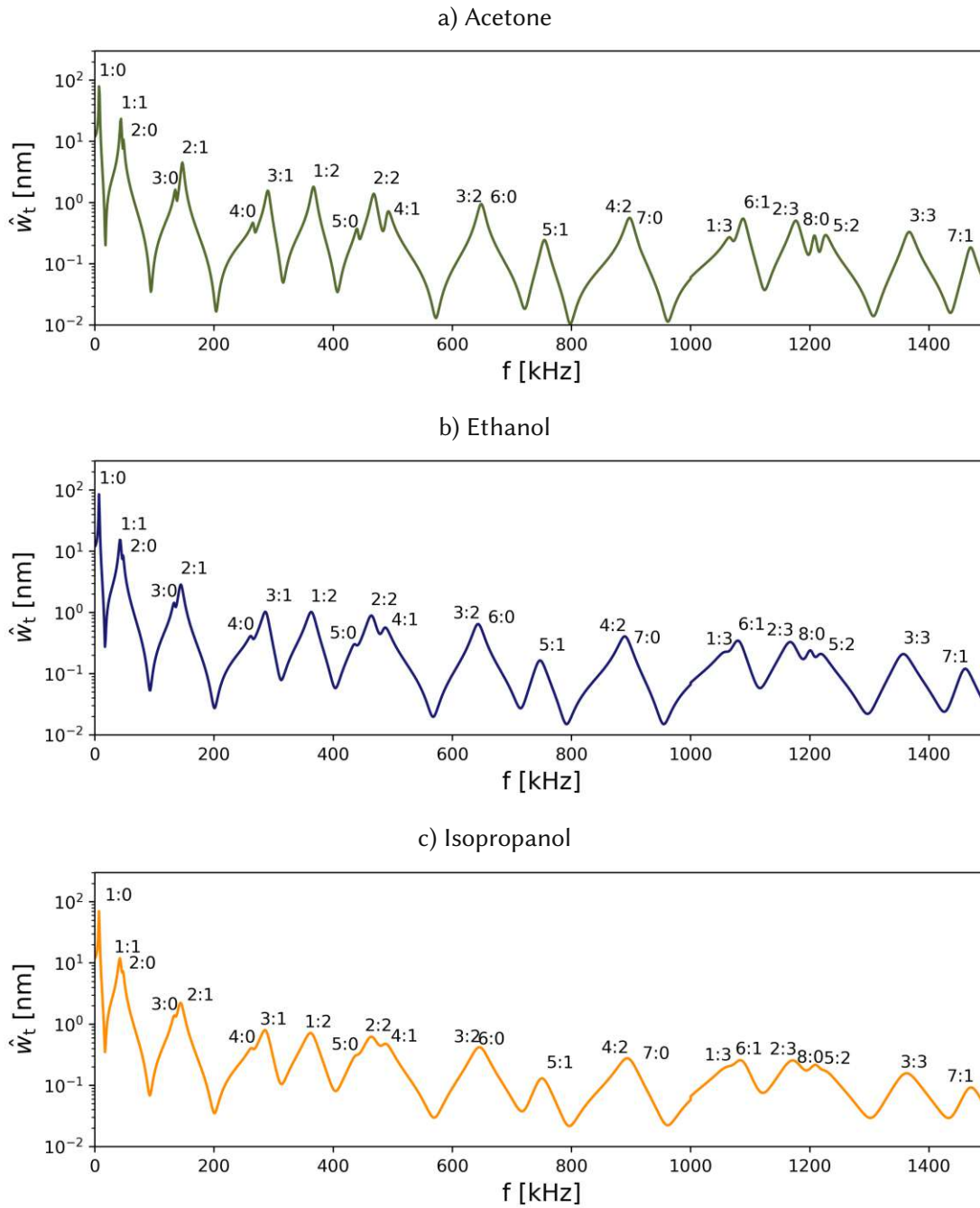


Figure 7.8: Displacement spectrum of the micro-plate in a) acetone, b) ethanol and c) isopropanol.

from gases to liquids we introduce the term “Gas-Liquid modal Q-factor-inversion”, or GL-Q-inversion. The GL-Q-inversion is illustrated in Fig. 7.10b.

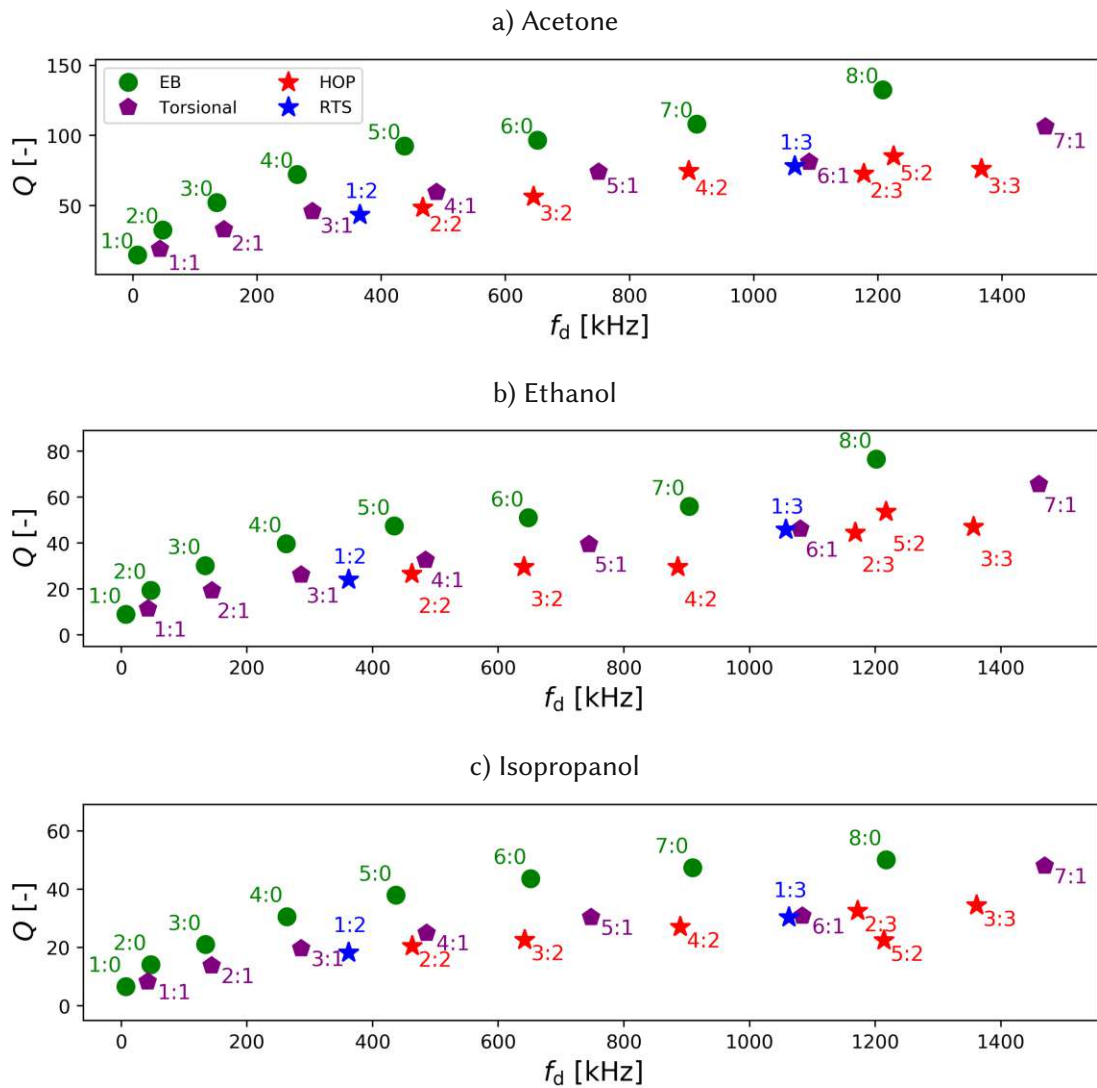


Figure 7.9: Q-factor of the micro-plate in a) acetone, b) ethanol and c) isopropanol.

7.5 Physical mechanism underlying the Gas-Liquid modal Q-factor-inversion

To investigate the GL-Q-inversion, we resort once more to the LEM model defined in Section 5.2.2 in which the Q-factor Q of a vibrational mode and its modal damping coefficient γ are inversely proportional according to

$$Q = \frac{m_p(1 + \mathcal{M})\omega_d}{\gamma}, \quad (7.7)$$

where m_p is the plate mass and \mathcal{M} is the fluid-added-mass-per-plate-mass-ratio, or added-mass coefficient.

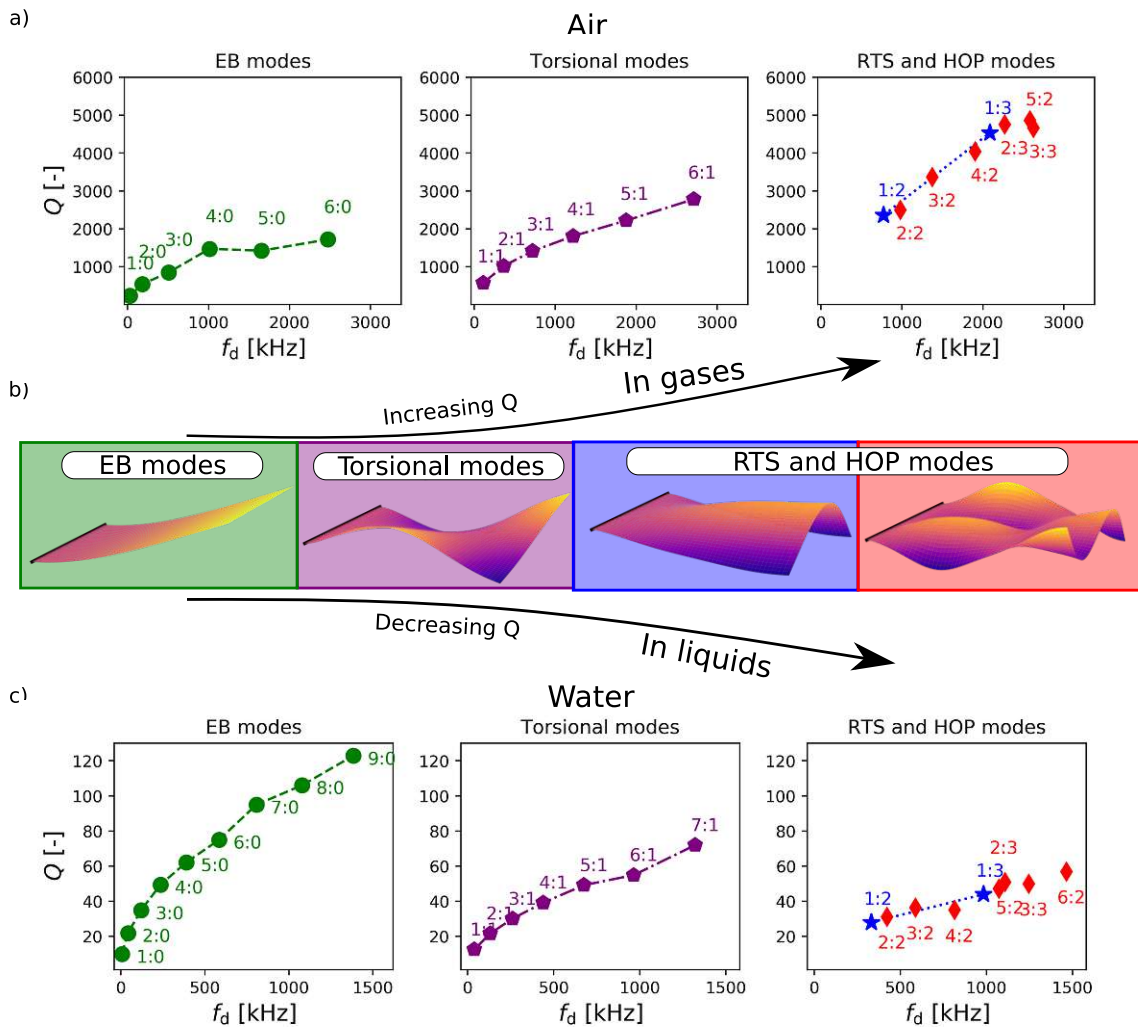


Figure 7.10: Q-factor of the micro-plate in a) air and c) water. EB modes ($n_y = 0$) are on the left, torsional modes ($n_y = 1$) on the center and high-order plate modes ($n_y \geq 2$) on the right. b) Illustration of the Gas-liquid modal Q-factor inversion effect.

In gases, the pattern $Q^{\text{HOP,RTS}} > Q^{\text{torsional}} > Q^{\text{EB}}$ can be directly related to a higher damping coefficient of the EB modes in comparison to the non-EB modes as shown in Fig. 7.11 in air. In the air, the added-mass coefficient is negligible. For modes with approximately similar f_d , the damping coefficient γ follows $\gamma^{\text{HOP,RTS}} < \gamma^{\text{torsional}} < \gamma^{\text{EB}}$.

The higher damping coefficient γ of the EB modes is also seen in the energy dissipation density map in Fig. 7.13. The kinetic and dissipated energy densities (Σ_k and Σ_D) for the different modes with approximately the same damped resonance frequency $f_d \approx 2.5$ MHz shown in Fig. 7.13. Those modes are 6:0, 6:1, 5:2 and 3:3, whose displacement field is shown in Fig. 7.12. The majority of the energy dissipation occurs at the plate's side edges $y = \pm b/2$ for all modes, however, the 6:0 mode shows an enlarged region of high energy dissipation. Here we consider a region with high energy dissipation where $\Sigma_D \geq 10^{-7}$ nJ m $^{-3}$. Regions with low dissipation $\Sigma_D < 10^{-7}$ nJ m $^{-3}$ are represented

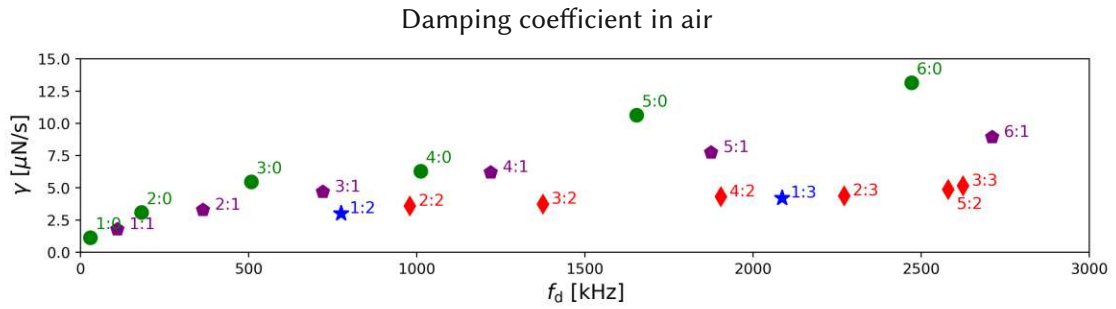


Figure 7.11: Damping coefficient of the micro-plate in vibrating in EB, torsional and RTS and HOP modes in air.

in black in Fig. 7.13. For RTS and HOP modes, Σ_D decreases in amplitude and also in the size of the high energy dissipation region.

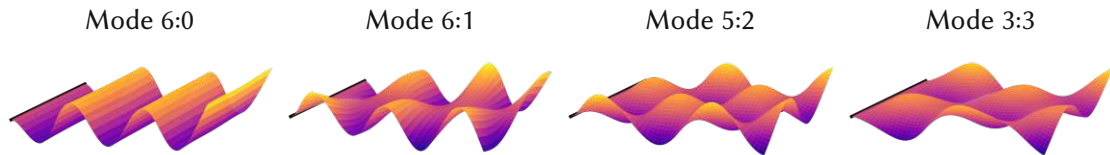


Figure 7.12: Displacement field of the 6:0, 6:1, 5:2 and 3:3 vibrational modes in air.

Furthermore, note in the energy dissipation maps in Fig. 7.13 the increase in Σ_D around the center of the plate $y = 0$, above and underneath the plate at $z \approx 15 \mu\text{m}$ for all the non-EB modes. The appearance of this additional region of energy dissipation occurs because of additional y -direction fluid flow around these non-EB modes both for the in-phase component \hat{u}_{IP} as well as for the out-of-phase component \hat{u}_{OP} as shown in Fig. 7.14.

In water, the pattern $Q^{\text{HOP,RTS}} < Q^{\text{torsional}} < Q^{\text{EB}}$ is not explained by the damping coefficient γ , since γ in water is higher for EB modes than for non-EB modes as shown in Fig. 7.15. Therefore, γ follows a similar pattern both in air in Fig. 7.11 and in water, that is, $\gamma^{\text{HOP,RTS}} < \gamma^{\text{torsional}} < \gamma^{\text{EB}}$, in which EB modes exhibit the highest damping coefficients.

The explanation for the higher Q-factor of the EB modes in water must rely on the added-mass effect. Fig. 7.16 shows that, indeed, the added-mass coefficient \mathcal{M} is much higher for the EB modes than for the non-EB modes. The added-mass coefficient \mathcal{M} for the HOP and RTS modes is the lowest among the plate vibrational modes. The fact that EB modes have a higher added-mass coefficient means the EB modes store more energy in form of kinetic energy in the fluid, which increases the EB mode's Q-factor in liquids.

Fig. 7.18 shows the dissipation and kinetic energy densities, Σ_D and Σ_k , for the different modes with approximately the same damped resonance frequency $f_d \approx 1.05 \text{ MHz}$ shown in Fig. 7.18. These modes are the 8:0, 5:2 and 2:3 modes, whose displacement field is shown in Fig. 7.17. The fluid flow around a plate vibrating in the 8:0 mode exhibits higher Σ_k and Σ_D than the flow around the non-EB modes (5:2 and 2:3) at a similar fre-

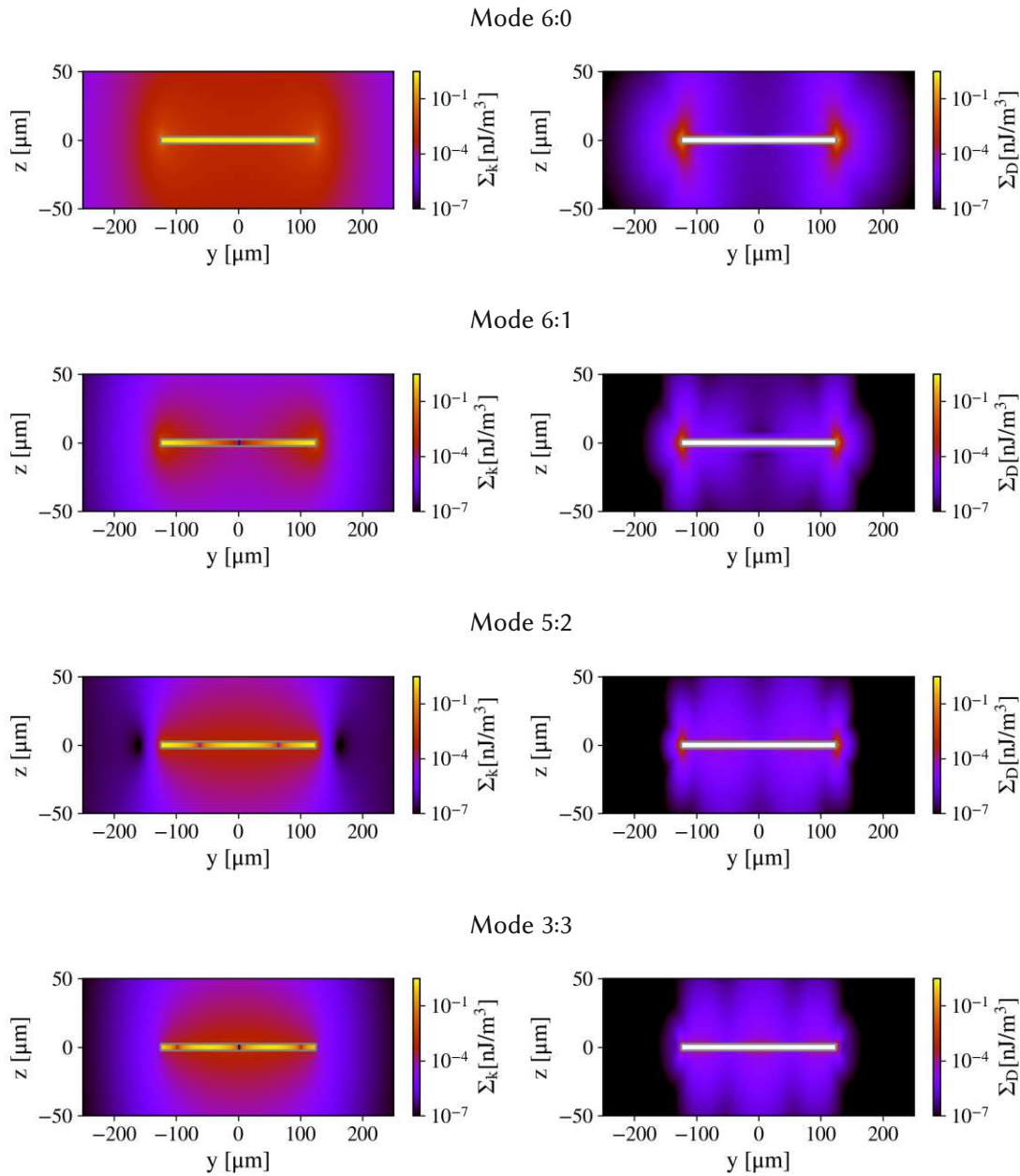


Figure 7.13: Kinetic and dissipated energy densities around plates in different modes in air. The plate’s boundaries are represented by a gray wire frame.

quency, which causes the EB mode’s higher added-mass coefficient \mathcal{M} and damping coefficient γ .

The efficiency of the proposed method for a single plate allows the investigation of the Q-factor, γ and \mathcal{M} in a fluid with continuously varying density and viscosity from a gas (air) to a liquid (water). Both the density and viscosity are simultaneously altered

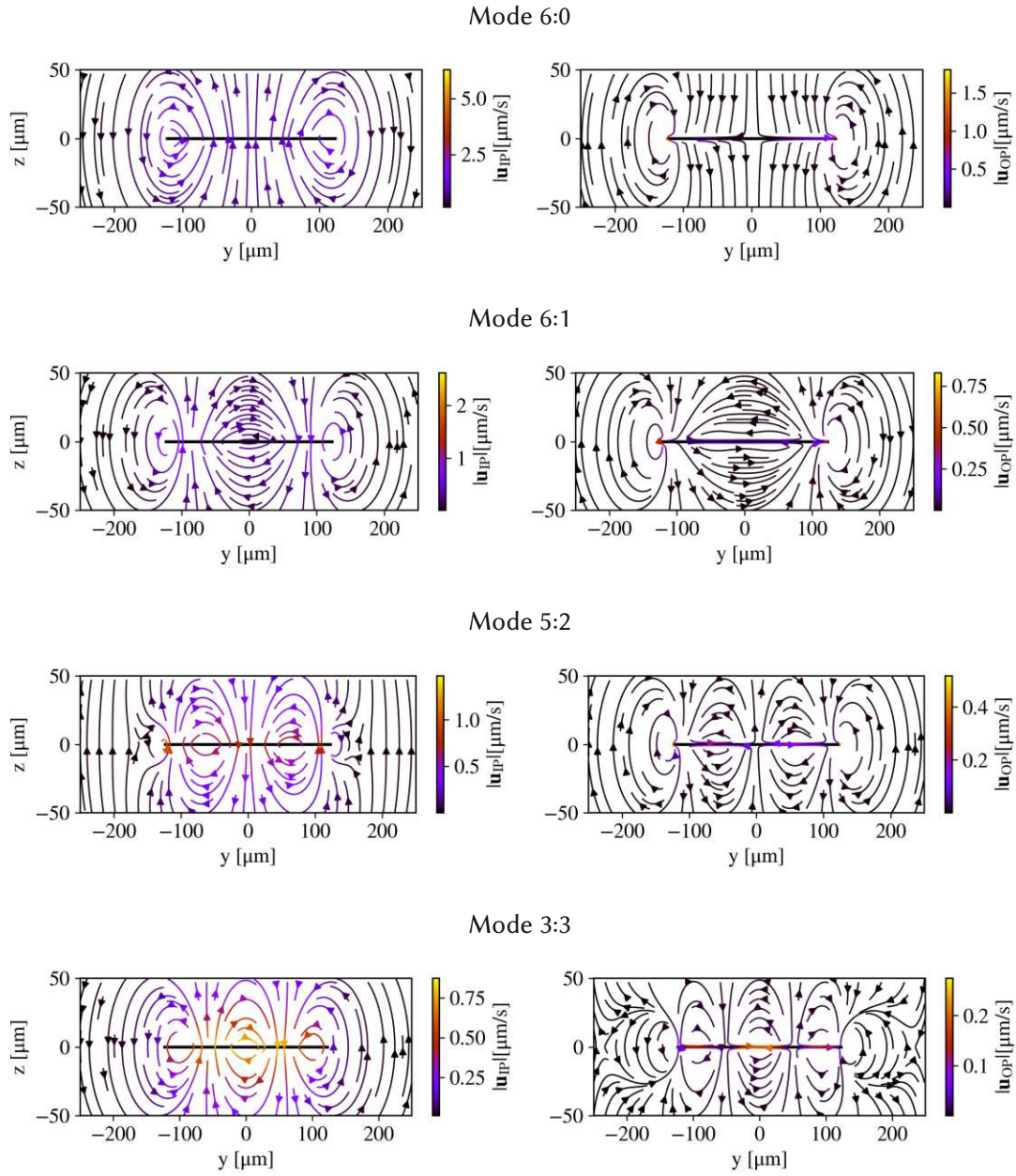


Figure 7.14: Fluid flow for modes 6:0, 6:1, 5:2 and 3:3 at the plate's tip in air. The in-phase flow is shown on the left, and the out-of-phase on the right.

from air to water following

$$\rho_f = \rho_{\text{air}} + r(\rho_{\text{water}} - \rho_{\text{air}}), \quad (7.8)$$

$$\mu_f = \mu_{\text{air}} + r(\mu_{\text{water}} - \mu_{\text{air}}), \quad (7.9)$$

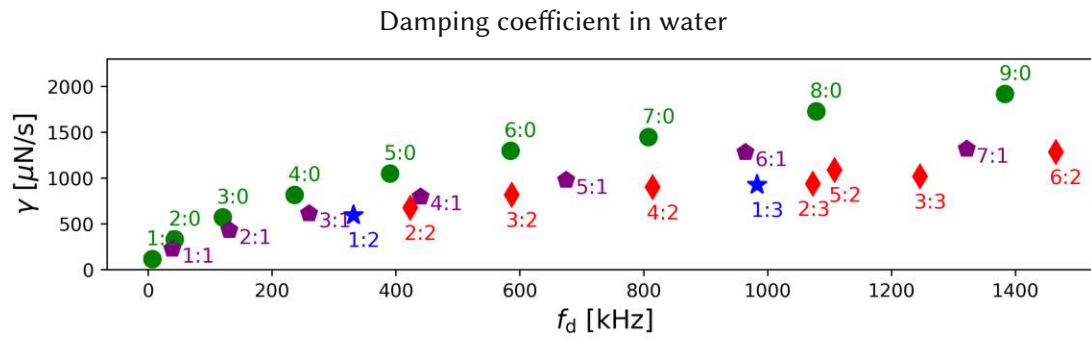


Figure 7.15: Damping coefficient of the micro-plate in vibrating in EB, torsional and RTS and HOP modes in water.

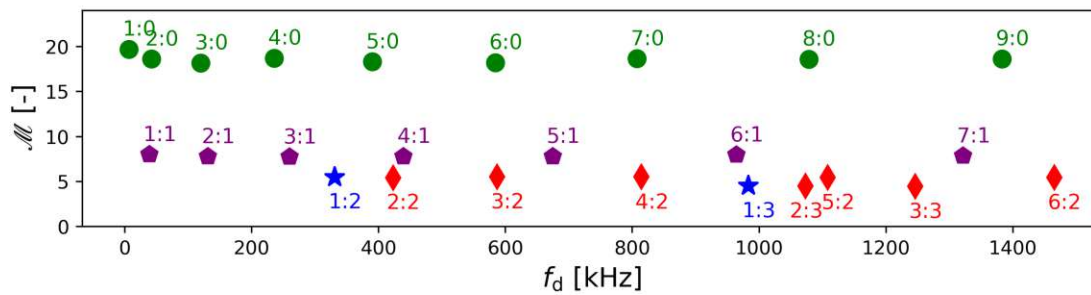


Figure 7.16: Added-mass coefficient of the micro-plate in vibrating in EB, torsional and RTS and HOP modes in water.

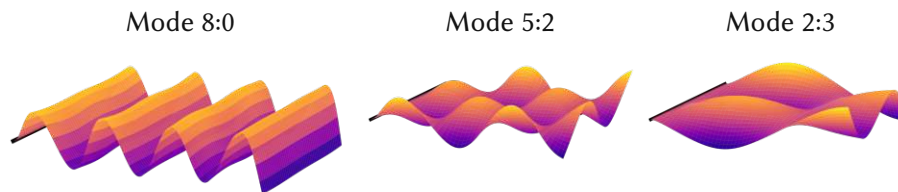


Figure 7.17: Displacement field of the 8:0, 5:2 and 2:3 vibrational modes in water.

where r varies between 0 and 1 logarithmically, which results in the μ_f, ρ_f pairs shown in Fig. 7.1.

Fig. 7.19 shows the plate's spectrum in the 2 MHz frequency range in the fluid ranging from the air (top) to water (bottom) as a function of a fluid parameter $\eta = \log 1/\sqrt{\rho_f \mu_f}$. For air, $\eta = 2.33$, while for water $\eta = 0.026$. Bright lines represent frequencies of maximum displacement, associated with the vibrational modes specified on the top and right side of the graph. As ρ_f and μ_f increase, the damped resonance frequencies f_d of all modes decrease. However, they do not decrease equally for all types of modes. EB modes exhibit a more accentuated decrease in f_d than non-EB modes.

As η increases it leads to the appearance of resonance frequencies in which two vibrational modes occur simultaneously. Fourteen of these resonance frequencies f_d on which two modes occur are highlighted in Fig. 7.19 from a) to n), following the order of

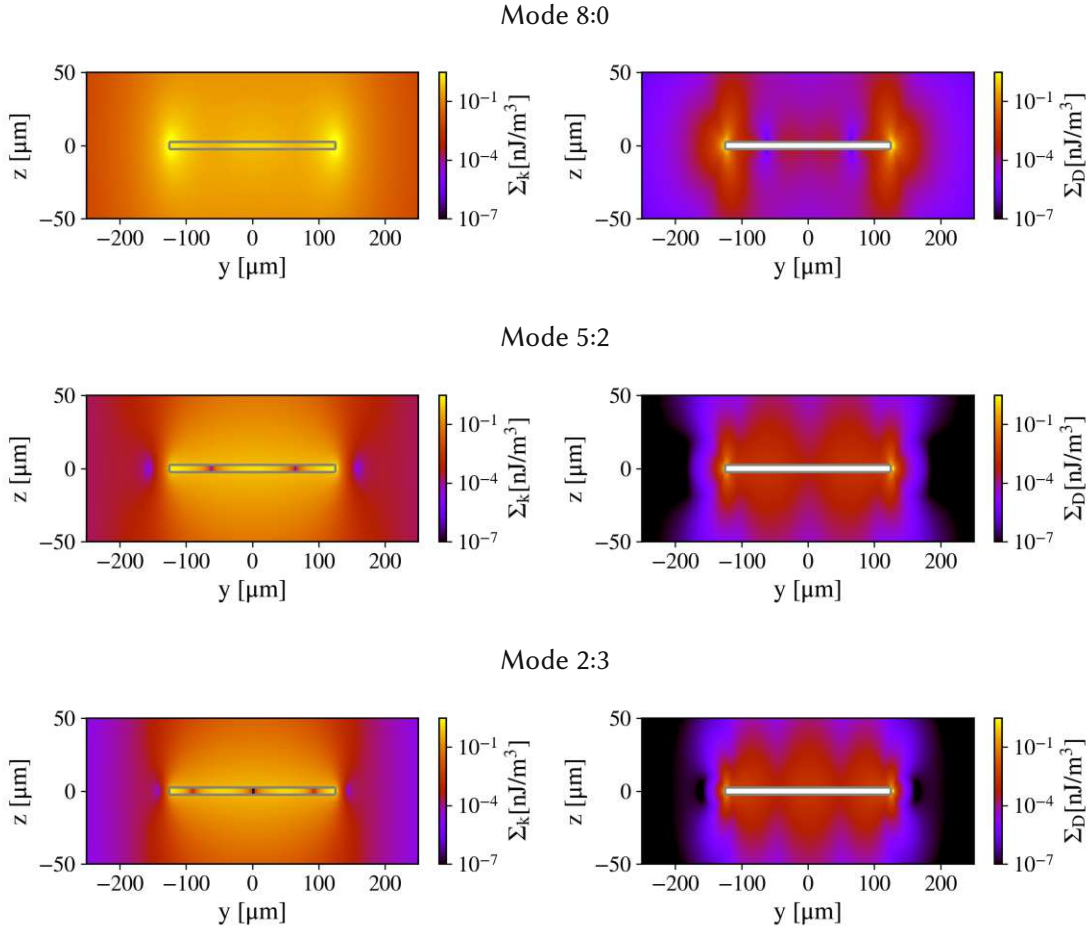


Figure 7.18: Kinetic and dissipated energy densities around plates in different modes in water. The plate's boundaries are represented by a gray wire frame.

decreasing η (from air to water). For instance, at point a) the mode 6:0 and mode 1:3 occur at the frequency $f_d = 1925\text{kHz}$ for a $\eta = 1.2$. These fourteen points are considered points of interest for understanding the GL-Q-inversion analysis since the analysis is restricted to modes with similar f_d .

To elucidate the GL-Q-inversion let us define the Q-factor ratio between an EB mode and a non-EB mode which share the damped resonance frequency f_d as

$$\frac{Q^{\text{EB}}}{Q^{\text{non-EB}}} = \frac{1 + \mathcal{M}^{\text{EB}}}{1 + \mathcal{M}^{\text{non-EB}}} \frac{\gamma^{\text{non-EB}}}{\gamma^{\text{EB}}}. \quad (7.10)$$

Fig. 7.20a shows the quality factor modal inversion in terms of the ratios between Q-factors. In gases, $Q^{\text{EB}}/Q^{\text{non-EB}}$ is smaller than 1 because EB modes have a lower Q-factor than non-EB modes. In liquids, the $Q^{\text{EB}}/Q^{\text{non-EB}}$ ratio is larger than 1, since EB modes have in liquids higher Q-factors. Interestingly, the ratio of damping coefficients is approximately constant in the entire fluid range and smaller than 1, as seen in Fig. 7.20b. Thus, EB modes exhibit a larger damping coefficient independently of the fluid regime.

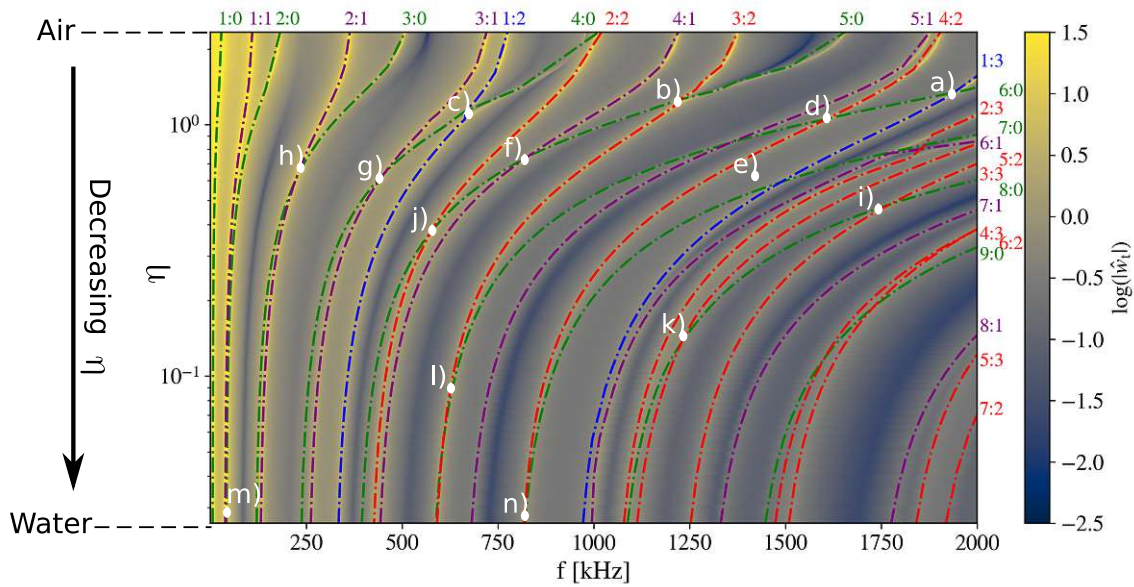


Figure 7.19: Spectral displacement of a micro-plate in a continuously changing fluid, from air to water. The colormap refers to the logarithmic value of the absolute displacement spectrum $\log(|\hat{w}_t|)$ of the plate in fluids between air (top) and water (bottom) as the function of the fluid’s parameter η .

Therefore, the explanation for the quality factor modal inversion lies in the fluid flow added mass of the different modes as expected. As shown in Fig. 7.20c, the ratio of added masses $\frac{1+\mathcal{M}^{EB}}{1+\mathcal{M}^{non-EB}}$ is approximately 1 for gases since \mathcal{M}^{EB} and \mathcal{M}^{non-EB} are negligible in gases. $\frac{1+\mathcal{M}^{EB}}{1+\mathcal{M}^{non-EB}}$ continuously increases as the fluid is altered from a gas to a liquid, reaching a ratio higher than 3 in water.

7.6 Conclusions

Investigating the HOP and RTS modes of micro-plates in gases and liquids revealed opposite trends in the different fluid regimes. While in gases Q increases from EB modes, to torsional and then to HOP and RTS modes $Q^{HOP,RTS} > Q^{torsional} > Q^{EB}$, in liquids, the opposite happens, and Q decreases from EB modes to HOP modes $Q^{EB} > Q^{torsional} > Q^{HOP,RTS}$. This change in the Q -factor trend from gases to liquids we named the “Gas-Liquid-modal- Q -factor inversion” (GL- Q -inversion). An analysis of the Q -factor as a ratio of the damping coefficient and added-mass coefficient revealed that in gases, Q increases for HOP modes due to their lower damping coefficients. In liquids, even though EB-modes dissipate more energy, they also exhibit a higher stored energy in form of added mass, which increases Q^{EB} .

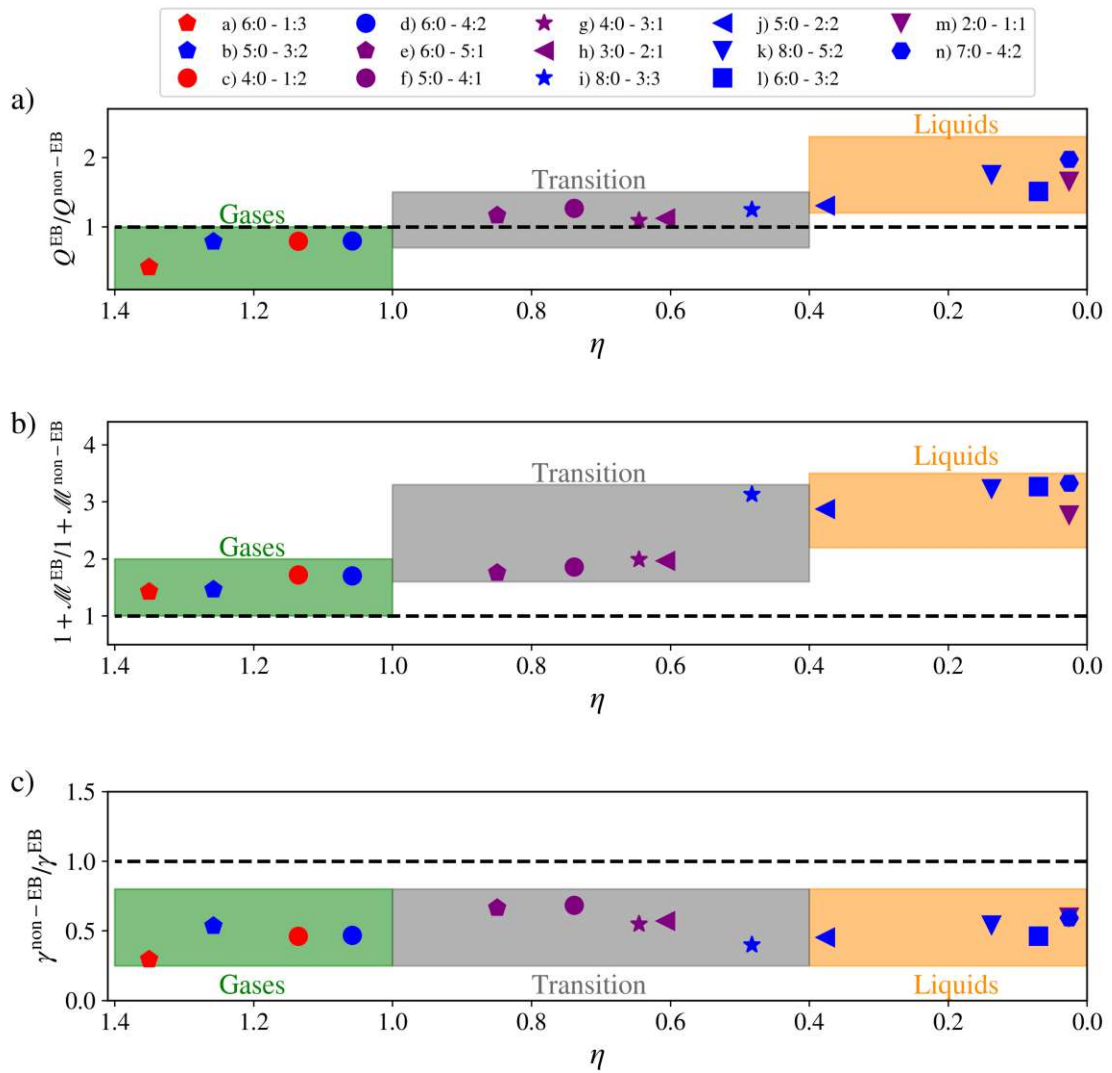


Figure 7.20: Ratio of the a) Q-factor, b) added-mass coefficients and c) damping coefficient of the vibrational modes over frequency in the gas-liquids transition.

8 Experimental analysis

Results of this chapter were partially published in [72].

Experimental investigations of MEMS resonators immersed in gases and liquids are essential to give confidence in the proposed numerical method. Here, we use the in-house capabilities to fabricate MEMS resonators with different geometries. This allows for an in-depth investigation to go way beyond the experimental data of fluid-micro-plate interaction available in the literature.

8.1 Fabrication of silicon MEMS resonators

For the experimental analysis, we fabricate micro-plates that have a length equal to 1500 μm and a thickness of 20 μm . A 500 nm piezoelectric layer of Aluminium Nitride (AlN) is sputter-deposited on the micro-plate so that integrated actuation and sensing can be performed in liquids as well as in gases. Two electrode layers of chromium/gold (Cr/Au) having a thickness of 50 nm and 150 nm, respectively, are evaporated on the top and bottom of the piezoelectric AlN-layer. Plates with two different widths are fabricated: plates with width equals 750 μm have an aspect ratio $r_a = 2$ and are named “w750” and plates with width equals 500 μm (aspect ratio $r_a = 3$) are named “w500”. Fig. 8.1 shows the example of prototypes “w500” and “w750” fixed to a ceramic package and electrically connected through gold wires.

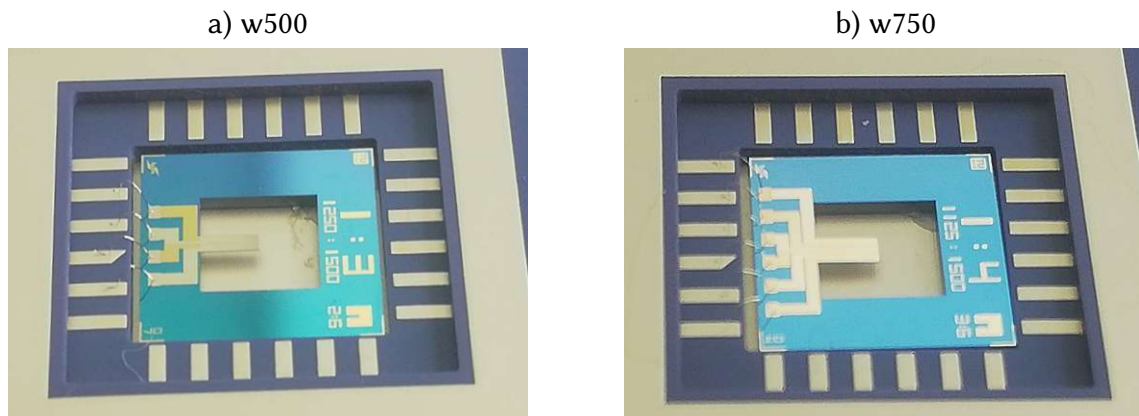


Figure 8.1: Prototypes fabricated for experimental analysis, in a) plates “w500” and in b) plates “w750”. The prototypes are fixed to a ceramic package and electrically connected through gold wires.

The silicon micro-plates are tailored with a different number of pairs (top and bottom) of electrodes as represented in Fig. 8.2. These tailored electrodes allow the excitation of specific vibrational modes with different external electric connections. For instance, providing a similar signal to all electrodes excites most efficiently EB modes, because EB modes are symmetric concerning the y -direction. In the w500 example in Fig. 8.2a, providing opposite signal voltages to E1 and E3 excites most efficiently torsional and HOP modes with $n_y = 3$. In the w750 example in Fig. 8.2b, exciting E1∪E2

and E3∪E4 with opposite signals excites torsional and HOP modes with $n_y = 3$, while exciting E1∪E3 and E2∪E4 with opposite signals excites predominantly modes with $n_y = 4$.

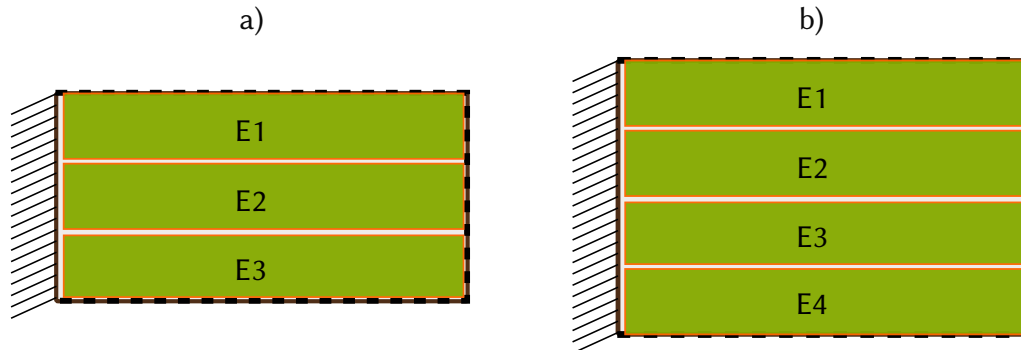


Figure 8.2: Tailored electrodes for symmetric and anti-symmetric excitation. In a) a w500 plate is shown with three tailored electrodes (E1 to E3). In b) a w750 plate is shown with four tailored electrodes (E1 to E4).

8.2 Experiments in water

The plate's spectral displacement is measured using a laser Doppler vibrometer (LDV) Polytech MSA 500. For the measurement in water, a water droplet is placed on the micro-plate as shown in Fig. 8.3.

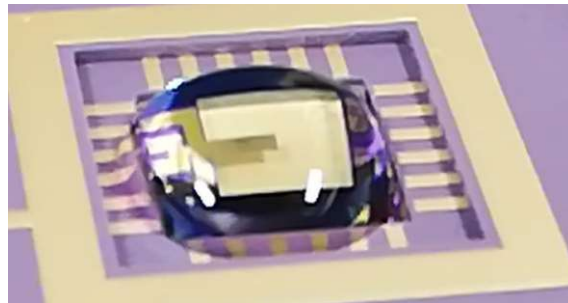


Figure 8.3: w750 micro-plate immersed in a droplet of water during measurements.

Fig. 8.4 shows, on the right, the real part of the measured velocity $\mathcal{R}(u)$ of the micro-plate in water with the LDV at the lowest ten vibrational modes of the micro-plate w750 at each damped resonance frequency f_d . On the left, the average displacement field \bar{u} of the measured points at frequencies near f_d is given.

The quality factor is obtained from a fit with the damped harmonic oscillator equation (Eq. 5.10) to the average displacement field \bar{u} . The resulting fit is shown in Fig. 8.4. Fig. 8.5 shows the Q-factor of the w500 and w750 micro-plate in a 750 kHz frequency range in water. In this frequency range, sixteen vibrational modes of the w500 plate are experimentally identified, six EB modes, six torsional, the first RTS and three HOP modes. From the w750 plate resonator, seventeen vibrational modes were identified in

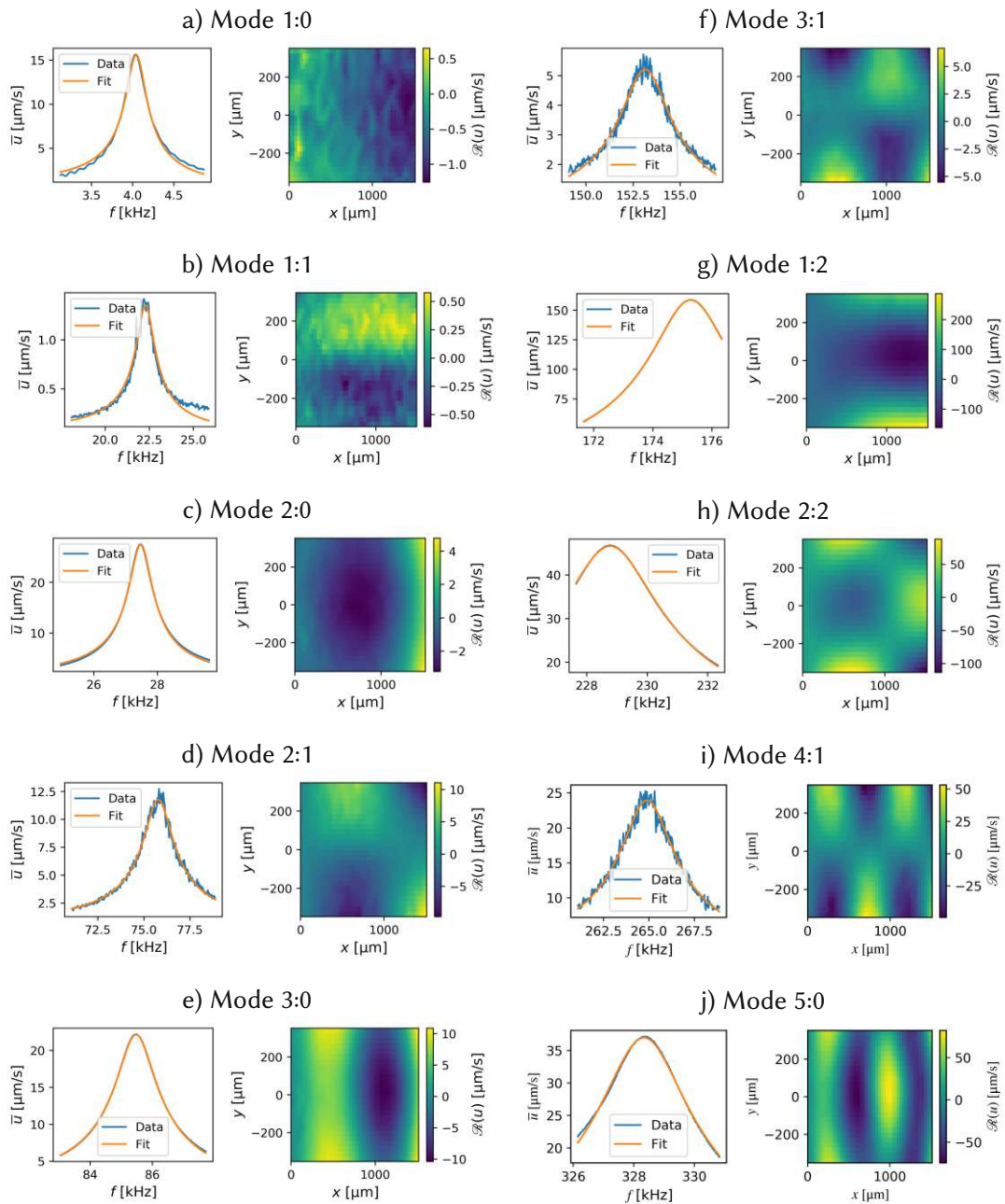


Figure 8.4: Experimental data of the w750 micro-plate in water for the eight lowest vibrational modes. On the left, the average of \bar{u} at the measure points at frequencies near f_d is given. On the right, the real part of the measured velocity u of the micro-plate is shown.

this frequency range, including two RTS modes and five HOP modes. The 4:0 mode was not identified, likely due to spectral overlap with a HOP mode (the 2:2 mode), which prevents the 4:0 mode's identification. Similarly, the 5:1 mode was not found due to spectral overlap with the 1:3 mode. Note in Fig. 8.5 that EB modes exhibit the highest Q-factors, followed by torsional modes and HOP/RTS modes. This $Q_{\text{water}}^{\text{EB}} > Q_{\text{water}}^{\text{torsional}} > Q_{\text{water}}^{\text{HOP}}$ pat-

tern found experimentally agrees with the pattern seen in the simulations in liquids in Chapter 7.

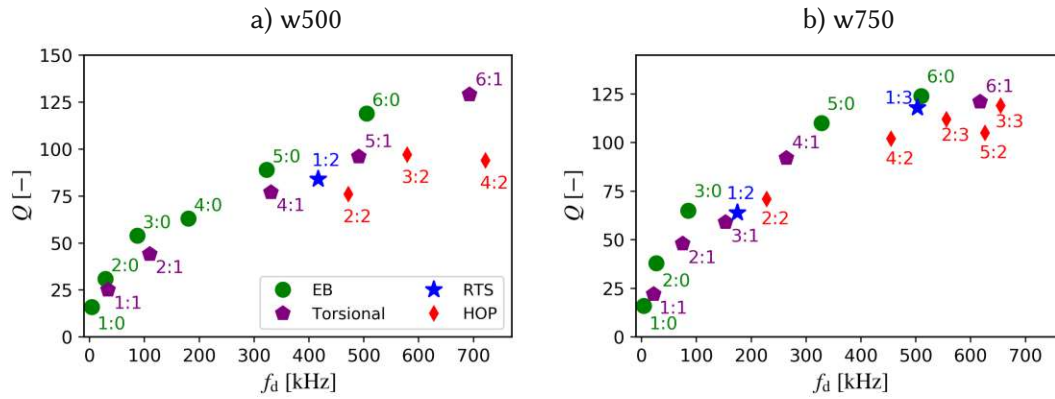


Figure 8.5: Experimentally obtained Q-factor of the a) w500 and b) w750 micro-plates in water.

The difference between simulation and experimental damped resonance frequency $\text{Diff}(f_d)$ is determined as

$$\text{Diff}(f_d) = \frac{f_d^{\text{Sim}} - f_d^{\text{Exp}}}{f_d^{\text{Sim}}}. \quad (8.1)$$

Hence, negative values of $\text{Diff}(f_d)$ means the simulation under-estimates f_d , and positive values of $\text{Diff}(f_d)$ indicates the simulated values of f_d are over-estimated.

Fig. 8.6 shows $\text{Diff}(f_d)$ for both w500 and w750 plate resonators. In both micro-plates, the numerical method under-estimates f_d for the EB modes, reaching a difference of 22% for the w500 plate and up to 35% for the w750 plate. The f_d under-prediction for EB modes is expected due to the two-dimensional fluid flow approximation in the proposed numerical method. For the torsional, HOP and RTS modes, the difference in f_d is in the range $0 \leq \text{Diff}(f_d) \leq 12\%$ for the w500 plate, and within the $-15\% \leq \text{Diff}(f_d) \leq 5\%$ range for the w750 plate.

The difference between simulation and experimental Q-factors $\text{Diff}(Q)$ is determined as

$$\text{Diff}(Q) = \frac{Q^{\text{Sim}} - Q^{\text{Exp}}}{Q^{\text{Sim}}}. \quad (8.2)$$

Fig. 8.7 shows $\text{Diff}(Q)$ for both w500 and w750 plate resonators. For most EB modes (in both plates), the simulated Q-factors are overestimated, whereas torsional, HOP and RTS modes have underestimated Q-factors. For the w500 plate, the difference in Q is in the range $-30\% \leq \text{Diff}(Q) \leq 20\%$, and within the $-20\% \leq \text{Diff}(Q) \leq 25\%$ range for the w750 plate. We consider these results to indicate great agreement between simulation and experimental data in water. The main limitation of the proposed method is the estimation of the damped resonance frequency f_d of the EB modes, whose error increases with the number of nodal lines n_x .

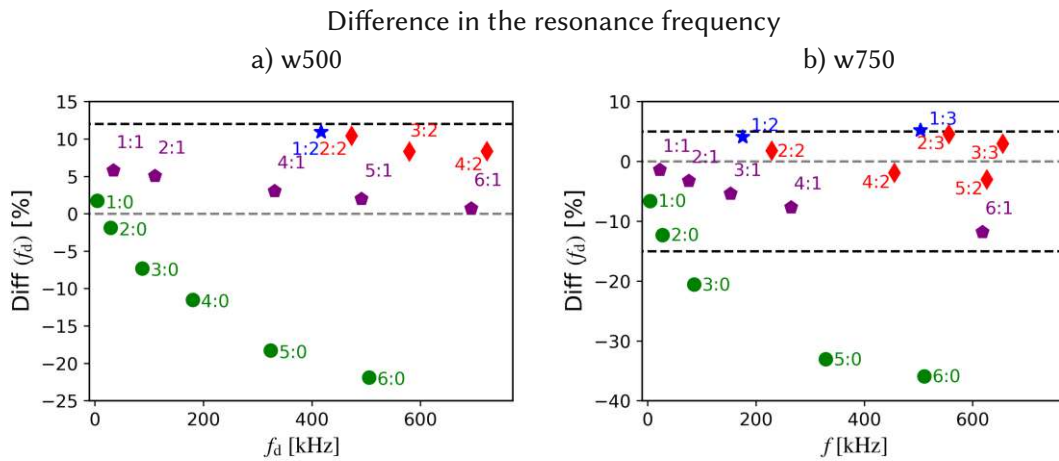


Figure 8.6: Difference in f_a , $\text{Diff}(f_a)$, for the a) w500 and b) w750 micro-plate in water.

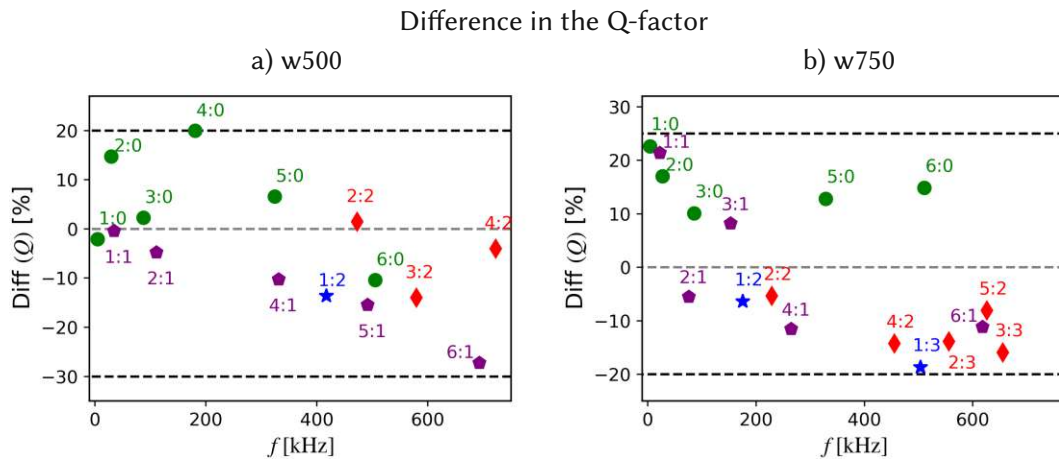


Figure 8.7: Difference in Q , $\text{Diff}(Q)$, for the a) w500 and b) w750 micro-plate in water.

8.3 Experiments in air

Experimentally determining the Q -factor of the w500 and w750 micro-plates in air yields surprisingly low Q -factors. As shown in Fig. 8.8, Q of the EB and torsional modes initially increase (from modes 1:0 to 2:0, and from modes 1:1 to 2:1), similarly to the increase expected from simulations. What is more, the torsional modes exhibit a higher Q -factor than the EB modes, similar to the simulation results. However, this initial increase in Q is followed by a decrease for all modes with resonance frequencies higher than 200 kHz. While the simulated Q -factor for these modes with $f_a \geq 200$ kHz is in the order of thousands, the measured Q -factors are in the order of the hundreds.

The reason for this decrease in Q is the occurrence of acoustic losses. Acoustic losses refer to the fluid's compressibility, which becomes significant when the acoustic wavelength λ_{ac} is of the same order of magnitude or smaller than the flexural wavelength λ_{flex} [30, 54].

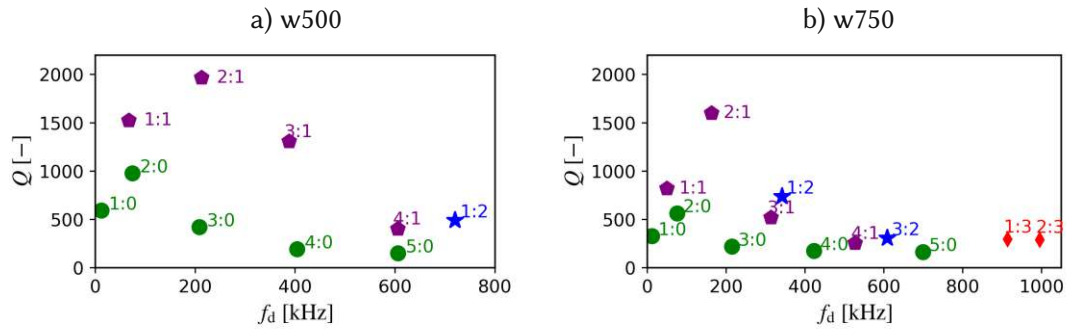
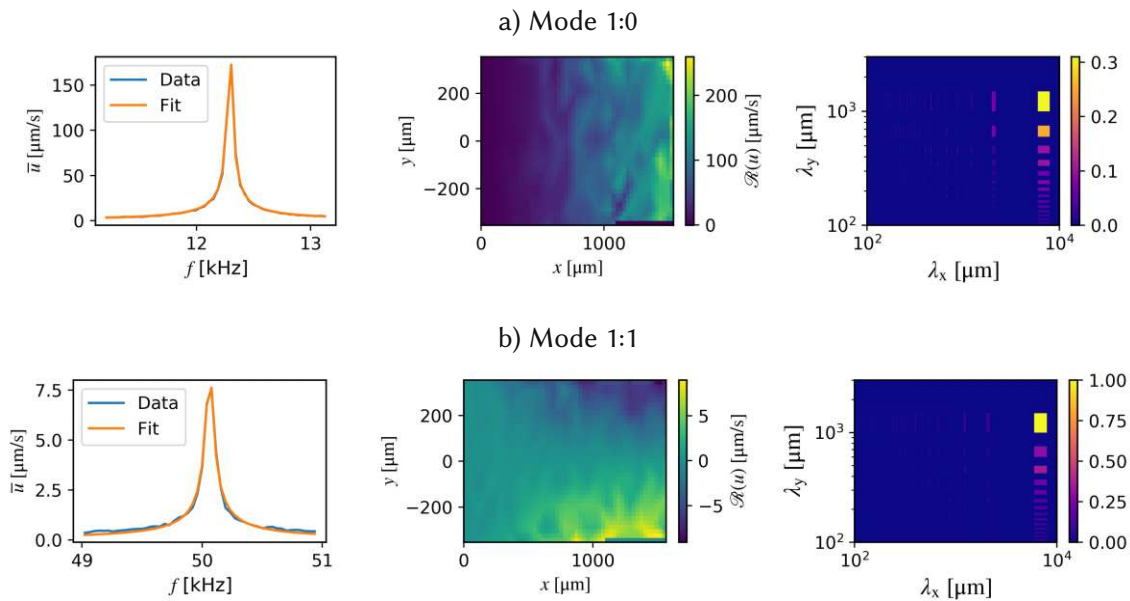


Figure 8.8: Experimentally obtained Q-factor of the a) w500 and b) w750 micro-plates in air.

The two-dimensional vibrational modes of plates exhibit flexural wavelengths in both directions, x and y , denoted by λ_x and λ_y , respectively. λ_x and λ_y are determined with a two-dimensional Fast Fourier Transform (FFT) of the experimental displacement field. Fig. 8.8 shows on the left, the average of \bar{u} at the measure points at frequencies near f_d . On the center is the real part of the measured velocity u of the micro-plate and on the right, is the result of the two-dimensional FFT of the vibrational mode as a function of λ_x and λ_y . For the 1:0 mode, the dominant λ_x is 6000 μm and λ_y is 3000 μm . All the torsional modes exhibit λ_y equals to 1500 μm , whereas the EB modes have $\lambda_y = 3000 \mu\text{m}$. The 1:2 mode has $\lambda_y = 600 \mu\text{m}$, slightly smaller than the plate's width.



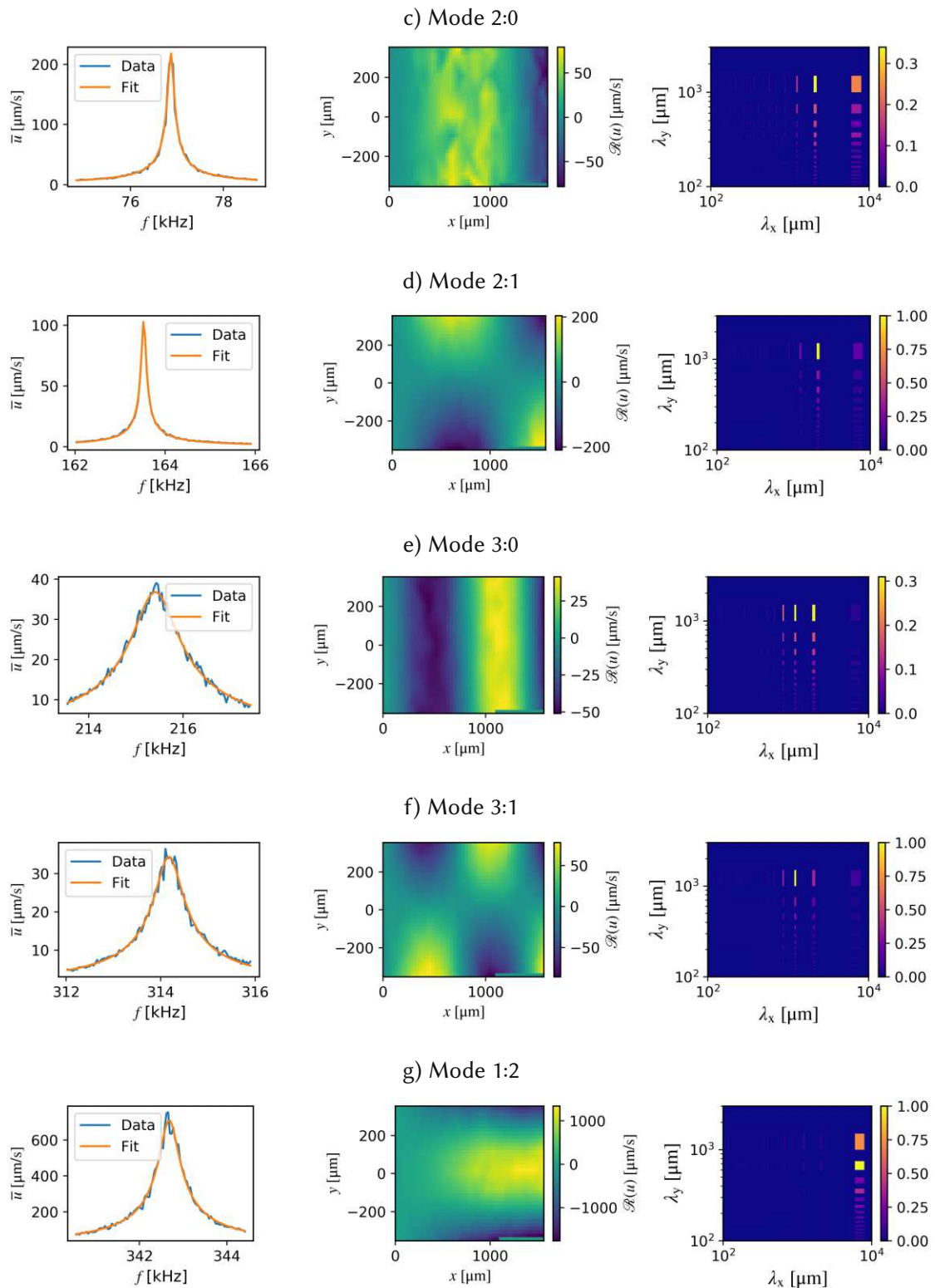


Figure 8.8: Experimental data of the w750 micro-plate in water for the eight lowest vibrational modes. On the left, the average of \bar{u} at the measure points at frequencies near f_d . On the center, is the real part of the measured velocity u of the micro-plate. On the right, the result of the two-dimensional FFT of the vibrational mode.

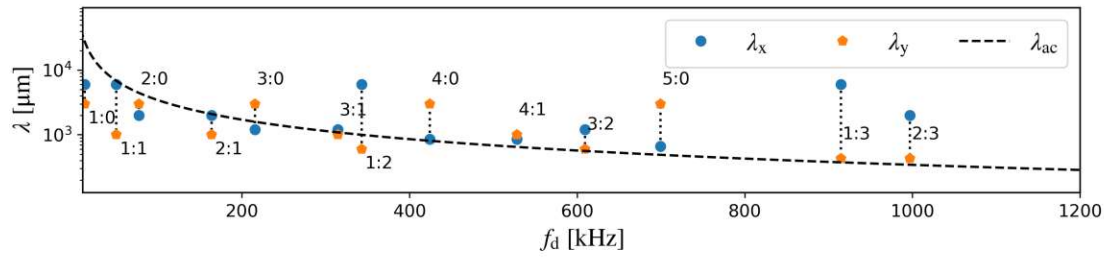


Figure 8.9: Flexural and acoustic wavelengths of the vibrational modes of the micro-plate w750 in air.

Fig. 8.9 shows the flexural wavelengths λ_x and λ_y as well as the acoustic wavelength λ_{ac} for the w750 plate in air. The acoustic wavelength as $\lambda_{ac} = c/f$ considering the speed of sound c of air as 340 m s^{-1} [66]. The 2:1 mode is the last one to have both flexural wavelengths λ_x and λ_y smaller than the acoustic wavelength λ_{ac} . All modes above the 2:1 mode have at least one of the flexural wavelengths larger than the acoustic wavelength, hence acoustic losses play a prominent role in such vibrational modes.

8.4 Minimizing the influence of acoustic losses

Including compressibility effects to account for acoustic losses in the proposed method is not trivial. Hence, we use an alternative strategy to experimentally demonstrate the GL-Q-inversion effect (found in the previous chapter). We design resonators for which acoustic losses are minimized. Using a thinner and longer micro-plate, resonance frequencies f_d are lower, hence the number of vibrational modes occurring at frequencies before acoustic losses become dominant is increased. We fabricate a micro-plate with length equals to $2524 \mu\text{m}$, width equal to $1274 \mu\text{m}$ and thickness of $5 \mu\text{m}$. Similarly to the numerical example and previous experimental analysis, this micro-plate has an aspect ratio approximately equal to 2.

Given the plate's small thickness ($5 \mu\text{m}$), the device's layer stress must be small, so that static out-of-plane bending is minimized and the plate's spectral displacement can be measured with the LDV. To achieve low layer stress we use a stress-engineered polycrystalline diamond layer as the plate's material. A polycrystalline diamond layer is deposited on a $\langle 100 \rangle$ -silicon substrate using hot filament chemical vapor deposition (CVD) in a CVD reactor from CarbonCompetence GmbH. A preliminary seeding step with nanodiamond crystals is used to grow the diamond layer on a non-diamond substrate. Subsequently, the plate resonators are patterned on the diamond layer with chemical dry etching in an inductively coupled plasma reactive ion etcher (ICP RIE) with oxygen as the etching gas and aluminium as the etching mask. The silicon substrate beneath the polycrystalline diamond layer is removed with the so-called Bosch process etch from the backside in the same ICP RIE equipment, which concludes the plate resonator fabrication. With this fabrication method, the layer's stress is smaller

than 100 MPa and the out-of-plane static displacement is restricted to a few tens of micrometers. The resulting micro-plate is shown in Fig. 8.10).

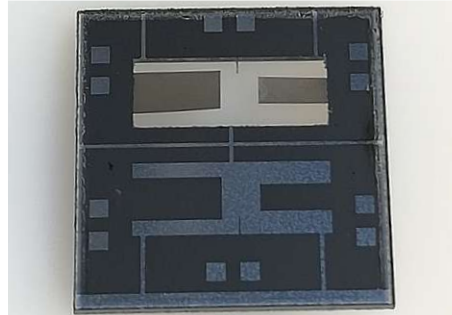


Figure 8.10: Polycrystalline diamond micro-plate with minimized static out-of-plane displacement.

Fig. 8.11a shows the Q-factor of this thin diamond micro-plate in air in the 200 kHz frequency range. EB modes exhibit the lowest Q-factors in this frequency range, while torsional and HOP modes with $n_y = 2$ have intermediate Q-factors. HOP modes with $n_y = 3$ exhibit the highest Q-factors in this frequency range. For instance, the 3:3 mode has a Q-factor of 982, almost 5 times higher than the Q-factor of the 6:0 EB mode at a similar resonance frequency with $Q = 205$. In Fig. 8.11b it is clear that using the thin plate successfully avoided the acoustic losses, and in this frequency regime, the Q-factor follows the pattern $Q_{\text{air}}^{\text{HOP}} > Q_{\text{air}}^{\text{torsional}} > Q_{\text{air}}^{\text{EB}}$, in agreement with the numerical findings.

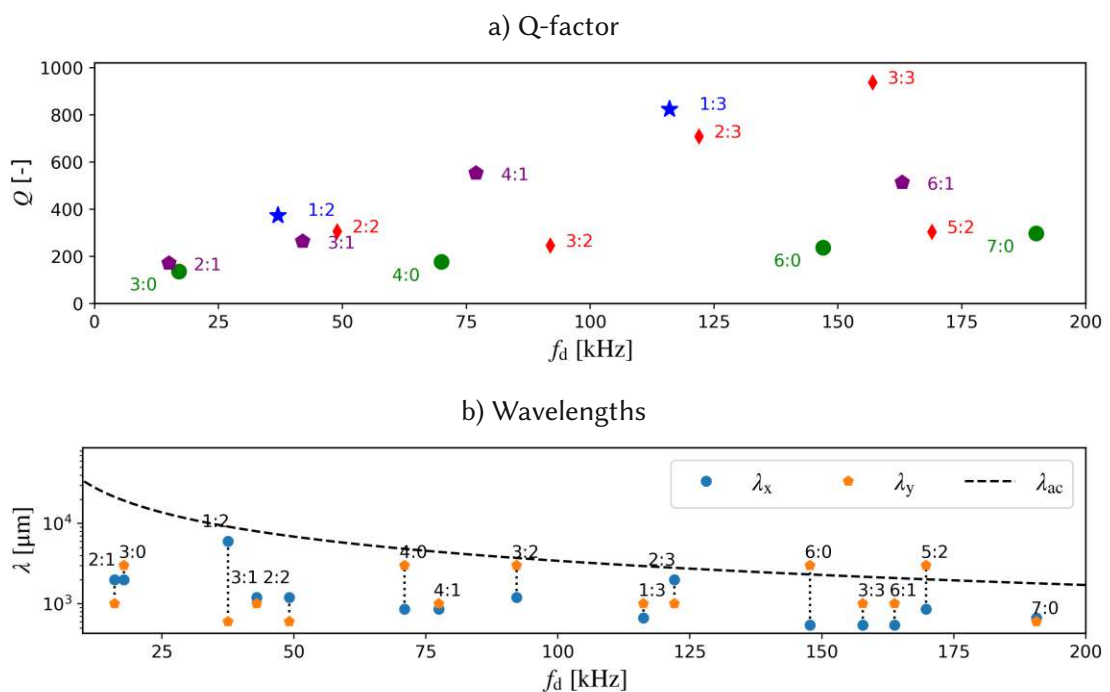


Figure 8.11: a) Q-factor and b) flexural and acoustic wavelengths of the diamond micro-plate in air.

A comparison between the simulated Q-factor and measured Q-factor in air was not possible, because, for such analysis, an extensive characterization of the mechanical properties of the polycrystalline diamond layer would be necessary, given the anisotropic properties of the material and the specific fabrication process. Also, experimentally measuring the Q-factor of the thin diamond micro-plate in water was not possible, since no piezoelectric layer was deposited on the device.

8.5 Conclusions

Experiments in water showed a Q-factor following the numerically predicted pattern of $Q^{\text{EB}} > Q^{\text{torsional}} > Q^{\text{HOP}}$. The difference in f_d between simulation and experiments was within the $-15\% \leq \text{Diff}(f_d) \leq 5\%$ range for the w750 plate for non-EB modes. For EB modes, $\text{Diff}(f_d)$ grows with n_x and reached 35% for the 6:0 mode. The difference in Q-factor was within the $-20\% \leq \text{Diff}(Q) \leq 25\%$ range for the w750 plate in water, which we consider a great agreement between simulated and experimental data.

Experiments in air showed that acoustic losses must also be considered, in addition to viscous losses for properly determining the Q-factor. Thin micro-plates were fabricated with polycrystalline diamond for enabling a low-stress device layer. For the thin micro-plates, the Q-factor in air follows the pattern $Q^{\text{HOP}} > Q^{\text{torsional}} > Q^{\text{EB}}$, in agreement with the numerical prediction of the gas-liquid Q-factor inversion.

Part III

Beyond two-dimensional

9 Hydrodynamic force on a micro-plate due to a three-dimensional fluid flow

One key assumption in the method introduced in this work so far is the restriction of the fluid flow to be two-dimensional $\mathbf{u}^T = (0, u_y, u_z)$. This hypothesis is expected to limit the applicability of the method because for wide plates the three-dimensional fluid flow increases its effect on the plate's dynamics [35, 62] as represented in Fig. 9.1. However, the exact length to which the three-dimensional fluid flow affects the plate dynamics is yet undefined. Here, we propose to use formulation for the fluid flow that allows for the modeling of a three-dimensional fluid flow $\mathbf{u}^T = (u_x, u_y, u_z)$ around a micro-plate using a boundary integral formulation.

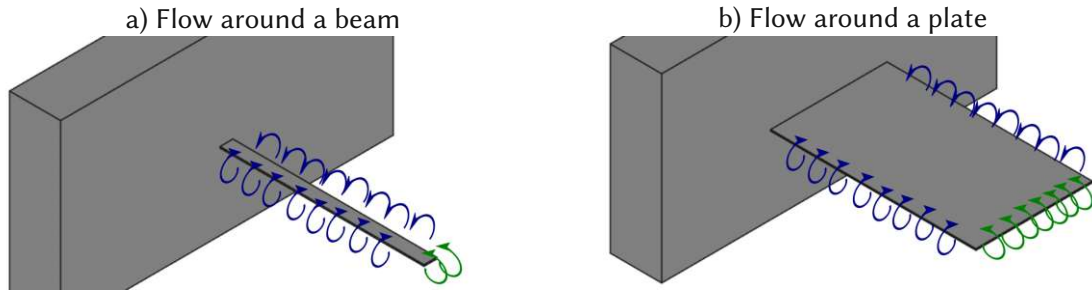


Figure 9.1: Representation of fluid the flow around a) beam and b) a plate. Green arrows indicate the fluid flow which is not characterized by the 2D fluid flow approximation.

9.1 The unsteady Stokeslet

The fundamental solution to the unsteady Stokes equations is the unsteady Stokeslet. That is, the unsteady Stokeslet is a Green's function that solves the singularly forced unsteady Stokes equations in the frequency domain

$$j\omega\hat{\mathbf{u}}(\mathbf{x}_f) = -\frac{1}{\rho_f}\nabla\hat{p}(\mathbf{x}_f) + \nu_f\nabla^2\hat{\mathbf{u}}(\mathbf{x}_f) + \hat{\mathbf{g}}\delta(\mathbf{x}_s), \quad (9.1)$$

$$\nabla \cdot \hat{\mathbf{u}}(\mathbf{x}_f) = 0. \quad (9.2)$$

where $\hat{\mathbf{g}}$ is a constant vector, \mathbf{x}_s is an arbitrary point in the three-dimensional space and δ is the three-dimensional delta function [94]. \mathbf{x}_s is typically called the *pole* or *source point*, and \mathbf{x}_f the *field point*.

In Einstein's summing notation, the unsteady Stokeslet \mathcal{S}_{ij} that solves the unsteady Stokes equations in an infinite unbounded domain is

$$\mathcal{S}_{ij}(\mathbf{x}_f, \mathbf{x}_s, \lambda) = A(\lambda, r)\frac{\delta_{ij}}{r} + B(\lambda, r)\frac{\bar{x}_i\bar{x}_j}{r^3} \quad (9.3)$$

where i, j represent x, y and z directions. \bar{x}_i and \bar{x}_j are the components of the vector $\bar{\mathbf{x}} = \mathbf{x}_f - \mathbf{x}_s$, and $r = |\bar{\mathbf{x}}|$. The functions $A(\lambda, r)$ and $B(\lambda, r)$ are

$$A(\lambda, r) = 2e^{-\lambda r} \left(1 + \frac{1}{\lambda r} + \frac{1}{\lambda^2 r^2} \right) - \frac{2}{\lambda^2 r^2}, \quad (9.4)$$

and

$$B(\lambda, r) = -2e^{-\lambda r} \left(1 + \frac{3}{\lambda r} + \frac{3}{\lambda^2 r^2} \right) + \frac{6}{\lambda^2 r^2}, \quad (9.5)$$

where $\lambda^2 = -j\omega l_{\text{char}}^2/\nu$, where l_{char} is the problems characteristic length. In the micro-plate case, l_{char} will be the plate's largest dimension, usually the plate's length l . The Stokeslet allows for defining the velocity components u_i at the field point \mathbf{x}_f due to the source $\hat{\mathbf{g}}$ at the pole \mathbf{x}_s as

$$u_i(\mathbf{x}_f) = \frac{1}{8\pi\mu_f} \mathcal{S}_{ij}(\lambda, \mathbf{x}_f, \mathbf{x}_s) \hat{\mathbf{g}}_j \delta(\mathbf{x}_s). \quad (9.6)$$

In addition to the unsteady Stokeslet \mathcal{S}_{ij} , the unsteady Stresslet is required for describing the stress components of a three-dimensional Stokes flow. The Stresslet, in index notation [93], is

$$T_{ijk} = -\frac{2}{r^3} (\delta_{ij} \bar{x}_{fk} + \delta_{kj} \bar{x}_{fi}) [e^{-\lambda r} (\lambda r + 1) - B(\lambda, r)] - \frac{2}{r^3} \delta_{ik} \bar{x}_{fj} [1 - B(\lambda, r)] - \frac{2\bar{x}_{fi} \bar{x}_{fj} \bar{x}_{fk}}{r^5} [5B(\lambda, r) - 2e^{-\lambda r} (\lambda r + 1)]. \quad (9.7)$$

The Stresslet describes the stress components σ_{ik} at the field point \mathbf{x}_f due to the source $\hat{\mathbf{g}}$ at the pole \mathbf{x}_s as

$$\hat{\sigma}_{ik}(\mathbf{x}_f) = \frac{1}{8\pi\mu_f} T_{ijk}(\lambda, \mathbf{x}_f, \mathbf{x}_s) \hat{\mathbf{g}}_j \delta(\mathbf{x}_s). \quad (9.8)$$

9.2 The boundary integral equation

The boundary integral equation arises when considering a closed surface D in an infinite fluid domain as represented in Fig. 9.2. The boundary integral equation allows for determining the velocity at a field point \mathbf{x}_f due to the fluid flow and fluid stress at the surface D as

$$\hat{u}_j(\mathbf{x}_f) = -\frac{1}{8\pi\mu_f} \int_D \left[\hat{f}_i \mathcal{S}_{ij}(\lambda, \mathbf{x}_f, \mathbf{x}_s) - \hat{u}_i(\mathbf{x}_s) \mathcal{T}_{ijk}(\lambda, \mathbf{x}_f, \mathbf{x}_s) n_k \right] dS(\mathbf{x}_s), \quad (9.9)$$

where \hat{f}_i are the components of the vector $\hat{\mathbf{f}} = \hat{\boldsymbol{\sigma}} \cdot \mathbf{n}$, and n_k are components of the normal vector \mathbf{n} pointing outward from the surface D to the flow as depicted in Fig. 9.2. In Eq. 9.9, \mathbf{x}_s are source points at the surface D which are also used to describe the surface D [93, 94]. The integral of the first term inside the RHS of Eq. 9.9 is known as the single-layer potential, and the integral of the second is the double-layer potential.

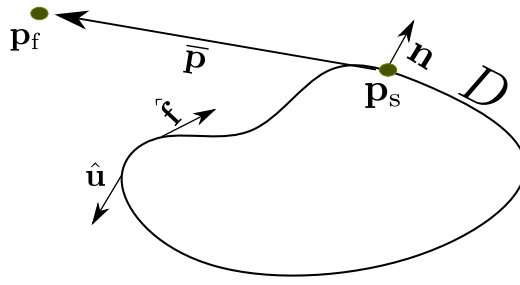


Figure 9.2: Body with a closed surface D immersed in a fluid. The normal vector \mathbf{n} points out of the body into the fluid domain.

For certain scenarios, Eq. 9.9 can be written simply as a single-layer formulation, while the double-layer potential may be neglected. For a single-layer representation to be valid, the requirement is that the flow rate through any closed surface S in the fluid domain is zero, that is

$$\int_S \hat{\mathbf{u}} \cdot \mathbf{n} dS = 0. \quad (9.10)$$

Hence, the single-layer potential formulation can not describe flows where sources or sinks of fluid exist [93]. For the micro-plate-fluid problem, from the continuity equation, as well as the no-penetration and no-slip boundary condition at the plate's surfaces, Eq. 9.10 is fulfilled. Therefore, the fluid flow around the micro-plate is represented by the single-layer formulation as

$$\hat{\mathbf{u}}_j(\mathbf{x}_f) = -\frac{1}{8\pi\mu} \int_D \left[\hat{f}_i(\mathbf{x}_s) \mathcal{S}_{ij}(\lambda, \mathbf{x}_f, \mathbf{x}_s) \right] dS. \quad (9.11)$$

Neglecting the plate's lateral surfaces, the fluid flow velocity at a field position \mathbf{x}_f is determined from the fluid forces, $\hat{\mathbf{f}}^t$ and $\hat{\mathbf{f}}^b$, acting on top and bottom plate surfaces, Σ^t and Σ^b , respectively, as represented in Fig. 9.3, yielding

$$\hat{\mathbf{u}}_j(\mathbf{x}_f) = -\frac{1}{8\pi\mu_f} \int_{\Sigma^t} \hat{f}_i^t(\mathbf{x}_s) \mathcal{S}_{ij}(\lambda, \mathbf{x}_f, \mathbf{x}_s) dS - \frac{1}{8\pi\mu_f} \int_{\Sigma^b} \hat{f}_i^b(\mathbf{x}_s) \mathcal{S}_{ij}(\lambda, \mathbf{x}_f, \mathbf{x}_s) dS. \quad (9.12)$$

Eq. 9.11 has analytic solutions only for a couple of examples, e.g. sphere translating with constant velocity [93]. For the micro-plate problem, Eq. 9.12 must be discretized and solved numerically. The discretization of the plate's top surface Σ_t is $\mathcal{F}(\Sigma_t)$ as exemplified in Fig. 9.4a), where Σ_t is discretized with rectangular elements. Discretizing the force acting on the plate's top surface $\hat{\mathbf{f}}^t$ with piece-wise continuous elements in \mathbf{t} leads to the collocation discretization scheme. Hence, each element of the partitioning \mathbf{t} is subject to a vector force $\hat{\mathbf{f}}^t$ with constant values. The set of the vector forces $\hat{\mathbf{f}}^t$ at \mathbf{t} is denoted $\hat{\mathbf{F}}^t$ and is represented in Fig. 9.4b). This discretization scheme where forces are described on all surfaces, in this case on the top and bottom plate surfaces, is typically called the Boundary Element Method (BEM).

To obtain an equation between the plate's velocity u_p and the force distributions $\hat{\mathbf{F}}^t$ (acting on the top surface) and $\hat{\mathbf{F}}^b$ (acting on the bottom surface), the fluid velocity is

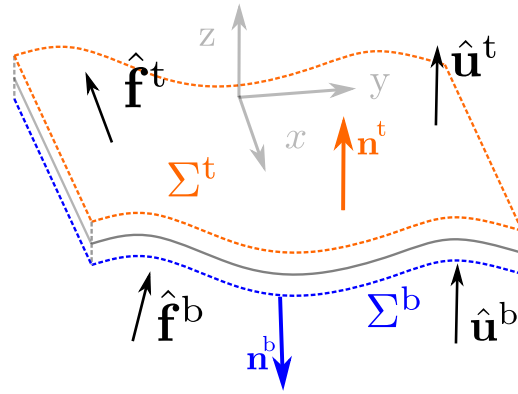


Figure 9.3: Forces acting on the top and bottom plate surfaces, Σ^t and Σ^b , respectively.

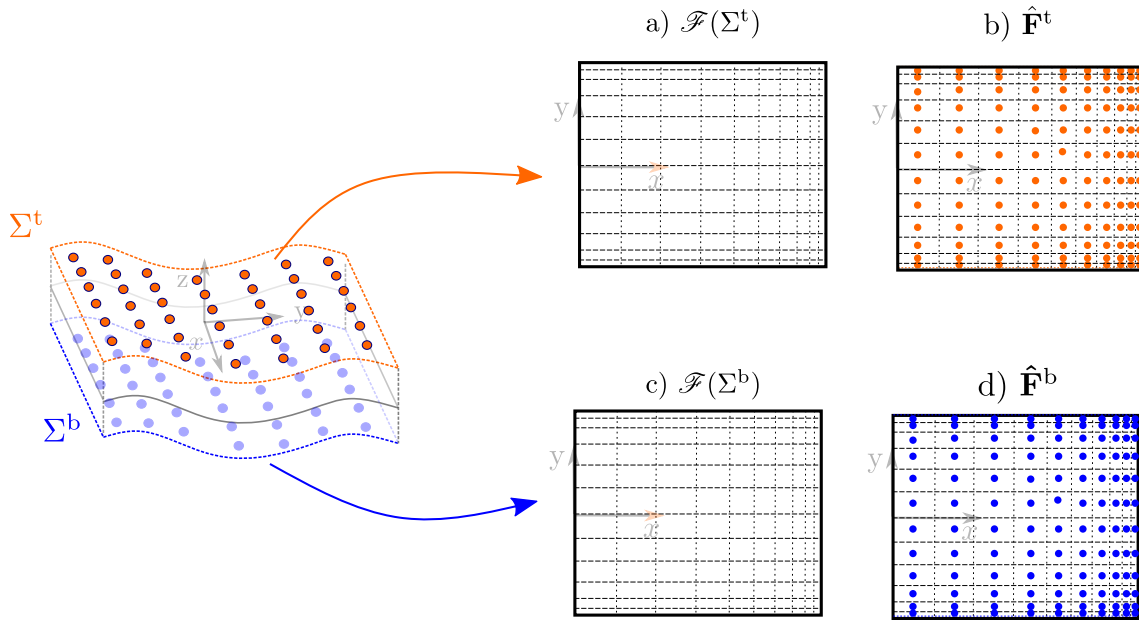


Figure 9.4: Example of the plate's a) top surface partitioning $\mathcal{F}(\Sigma^t)$ and c) bottom surface partitioning $\mathcal{F}(\Sigma^b)$ with rectangular elements. b) On the top surface, discretization of the vector forces $\hat{\mathbf{f}}^t$ in the partitioning $\mathcal{F}(\Sigma_t)$ leads to the discretized vector force distribution $\hat{\mathbf{F}}^t$. d) On the bottom surface, it leads to $\hat{\mathbf{F}}^b$.

discretized on Σ^t at a field point distribution \mathbf{p}_f^t , which leads to

$$\begin{bmatrix} \hat{\mathbf{u}}_x^t(\mathbf{p}_f^t) \\ \hat{\mathbf{u}}_y^t(\mathbf{p}_f^t) \\ \hat{\mathbf{u}}_z^t(\mathbf{p}_f^t) \end{bmatrix} = -\frac{1}{8\pi\mu_f} \begin{bmatrix} \int_{\Sigma^t} \mathcal{S}_{xx} & \int_{\Sigma^t} \mathcal{S}_{xy} & \int_{\Sigma^t} \mathcal{S}_{xz} & \int_{\Sigma^b} \mathcal{S}_{xx} & \int_{\Sigma^b} \mathcal{S}_{xy} & \int_{\Sigma^b} \mathcal{S}_{xz} \\ \int_{\Sigma^t} \mathcal{S}_{yx} & \int_{\Sigma^t} \mathcal{S}_{yy} & \int_{\Sigma^t} \mathcal{S}_{yz} & \int_{\Sigma^b} \mathcal{S}_{yx} & \int_{\Sigma^b} \mathcal{S}_{yy} & \int_{\Sigma^b} \mathcal{S}_{yz} \\ \int_{\Sigma^t} \mathcal{S}_{zx} & \int_{\Sigma^t} \mathcal{S}_{zy} & \int_{\Sigma^t} \mathcal{S}_{zz} & \int_{\Sigma^b} \mathcal{S}_{zx} & \int_{\Sigma^b} \mathcal{S}_{zy} & \int_{\Sigma^b} \mathcal{S}_{zz} \end{bmatrix} \cdot \begin{bmatrix} \hat{\mathbf{F}}_x^t \\ \hat{\mathbf{F}}_y^t \\ \hat{\mathbf{F}}_z^t \\ \hat{\mathbf{F}}_x^b \\ \hat{\mathbf{F}}_y^b \\ \hat{\mathbf{F}}_z^b \end{bmatrix}. \quad (9.13)$$

In Eq. 9.13, all components of the Stokeslet take as argument the distance between the field points \mathbf{p}_f^t and the coordinates of the elements of the partitionings $\mathcal{F}(\Sigma_t)$ and $\mathcal{F}(\Sigma_b)$. The integral in Eq. 9.13 are surface integrals, where the differential element dS is omitted for more compact notation.

A similar analysis for the fluid velocity at the plate's bottom surface leads to

$$\begin{bmatrix} \hat{\mathbf{u}}_x^b(\mathbf{p}_f^b) \\ \hat{\mathbf{u}}_y^b(\mathbf{p}_f^b) \\ \hat{\mathbf{u}}_z^b(\mathbf{p}_f^b) \end{bmatrix} = -\frac{1}{8\pi\mu_f} \begin{bmatrix} \int_{\Sigma^t} \mathcal{S}_{xx} & \int_{\Sigma^t} \mathcal{S}_{xy} & \int_{\Sigma^t} \mathcal{S}_{xz} & \int_{\Sigma^b} \mathcal{S}_{xx} & \int_{\Sigma^b} \mathcal{S}_{xy} & \int_{\Sigma^b} \mathcal{S}_{xz} \\ \int_{\Sigma^t} \mathcal{S}_{yx} & \int_{\Sigma^t} \mathcal{S}_{yy} & \int_{\Sigma^t} \mathcal{S}_{yz} & \int_{\Sigma^b} \mathcal{S}_{yx} & \int_{\Sigma^b} \mathcal{S}_{yy} & \int_{\Sigma^b} \mathcal{S}_{yz} \\ \int_{\Sigma^t} \mathcal{S}_{zx} & \int_{\Sigma^t} \mathcal{S}_{zy} & \int_{\Sigma^t} \mathcal{S}_{zz} & \int_{\Sigma^b} \mathcal{S}_{zx} & \int_{\Sigma^b} \mathcal{S}_{zy} & \int_{\Sigma^b} \mathcal{S}_{zz} \end{bmatrix} \begin{bmatrix} \hat{\mathbf{F}}_x^t \\ \hat{\mathbf{F}}_y^t \\ \hat{\mathbf{F}}_z^t \\ \hat{\mathbf{F}}_x^b \\ \hat{\mathbf{F}}_y^b \\ \hat{\mathbf{F}}_z^b \end{bmatrix}. \quad (9.14)$$

The BEM formulation in Eqs. 9.13 and 9.14 is valid for thick as well as thin structures. For thin structures, an alternative discretization scheme to BEM exists in which the thickness of the structure is considered to be zero for Stokeslet's evaluation and for the discretization scheme, i.e. the pole points and the field points are considered inside the domain of the structure [44, 69, 101, 102]. This method is called the Slender Body Method (SBM) or the singularity method. Even though the name of the method uses the word slender, its validity includes thin geometries such as micro-plates which are not necessarily slender (thin and narrow).

For the micro-plate fluid problem, using SBM implies that \mathbf{x}_f and \mathbf{x}_s are considered to be on the plate's midplane Ω_p as represented in Fig. 9.5. The plate's midplane partitioning in SBM is defined as $\mathcal{F}(\Omega_p)$, and discretization of the vector forces $\hat{\mathbf{f}}$ in the partitioning $\mathcal{F}(\Omega_p)$ leads to the discretized vector force distribution $\hat{\mathbf{F}}^{\text{mp}}$.

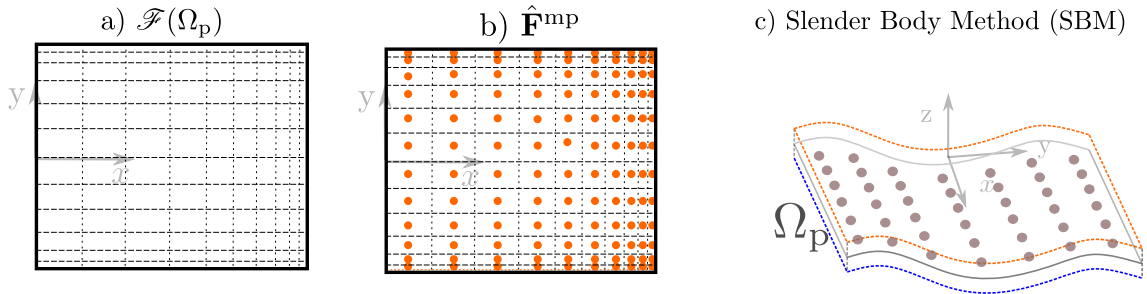


Figure 9.5: a) Example of the plate's midplane partitioning $\mathcal{F}(\Omega_p)$ with rectangular elements. b) Discretization of the vector forces $\hat{\mathbf{f}}$ in the partitioning $\mathcal{F}(\Omega_p)$ leads to the discretized vector force distribution $\hat{\mathbf{F}}^{\text{mp}}$. c) Discretization of the plate's midplane plate yields the slender body method.

The governing equation for the micro-plate-fluid interaction problem with SBM is

$$\begin{bmatrix} \hat{\mathbf{u}}_x^{\text{mp}}(\mathbf{x}_f^{\text{mp}}) \\ \hat{\mathbf{u}}_y^{\text{mp}}(\mathbf{x}_f^{\text{mp}}) \\ \hat{\mathbf{u}}_z^{\text{mp}}(\mathbf{x}_f^{\text{mp}}) \end{bmatrix} = -\frac{1}{8\pi\mu_f} \begin{bmatrix} \int_{\Omega_p} \mathcal{S}_{xx} & \int_{\Omega_p} \mathcal{S}_{xy} & \int_{\Omega_p} \mathcal{S}_{xz} \\ \int_{\Omega_p} \mathcal{S}_{yx} & \int_{\Omega_p} \mathcal{S}_{yy} & \int_{\Omega_p} \mathcal{S}_{yz} \\ \int_{\Omega_p} \mathcal{S}_{zx} & \int_{\Omega_p} \mathcal{S}_{zy} & \int_{\Omega_p} \mathcal{S}_{zz} \end{bmatrix} \begin{bmatrix} \hat{\mathbf{F}}_x^{\text{mp}} \\ \hat{\mathbf{F}}_y^{\text{mp}} \\ \hat{\mathbf{F}}_z^{\text{mp}} \end{bmatrix}, \quad (9.15)$$

where all components of the Stokeslet assume the z -distance between the field points \mathbf{x}_f^{mp} and the pole points in $\mathcal{F}(\Omega_p)$ to be zero.

The fluid's force acting on the plate's midplane $\hat{\mathbf{f}}^{\text{mp}}$ (whose discretized version is $\hat{\mathbf{F}}^{\text{mp}}$) is the sum of the forces acting on top and bottom surfaces as

$$\hat{\mathbf{f}}^{\text{mp}} = \hat{\mathbf{f}}^{\text{t}} + \hat{\mathbf{f}}^{\text{b}}. \quad (9.16)$$

Remembering the fluid stress definition in an incompressible Newtonian fluid

$$\hat{\boldsymbol{\sigma}} = -\mathbf{I} \hat{p} + \mu_f (\nabla \hat{\mathbf{u}} + \nabla \hat{\mathbf{u}}^T), \quad (9.17)$$

and defining the normal on Σ^{t} to be $\mathbf{n}^{\text{t}}(0, 0, 1)^{\text{T}}$, the fluid force on the top surface is

$$\hat{\mathbf{f}}^{\text{t}} = \hat{\boldsymbol{\sigma}}^{\text{t}} \cdot \mathbf{n}^{\text{t}} = [-\mathbf{I} \hat{p}^{\text{t}} + \mu_f (\nabla \hat{\mathbf{u}} + \nabla \hat{\mathbf{u}}^T)] \cdot \mathbf{n}^{\text{t}}. \quad (9.18)$$

From the no-slip and no-boundary conditions, the fluid velocity at the plate's top and bottom surfaces, $\hat{\mathbf{u}}^{\text{t}}$ and $\hat{\mathbf{u}}^{\text{b}}$ are equal to the plate's midplane velocity $(0, 0, \hat{u}_p)$, yielding

$$\hat{\mathbf{f}}^{\text{t}} = \left(\frac{\partial \hat{u}_p}{\partial x}, \frac{\partial \hat{u}_p}{\partial y}, -\hat{p}^{\text{t}} + 2\mu_f \frac{\partial \hat{u}_p}{\partial z} \right)^{\text{T}}. \quad (9.19)$$

Similarly, the fluid force acting on the plate's bottom surface is determined, assuming $\mathbf{n}^{\text{b}}(0, 0, -1)^{\text{T}}$, as

$$\hat{\mathbf{f}}^{\text{b}} = \left(-\frac{\partial \hat{u}_p}{\partial x}, -\frac{\partial \hat{u}_p}{\partial y}, +\hat{p}^{\text{b}} - 2\mu_f \frac{\partial \hat{u}_p}{\partial z} \right)^{\text{T}}. \quad (9.20)$$

Hence, $\hat{\mathbf{f}}^{\text{mp}}$ is

$$\hat{\mathbf{f}}^{\text{mp}} = (0, 0, \hat{p}^{\text{b}} - \hat{p}^{\text{t}})^{\text{T}}. \quad (9.21)$$

The plate's midplane velocity is $\hat{\mathbf{u}}^{\text{mp}}(0, 0, \hat{u}_p)^{\text{T}}$, therefore Eq. 9.15 renders

$$\begin{bmatrix} 0 \\ 0 \\ \hat{\mathbf{u}}^{\text{p}}(\mathbf{x}_f^{\text{mp}}) \end{bmatrix} = -\frac{1}{8\pi\mu_f} \begin{bmatrix} \int_{\Omega_p} \mathcal{S}_{xx} & \int_{\Omega_p} \mathcal{S}_{xy} & \int_{\Omega_p} \mathcal{S}_{xz} \\ \int_{\Omega_p} \mathcal{S}_{yx} & \int_{\Omega_p} \mathcal{S}_{yy} & \int_{\Omega_p} \mathcal{S}_{yz} \\ \int_{\Omega_p} \mathcal{S}_{zx} & \int_{\Omega_p} \mathcal{S}_{zy} & \int_{\Omega_p} \mathcal{S}_{zz} \end{bmatrix} \begin{bmatrix} 0 \\ 0 \\ \hat{\mathbf{p}}^{\text{b}} - \hat{\mathbf{p}}^{\text{t}} \end{bmatrix}, \quad (9.22)$$

which, considering that $\mathcal{S}_{yz} = 0$ and $\mathcal{S}_{xz} = 0$ from the Stokeslet's definition in Eq. 9.3, renders

$$\hat{\mathbf{u}}^{\text{p}}(\mathbf{x}_f^{\text{mp}}) = -\frac{1}{8\pi\mu_f} \int_{\Omega_p} \mathcal{S}_{zz} \, d\Omega \, \Delta \hat{\mathbf{p}}. \quad (9.23)$$

9.3 Integration of the Stokeslet

Eq. 9.23 is solved numerically by writing it as a matrix-vector product that relates the plate's displacement $\hat{\mathbf{w}}$ in the field points \mathbf{x}_f^{mp} with the pressure jump $\Delta\hat{\mathbf{p}}$ discretized in the partitioning $\mathcal{F}(\Omega_p)$. Eq. 9.23 is written using the plate's displacement $\hat{\mathbf{w}}$ as

$$\mathbf{j}\omega\hat{\mathbf{w}}(\mathbf{x}_f^{\text{mp}}) = \mathbf{A}_{3\text{D}}\Delta\hat{\mathbf{p}}. \quad (9.24)$$

The matrix elements $A_{3\text{D}ij}$ are given by

$$A_{3\text{D}ij} = -\frac{1}{8\pi\mu_f} \int_{S_j} \mathcal{S}_{zz}(\lambda, \mathbf{x}_{f_i}^{\text{mp}}, \mathbf{x}') dS_j(\mathbf{x}'), \quad (9.25)$$

where $\mathbf{x}_{f_i}^{\text{mp}}$ is the i -th point in the field fluid grid \mathbf{x}_f^{mp} , and S_j is the j -th element in the plate's partitioning $\mathcal{F}(\Omega_p)$ on which j -th element of $\Delta\hat{\mathbf{p}}$ acts. The i -th row of the $A_{3\text{D}}$ matrix is the integral of the Stokeslet \mathcal{S}_{zz} with a field position at $\mathbf{x}_{f_i}^{\text{mp}}$ over the entire plate's partitioning $\mathcal{F}(\Omega_p)$.

The geometric center of each surface element is denoted \mathbf{x}_s^{mp} . Note that the field points \mathbf{x}_f^{mp} and the center of the surface elements \mathbf{x}_s^{mp} must not necessarily be equal. However, a different number of elements in \mathbf{x}_f^{mp} and \mathbf{x}_s^{mp} leads to a non-square $A_{3\text{D}}$. Since later stages of the method require the determination of the inverse of $A_{3\text{D}}$, we opt for the most common strategy in which $\mathbf{x}_s^{\text{mp}} = \mathbf{x}_f^{\text{mp}}$ as represented in Fig. 9.6.

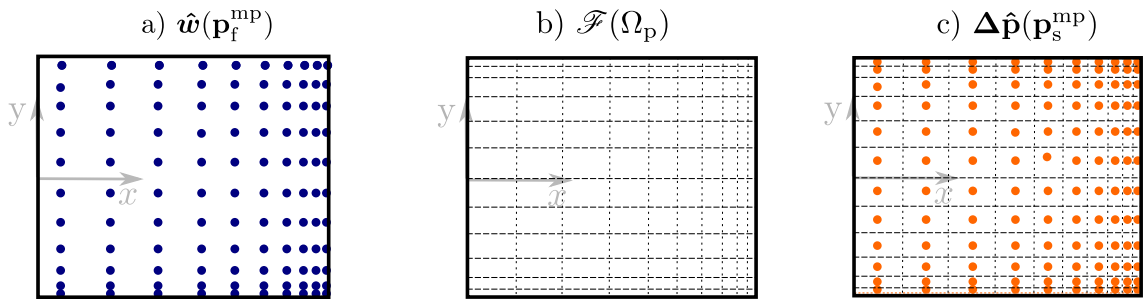


Figure 9.6: a) Plate's displacement $\hat{\mathbf{w}}$ discretized at the field points (\mathbf{x}_f^{mp}), b) partitioning of the plate's midplane domain $\mathcal{F}(\Omega_p)$ and c) pressure jump discretized at (\mathbf{x}_s^{mp}).

One of the challenges in using BEM/SBM is that the Stokeslet functions are singular. For instance, \mathcal{S}_{zz} is singular at $\mathbf{x}_{f_i}^{\text{mp}} = \mathbf{p}_{s_j}^{\text{mp}}$. This characteristic of the Stokeslet is so critical that it gave rise to a new set of methods called the regularized Stokeslets [103, 104]. In the regularized Stokeslet, the Stokeslet function is regularized by altering it with a "cutoff" function [103, 104], which effectively removes the singularity from the Stokeslet components. Here, given the fact that only the \mathcal{S}_{zz} component needs to be integrated over, we use the fact that there exists an analytic solution to the integral of \mathcal{S}_{zz} in a circular region of radius r_{analytic} as

$$I_{\text{analytic}} = \frac{(\lambda r_{\text{analytic}} + 1)e^{-\lambda r_{\text{analytic}}} - 1}{2\mu_f \lambda^2 r_{\text{analytic}}}. \quad (9.26)$$

Since we assume a continuous pressure jump $\Delta\hat{p}$ in each element of $\mathcal{F}(\Omega_p)$, we may use Eq. 9.26 to evaluate Eq. 9.25 when $\mathbf{x}_{f_i}^{\text{mp}} \in S_j$. The strategy we propose relies on the analytic integration around a circular region, and numerical integration using triangular elements between the circular region and a square with side $2r_{\text{analytic}}$ and rectangular elements to evaluate the integral in the remaining region in the element S_j as represented in Fig. 9.7.

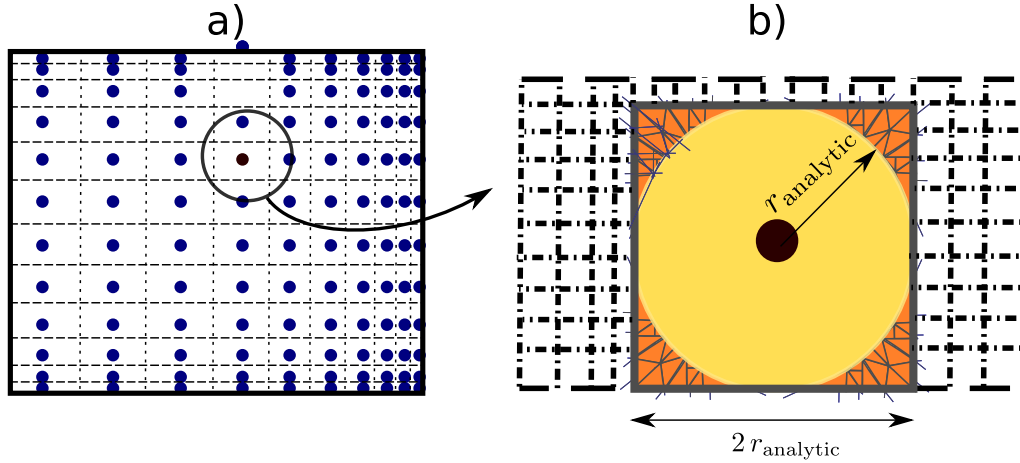


Figure 9.7: a) Plate's partitioning $\mathcal{F}(\Omega_p)$ and b) integration scheme around the singularity when $\mathbf{x}_{f_i}^{\text{mp}} \in S_j$. The yellow circular region corresponds to the analytic integration domain. In the orange region, numerical integration is performed with triangular elements, and in the remaining domain, rectangular elements are employed.

Hence, the ij element of the \mathbf{A}_{3D} matrix, when $\mathbf{x}_{f_i}^{\text{mp}} \in S_j$ is

$$A_{3Dij} = I_{\text{analytic}} + I_{\text{triangular}} + I_{\text{rectangular}}, \quad \mathbf{x}_{f_i}^{\text{mp}} \in S_j. \quad (9.27)$$

For the other surface elements, when $\mathbf{x}_{f_i}^{\text{mp}} \notin S_j$, Eq. 9.25 is evaluated using rectangular elements as

$$A_{3Dij} = I_{\text{rectangular}}, \quad \mathbf{x}_{f_i}^{\text{mp}} \notin S_j. \quad (9.28)$$

To evaluate Eqs. 9.27 and 9.28 efficiently, we use the numerical integration package Quadpy available in Python for both triangular and rectangular elements. Each element of $\mathcal{F}(\Omega_p)$ is refined until convergence of the element A_{3Dij} is achieved, that is, the relative difference between two iterations of A_{3Dij} is smaller than τ_{Szz} .

9.4 Hydrodynamic force due to different vibrational modes

To define a proper discretization scheme for the field points $\mathbf{x}_{f_i}^{\text{mp}}$ and the fluid partitioning $\mathcal{F}(\Omega_p)$, it is crucial to understand how $\Delta\hat{p}$ behaves for the different vibrational modes of a plate using the 3D fluid flow formulation. The pressure jump $\Delta\hat{p}$ is calculated as

$$\Delta\hat{p} = \mathbf{A}_{3D}^{-1} \mathbf{j} \omega \hat{\mathbf{w}}(\mathbf{x}_f^{\text{mp}}). \quad (9.29)$$

\mathbf{A}_{3D}^{-1} is the inverse of the \mathbf{A}_{3D} matrix.

Given that $\Delta\hat{p}$ is expected to exhibit a singularity at the plate's side edges at $y = \pm b/2$ as well as at the plate's free edge $x = l$, we use the Chebyshev-Gauss quadrature points both in x and y - direction [96, 95]. Hence, in y -direction, \mathcal{M}_y points are distributed over the plate's width as defined in Eq. 4.26. In x -direction, we use only the positive values of a Chebyshev-Gauss quadrature, that is

$$x_i = l \cos \left(\frac{2i - 1}{2\mathcal{M}_x} \pi + \frac{\pi}{2} \right), \quad (9.30)$$

where \mathcal{M}_x is the number of grid points in the x -direction and $i = 1 \dots \mathcal{M}_x$. The limits of integration $x_j^{(l)}$ are the mid-points between x_j for $j = 1 \dots \mathcal{M}_x - 1$, with the endpoints $x_0^{(l)} = 0$ and $x_{\mathcal{M}_x}^{(l)} = l$ as depicted in Fig. 9.8.

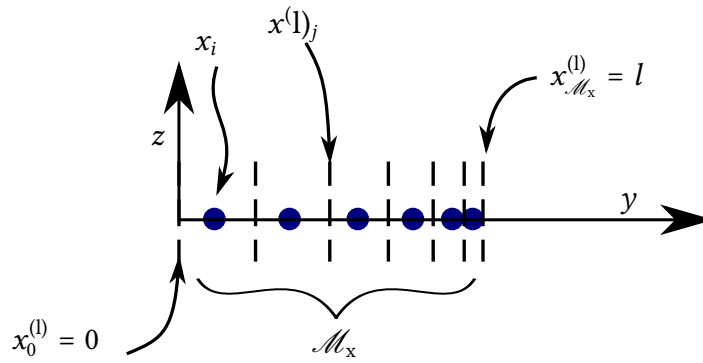


Figure 9.8: Quadrature points x_i (blue dots) and limiting points $x_j^{(l)}$ (dashed lines) in the Chebyshev-Gauss quadrature in x -direction.

The fluid flow around slender beams is expected to be predominantly two-dimensional [35, 64]. Hence, a slender beam is an ideal example to investigate the accuracy of the 3D fluid formulation here proposed. We consider a slender beam with $l = 1000 \mu\text{m}$, aspect ratio $r_a = 32$ and thickness $h = 5 \mu\text{m}$. As a fluid, air is used at SATP (properties given in Table 2.3). For this analysis, the fluid grid consists of $\mathcal{M}_x = 64$ and $\mathcal{M}_y = 32$ and $\tau_{Szz} = 10^{-3}$.

Fig.9.9a) and b) show the real part of the pressure jump $\mathcal{R}(\Delta\hat{p})$ with the 2D and 3D fluid formulation, respectively, for the mode 2:0 over the entire plate domain. Fig.9.9c shows $\mathcal{R}(\Delta\hat{p})$ at different cross-sections of the plate, at $x = 100 \mu\text{m}$, $x = 200 \mu\text{m}$, $x = 400 \mu\text{m}$, $x = 600 \mu\text{m}$, $x = 800 \mu\text{m}$ and $x = 900 \mu\text{m}$, where great agreement between 2D and 3D results is seen. For visualizing the plate's cross sections, see Fig. 9.10. Fig.9.9d shows $\mathcal{R}(\Delta\hat{p})$ at the plate's center line at $y = 0$ over x . Near the free edge of the beam at $x = l$ there is a small difference in $\mathcal{R}(\Delta\hat{p})$, which indicates the influence of the 3D fluid flow in this region. A similar agreement is obtained for the imaginary component of the pressure jump $\mathcal{I}(\Delta\hat{p})$.

For higher order EB modes, the influence of the 3D fluid flow is expected to increase [35], hence we investigate here how the pressure jump varies in the first five EB modes for this slender beam. Fig. 9.11 shows $\mathcal{R}(\Delta\hat{p})$ as a function of the position x at

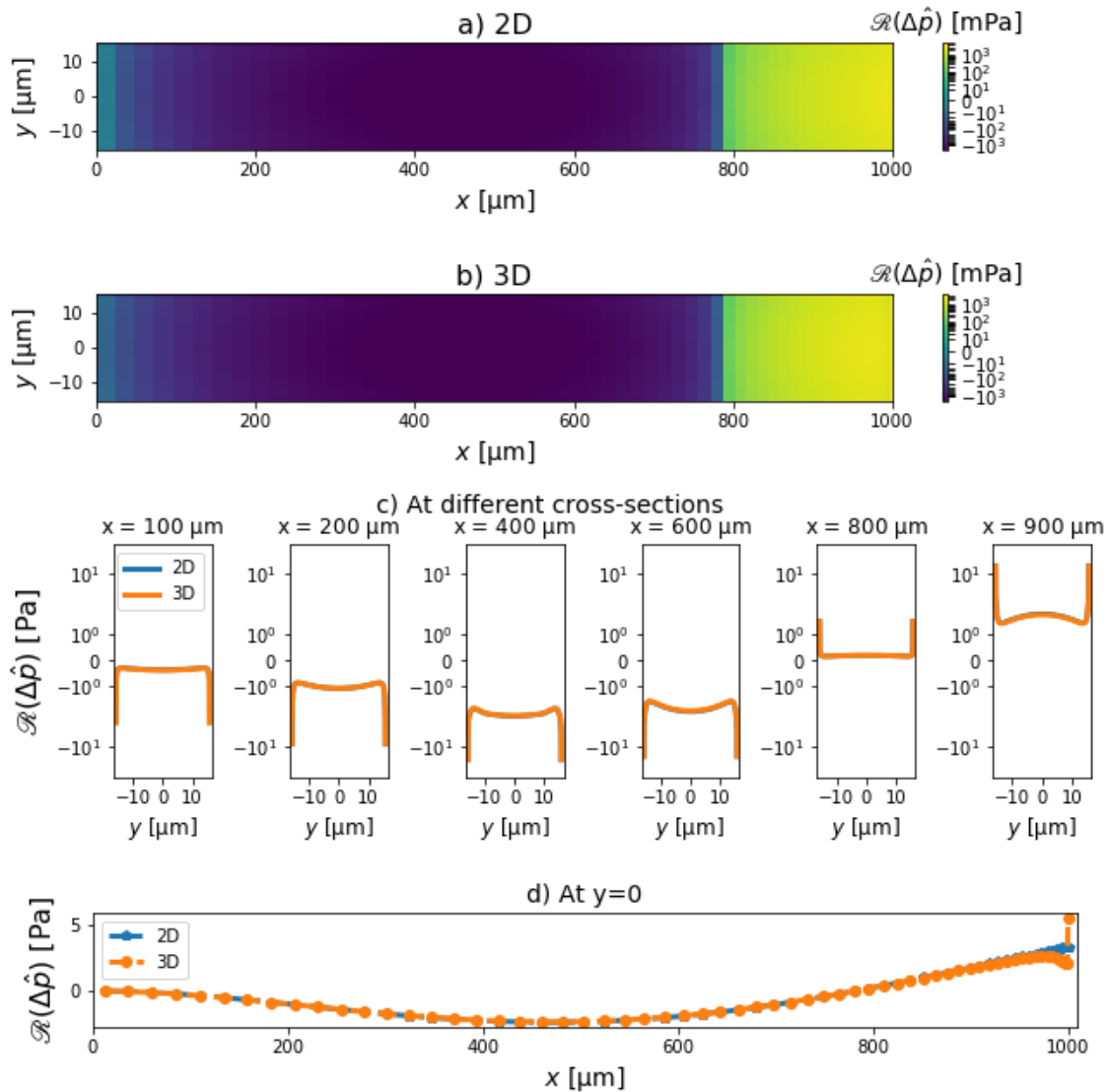


Figure 9.9: Real part of the pressure jump $\mathcal{R}(\Delta \hat{p})$ with the a) 2D and b) 3D fluid formulation, respectively, for the mode 2:0 in air. In c), $\mathcal{R}(\Delta \hat{p})$ at different cross-sections of the plate, at $x = 100 \mu\text{m}$, $x = 200 \mu\text{m}$, $x = 400 \mu\text{m}$, $x = 600 \mu\text{m}$, $x = 800 \mu\text{m}$ and $x = 900 \mu\text{m}$, in d) over the x coordinate at $y = 0$.

the center of the beam ($y = 0$) for the first to the fifth EB mode. 3D results agree well with 2D in a great extension of the plate. Near the plate's free edge, the pressure jump obtained with the 3D method exhibits a reduction in amplitude followed by a singularity for all EB modes at $x = l$. Such singularity, the 2D method is, of course, not able to predict.

For a wider plate, the influence of the 3D dimensional fluid flow is expected to increase [64]. For an initial investigation into the effect of the width on the pressure jump, we use once more the wide plate which was introduced in Section 3.4.3. Fig. 9.12 shows $\mathcal{R}(\Delta \hat{p})$ at $y = 0$ for the EB and 1:2 modes, and at $y = b/2$ for the torsional modes.

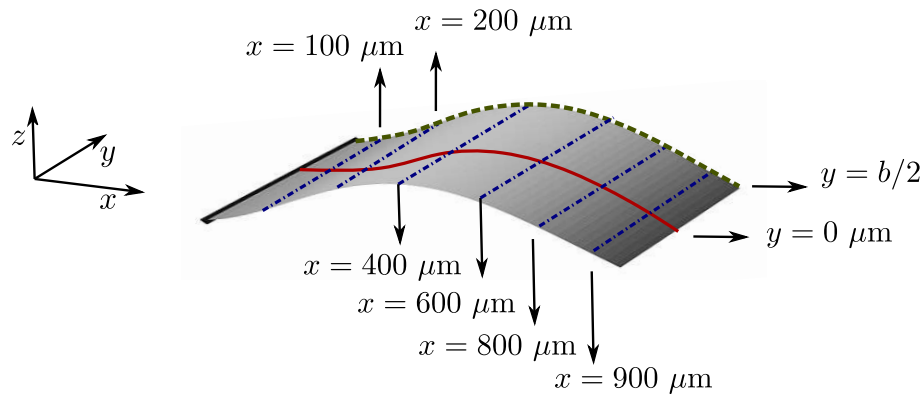


Figure 9.10: Cross-sections parallel to the y -direction are represented by a dashed blue line. Cross-sections parallel to the x -direction are represented by a red continuous line for the EB mode, and by a dashed green line for the torsional mode.

Differently than for the slender beam example, for the wide plate, $\mathcal{R}(\Delta\hat{p})$ exhibits a noticeable difference between the 2D and 3D formulations. The amplitude of $\mathcal{R}(\Delta\hat{p})$ is overestimated with the 2D method over the entire length of the plate, and these differences are even more significant for the EB modes than for other modes.

9.5 Conclusions

In this chapter a three-dimensional fluid flow formulation for the micro-plate-fluid structure interaction based on the free space Stokeslet was introduced. For the micro-plate-fluid problem, the single-layer formulation suffices and the double-layer term may be ignored. With the SBM, the \mathcal{S}_{zz} component of the Stokeslet suffices for determining the hydrodynamic force $\Delta\hat{p}$ acting on the micro-plate, which further simplifies the problem. To account for the singularities in all free edges of the plate, the Chebyshev-Gauss quadrature was implemented in both x and y directions. An example with a slender beam showed great agreement between 2D and 3D formulations over a great extension of the beam, which provides confidence in the implementation of the new method. Furthermore, an initial investigation with a wide plate example revealed great differences between 2D and 3D results.

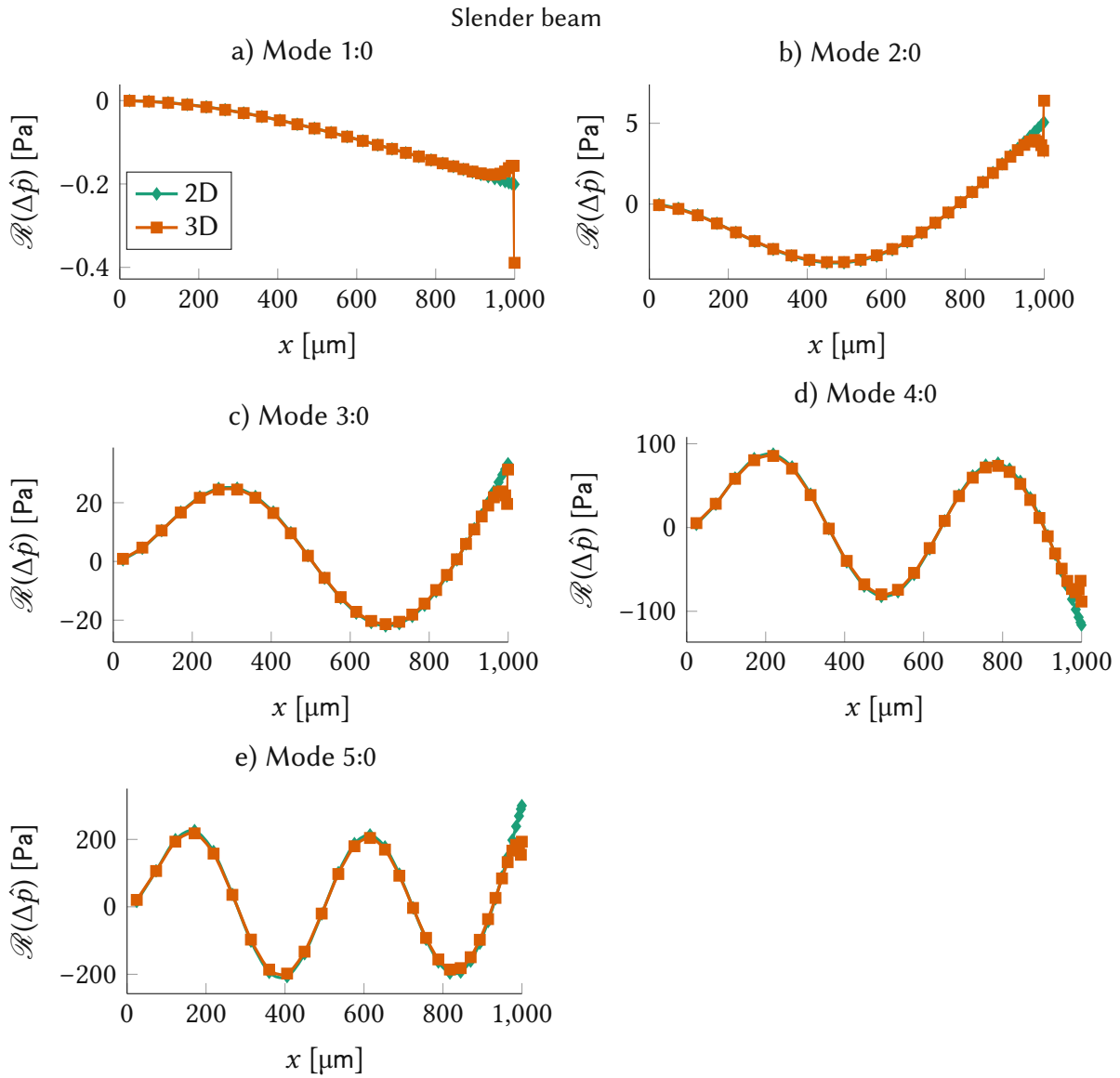


Figure 9.11: Real part of the pressure jump $\mathcal{R}(\Delta\hat{p})$ with the 2D and 3D fluid formulation for a slender beam in air.

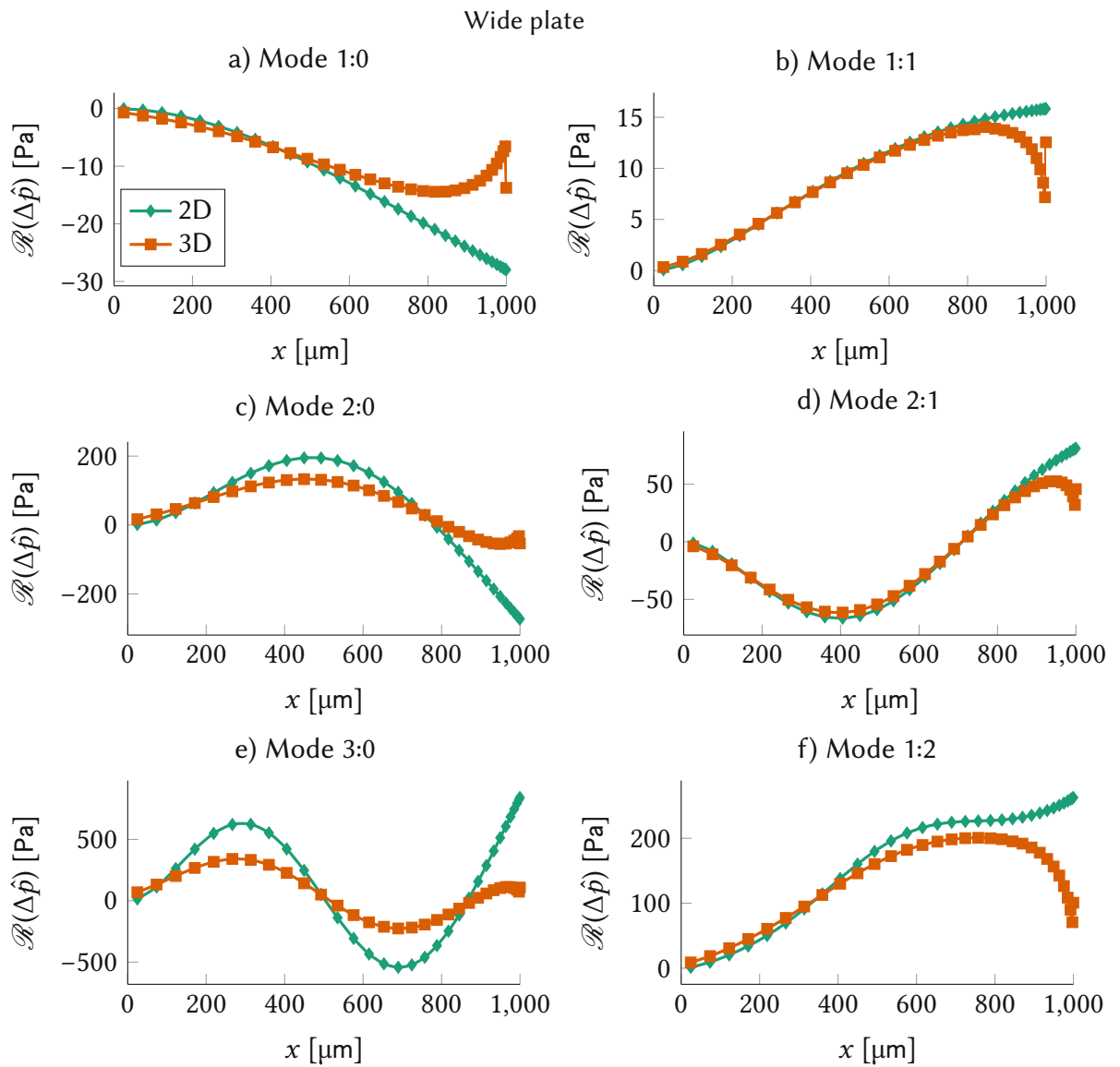


Figure 9.12: Real part of the pressure jump $\mathcal{R}(\Delta\hat{p})$ with the 2D and 3D fluid formulation for a wide plate in air.

10 A semi-numerical method for micro-plates in viscous fluids considering a three-dimensional fluid flow

The governing equation for the micro-plate-fluid interaction problem is

$$\frac{h^3}{12} C_{\alpha\beta\gamma\delta} \hat{w}_{,\alpha\beta\gamma\delta} - \omega^2 \rho_p h \hat{w} = \hat{F} + \Delta \hat{p}, \quad (10.1)$$

whose weak form is: find \hat{w}^h in \mathcal{W}^h such that

$$\begin{aligned} \int_{\Omega_p} \frac{h^3}{12} C_{\alpha\beta\gamma\delta} \hat{w}_{,\alpha\beta}^h v_{,\gamma\delta}^h d\Omega - \int_{\Gamma} \frac{h^3}{12} \{C_{\alpha\beta\gamma\delta} \hat{w}_{,\alpha\beta}^h\} \llbracket v_{,\delta}^h n_\gamma^e \rrbracket ds - \int_{\Gamma} \frac{h^3}{12} \llbracket C_{\alpha\beta\gamma\delta} \hat{w}_{,\alpha\beta}^h \rrbracket \{[v_{,\delta}^h n_\gamma^e]\} ds \\ + \int_{\Gamma} \frac{h^3}{12} \frac{\tau_{ip}}{h_E} C_{\alpha\beta\gamma\delta} \llbracket \hat{w}_{,\alpha}^h n_\beta \rrbracket \llbracket v_{,\gamma}^h n_\delta \rrbracket ds + \int_{\Gamma_c} \frac{h^3}{12} \frac{\tau_{ip}}{2h_E} C_{\alpha\beta\gamma\delta} \hat{w}_{,\alpha}^h n_\beta v_{,\gamma}^h n_\delta ds \\ - \int_{\Gamma_c} \frac{h^3}{12} C_{\alpha\beta\gamma\delta} \hat{w}_{,\alpha\beta}^h v_{,\delta}^h n_\gamma^b ds - \int_{\Omega_p} \omega^2 \rho_p h \hat{w}^h v^h d\Omega \\ = \int_{\Omega_p} \hat{F} v^h d\Omega + \int_{\Omega_p} \Delta \hat{p} v^h d\Omega, \quad \forall v^h \in \mathcal{V}^h \end{aligned} \quad (10.2)$$

Eq. 10.2 is similar to the weak form of the 2D fluid flow formulation (Eq. 5.3) with the difference that, here, $\Delta \hat{p}$ is determined using the free-space 3D Stokeslet formulation introduced in Chapter 9. Hence, a different numerical quadrature is here required to evaluate $\int_{\Omega_p} \Delta \hat{p} v^h d\Omega$.

10.1 Numerical integration of the hydrodynamic force

Using the Chebyshev-Gauss quadrature in y -direction as well as in the x -direction, the domain integral of the pressure jump is given by

$$F_{\text{resultant}} = \int_{\Omega_p} \Delta \hat{p}(x^c, y) d\Omega = \sum_{i=1}^{\mathcal{M}_x} \frac{\pi}{2\mathcal{M}_x} \sqrt{l^2 - x_i^2} \sum_{j=1}^{\mathcal{M}_y} \frac{\pi}{\mathcal{M}_y} \Delta \hat{p}(x_i, y_j) \sqrt{(b/2)^2 - y_j^2}. \quad (10.3)$$

$F_{\text{resultant}}$ must converge as the number of grid points \mathcal{M}_y and \mathcal{M}_x increase. The convergence with the fluid grid is quantified with $\epsilon_{\text{resultant}}$ as defined in Eq. 4.34.

Fig. 10.1 shows $\epsilon_{\text{resultant}}$ for the lowest three vibrational modes of the wide plate in the air as shown in Section 9.4. Different combinations of the number of points in x and y directions are here investigated, those are $\mathcal{M}_y = \mathcal{M}_x$, $\mathcal{M}_y = 2\mathcal{M}_x$ and $\mathcal{M}_y = 4\mathcal{M}_x$ and $\mathcal{M}_y = 8\mathcal{M}_x$. For the three modes, the fluid grid with $\mathcal{M}_y = \mathcal{M}_x$ fails to provide a convergent $F_{\text{resultant}}$ up to $\mathcal{M}_x = 64$. $F_{\text{resultant}}$ obtained with the $\mathcal{M}_y = 2\mathcal{M}_x$, $\mathcal{M}_y = 4\mathcal{M}_x$ and $\mathcal{M}_y = 8\mathcal{M}_x$ fluid grids converge to similar values. What is more, the $\mathcal{M}_y = 4\mathcal{M}_x$ and $\mathcal{M}_y = 8\mathcal{M}_x$ grids required only $\mathcal{M}_x = 32$ to exhibit $\epsilon_{\text{resultant}} \leq 0.01$, which is a threshold value used throughout this thesis for a quantity to be considered converged.

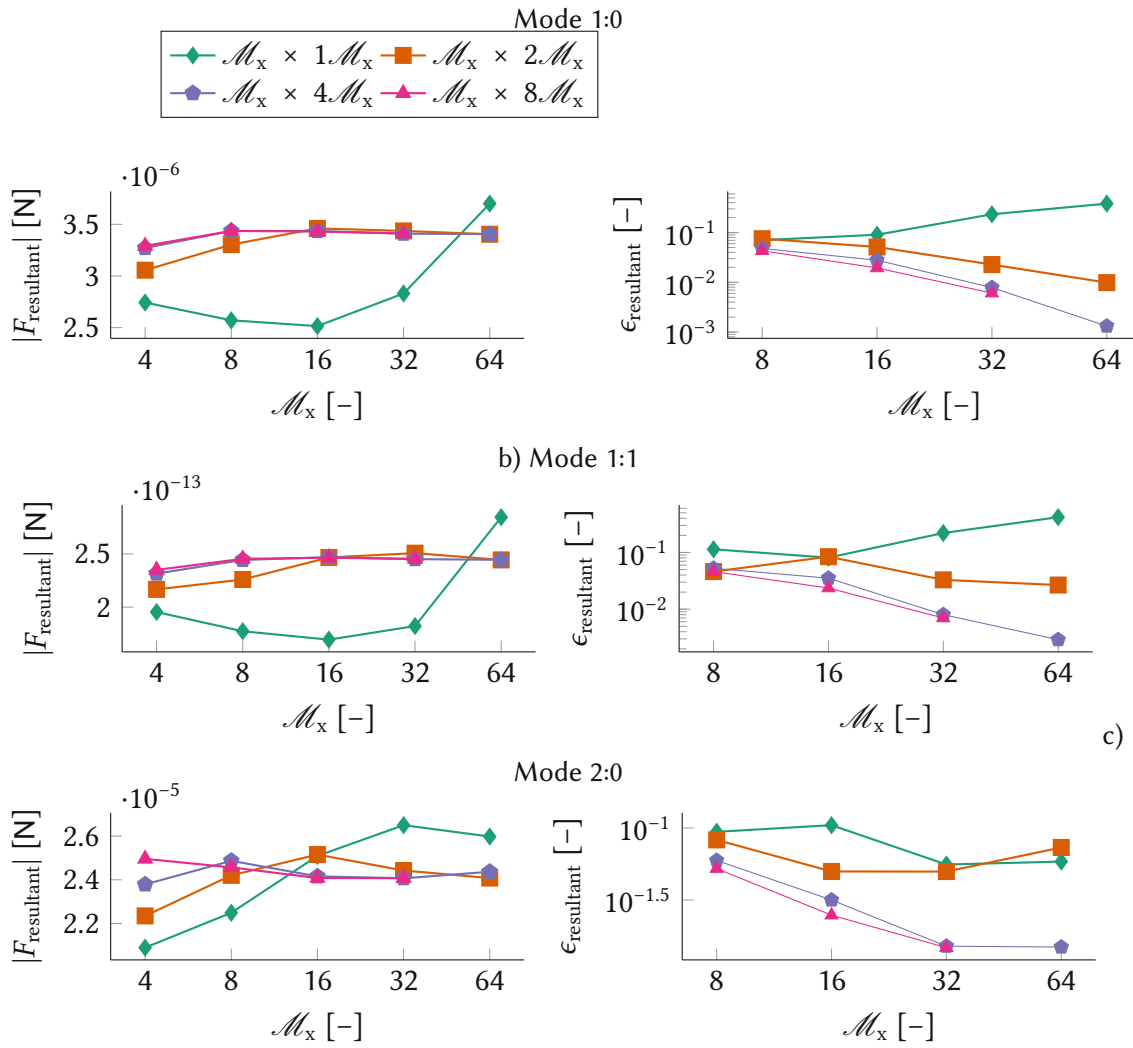


Figure 10.1: Resultant force $|F_{\text{resultant}}|$ and convergence error $\epsilon_{\text{resultant}}$ for the a) 1:0, b) 1:1 and c) 2:0 mode.

The projection of $\Delta \hat{p}$ to the basis functions v^h is obtained by applying the Chebyshev-Gauss quadrature in the y -direction and x -direction, yielding

$$\int_{\Omega_p} \Delta \hat{p}(x, y) v^h d\Omega = j\omega \frac{\pi}{M_y} \frac{\pi}{2 \cdot M_x} \sum_{i=1}^{M_x} \sum_{j=1}^{M_y} A_{3Dij}^{-1} \hat{w}^h(x_i, y_j) v^h(x_j, y_j) \sqrt{(b/2)^2 - y_j^2} \sqrt{l^2 - x_i^2}, \forall v^h \in \mathcal{V}^h. \quad (10.4)$$

(x_i, y_i) and (x_j, y_j) are two points in the fluid grid $\mathcal{F}(\Omega_p)$ with coordinates given in Eqs. 9.30 and 4.26. With the 3D formulation, the points (x_i, y_i) and (x_j, y_j) in different cross-sections (different coordinates x) influence each other, which is also reflected in the inverse of the matrix \mathbf{A}^{3D} .

With the projection of $\Delta \hat{p}(x, y)$ into \mathcal{V}^h as given in Eq. 10.4, the equation of motion of the plate in a viscous fluid with the 3D fluid formulation is written as: find \hat{w}^h in \mathcal{W}^h such that

$$\begin{aligned} \int_{\Omega_p} \frac{h^3}{12} C_{\alpha\beta\gamma\delta} \hat{w}_{,\alpha\beta}^h v_{,\gamma\delta}^h d\Omega - \int_{\Gamma} \frac{h^3}{12} \{C_{\alpha\beta\gamma\delta} \hat{w}_{,\alpha\beta}^h\} \llbracket v_{,\delta}^h n_\gamma^e \rrbracket ds - \int_{\Gamma} \frac{h^3}{12} \llbracket C_{\alpha\beta\gamma\delta} \hat{w}_{,\alpha\beta}^h \rrbracket \{v_{,\delta}^h n_\gamma^e\} ds \\ + \int_{\Gamma} \frac{h^3}{12} \frac{\tau_{ip}}{h_E} C_{\alpha\beta\gamma\delta} \llbracket \hat{w}_{,\alpha}^h n_\beta \rrbracket \llbracket v_{,\gamma}^h n_\delta \rrbracket ds + \int_{\Gamma_c} \frac{h^3}{12} \frac{\tau_{ip}}{2h_E} C_{\alpha\beta\gamma\delta} \hat{w}_{,\alpha}^h n_\beta v_{,\gamma}^h n_\delta ds \\ - \int_{\Gamma_c} \frac{h^3}{12} C_{\alpha\beta\gamma\delta} \hat{w}_{,\alpha\beta}^h v_{,\delta}^h n_\gamma^b ds - \int_{\Omega_p} \omega^2 \rho_p h \hat{w}^h v^h d\Omega \\ - j\omega \frac{\pi}{\mathcal{M}_y} \frac{\pi}{2\mathcal{M}_x} \sum_{i=1}^{\mathcal{M}_x} \sum_{j=1}^{\mathcal{M}_y} A_{3Dij}^{-1} \hat{w}^h(x_i, y_j) v^h(x_j, y_j) \sqrt{(b/2)^2 - y_j^2} \sqrt{l^2 - x_i^2} \\ = \int_{\Omega_p} \hat{F} v^h d\Omega, \forall v^h \in \mathcal{V}^h \end{aligned} \quad (10.5)$$

Therefore, the proposed method is resumed to a single equation to determine the plate dynamics accounting for the viscous forces of an incompressible fluid in an unbounded domain around a micro-plate undergoing purely out-of-plane displacement. The elements A_{ij}^{-1} of the inverse of the A^{3D} matrix are obtained from Eq. 4.19 using the Chebyshev-Gauss quadrature scheme.

10.2 Convergence

The proposed method must be convergent with the number of elements of the FE-mesh (represented by N_x) as well as with the fluid grid discretization (represented by \mathcal{M}_x). Here, the convergence of the method is analyzed in air and water at SATP as representing fluids for gases and liquids. For the convergence analysis, we consider once again the wide plate with $l = 1000 \mu\text{m}$ and $b = 500 \mu\text{m}$. The plate has thickness $h = 5 \mu\text{m}$ and is comprised of silicon with anisotropic properties.

10.2.1 Convergence with the FE-mesh

The finite element mesh consists of N_x elements in x -direction and, in y -direction $N_y = N_x r_a$. The convergence is analyzed with $\epsilon_{\text{convergence}}$ as defined in Eq. 3.29 between consecutively refined FE-meshes. The fluid grid is the same in all simulations with 32×128 points, which follows a ratio of 4 points in the y -direction for each point in the x -direction.

Fig. 10.2 shows $\epsilon_{\text{convergence}}$ at 10 kHz, 100 kHz and 1000 kHz with the number of FE-mesh elements in x -direction N_x in air and in water. In air, at 10 kHz, the proposed method converges with a convergence rate equal to 1.8 for an FE-mesh discretized up to $N_x = 64$ elements. For $N_x > 64$, solution \hat{w} diverges due to the IP-method. At 100 kHz and 1 MHz, the method converges with a rate equal to 1.8 as well. The convergence rate

of the proposed method is at all frequencies equal to 1.8 in air, which is exactly the same as the convergence rate of the proposed method with the 2D fluid flow formulation in air (Fig. 5.2).

In water, at 10 kHz and 100 kHz, a convergence rate of 1.7 is obtained, and at 100 kHz the convergence rate is equal to 2. At 1 MHz, $\epsilon_{\text{convergence}}$ initially increases and then decreases for $N_x \geq 32$, the convergence rate considering only the FE-meshes $N_x \geq 32$ is 1.4. From the convergence results shown in this section, we show that the proposed method is convergent in a gas (air) and in a liquid (water) with a minimum convergence rate of 1.4. The only exception is, once again, the low frequency (10 kHz) in air with a very fine mesh ($N_x \geq 64$), for which case the method diverges due to the IP method.

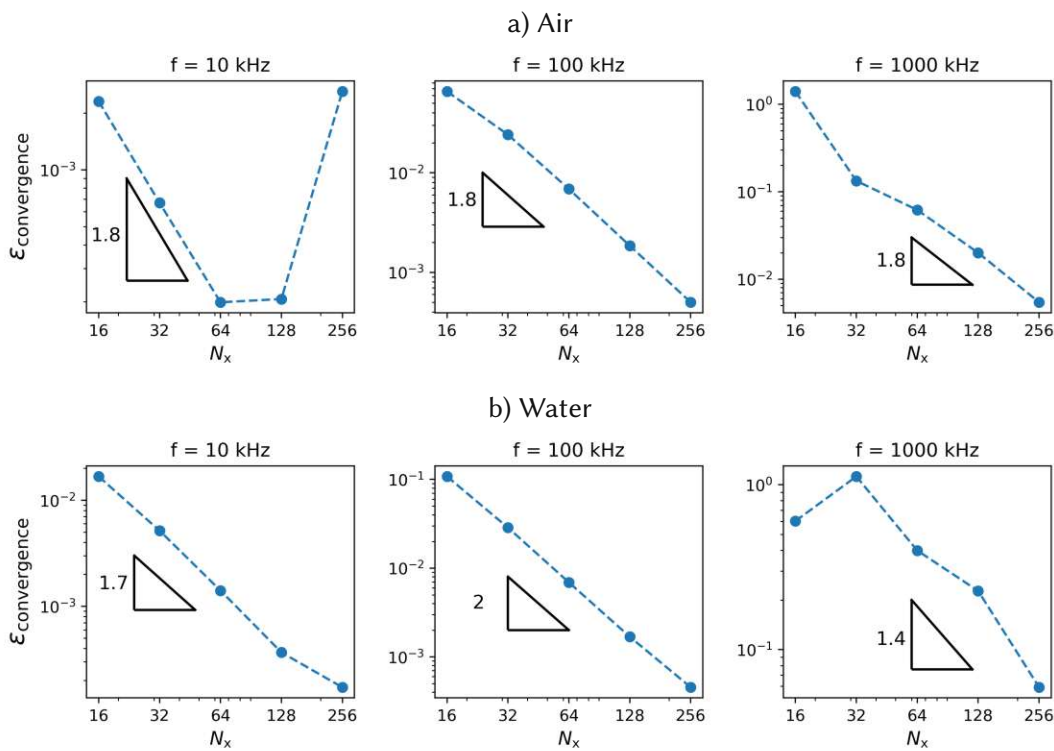


Figure 10.2: a) In air, and b) in water, convergence as a function of the number of elements N_x in the FE-mesh of the plate with $r_a = 1/2$ at 10 kHz, 100 kHz and 1 MHz.

10.2.2 Convergence with the fluid grid

To investigate the method's convergence with the fluid grid, we resort once again to ϵ_{fg} as defined in Eq. 5.6. The FE-mesh is constant with 64×32 elements, and the fluid grid follows a pattern of $\mathcal{M}_y = 4 \cdot \mathcal{M}_x$.

Fig. 10.3 shows ϵ_{fg} at 10 kHz, 100 kHz and 1000 kHz with the number of fluid grid points in x -direction \mathcal{M}_x in air and in water. In air, at all frequencies, the method converges, and the convergence rate varies between 1.5 and 1.7. In water, at low frequencies ϵ_{fg} exhibits convergence with a convergence rate between 1.9 and 2. At the high

frequency of 1000 kHz, ϵ_{fg} initially diverges ($\mathcal{M}_x < 16$), and once a fine enough fluid grid is used ($\mathcal{M}_x > 16$), ϵ_{fg} converges with a convergence rate equals 2.

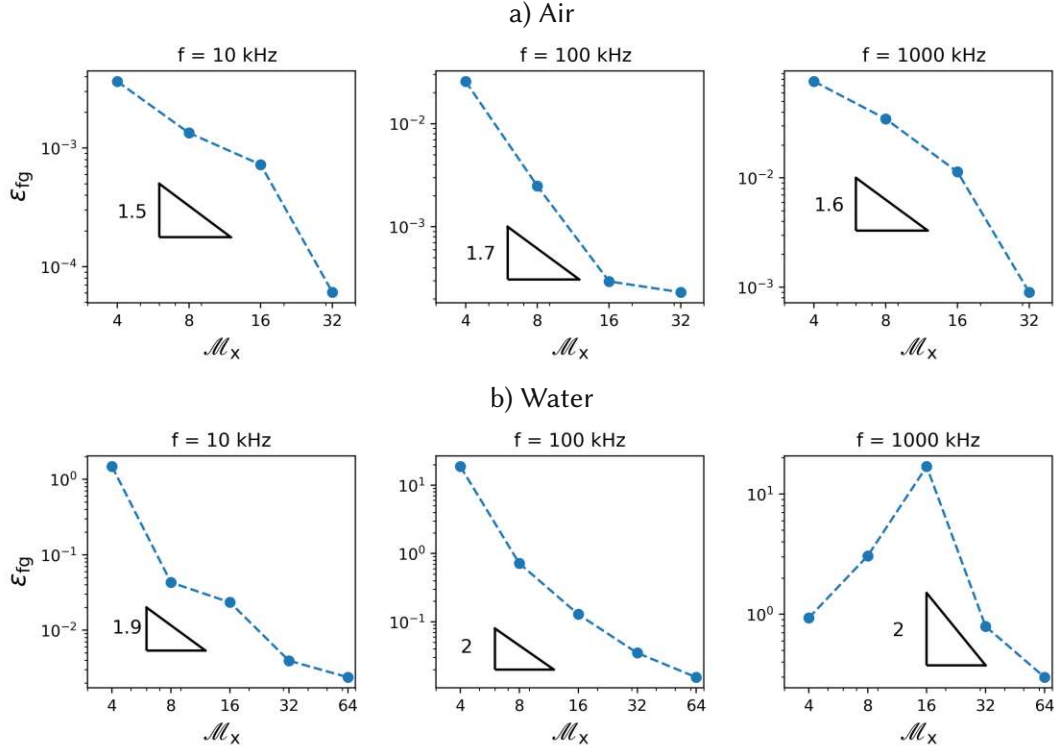


Figure 10.3: Convergence as a function of the number of points \mathcal{M}_x in the fluid grid of the plate with $r_a = 1/2$ at 10 kHz, 100 kHz and 1 MHz in a) air and b) water.

In addition to convergence with the fluid grid and with the FE-mesh, the influence of the tolerance τ_{Szz} in the calculated displacement is also investigated. τ_{Szz} is the tolerance with which, each element of $\mathcal{F}(\Omega_p)$ is refined until convergence of the matrix element $A_{3D_{ij}}$ is achieved, that is, the relative difference between two iterations of $A_{3D_{ij}}$ must be smaller than τ_{Szz} . Note that, in the 2D method, this was not required, since the integral of the fundamental solution in each element was determined analytically. This analysis is shown in C, where we conclude that selecting a very small value of τ_{Szz} can make the simulation time prohibitively long. Therefore, we define $\tau_{Szz} = 10^{-3}$ to be used through the next analysis, as it provides $\epsilon_{\tau_{Szz}} \leq 0.01$ (see Eq. C.1) while maintaining a relatively low computing time.

10.3 Validation

For slender beams, 3D fluid effects are expected to be small [19, 35]. Hence, for validation of the 3D fluid flow method, we resort once again to the key semi-analytic method proposed by Sader [31], as well as the 2D fluid flow method proposed in this study. For this comparison, consider a slender beam with width equals $b = 15 \mu\text{m}$, $l = 800 \mu\text{m}$ and $h = 5 \mu\text{m}$ as shown in Fig. 10.4.

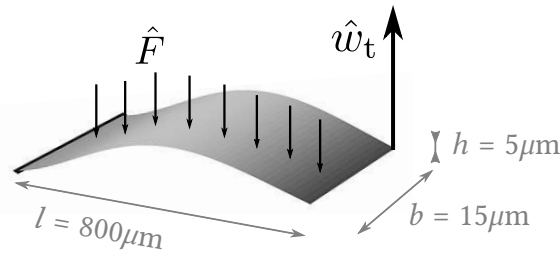


Figure 10.4: Dimensions of a cantilevered plate used in the validation analysis. The plate is excited by a uniform distributed force \hat{F} .

10.3.1 Spectral displacement

Fig. 10.5 shows the absolute displacement spectrum \hat{w}_t of the slender beam in water obtained with the present 3D formulation as well as the 2D formulation and Sader's method. In both 2D and 3D formulation, the FE-mesh consists of 64×4 elements and the fluid grid of 32×128 points. In the 3D formulation, $\tau_{Szz} = 10^{-3}$. Excellent agreement (maximum difference smaller than 1 %) is found in the spectral displacement \hat{w}_t in the 500 kHz frequency range between the three formulations.

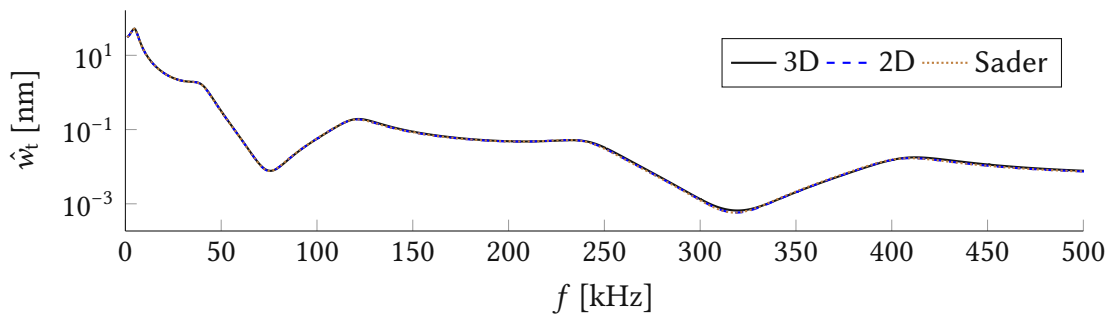


Figure 10.5: Displacement spectrum of the slender beam with $b = 15\mu\text{m}$ in water.

10.3.2 Q-factor and damped resonance frequency

The spectrum displacement \hat{w}_t (and by consequence, Q and f_d) vary with the fluid grid discretization for each mode. Fig. 10.6 shows the spectrum displacement \hat{w}_t , the Q-factor and f_d for the lowest five vibrational modes as a function of the fluid grid. Hence, a convergence analysis is necessary to determine whether Q and f_d converge with the fluid grid.

Fig. 10.7a) shows the convergence of f_d evaluated with ϵ_f as defined in Eq. 5.13 for the five vibrational modes which occur in the 500 kHz frequency range in water. For the modes 1:0 and 2:0, a fluid grid with 8×32 points already provides a converged f_d with $\epsilon_f \leq 0.01$. The 3:0 and 4:0 modes require a fluid grid of at least 16×64 points, while the 5:0 mode converges only for a fluid grid of 32×128 points.

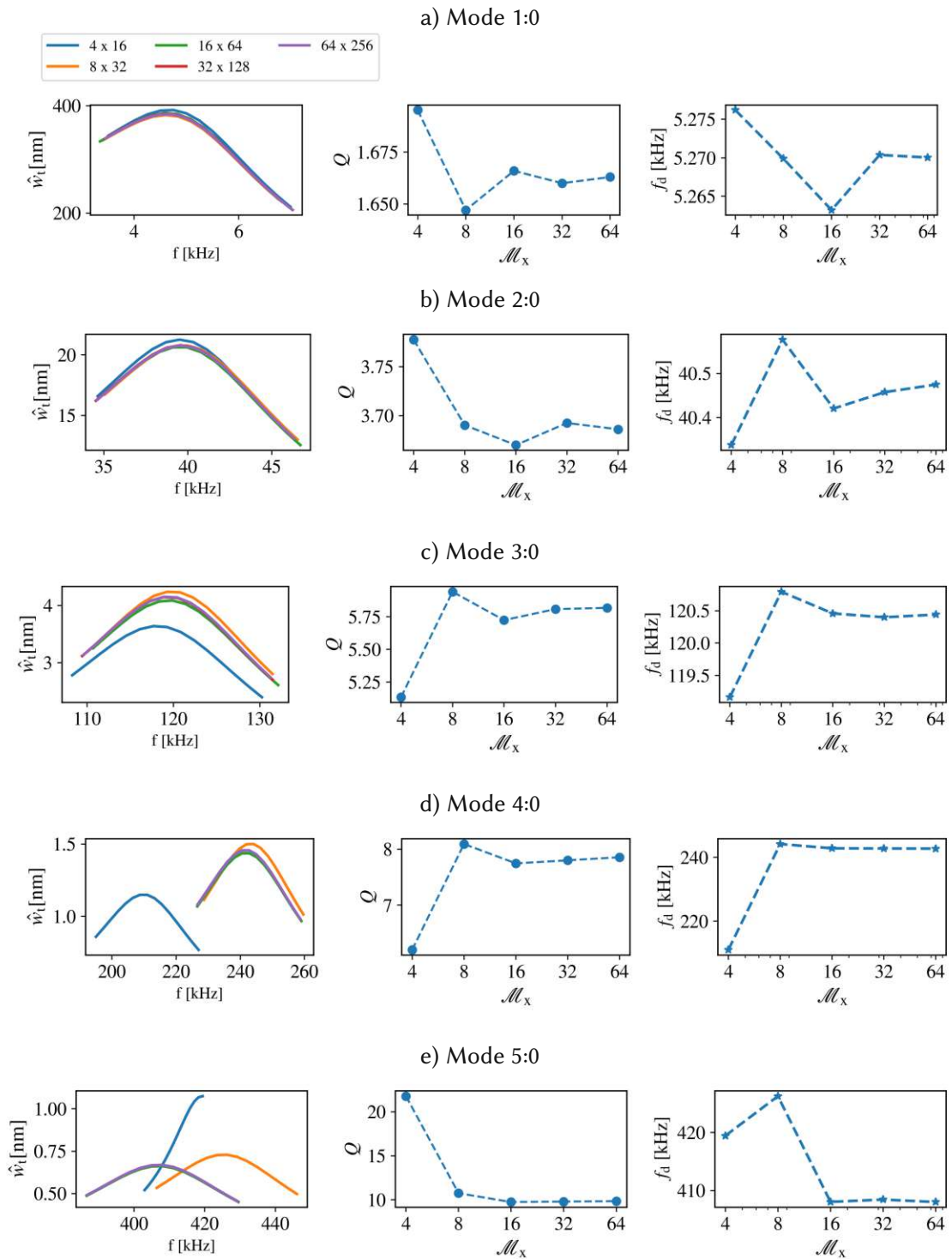


Figure 10.6: Spectrum displacement \hat{w}_t , Q-factor and f_d for the a) 1:0, b) 2:0, c) 3:0, d) 4:0 and e) 5:0 vibrational modes as a function of the fluid grid in water.

In Fig. 10.7b), the convergence of Q evaluated with ϵ_q is shown. For all modes, Q requires a finer fluid grid for convergence with $\epsilon_q \leq 0.01$ to be achieved. For instance,

modes 1:0 and 2:0 require a fluid grid of 16×64 , whereas modes 3:0, 4:0 and 5:0 required fluid grids with 64×256 points for a converged Q-factor.

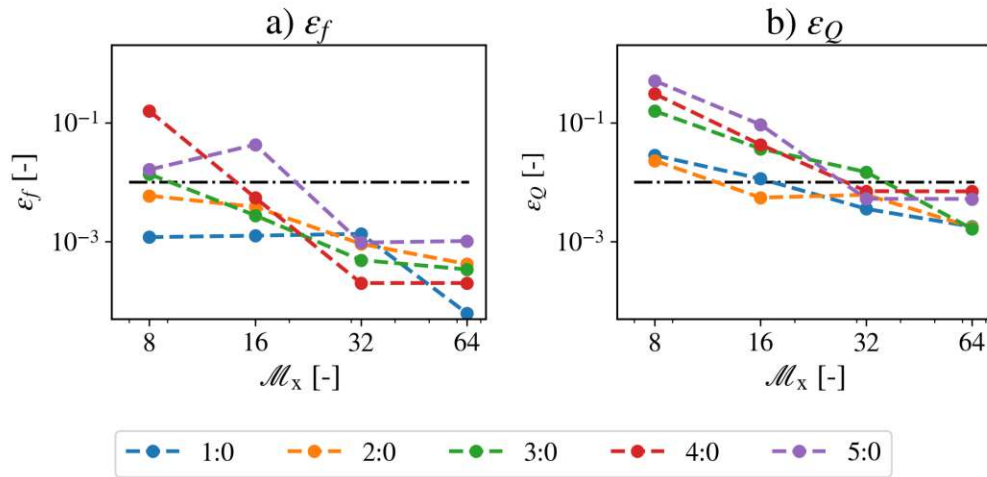


Figure 10.7: Convergence of the a) damped resonance frequency and b) Q-factor of the slender beam in water.

Fig. 10.8 shows the converged quality factors of the EB modes in water obtained with the 3D fluid formulation, the 2D fluid formulation and Sader's method [31]. The three methods exhibit a remarkable agreement, thus providing an important validation of the 3D fluid formulation in this chapter introduced.

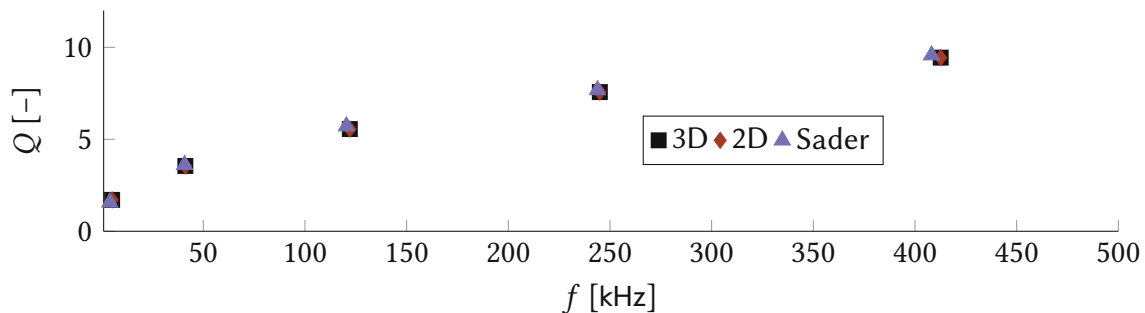


Figure 10.8: Quality factor of the vibrational modes of the slender beam in water obtained with the 3D fluid formulation, the 2D fluid formulation and Sader's method.

10.4 Conclusions

In this chapter, the semi-numerical method for determining the dynamics of micro-plates immersed in incompressible viscous fluids with a three-dimensional fluid flow formulation was defined. The proposed method converges at all frequencies tested in water and in air both with the fluid grid and with the FE-mesh. What is more, for a

slender beam in water, the proposed method exhibits excellent agreement with Sader's method and with the 2D fluid flow formulation introduced in the previous chapters, both for the spectral displacement as well as for the Q-factor.

11 On the limits between two-dimensional and three-dimensional fluid flow

With both 2D and 3D fluid flow formulations defined and validated, it becomes possible to investigate the limit of the two-dimensional fluid flow approximation around micro-plates.

To determine the limit of the 2D fluid flow, we investigate the dynamics of structures ranging from a slender beam to a wide plate. That is, the plate's dimensions are $l = 800 \mu\text{m}$, $h = 5 \mu\text{m}$, and the widths span from $b = 15 \mu\text{m}$ to $b = 400 \mu\text{m}$ as depicted in Fig. 11.1.



Figure 11.1: Example of plates with different widths a) $b = 15 \mu\text{m}$, b) $b = 100 \mu\text{m}$, c) $b = 200 \mu\text{m}$ and d) $b = 400 \mu\text{m}$ here investigated.

11.1 Spectral displacement and damped resonance frequency in water

We focus on the influence of the three-dimensional flow on the damped resonance frequency f_d in the beam-plate transition. Since f_d in the air is not hugely impacted by the flow, this analysis considers only water as the fluid. In order to more easily identify and visualize the difference in the plate's displacement with the 2D and 3D formulation, the plate is considered either under actuation of a symmetric or an anti-symmetric force as shown in Fig. 11.2.

Initially, we investigate the spectral displacement as the plate varies from a slender beam to a wide plate in the 1 MHz frequency range. Fig. 11.3 shows the absolute displacement spectrum \hat{w}_t of the micro-plates with $b = 25 \mu\text{m}$, $b = 50 \mu\text{m}$, $b = 100 \mu\text{m}$ and $b = 200 \mu\text{m}$ due to the symmetric excitation. The arrows indicate the increase in the damped resonance frequency f_d from the 2D to the 3D formulation for the same vibrational modes. For the slender beam, both formulations render essentially equal results.

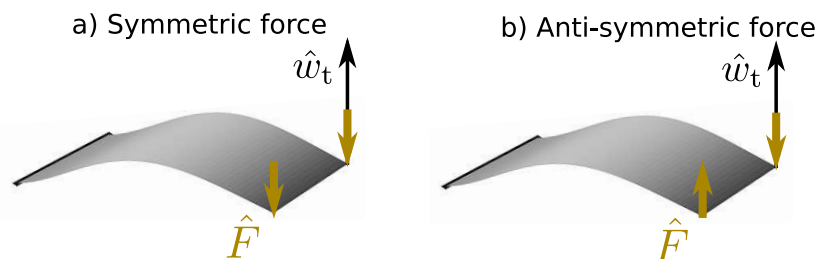


Figure 11.2: Symmetric and anti-symmetric forces applied at the plate's free corners.

As the plate's width increases, so increases the influence of the three-dimensional flow, as clearly seen with the help of the arrows in Figs. 11.3b and 11.3c. For the wide plate with $b = 200 \mu\text{m}$ in Fig 11.3d, the differences in \hat{w}_t between 2D and 3D formulations are so significant that a simple indication in the plate's spectrum to indicate the same vibrational mode would render the graph confusing.

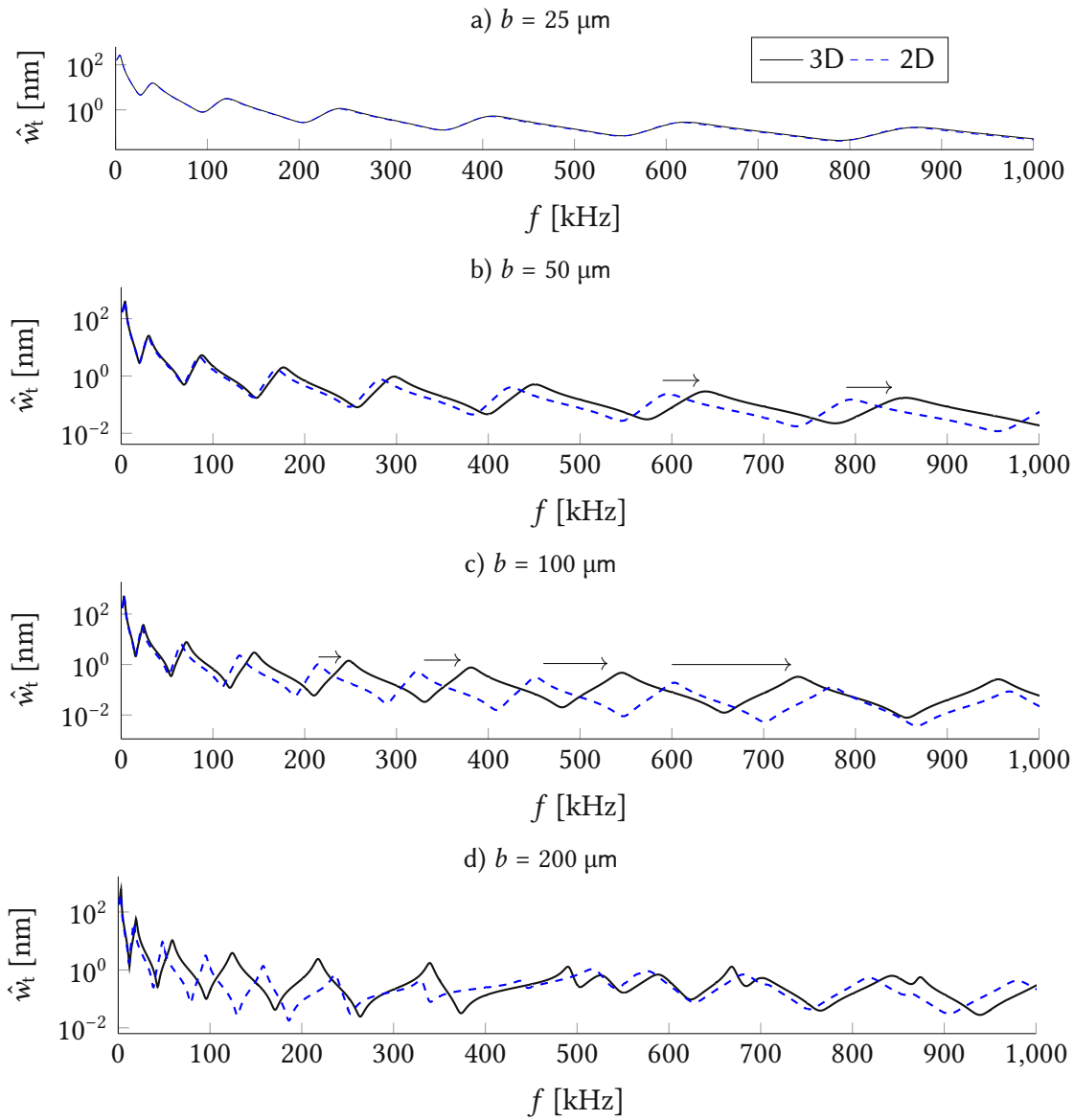


Figure 11.3: Displacement spectrum of the slender beam with a) $b = 15 \mu\text{m}$, b) $b = 50 \mu\text{m}$, c) $b = 100 \mu\text{m}$ and d) $b = 200 \mu\text{m}$ in water under symmetric excitation. The arrows indicate the increase in the damped resonance frequency f_d from the 2D to the 3D formulation for the same vibrational modes.

In Fig. 11.3, only symmetric vibrational modes appear due to the symmetric excitation. Fig. 11.4 shows the absolute displacement spectrum \hat{w}_t due to an anti-symmetric excitation. For the anti-symmetric modes (here all maxima correspond to torsional

modes), the influence of the three-dimensional fluid flow seems much smaller. Thus, the torsional modes are better represented by a 2D fluid flow than EB modes, at least in terms of damped resonance frequency f_d .

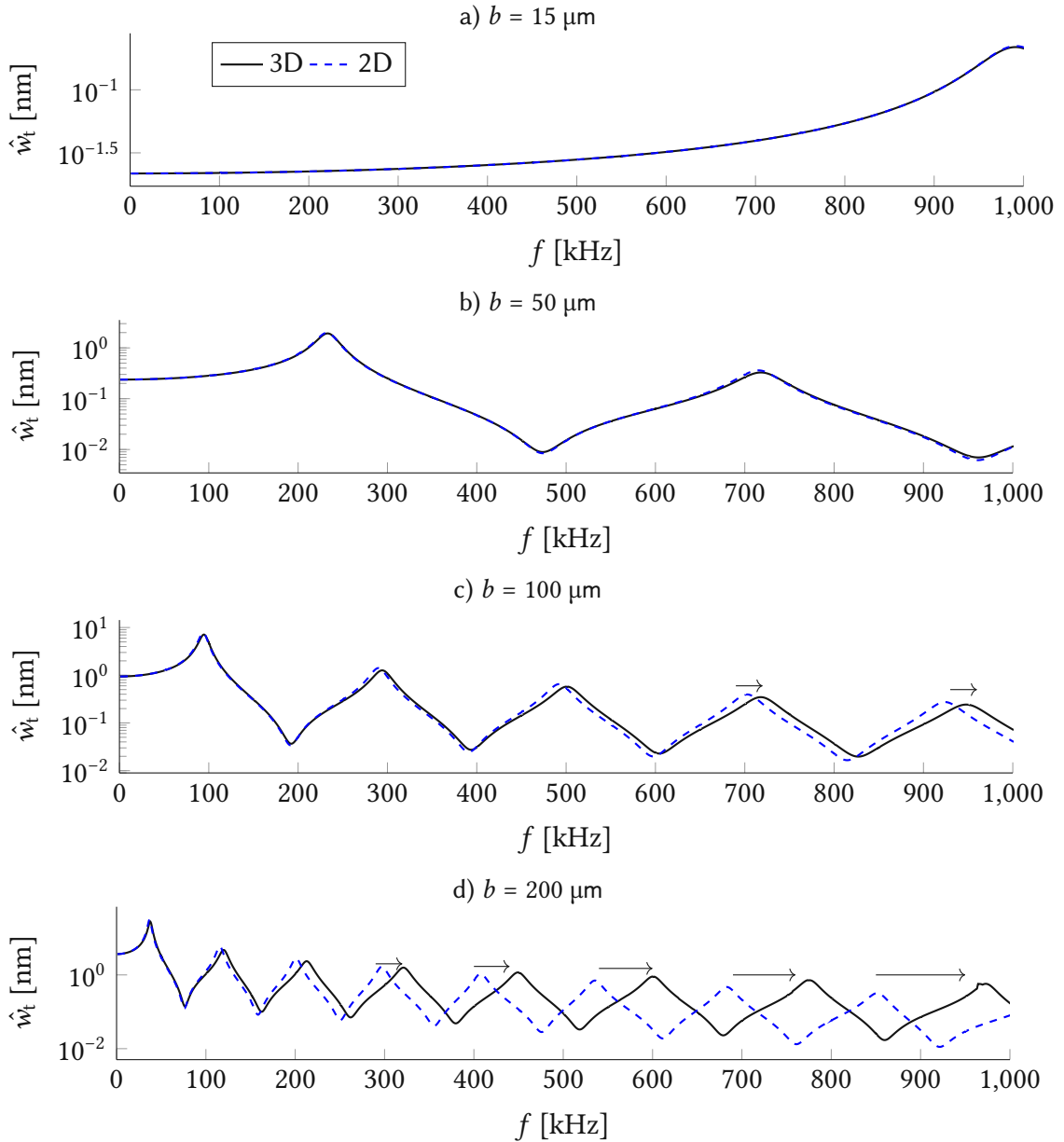


Figure 11.4: Displacement spectrum of the slender beam with a) $b = 15 \mu\text{m}$, b) $b = 50 \mu\text{m}$, c) $b = 100 \mu\text{m}$ and d) $b = 200 \mu\text{m}$ in water under anti-symmetric excitation. The arrows indicate the increase in the damped resonance frequency f_d from the 2D to the 3D formulation for the same vibrational modes.

The percentile difference in f_d between 2D and 3D formulations is defined by

$$\text{Diff}(f_d) = 100 \frac{f_d^{2D} - f_d^{3D}}{f_d^{3D}}, \quad (11.1)$$

where f_d^{2D} is the converged frequency obtained with the 2D fluid flow method, and f_d^{3D} is obtained with the 3D fluid formulation.

Fig. 11.5 shows $\text{Diff}(f_d)$ for the lowest four EB and torsional modes for micro-plates with $25 \mu\text{m} \leq b \leq 400 \mu\text{m}$ ¹. For all EB and torsional modes, $\text{Diff}(f_d)$ increases with the plate's width b , as well as with the number of nodal lines n_x . EB modes are more affected by the 3D fluid flow in terms of $\text{Diff}(f_d)$. For instance, for the 4:0 mode $\text{Diff}(f_d)$ reaches -40 % for the wide plate with $b = 400 \mu\text{m}$, while the 4:1 mode exhibits $\text{Diff}(f_d) = -20 \%$ for the same width. Results in Fig. 11.5 are of key importance, as they highlight that each vibrational mode is influenced to a different degree by the 3D fluid flow.

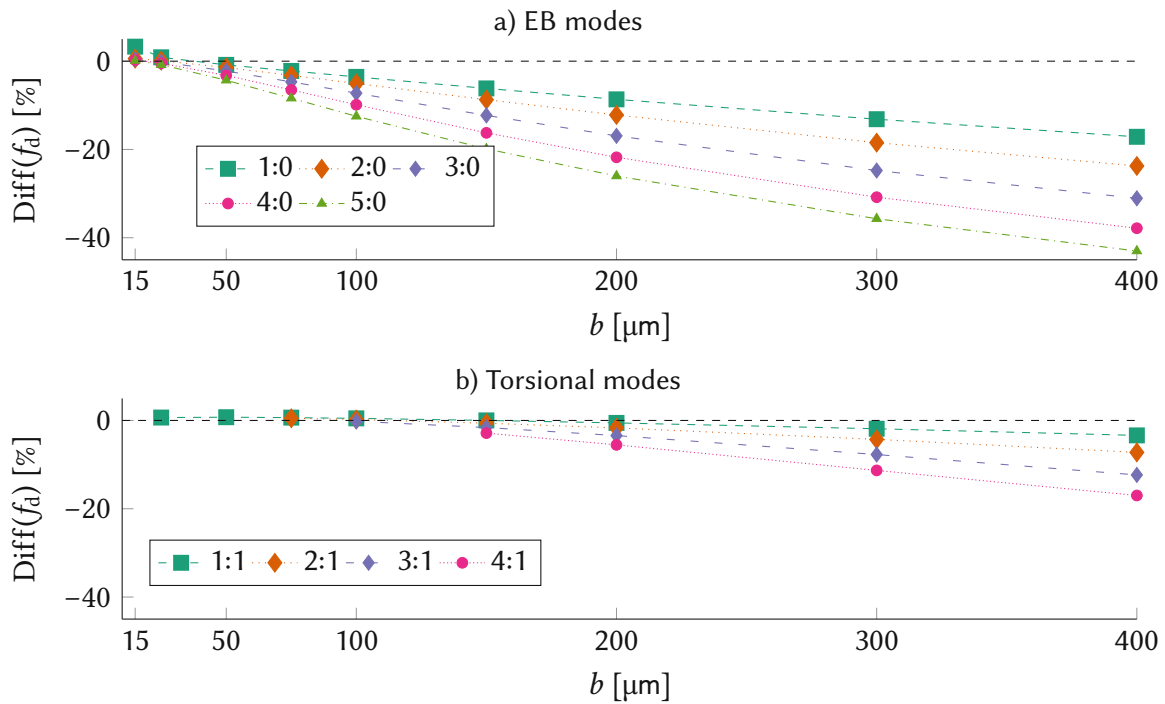


Figure 11.5: Difference in f_d obtained between 2D and 3D methods in water for a) EB and b) torsional modes.

11.2 Three-dimensional fluid flow in water

The fluid flow around the plate can be determined with

$$\hat{u}_j(\mathbf{x}_f) = -\frac{1}{8\pi\mu_f} \int_{\Omega_p} \Delta \hat{p} \mathcal{S}_{zj}(\lambda, \mathbf{x}_f, \mathbf{x}_s^{\text{mp}}) d\Omega(\mathbf{x}_s^{\text{mp}}), \quad (11.2)$$

where \mathbf{x}_f is a three-dimensional distribution of field points in the fluid domain.

As an object of study to illustrate the 3D fluid flow, we select the $100 \mu\text{m}$ wide plate vibrating at the lowest five EB modes. Fig. 11.6 shows the in-phase fluid flow along the

¹Convergence of f_d with the fluid grid is shown in D

plate's center line ($y = 0$). Importantly, note in the five EB modes, the fluid flow over the plate's free edge at $x > l$ ($x > 800 \mu\text{m}$, in this case). Such fluid flow can of course, only be accounted for with the 3D fluid flow formulation. With the 2D method, the fluid velocity at $x > l$ is simply zero. What is more, as the number of nodal lines n_x increases (from mode 1:0 to 5:0), re-circulation fluid flow zones appear at the fluid regions above and underneath the mode's nodal lines. For instance, for the mode 2:0, at $x = 580 \mu\text{m}$ and $z = \pm 30 \mu\text{m}$, fluid flow in x -direction becomes significant as the fluid moves from one region of the plate's maximum displacement to one of minimum. Considering the 3:0 mode, these flow regions with intense x -direction velocity occur at $x = 4000 \mu\text{m}$ and at $x = 650 \mu\text{m}$, in addition to the free edge flow at $x > 800 \mu\text{m}$. This increase in the x -direction flow with the number of nodal lines n_x is the leading cause of $\text{Diff}(f_d)$ increasing with n_x shown in Fig. 11.5.

11.3 Q-factor in the beam-plate transition in water

Determining the Q-factor of the different vibrational modes in water requires using a finer fluid grid than for f_d as seen in the validation results shown in Fig. 10.7. The requirement for finer fluid grids becomes especially important considering that the computation time increases exponentially with \mathcal{M}_x^3 as shown in Fig. 11.7. For instance, while one frequency step simulation with a 32×128 fluid grid consumes an average of 5 minutes, using a 64×256 fluid grid requires 40 minutes per frequency step². This high computation time becomes prohibitively lengthy using the DHO model, given that this method requires the determination of \hat{w}_t in several frequencies around f_d . For instance, using twenty frequency steps around f_d with a fluid grid of 128×512 consumes around 6 days of simulation for each vibrational mode.

Hence, the need for a more efficient method to determine Q than based on the damped harmonic oscillator equation is imperative. Given that f_d converges with coarse grids, one more efficient strategy to determine Q is using the Q-factor definition as the ratio of the maximum elastic energy stored in the structure E_b and the energy dissipated by the fluid in one cycle of oscillation E_D [28] at f_d as

$$Q = 2\pi \frac{E_b(f = f_d)}{E_D(f = f_d)}. \quad (11.3)$$

The dissipated energy E_D for the micro-plate fluid system is [70, 71]

$$E_D = \frac{\pi}{2\pi f_d} \int_{\Omega_p} \mathcal{R}(j\omega \hat{w} \Delta \hat{p}^*) d\Omega_p, \quad (11.4)$$

where the $*$ superscript means the complex conjugate and \mathcal{R} is the real operator. E_b is the maximum bending energy over one oscillation cycle when the plate vibrates at f_d as

²Timing results obtained in one node at the VSC with 40 cores and 1024 GB RAM. The fluid grid consists of $\mathcal{M}_x \times 4 \times \mathcal{M}_x$, and $\tau_{Szz} = 10^{-3}$.

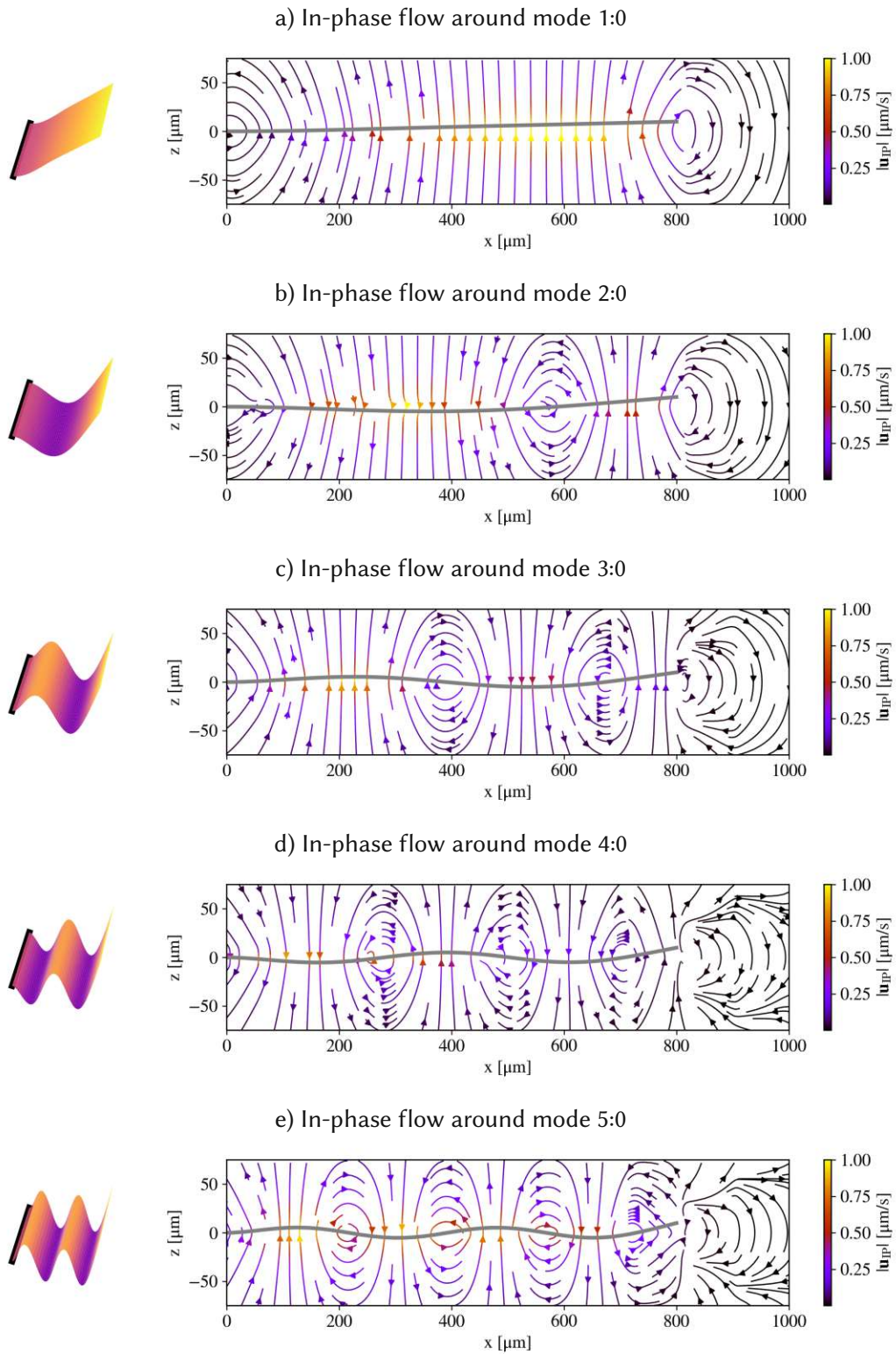


Figure 11.6: In-phase fluid flow along the plate's center line ($y = 0$) for modes a) 1:0, b) 2:0, c) 3:0, d) 4:0 and e) 5:0. The plate is $100 \mu\text{m}$ wide. On the left, the vibrational modes are represented.

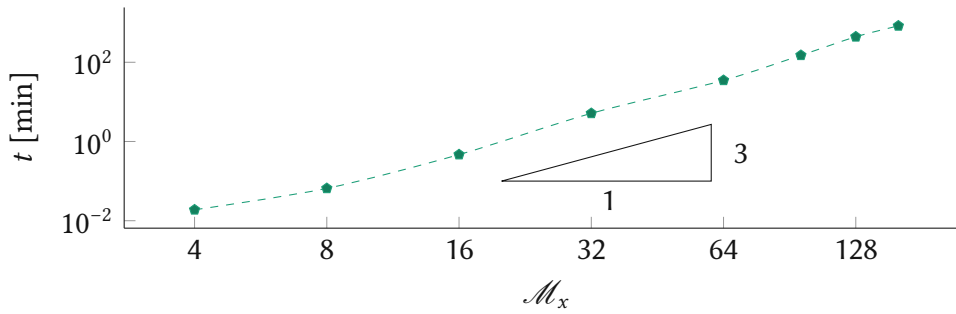


Figure 11.7: Average computation time per frequency step for different values of M_x .

$$E_b = \max_{t \in [0, T]} \int_{\Omega_p} C_{\alpha\beta\gamma\delta} w_{,\alpha\beta}(t) w_{,\gamma\delta}(t) d\Omega_p. \quad (11.5)$$

The Q-factors obtained from the energy definition in Eq. 11.3 with the dissipated energy in Eq. 11.4 and the stored bending energy in Eq. 11.5 are similar to the ones obtained with a fitting to the DHO equation [70, 71].

Fig. 11.8 shows the Q of the micro-plates with $b = 25 \mu\text{m}$, $b = 50 \mu\text{m}$, $b = 75 \mu\text{m}$ and $b = 100 \mu\text{m}$ in the 500 kHz frequency range obtained with the 2D and 3D fluid flow formulations³. Up to $100 \mu\text{m}$, Q-factors obtained with 3D formulation are higher than with the 2D formulation. Thus, the 2D fluid flow formulation underpredicts Q for slender plates in water, which agrees with previous numerical studies [35]. Furthermore, the difference increases with the increase in the number of nodal lines n_x . The Q-factors and resonance frequencies of the torsional modes are only slightly different from the two methods in this width and frequency range.

As the plate becomes wider, an interesting effect occurs. For the plates with width $b = 150 \mu\text{m}$ and $b = 200 \mu\text{m}$, values of Q obtained with both methods (2D and 3D) are roughly similar, as shown in Fig. 11.9a and 11.9b in a 150 kHz frequency range. For even wider plates with $b = 300 \mu\text{m}$ and $b = 400 \mu\text{m}$, the 2D method overpredicts Q , an effect which occurs both for the EB and torsional modes here investigated.

Fig. 11.10 shows the Q-factor for the lowest four EB and four torsional modes for plates with widths ranging from $25 \mu\text{m}$ to $400 \mu\text{m}$. With Fig. 11.10 it becomes more clear that the Q-factor for plates with widths up to $200 \mu\text{m}$ are underestimated by the 2D method, whereas for wider plates, the 2D method over-predicts Q . In Fig. 11.10, for the EB modes also the Q-factor prediction with Sader's method [31] is shown, which agrees very well with the 2D fluid flow method, given that also in Sader's method, 2D fluid flow is assumed.

The percentile difference in Q between 2D and 3D formulations is defined by

$$\text{Diff}(Q) = 100 \frac{Q^{2D} - Q^{3D}}{Q^{3D}}, \quad (11.6)$$

³Convergence of Q with the 3D method is shown in D.

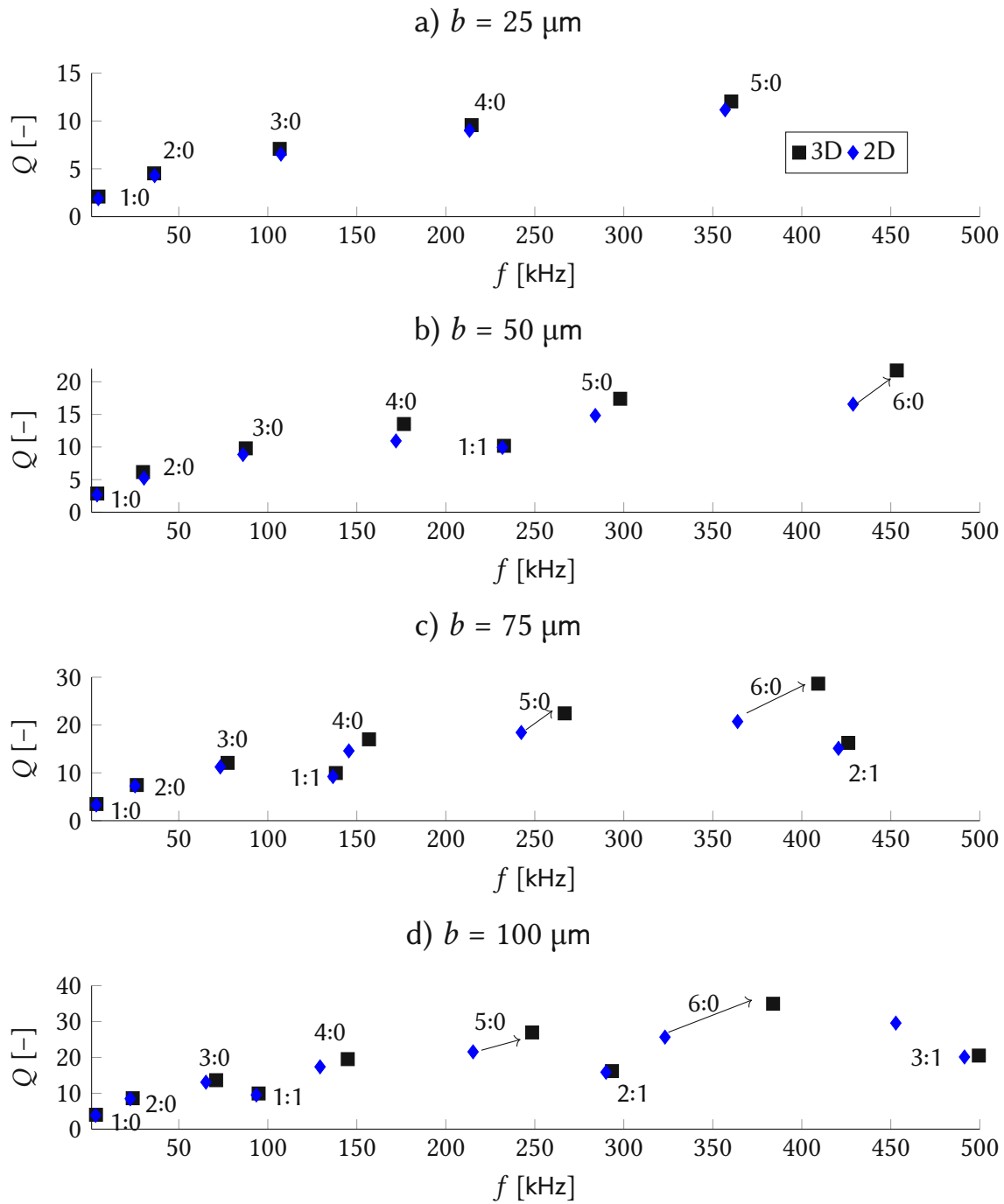


Figure 11.8: Quality factor of the vibrational modes of the plate with a) $b = 25 \mu\text{m}$, b) $b = 50 \mu\text{m}$, c) $b = 75 \mu\text{m}$ and d) $b = 100 \mu\text{m}$ in water obtained with the 3D and 2D fluid formulation. The arrows indicate the increase in the damped resonance frequency f_d and Q -factor from the 2D to the 3D formulation for the same vibrational modes.

where Q^{2D} is the converged frequency obtained with the 2D fluid flow method, and Q^{3D} is obtained with the 3D fluid formulation. Fig. 11.11 shows the percentage difference between the Q -factor obtained with the 2D and 3D methods. Q -factor of the EB modes

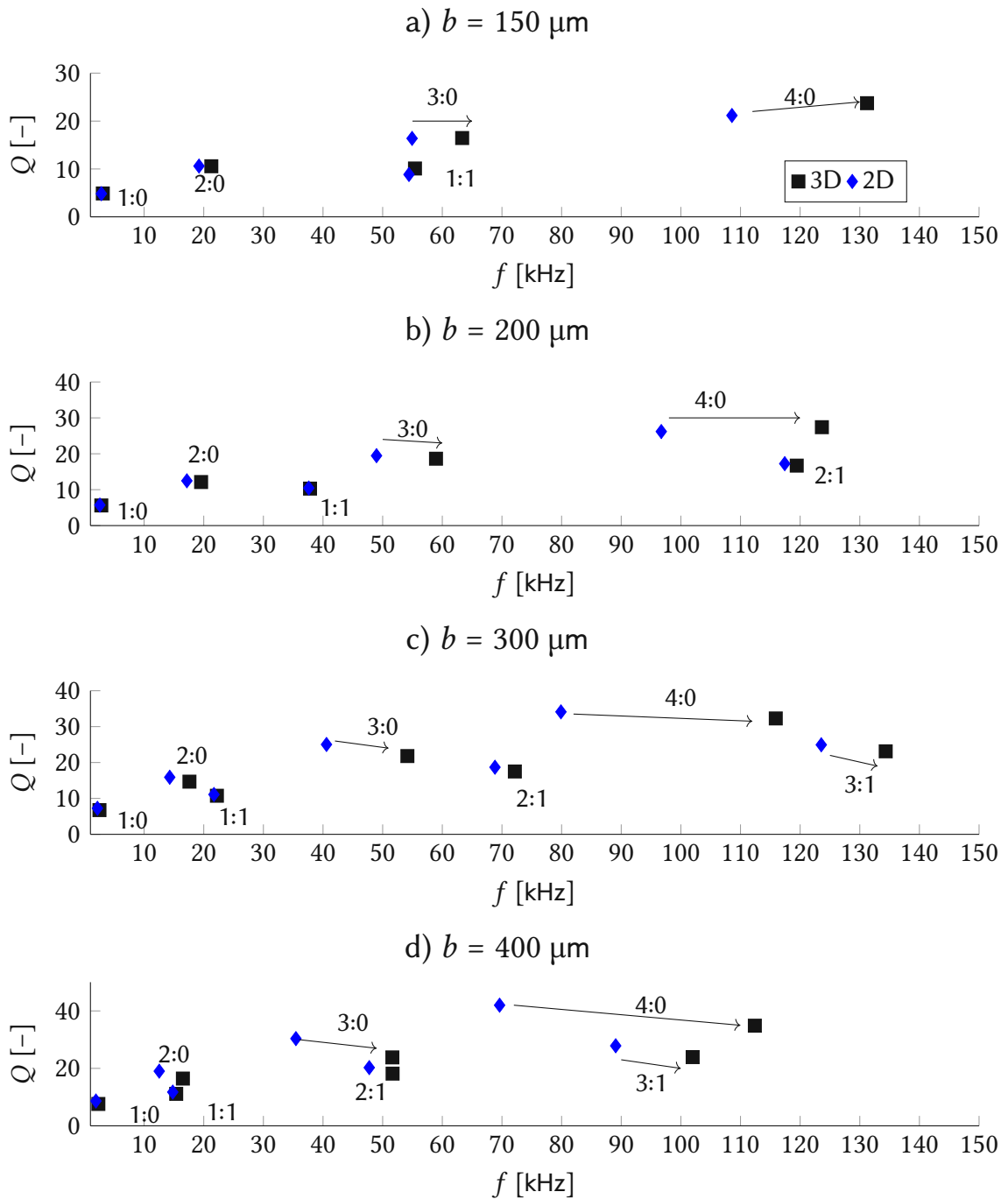


Figure 11.9: Quality factor of the vibrational modes of the plate with a) $b = 150 \mu\text{m}$, b) $b = 200 \mu\text{m}$, c) $b = 300 \mu\text{m}$ and d) $b = 400 \mu\text{m}$ in water obtained with the 3D and 2D fluid formulation. The arrows indicate the increase in the damped resonance frequency f_d and the decrease in Q -factor from the 2D to the 3D formulation for the same vibrational modes.

are underpredicted with the 2D fluid flow approximation by as much as 15% for slender plates ($b \leq 200 \mu\text{m}$), and overpredicted by as much as 30% for wider plates. For torsional

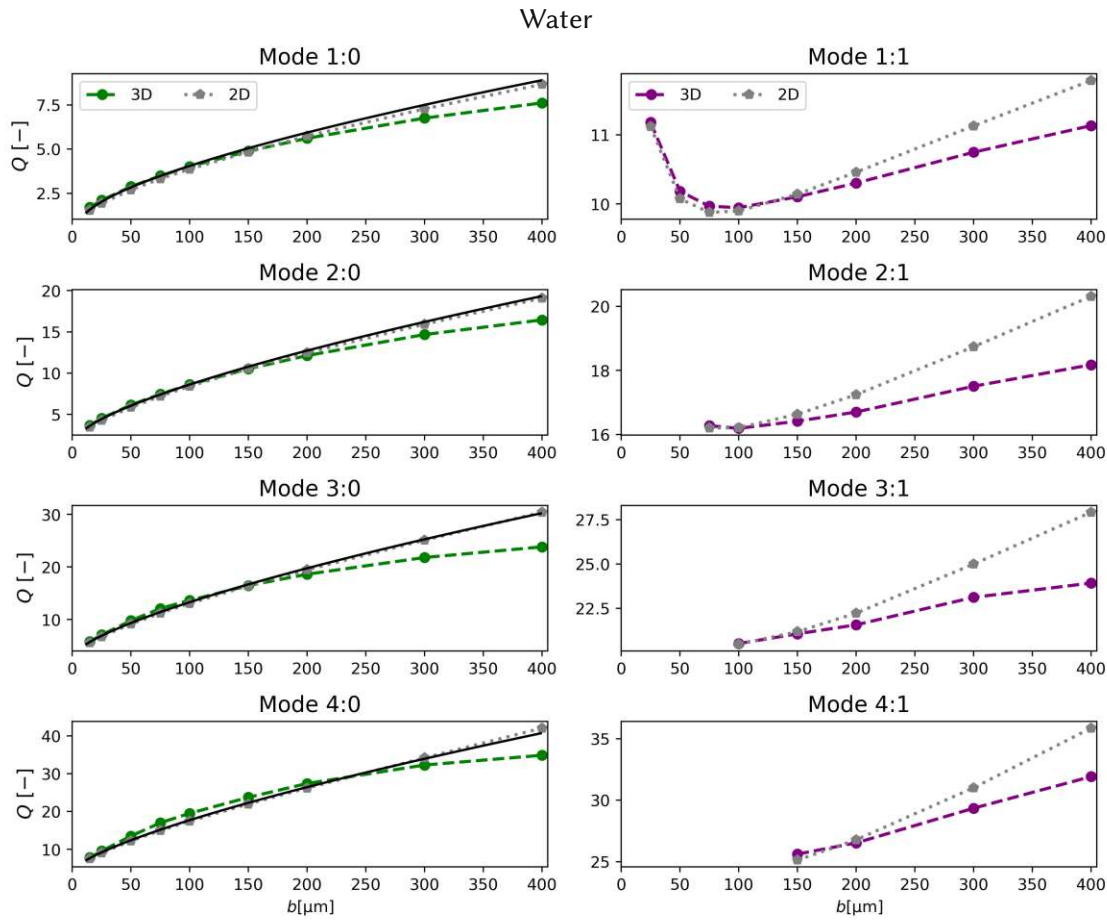


Figure 11.10: Quality factor of EB and torsional modes as the structure is altered from a slender beam with $b = 15 \mu\text{m}$ to a plate with $b = 400 \mu\text{m}$ in water. For EB modes, Sader’s Q -factors predictions are shown in black.

modes, this difference is very small (smaller than 5%) for slender plates ($b \leq 200 \mu\text{m}$) and increase up to 20% for wider plates.

11.4 Q-factor in the beam-plate transition in air

In air, the damped resonance frequencies f_d of micro-plates are not significantly influenced by the fluid formulation. However, the Q -factor can be impacted by the 3D fluid flow and this influence is here investigate.

Fig. 11.12 shows the Q -factor for the lowest four EB and four torsional modes for plates with widths ranging from $25 \mu\text{m}$ to $400 \mu\text{m}$ in air. For the four EB modes, there is a great difference in Q values and the 2D method underpredicts Q . Interestingly, the torsional modes 1:1 and 2:1 are little influenced by the 3D fluid flow, but the Q -factor for modes 3:1 and 4:1 are once more underpredicted by the 2D fluid flow approximation.

Fig. 11.13 shows the percentage difference between the Q -factor obtained with the 2D and 3D methods. Fig. 11.13 shows clearly how $\text{Diff}(Q)$ increases with the plate’s

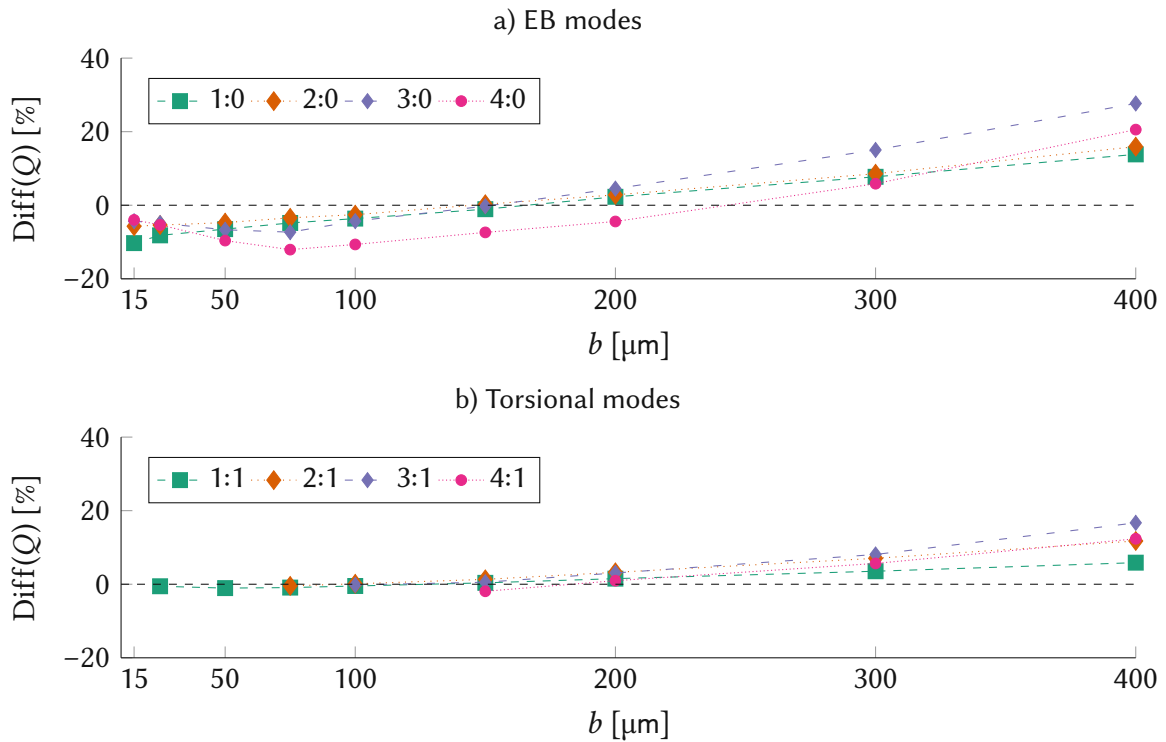


Figure 11.11: Difference in Q -factor obtained between 2D and 3D methods in air for EB and torsional modes.

width b and the number of nodal lines n_x . For the slender beam with $b = 15 \mu\text{m}$, the 2D fluid flow and 3D methods render similar results and the difference for all modes is near zero. As the width increases, the difference in Q reaches values as high as 50 % difference for the 4:0 mode, and 20% for the 4:1 mode.

11.5 Comparison to experiments

To further investigate the accuracy of the 3D fluid flow method, we resort to the experimental data of the w500 and w750 micro-plates in water reported in Chapter 8. The difference between simulation and experimental damped resonance frequency $\text{Diff}(f_d)$ is determined as Eq. 8.1, where negative values of $\text{Diff}(f_d)$ means the simulation underestimates f_d , and positive values of $\text{Diff}(f_d)$ indicates the simulated values of f_d are overestimated.

Fig. 11.14 shows $\text{Diff}(f_d)$ for the w500 plate obtained with the 2D and 3D methods. While the 2D method exhibited an increasing error for the EB modes with increasing n_x and values of $\text{Diff}(f_d)$ were in a $-25\% \leq \text{Diff}(f_d) \leq 15\%$ range, with the 3D method $\text{Diff}(f_d)$ is consistently within a $8\% \leq \text{Diff}(f_d) \leq 18\%$ range. Hence, a reduction from a 40% error range in f_d is reduced to only a 10% difference range by using the 3D fluid flow formulation.

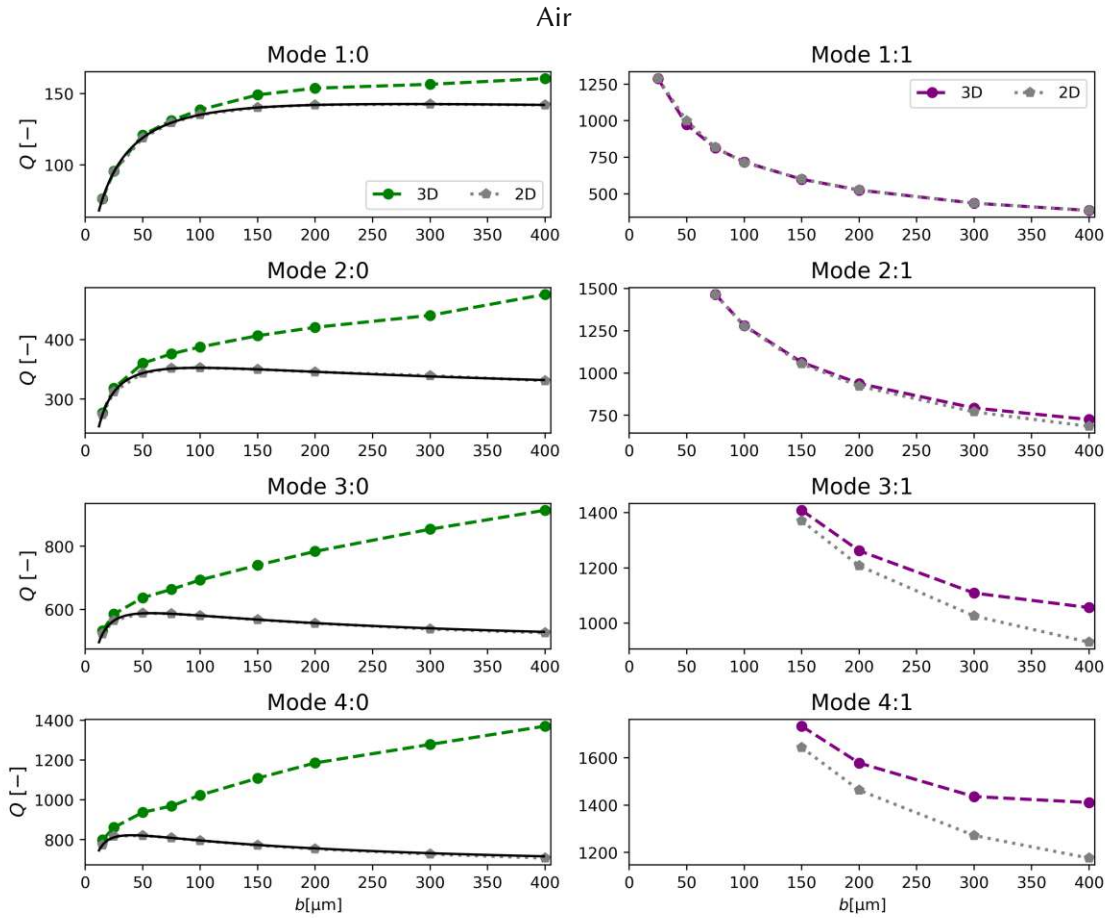


Figure 11.12: Quality factor of EB and torsional modes as the structure is altered from a slender beam with $b = 12.5 \mu\text{m}$ to a plate with $b = 400 \mu\text{m}$ in air. For EB modes, Sader’s Q -factors predictions are shown in black.

For the w750 micro-plate in water, with the 3D method, $\text{Diff}(f_d)$ is within a 1% to 16% difference range as seen in Fig. 11.15b. Whereas with the 2D fluid flow method, $\text{Diff}(f_d)$ is in a $-40\% \leq \text{Diff}(f_d) \leq 10\%$. Thus a reduction from 50% error range in f_d to only 15% is achieved. What is more, the increasing value of $\text{Diff}(f_d)$ with n_x from the 2D method is no longer an issue. Also, results in Figs. 11.14 and 11.14 were obtained considering the nominal dimensions of the micro-plates. Given that $\text{Diff}(f_d)$ is consistently positive in this frequency range, $\text{Diff}(f_d)$ could even be further reduced by considering measured dimensions of the micro-plates (instead of nominal)⁴.

Comparing the simulated Q -factor with the 3D method and the experiments was not possible because the convergency of the Q -factors for the w500 and w750 in water was not achieved. With the finest fluid grid of 192×768 , $\epsilon(Q)$ for most modes is well above 0.01, as shown in D. With this fluid grid, the simulation time for one frequency step reaches 48 hours, and the required memory reaches 1800 GB in a computing node

⁴Results in Figs. 11.14 and 11.15 were obtained with FE-meshes consisting of $64 \times 64/r_a$ elements and a fluid grid of 64×256 points in the 3D formulation. The convergence with the fluid grid is shown in B.

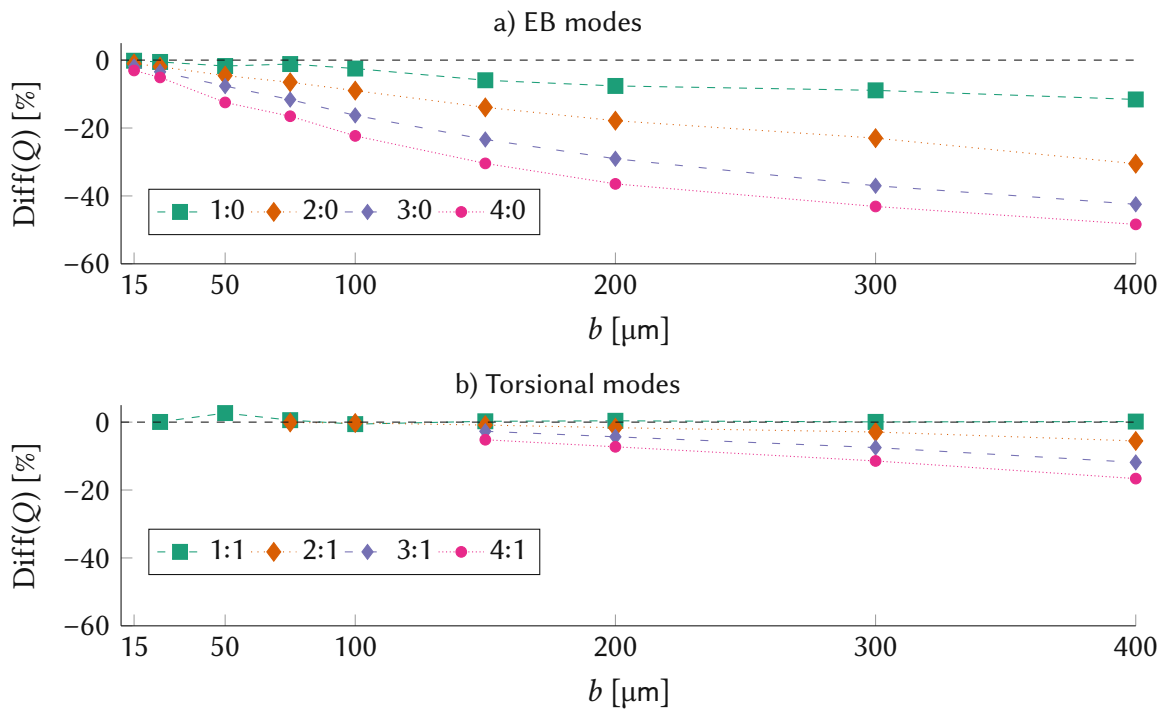


Figure 11.13: Difference in Q-factor obtained between 2D and 3D methods in air for EB and torsional modes

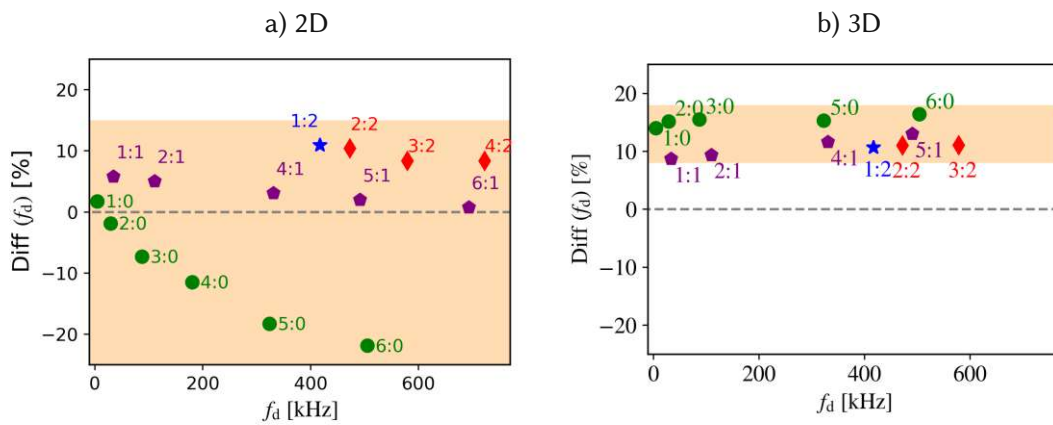


Figure 11.14: Difference in f_d for the w500 plate with the a) 2D and b) 3D fluid formulation. The dark-orange band represents the limits to which Diff(f_d) extends.

of the Vienna Scientific Cluster (VSC) with 40 physical cores and 2048 GB memory. Hence, the Q-factor comparison of very wide structures ($b \geq 500 \mu\text{m}$) requires strategies to improve the implementation of the 3D formulation, a couple of which are discussed in the outlook section of this thesis.

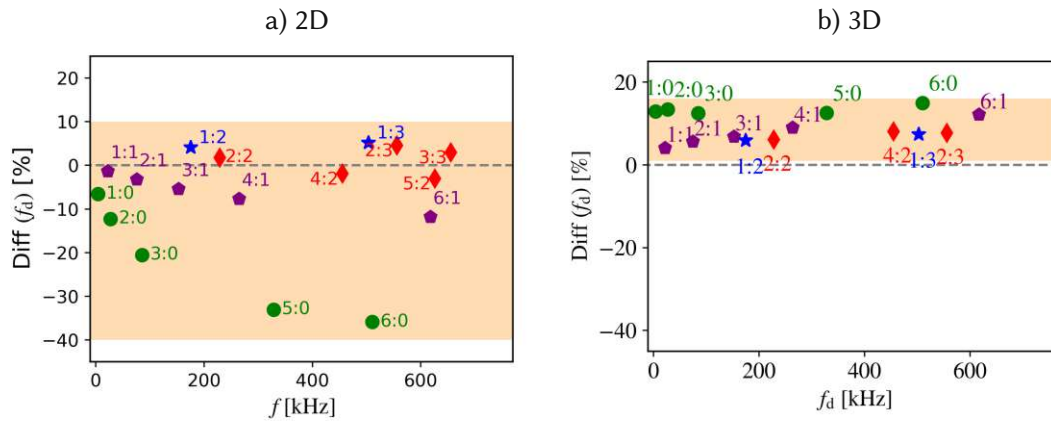


Figure 11.15: Difference in f_d for the w750 plate with the a) 2D and b) 3D fluid formulation. The dark-orange band represents the limits to which $\text{Diff}(f_d)$ extends.

11.6 Conclusions

This chapter used the 2D and 3D fluid flow semi-numerical methods to understand the limits of the two-dimensional flow approximation in the beam plate transition in air and water. From the results in water, we see that the 2D formulation has a considerable impact on the resonance frequencies, as differences in f_d reached values up to 45 % (for the 5:0 mode). These differences were explained with the help of the fluid flow visualization, which showed regions of re-circulation on the top and bottom regions of the plates associated with the number of nodal lines n_x . An interesting effect appeared concerning the Q-factor in water. While for slender plates with $b \leq 200 \mu\text{m}$, the 2D method provides underestimated Q-factors, for wider plates with $b > 200 \mu\text{m}$, the 2D method overpredicts Q , reaching differences up to 30 %. The 2D method underpredicts Q for all modes in air, reaching differences as high as 50 %. Applying the 3D method to find f_d of the w500 and w750 plates in water yielded a much better agreement with experiments. For instance, for the w500 plate, a reduction from the 40 % error range in f_d with the 2D fluid flow method to merely 10% with the 3D method is achieved. For the w750 plate, this error drops from 50 % to 15 %.

Part IV

Conclusions and outlook

12 Conclusions and outlook

12.1 Conclusions

Even though fluid-structure interaction is a well-established research and application field in MEMS, the geometry of the MEMS resonator is most commonly limited to slender beams. With the numerical and experimental results shown here, we highlight that non-slender geometries represent a promising alternative for MEMS resonators in viscous fluids whose application has been hindered due to the need for efficient methods for determining their dynamics. The proposed semi-numerical methods enable studying novel effects and geometries in the MEMS-fluid interaction field, thus inspiring new device architectures to perform with unprecedented high quality-factors in fluidic operation.

The methods are based on the Kirchhoff plate equation. Hence the proposed method generalizes the existent beam-based semi-analytic methods for the out-of-plane modes in incompressible viscous fluids and, more importantly, overcomes their limitations by accounting for two-dimensional vibrational modes. From dimensional analysis, the governing equations for the fluid dynamics of the micro-plate-fluid interaction problem were defined as the Stokes equations. The hydrodynamic force is determined in the first semi-numerical method proposed here, assuming the fluid flow around micro-plates is two-dimensional. The use of the two-dimensional flow approximation makes the method very efficient since the integration of the fundamental solution can be performed analytically. To investigate the extent to which the two-dimensional fluid flow affects the plate dynamics and if an even better agreement with the experimental data is achieved, we propose a formulation that considers three-dimensional fluid flow around a micro-plate. The method is based on the free-space unsteady Stokeslet, the fundamental solution to the unsteady Stokes equations in three dimensions for incompressible fluids. The formulation to the micro-plate-fluid interaction problem is simplified using a single-layer formulation, and we show that only one component of the Stokeslet (\mathcal{S}_{zz}) is required for determining the hydrodynamic force on a micro-plate undergoing purely out-of-plane displacement. The numerical integration of \mathcal{S}_{zz} over the plate's domain required a tailored scheme to account for the fact that \mathcal{S}_{zz} is singular. With the analytic integration around a circular region, we were able to avoid singularity issues, which enabled much finer fluid grids than previous studies which relied on the free space Stokeslet [44, 69, 101]. Both methods converge at all frequencies tested in water and air and exhibit excellent agreement with Sader's method. The difference in Q-factor prediction between the proposed methods and semi-analytical models [31] was minimal (less than 0.5%) for a slender beam in water, showing the proposed methods' accuracy.

Investigating the beam-plate transition in different fluids revealed the importance of the stored kinetic energy in the fluid for the Q-factor of different modes. Specifically, we highlight that in water, the damping coefficients of all modes increase as the plate becomes wide. Similarly, the added-mass effect (through the fluid's kinetic energy) increases with the plate's width. Hence, despite the increase in the damping coefficient, Q for all out-of-plane modes increases with the plate's width in water. For instance, the

5:0 mode reaches a 500 % increase in Q when altering a slender beam with $b = 15 \mu\text{m}$ for a wide plate with $b = 400 \mu\text{m}$. These results indicate a counter-intuitive explanation for the increased Q-factor of micro-plates in liquids, which resides in increased stored energy rather than decreased dissipation.

Non-beam modes, e.g., HOP and RTS modes, revealed opposite trends in gases and liquids. While in gases, Q increases from EB modes to torsional and then to HOP and RTS modes $Q^{\text{HOP,RTS}} > Q^{\text{torsional}} > Q^{\text{EB}}$, in liquids, the opposite happens, and Q decreases from EB modes to HOP modes $Q^{\text{EB}} > Q^{\text{torsional}} > Q^{\text{HOP,RTS}}$. We named this change in the Q-factor trend from gases to liquids the "Gas-Liquid modal Q-factor inversion" (GL-Q-inversion). An analysis of the Q-factor as a ratio of the damping coefficient and added-mass coefficient revealed that Q increases for HOP modes in gases due to their lower damping coefficients. In liquids, even though EB-modes dissipate more energy than all other modes, they also exhibit a higher stored energy in the form of added mass than other modes, which increases Q^{EB} . Since the added-mass effect is only significant in liquids, this leads to the GL-Q-inversion.

Experiments in water showed a Q-factor following the numerically predicted pattern of $Q^{\text{EB}} > Q^{\text{torsional}} > Q^{\text{HOP}}$. Experiments to determine the Q-factor in air showed that acoustic losses play a significant role in the overall Q-factor. We designed resonators for which acoustic losses are minimized, whose Q-factor in air follows the pattern $Q^{\text{HOP}} > Q^{\text{torsional}} > Q^{\text{EB}}$, in agreement with the numerical prediction of the Gas-Liquid modal Q-factor inversion.

With the 2D fluid flow and 3D fluid flow semi-numerical methods, it was possible to understand the limits of the two-dimensional flow approximation in the beam plate transition. From results in water, we find that the 2D formulation considerably impacts the resonance frequencies, as differences in f_d between the two formulations reached values as high as 45 % (for the 5:0 mode, for instance). These differences occur due to regions of re-circulation on the top and bottom regions of the plates associated with the number of nodal lines n_x , in addition to the fluid flow around the plate's free edge, which of course, exhibits a significant x component. Comparing results from the 3D method to experiments showed a reduction from the 40 % error range in f_d with the 2D fluid flow method to merely 10% with the 3D method. An unexpected pattern emerged concerning the Q-factor in water. While the 2D method underestimates Q for slender plates, the 2D method overpredicts Q for wider plates. This overestimation reaches differences up to 30 % for modes as low as 3:0. In air, the 2D method underpredicts Q for all modes, reaching differences as high as 50 % for the wide plate. These numerical results are well beyond previous investigations on the three-dimensional flow influence of non-slender geometries on which only one or few vibrational modes were investigated [64, 61].

12.2 Outlook

The results in this thesis highlight that research with non-slender MEMS resonators has limitless possibilities.

One exciting research field for non-slender geometries is MEMS resonators for biological applications. By exploiting the large surface area, the resonator's surface can

be functionalized to bond with different proteins, enzymes, bacteria and others [105], which in association with the high Q-factor of non-slender geometries in viscous fluids enables measurements in blood. Research in high-speed AFM also benefits from non-slender geometries, not only due to their high Q-factor but also by exploiting non-beam modes, which further enables applications to soft samples [106, 107].

Further MEMS research also benefits from non-slender geometries by exploiting novel physical effects not present in slender geometries. For instance, micro-plates in vacuum are susceptible to the veering effect. Veering effect refers to a system where one parameter is altered and two eigenvalues and eigenvectors effectively “repel” each other instead of simply crossing each other as the system’s parameter varies, which is why veering is also known as avoided-crossing [108]. According to preliminary results, a micro-plate immersed in a viscous fluid is also susceptible to veering, but in this case, a fluid-induced mode-veering occurs. Fluid-induced mode-veering occurs by altering the fluid’s properties, which leads to a non-linear response of the modes’ resonance frequencies and Q-factor with the fluid parameter. A further physical effect in micro-plates is the linear mode coupling of vibrational modes through the fluid [109]. Preliminary results indicate the existence of mode-splitting and other types of mode-coupling in the micro-plate-fluid problem [110], which are not present in the slender beam case in fluids.

The proposed semi-numerical methods are powerful tools and can be altered for other geometries not limited to plate resonators. For instance, it is simple to modify the elastic body formulation to determine the out-of-plane dynamics of other structures found in MEMS resonators, e.g., V-shaped beams [111], double-clamped bridges [112], and membranes [113]. Additionally, one may alter the elastic domain formulation to shells for accounting for non-planar geometries, as done elsewhere for the steady Stokes equations [114].

As a further improvement to the method, it is interesting to make the 3D fluid flow method more memory and time efficient. One promising approach to improving both aspects is implementing a fast multipole method (FMM) for the BEM formulation. The principle of FMM is to convert the element-to-element interactions (in this case, of the fluid grid) to cell-to-cell interactions, where cells are organized in a hierarchical structure. Using the FMM for the BEM alleviates the computation time and memory issues from BEM since, with FMM, time and memory requirements increase with order $\mathcal{O}(M_x^1)$, instead of $\mathcal{O}(M_x^2)$ [115].

Appendices

A Fluid properties

Table A.1 shows the viscosity and density of the selected gases and liquids at SATP conditions.

Fluid	μ_f [$\mu\text{Pa s}$]	ρ_f [kg m^{-3}]	ν_f [$\text{mm}^2 \text{s}^{-1}$]
Hydrogen	8.8	0.083	106
Air	18.2	1.204	15.1
Neon	31.3	0.9	34.7
Gasoline	504	711	0.7
Ethanol	1040	789	1.32
Isopropanol	2106	771	2.7
Water	890	997	0.9

Table A.1: Absolute viscosity μ_f , density ρ_f and kinematic viscosity ν_f of selected liquids and gases at SATP conditions [66].

B Convergence of the Q-factor and damped resonance frequency

As discussed in 5, the Q-factors and damped resonance frequencies f_d of all the vibrational modes alter with the number of points in the fluid grid, hence a convergence analysis is necessary for the data shown in the main text.

B.1 Convergence of the Q-factor shown in the validation

This section shows the convergence of the Q-factor of the microplates used in the experimental validation in 5.4. In Fig. B.1, convergence of Q and f_d is shown for the plate used in [30] in isopropanol. In liquids, we considered Q converged for $\epsilon_Q \leq 0.01$. The Q-factor of the lower-order modes (1:0 and 2:0) converge with a fluid grid with $\mathcal{M}_x = 32$, whereas the 1:3 and 1:4 modes require a fluid grid with $\mathcal{M}_x = 256$ for converged results.

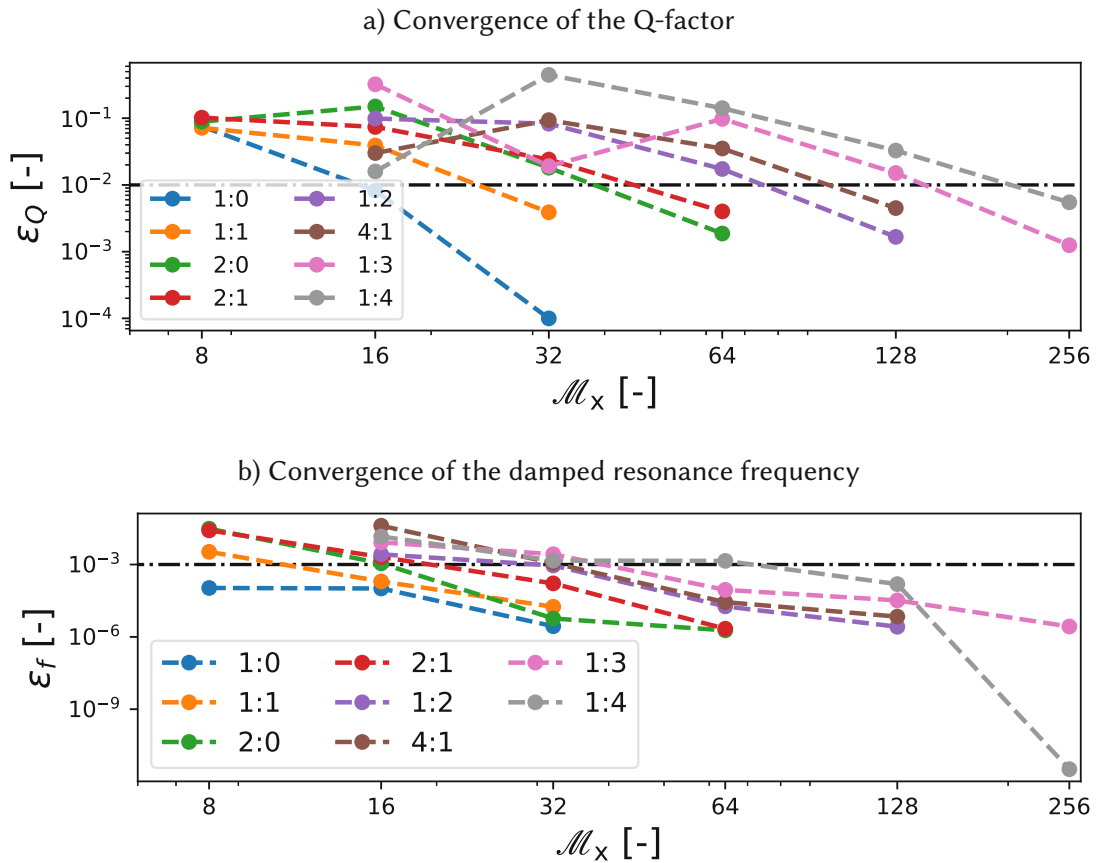


Figure B.1: Convergence of the a) Q-factor and b) damped resonance frequency of the microplate used in [66].

Fig. B.2 shows the convergence of Q and f_d for the RTS modes of the plate used in [66] in isopropanol. The higher RTS mode, the 1:8, requires a fluid grid of 512×4096 points for the Q-factor convergence.

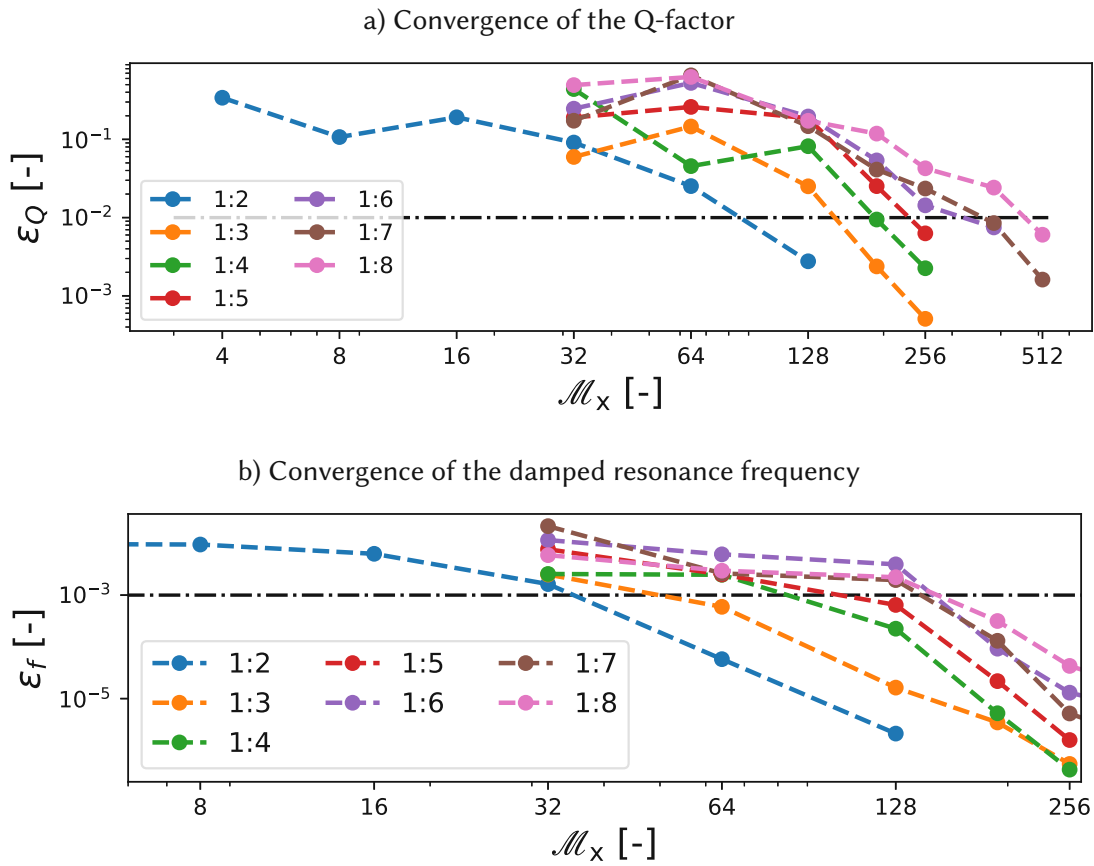


Figure B.2: Convergence of the a) Q-factor and b) damped resonance frequency of the microplate used in [66].

B.2 Convergence of the Q-factor in the beam-plate transition in air

This section shows the convergence of the Q-factor and f_d of all modes of the plates with widths ranging from 15 to 400 micrometers in air. In air, f_d is considered converged for $\epsilon_f \leq 10^{-4}$. For the slender plates with $b \leq 200 \mu\text{m}$, Q and f_d converge for a fluid grid with $\mathcal{M}_x = 32$ points. For the wider plates with $b \geq 250 \mu\text{m}$, a fluid grid with $\mathcal{M}_x = 64$ is required.

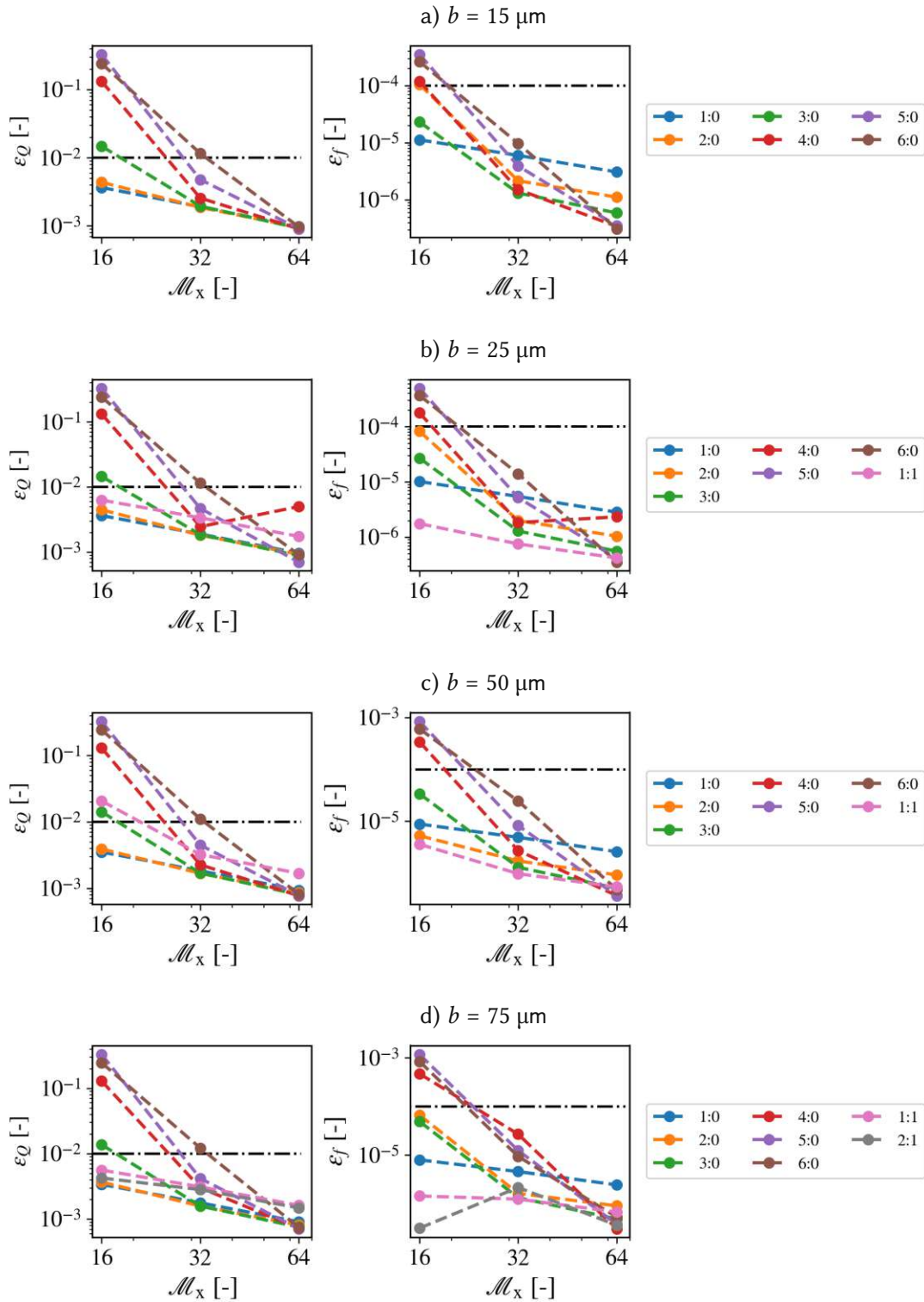


Figure B.3: Convergence of the Q-factor and damped resonance frequency with the fluid grid for the plates in air.

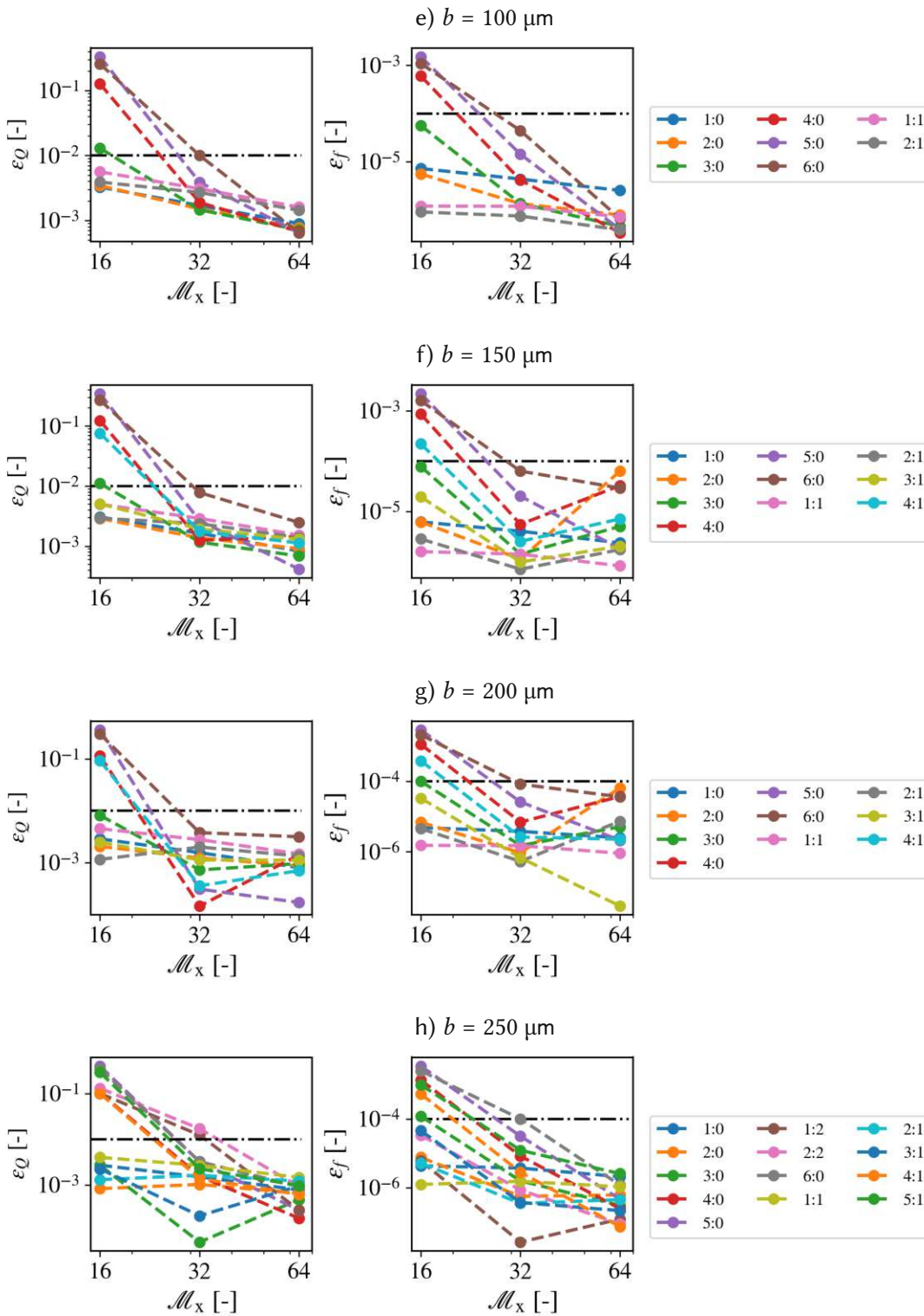


Figure B.3: (Cont.) Convergence of the Q-factor and damped resonance frequency with the fluid grid for the plates in air.

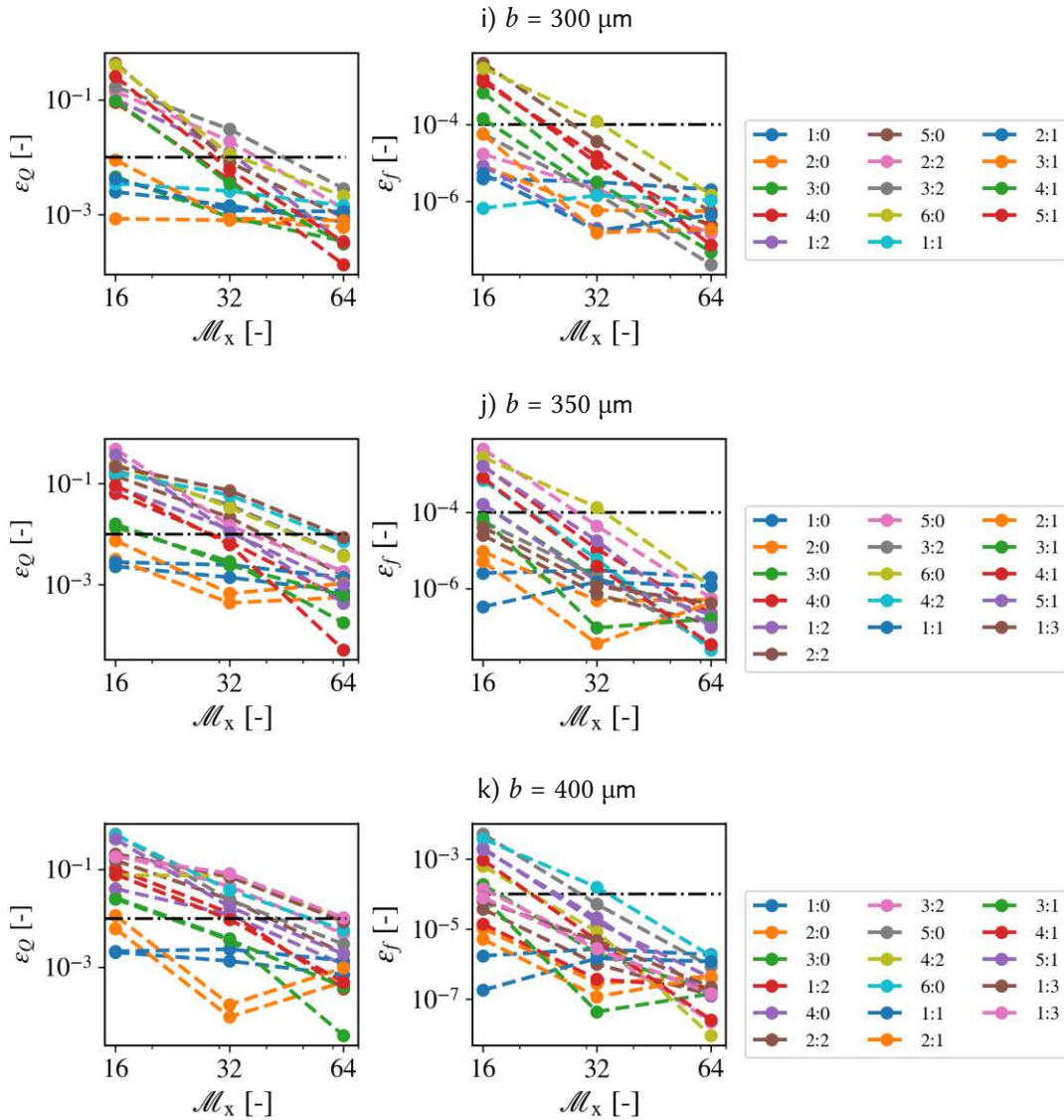


Figure B.3: (Cont.) Convergence of the Q-factor and damped resonance frequency with the fluid grid for the plates in air.

B.3 Convergence of the Q-factor in the beam-plate transition in water

This section shows the convergence of the Q-factor and f_d of all modes of the plates with widths ranging from 15 to 400 micrometers in water. For the slender plate with $b = 15 \mu\text{m}$ and for the wider plates with $b \geq 250 \mu\text{m}$, Q converges for a fluid grid with $M_x = 128$ points for all modes. For the other plates with $25 \leq b \leq 100 \mu\text{m}$, a grid with $M_x = 64$ suffices.

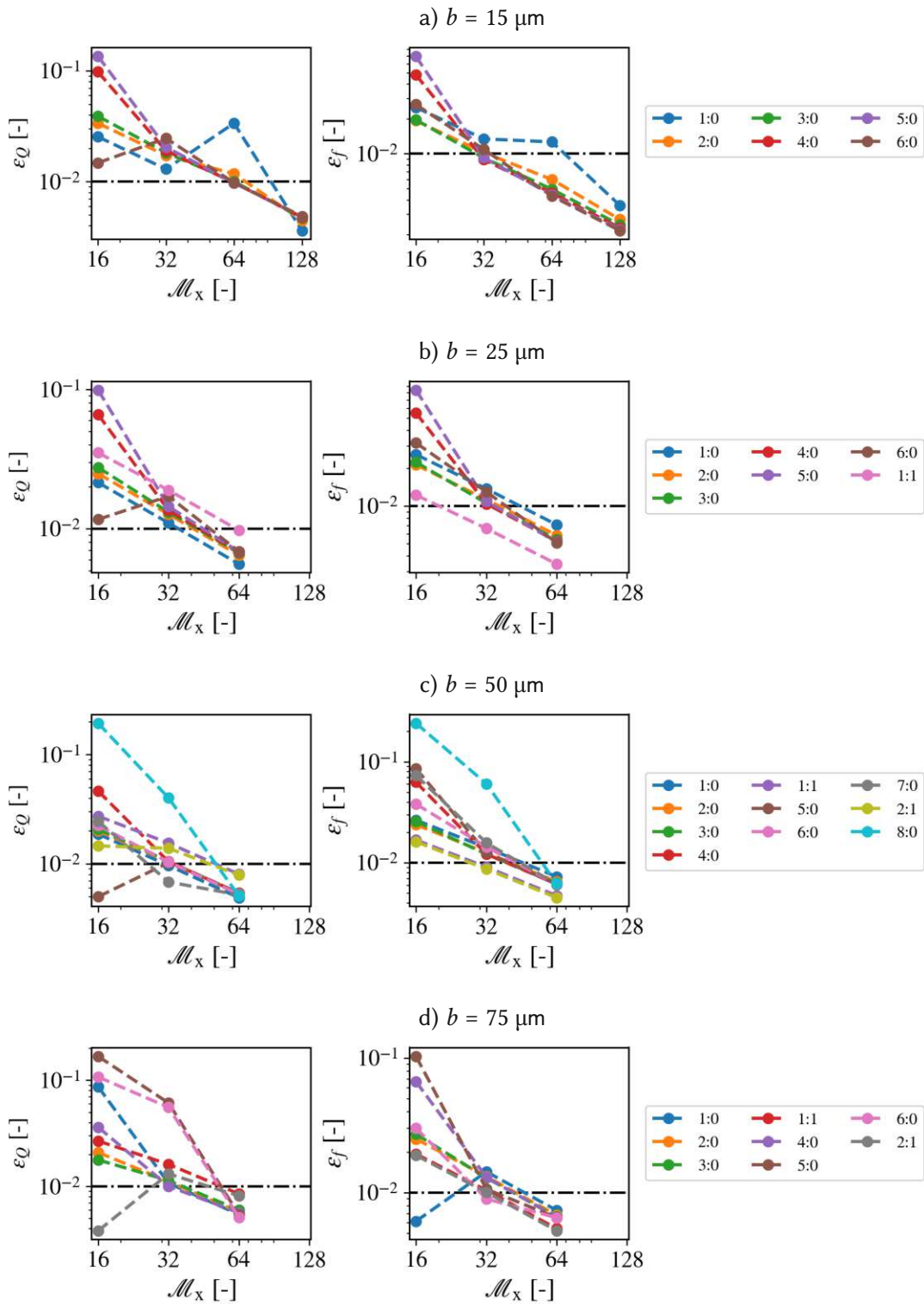


Figure B.4: Convergence of the Q-factor and damped resonance frequency with the fluid grid for the plates in water.

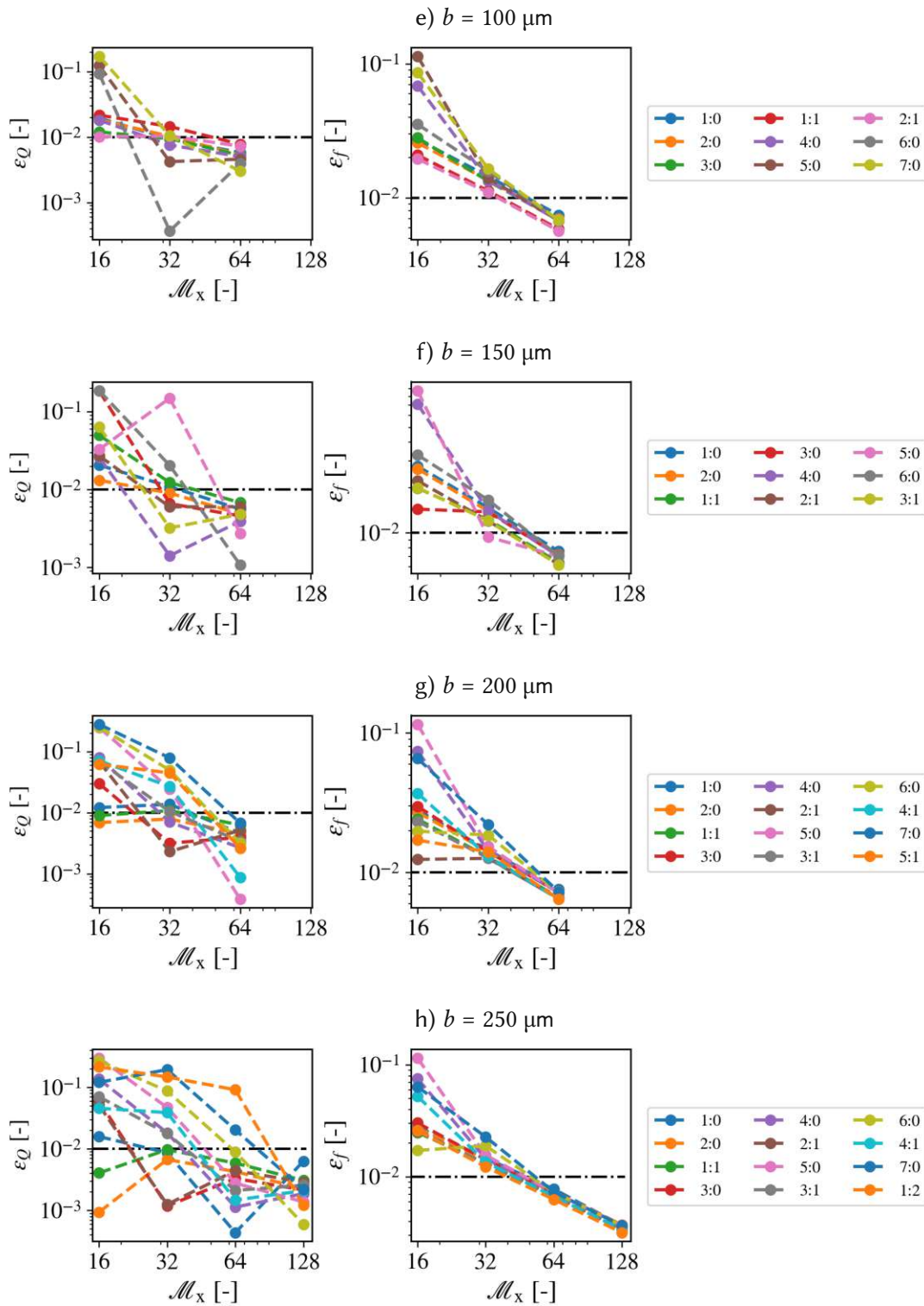


Figure B.4: (Cont.) Convergence of the Q-factor and damped resonance frequency with the fluid grid for the plates in water.

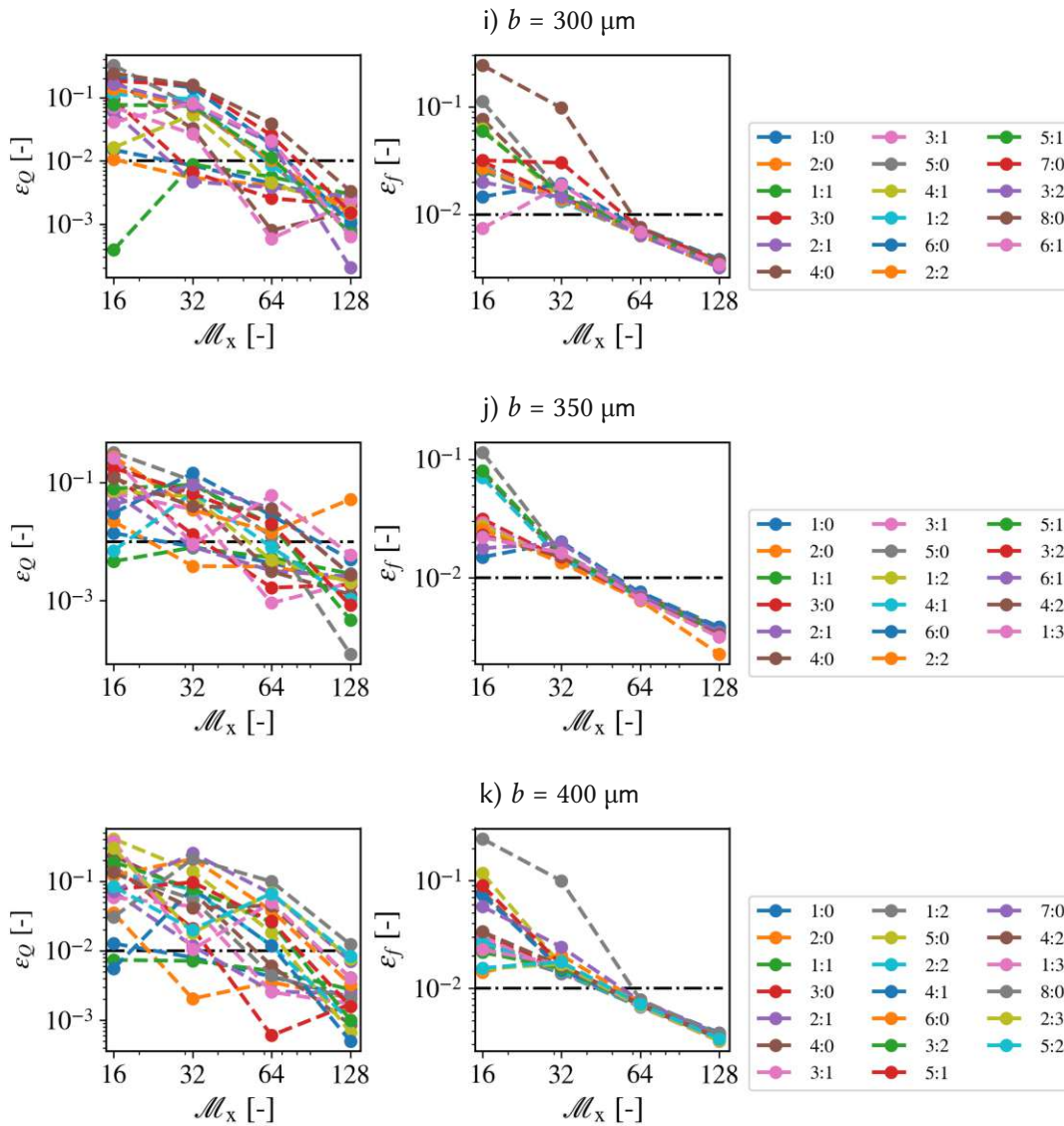


Figure B.4: (Cont.) Convergence of the Q-factor and damped resonance frequency with the fluid grid for the plates in water.

C Influence of the Stokeslet numerical integration

In addition to convergence with the fluid grid and with the FE-mesh, the influence of the tolerance τ_{Szz} in the calculated displacement field must be investigated. τ_{Szz} is the tolerance with which, each element of $\mathcal{F}(\Omega_p)$ is refined until convergence of the matrix element A_{3Dij} is achieved, that is, the relative difference between two iterations of A_{3Dij} must be smaller than τ_{Szz} . Note that, in the 2D method, this was not required, since the integral of the fundamental solution in each element was determined analytically.

To evaluate the influence of τ_{Szz} we introduce

$$\epsilon_{\tau_{Szz}} = \frac{\|\hat{w}^i - \hat{w}^{\text{ref}}\|_{L^2}}{\|\hat{w}^{\text{ref}}\|_{L^2}}, \quad (\text{C.1})$$

where \hat{w}^{ref} is a reference displacement field determined with $\tau_{Szz} = 10^{-5}$ and \hat{w}^i are solutions obtained with different values of τ_{Szz} . For this analysis, the FE-mesh is composed of 64×32 elements and the fluid grid of 32×128 points.

Fig. C.1 shows $\epsilon_{\tau_{Szz}}$ in air and in water at 10 kHz, 100 kHz and 1000 kHz as a function of τ_{Szz} . In air, the displacement field \hat{w} is little affected by τ_{Szz} , and values of $\epsilon_{\tau_{Szz}}$ are in the order of 10^{-4} or below. In water, on the other hand, to obtain values of $\epsilon_{\tau_{Szz}}$ smaller than 0.01, τ_{Szz} may have a maximum value of $3 \cdot 10^{-3}$ at 10 and 100 kHz, and of $2 \cdot 10^{-3}$ at 1000 kHz.

Note that the computation time per iteration increases as τ_{Szz} decreases, as shown in Fig. C.2 both in air and water. Hence, selecting a very small value of τ_{Szz} can make the simulation time prohibitively long. From hereon, we define $\tau_{Szz} = 10^{-3}$ to be used through the next analysis, as it provides $\epsilon_{\tau_{Szz}} \leq 0.01$ while maintaining a relatively low computing time.

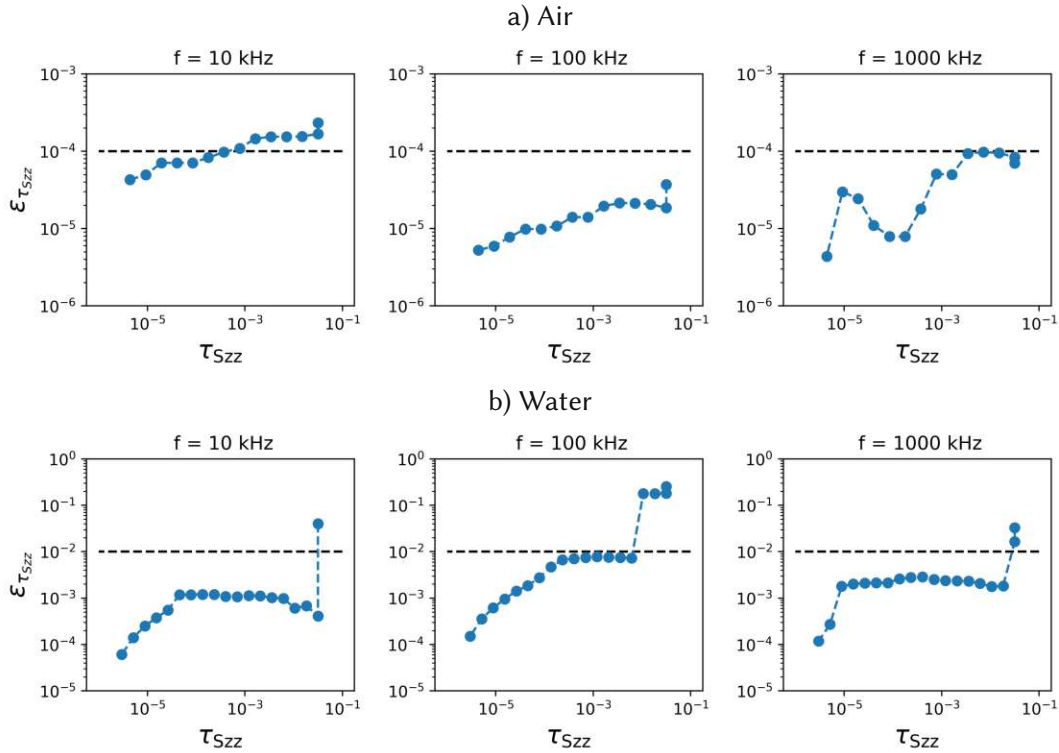


Figure C.1: Influence of the τ_{Szz} in the displacement field, convergence as a function of the number of points \mathcal{M}_x in the fluid grid of the plate with $r_a = 1/2$ at 10 kHz, 100 kHz and 1 MHz in a) air and b) water.

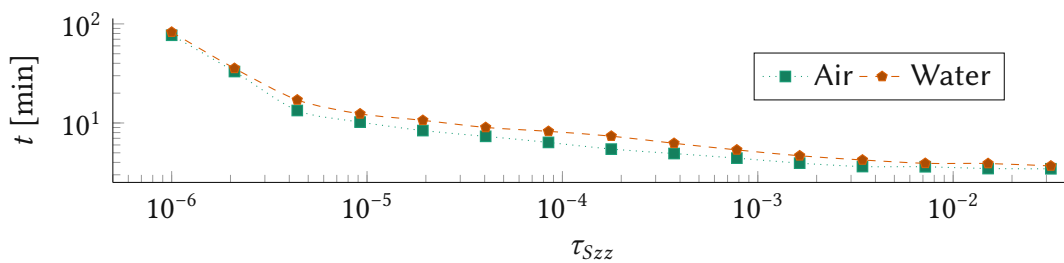


Figure C.2: Average computation time per frequency step for different values of τ_{Szz} .

D Convergence in the 3D method

In this section, we report on the convergence of Q and f_d with the 3D fluid flow method whose results are shown in Chapter 11. The fluid grid is composed with $\mathcal{M}_y = 4 \mathcal{M}_x$ points throughout this analysis.

D.1 Convergence of the Q-factor in the beam-plate transition in air

Here, the convergence of the Q-factor and f_d of the plates with widths ranging from 15 to 400 micrometers in air is shown. For the slender plates with $b \leq 25 \mu\text{m}$, Q converges for a fluid grid with $\mathcal{M}_x = 64$ points. For the wide plate with $b \geq 400 \mu\text{m}$, a fine fluid grid with $\mathcal{M}_x = 192$ is required for convergence.

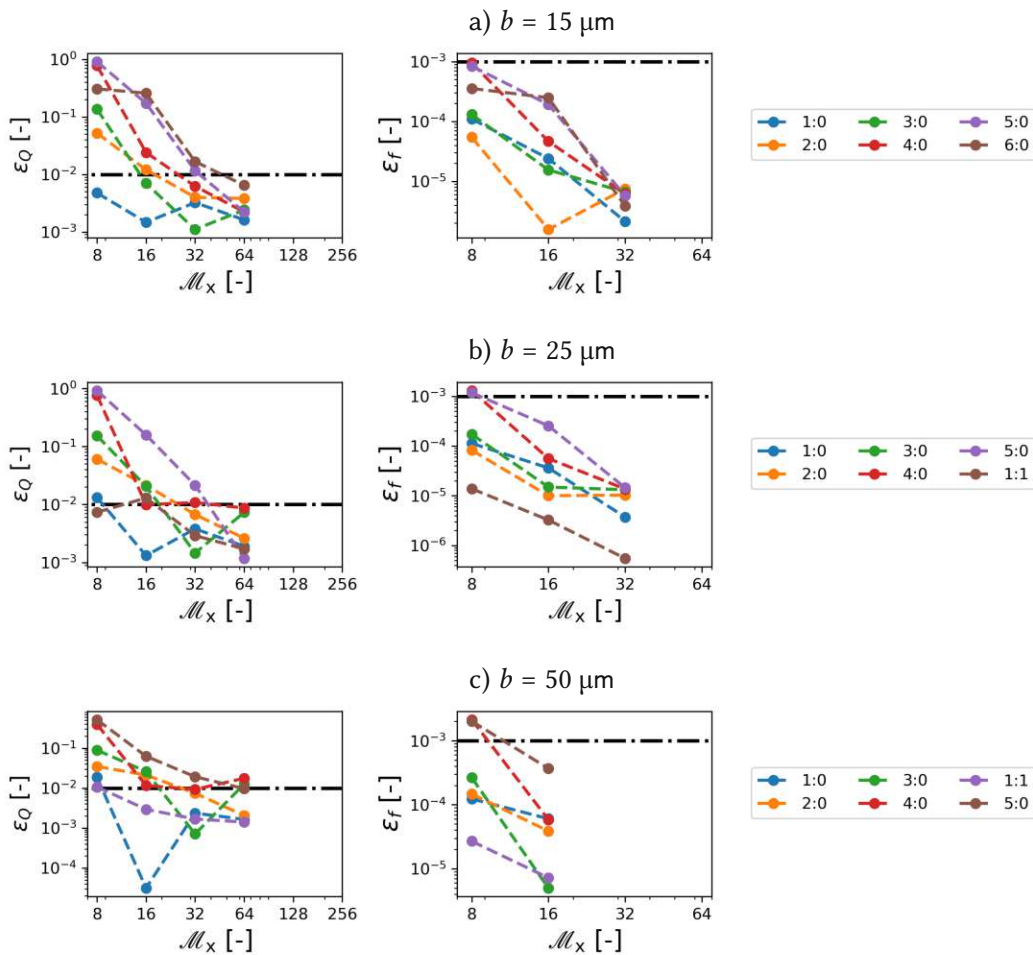


Figure D.1: Convergence of the Q-factor and damped resonance frequency with the fluid grid for the plates in air.

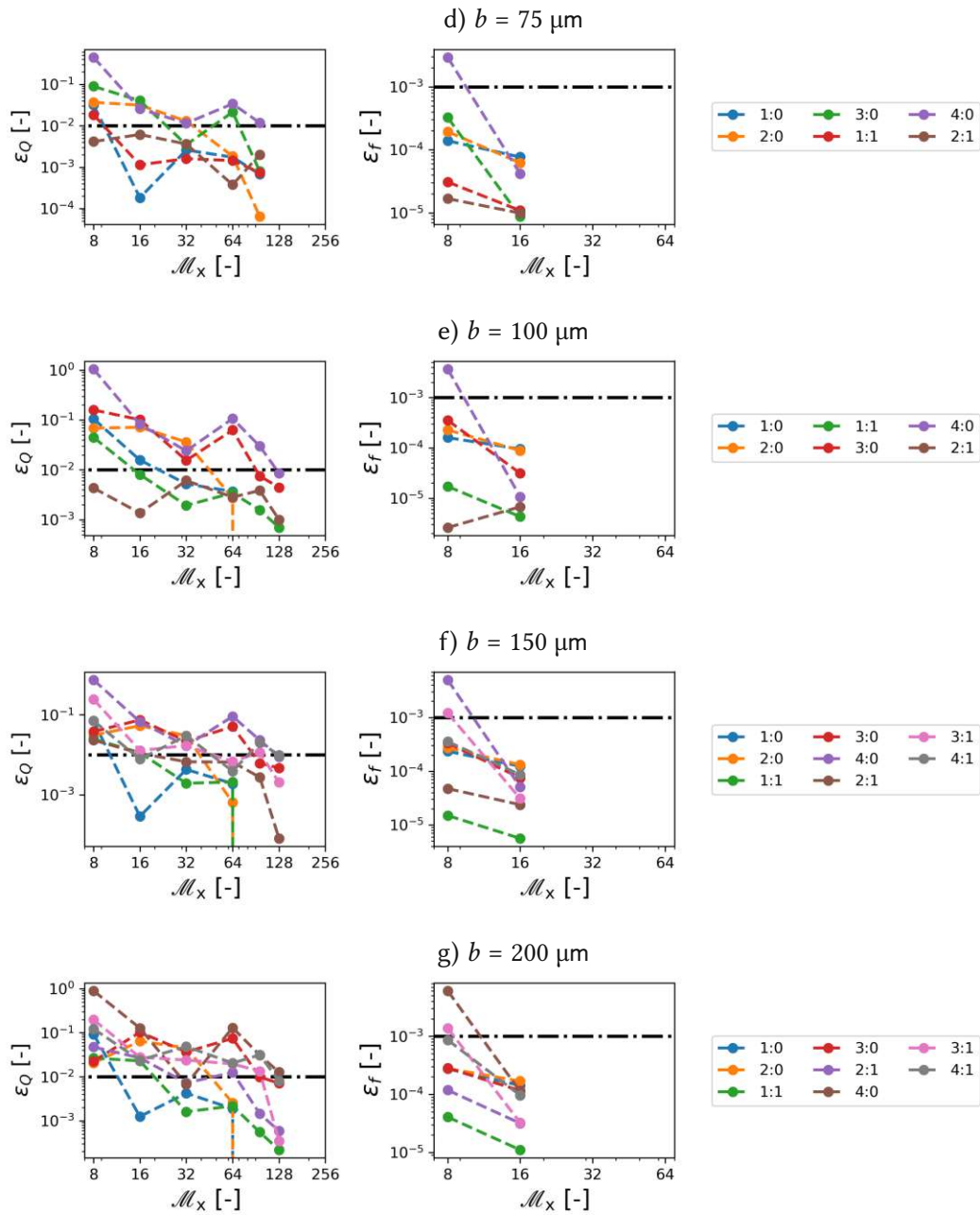


Figure D.1: (Cont.) Convergence of the Q-factor and damped resonance frequency with the fluid grid for the plates in air.

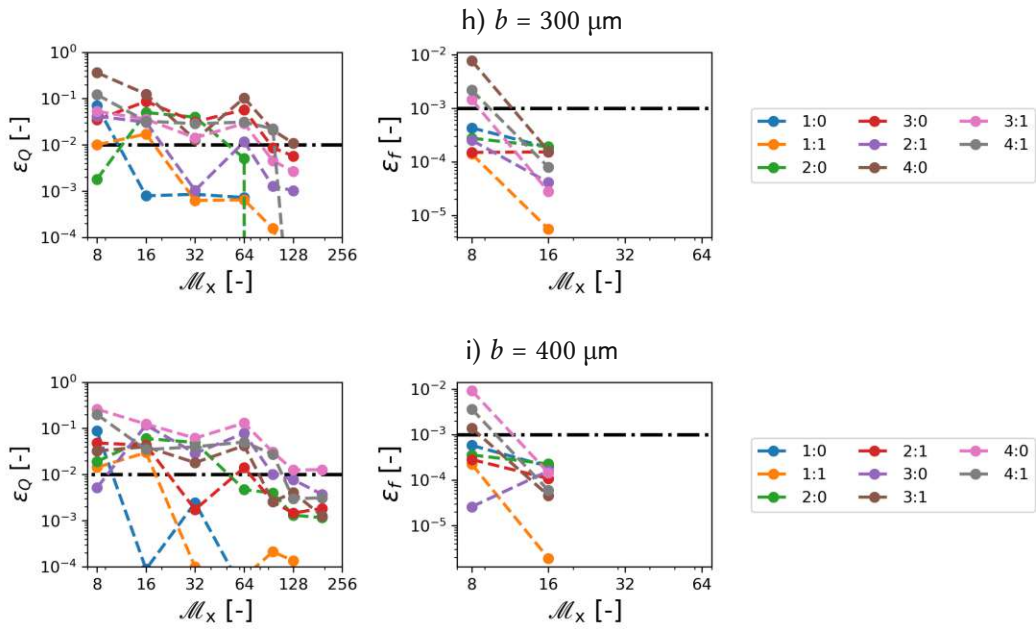


Figure D.1: (Cont.) Convergence of the Q-factor and damped resonance frequency with the fluid grid for the plates in air.

D.2 Convergence of the Q-factor in the beam-plate transition in water

This section shows the convergence of the Q-factor and f_d of all modes of the plates with widths ranging from 15 to 400 micrometers in water. For the slender plates with $b \leq 50 \mu\text{m}$, Q converges for a fluid grid with $\mathcal{M}_x=64$ points for the low-order modes shown. For wider plates with $b \geq 300 \mu\text{m}$, once more a fine fluid grid with $\mathcal{M}_x=192$ points is required.

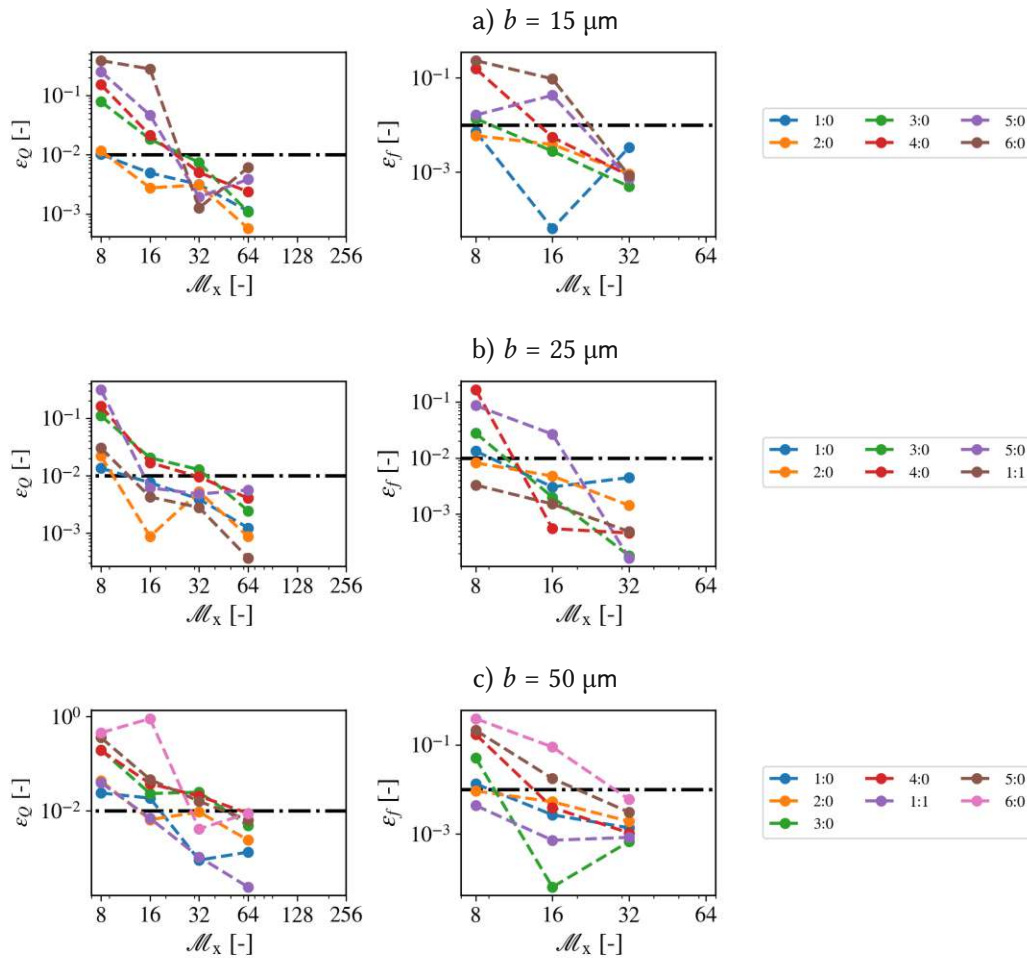


Figure D.2: Convergence of the Q-factor and damped resonance frequency with the fluid grid for the plates in water.

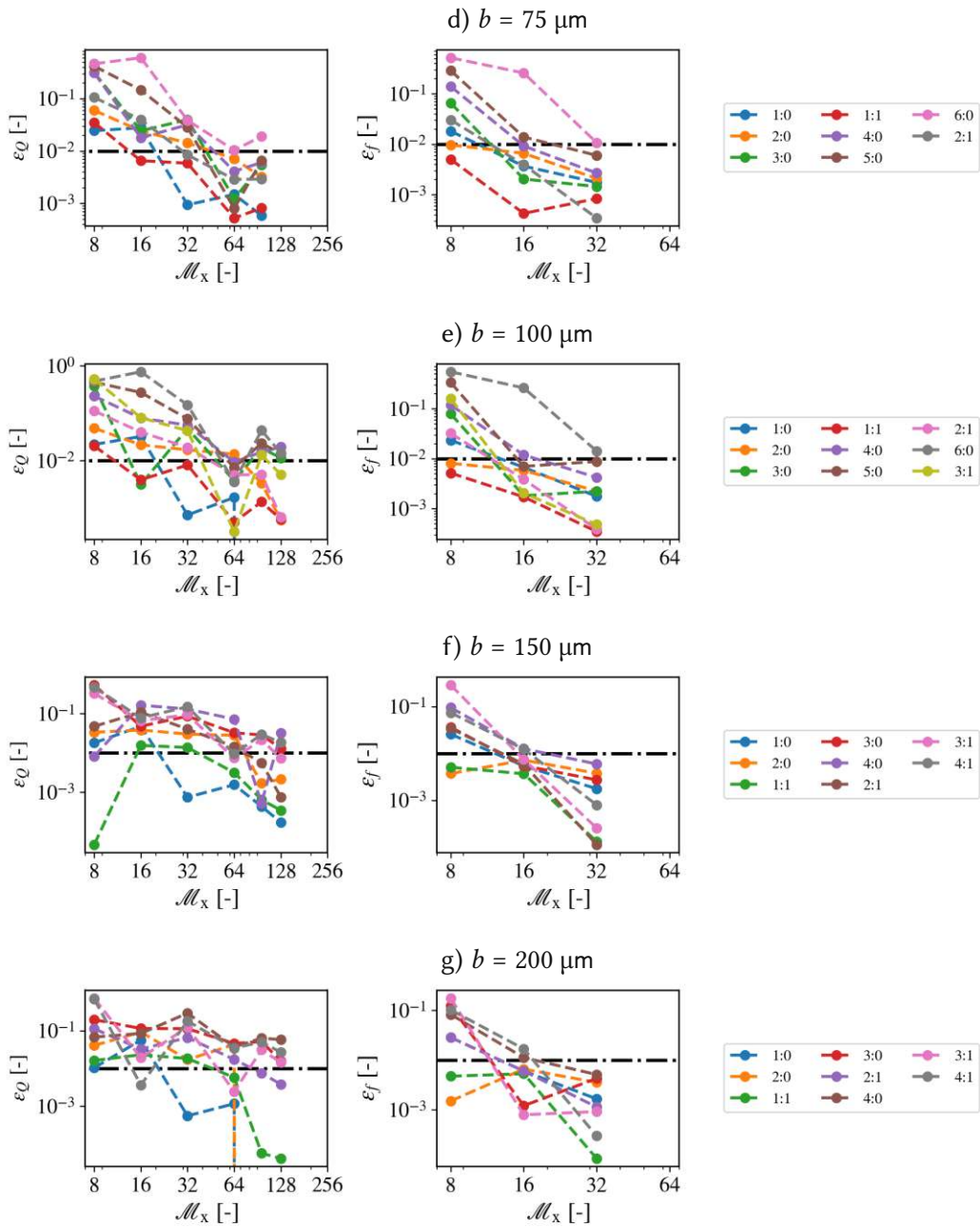


Figure D.2: (Cont.) Convergence of the Q-factor and damped resonance frequency with the fluid grid for the plates in water.

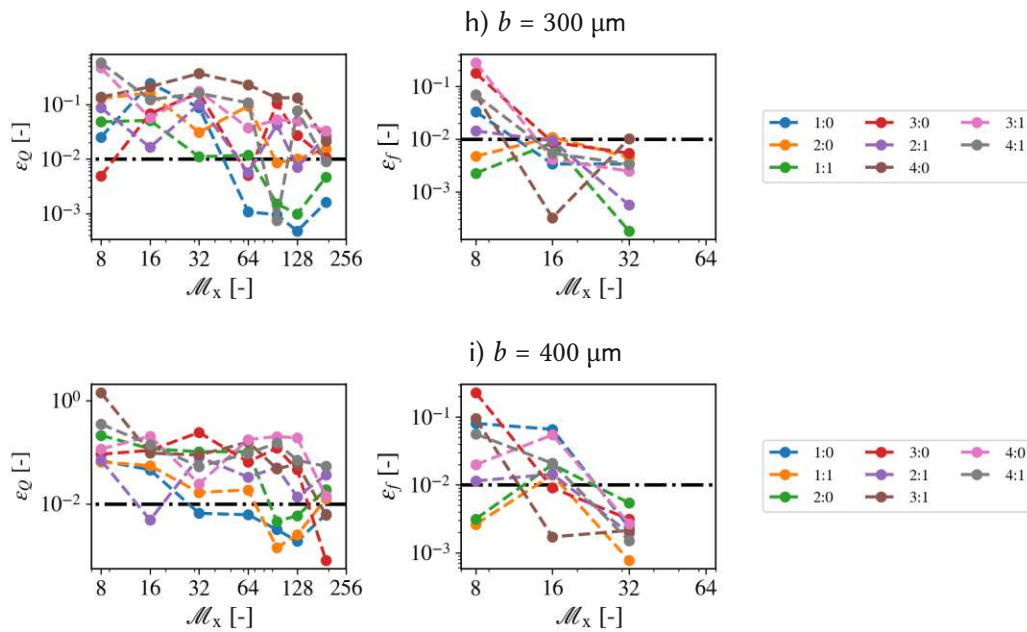


Figure D.2: (Cont.) Convergence of the Q-factor and damped resonance frequency with the fluid grid for the plates in water.

D.3 Experimental results

Here, the convergence of the Q-factor and f_d of the w750 and w500 plates with the 3D method is shown. For these wide plates, while it is possible obtaining a converged f_d (which occurs with $M_x=64$ points), Q does not converge even with a fine fluid grid with 192×768 points (total of 147456 points).

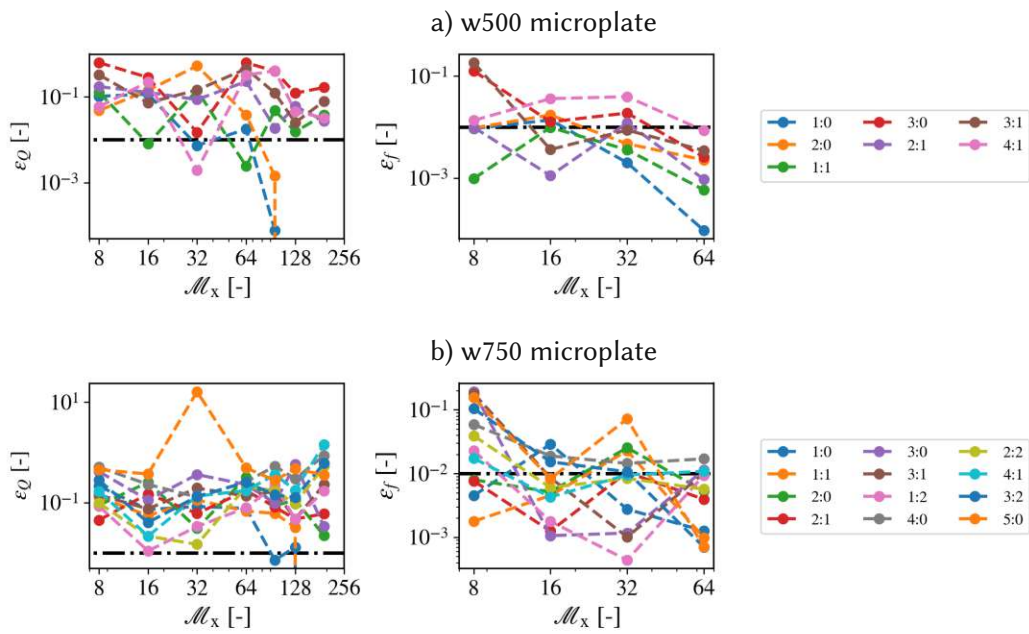


Figure D.3: Convergence of f_d and Q with the fluid grid for the a) w500 and b) w750 microplates in water.

List of Figures

1.1	Different effects explored in MEMS resonators	3
1.2	Common forms of energy dissipation in MEMS resonators	4
1.3	One-dimensional vibrational modes of beams.	5
1.4	Experimental Q-factor of beams and plates in water.	6
1.5	Fifteen vibrational modes of a cantilevered square plate.	7
1.6	Representation of the two-dimensional and three-dimensional fluid flow around a cantilever.	8
1.7	Semi-analytic methods for the transverse modes of micro-beams and micro-plates in viscous fluids.	10
1.8	Two different semi-numerical methods are proposed for investigating the dynamics of non-slender geometries in viscous fluids: a) assuming a two-dimensional fluid flow and b) assuming a three-dimensional fluid flow.	12
2.1	Elastic structure immersed in a viscous fluid.	17
2.2	Representation of the neutral axis and cross-sections in an Euler-Bernoulli beam and in a Timoshenko beam.	18
2.3	Representation of a deformed and b) undeformed thin plate.	19
2.4	Shear coefficient as a function of the aspect ratio and thickness ratio.	20
2.5	Fluid flow regimes due to rarefaction effects	22
2.6	Knudsen number of the fluid flow around micro-plates in air.	23
2.7	Mach number of the fluid flow around MEMS resonators as a function of frequency.	24
2.8	Structural wavelength of the first three modes of a cantilevered plate	24
2.9	Acoustic and flexural wavelengths of different plates in air.	26
2.10	Limiting frequency f_c of the different plates in air and in water.	27
2.11	Characteristic velocity u_{char} for the limiting Reynolds number of 0.01 in air and water. The black dashed line represents $u_{\text{char}} = 10 \mu\text{m s}^{-1}$ as a reference value.	28
2.12	Classification of the fluid flow around micro-plates	29
2.13	Representation of a thin micro-plate immersed in a viscous fluid and subject to an arbitrary load F	29
2.14	Surfaces and fluid stress acting on the surfaces of a plate	31
2.15	Kinematic interface conditions of the fluid flow around a micro-plate.	32
3.1	Plate's boundaries.	36
3.2	Partitioning of the plate's domain.	38
3.3	Example of the partitioning of the plate's domain.	38
3.4	Example of Lagrangian polynomial basis functions of different degrees.	39
3.5	Jump and average operators representation.	40
3.6	Simply supported square plate.	44
3.7	Static displacement of the simply supported static plate.	44

3.8	Convergence of the IP and LO methods with the polynomial function of second degree.	45
3.9	Convergence of the IP and LO methods with the polynomial function of second degree.	46
3.10	Elapsed time for the LO and IP method with different.	46
3.11	Error with the analytic solution for the LO and IP method with different.	46
3.12	Dimensions of a cantilevered plate used in the convergence analysis.	47
3.13	Spectral dynamic displacement of the plate's tip with the IP and LO methods.	47
3.14	Convergence of the IP method at different frequencies	48
3.15	Convergence of the LO method at different frequencies	48
3.16	Computation time of the IP and LO methods.	48
3.17	Dimensions of a cantilevered plate used in the eigenvalue analysis.	49
3.18	Resonance frequencies and difference obtained with the IP method and COMSOL multiphysics software.	50
3.19	Mode shapes of a cantilevered wide plate	50
4.1	a) The fluid flow is confined to a plane (in blue), which is parallel to the $y - z$ plane. b) Pressure and vorticity act both on the top and bottom surfaces of the plate. \mathbf{n} and \mathbf{s} stand for normal and transverse directions at each surface.	53
4.2	Quadrature points y_i and limiting points $y_j^{(l)}$ in the uniform discretization scheme.	57
4.3	Velocity and pressure jump when the plate vibrates with the third vibrational mode.	58
4.4	Velocity and pressure jump when the plate vibrates with the tenth vibrational mode.	60
4.5	Velocity and pressure jump when the plate vibrates with the sixth vibrational mode.	61
4.6	Quadrature points y_i and limiting points $y_j^{(l)}$ in the Chebyshev-Gauss quadrature.	62
4.7	Result and convergence of the integral of the pressure jump in y -direction for the third vibrational mode of the example plate.	63
4.8	Result and convergence of the integral of the pressure jump in y -direction for the tenth vibrational mode of the example plate.	63
4.9	Result and convergence of the integral of the pressure jump in y -direction for the sixth vibrational mode of the example plate.	64
4.10	Result and convergence of the integral of the pressure jump in x -direction	65
4.11	Result and convergence of the integral of the pressure jump in two dimensions.	66
5.1	Representation of the fluid grid defined with \mathcal{M}_x points in x -direction and \mathcal{M}_y points in y -direction.	70
5.2	In air, convergence as a function of the number of elements N_x in the FE-mesh of the plate with $r_a = 2$	71

5.3	In water, convergence as a function of the number of elements N_x in the FE-mesh of the plate with $r_a = 2$	72
5.4	In air, convergence as a function of the number of points \mathcal{M}_x in the fluid grid of the plate with $r_a = 2$	72
5.5	In water, convergence as a function of the number of points \mathcal{M}_x in the fluid grid of the plate with $r_a = 2$	73
5.6	Dimensions of a cantilevered plate used in the convergence analysis.	73
5.7	Spectral dynamic displacement of the slender plate's tip with air and in water.	74
5.8	Lumped element model of the micro-plate in a viscous fluid.	75
5.9	Spectrum displacement \hat{w}_t , Q-factor and f_d for the a) 1:0, b) 2:0 and c) 3:0 vibrational modes as a function of the fluid grid in water.	76
5.10	Convergence of quality factor ϵ_Q for the slender beam in water.	77
5.11	Quality factor of the vibrational modes of the plate with $r_a = 8$ in water obtained with the proposed method and Sader's method.	77
5.12	Convergence of the damped resonance frequency ϵ_f for the slender beam in water. The dotted black line stands for $\epsilon_f = 0.001$, the value at which we consider that the resonance frequency for this mode converged	78
5.13	Added-mass of the vibrational modes of the plate with $r_a = 8$ in water.	78
5.14	a) Q-factor Q and b) fluid-added-mass-per-plate-mass-ratio \mathcal{M} of flexural modes of a slender plate predicted by a purely numerical method [35] and with the present method.	79
5.15	Quality factor Q of different vibrational modes of a wide micro-plate in isopropanol.	80
5.16	Added mass ratio \mathcal{M} of roof tile-shaped modes of a rectangular micro-plate in isopropanol.	80
5.17	Q-factor of the roof tile-shaped modes of a rectangular micro-plate in isopropanol. Experimental and purely numerical results are obtained from Ruiz Diez et al. [42].	81
6.1	Example of plates with different aspect ratios which are investigated	85
6.2	Dimensions of the cantilevered plates used in the beam-plate transition analysis.	85
6.3	Displacement spectrum of the a) slender beam with $b = 12.5 \mu\text{m}$ and b) wide plate with $b = 400 \mu\text{m}$ in air.	86
6.4	Vibrational modes of the plate with $b = 400 \mu\text{m}$ in air.	87
6.5	Absolute displacement spectrum \hat{w}_t of plates with width ranging from $12.5 \mu\text{m}$ to $400 \mu\text{m}$ in air.	88
6.6	Q-factor of the a) slender beam with $b = 12.5 \mu\text{m}$ and b) wide plate with $b = 400 \mu\text{m}$ in air.	89
6.7	Quality factor of EB and torsional modes as the structure is altered from a slender beam with $b = 12.5 \mu\text{m}$ to a plate with $b = 400 \mu\text{m}$ in air	90
6.8	Absolute displacement spectrum \hat{w}_t of plates with width ranging from $12.5 \mu\text{m}$ to $400 \mu\text{m}$ in water.	91
6.9	Vibrational modes of the plate with $b = 400 \mu\text{m}$ in water.	92

6.10	Quality factor of EB and torsional modes as the structure is altered from a slender beam with $b = 12.5 \mu\text{m}$ to a plate with $b = 400 \mu\text{m}$ in water . . .	93
6.11	Illustration of the beam-plate transition effect on the Q-factor in air and in water.	94
6.12	Damping coefficient of EB and torsional modes as the structure is altered from a slender beam with $b = 12.5 \mu\text{m}$ to a plate with $b = 400 \mu\text{m}$ in air and in water	94
6.13	Fluid-added-mass-per-plate-mass-ratio \mathcal{M} of the EB and torsional modes of micro-plates.	95
6.14	Fluid flow representation around the free edge of a micro-plate vibrating in the 5:1 mode.	96
6.15	Fluid flow for the 1:0 mode around plates with different widths in air. . .	97
6.16	Energy density for the 2:0 mode around plates with different widths in air. 99	
6.17	Dissipated energy per unit length, stored energy per unit length and the ratio of the 1:0 mode in plates with different widths.	100
6.18	Energy for the 2:0 mode around plates with different widths in water. . .	101
6.19	Dissipated energy per unit length, stored energy per unit length and the ratio of the 2:0 mode in plates with different widths.	102
6.20	a) Q , b) γ and d) $m \omega_d$ of the EB modes of the plates as a function of the oscillatory Reynolds number β	103
6.21	a) Q , b) γ and d) $m \omega_d$ of the EB modes of the plates as a function of the oscillatory Reynolds number β	104
7.1	Density and viscosity of different gases and liquids	106
7.2	Twenty lowest-order vibrational modes of a cantilevered silicon micro-plate clamped at its left edge and free on all others.	108
7.3	Convergence of the GMD method in air and in water with the number of modes.	108
7.4	Convergence of the present method for a micro-plate in air and in water with the fluid grid $\mathcal{N}_x \times \mathcal{N}_y$	108
7.5	Spectral displacement of the plate with GMD and FEM in a) air and b) water.	109
7.6	Displacement spectrum of a micro-plate in air, neon and hydrogen. . . .	110
7.7	Q-factor of the micro-plate in a) air, b) neon and c) hydrogen vibrating in EB, torsional and RTS and HOP modes.	110
7.8	Displacement spectrum of the micro-plate in a) acetone, b) ethanol and c) isopropanol.	112
7.9	Q-factor of the micro-plate in a) acetone, b) ethanol and c) isopropanol. 113	
7.10	Q-factor of the micro-plate in air and water, and representation of the gas-liquid modal Q-factor inversion effect.	114
7.11	Damping coefficient of the micro-plate in vibrating in EB, torsional and RTS and HOP modes in air.	115
7.12	6:0, 6:1, 5:2 and 3:3 vibrational modes in air.	115
7.13	Energy density for the different modes in air.	116
7.14	Fluid flow for the different modes in air.	117

7.15	Damping coefficient of the micro-plate in vibrating in EB, torsional and RTS and HOP modes in water.	118
7.16	Added-mass coefficient of the micro-plate in vibrating in EB, torsional and RTS and HOP modes in water.	118
7.17	8:0, 5:2 and 2:3 vibrational modes in water.	118
7.18	Energy density for the different modes in water.	119
7.19	Spectral displacement of a micro-plate in a continuously changing fluid, from air to water.	120
7.20	Ratio of the a) Q-factor, b) added-mass coefficients and c) damping coefficient of the vibrational modes over frequency in the gas-liquids transition.	121
8.1	Prototypes fabricated for experimental analysis	123
8.2	Tailored electrodes for symmetric and anti-symmetric excitation.	124
8.3	w750 micro-plate immersed in a droplet of water during measurements.	124
8.4	Experimental data of the w750 micro-plate in water	125
8.5	Experimentally obtained Q-factor of the a) w500 and b) w750 micro-plates in water.	126
8.6	Difference in f_d , $\text{Diff}(f_d)$, for the a) w500 and b) w750 micro-plate in water.	127
8.7	Difference in Q , $\text{Diff}(Q)$, for the a) w500 and b) w750 micro-plate in water.	127
8.8	Experimentally obtained Q-factor of the a) w500 and b) w750 micro-plates in air.	128
8.8	Experimental data of the w750 micro-plate in air	129
8.9	Flexural and acoustic wavelengths of the vibrational modes of the micro-plate w750 in air.	130
8.10	Polycrystalline diamond micro-plate with minimized static out-of-plane displacement.	131
8.11	a) Q-factor and b) flexural and acoustic wavelengths of the diamond micro-plate in air.	131
9.1	Representation of fluid the flow around a) beam and b) a plate. Green arrows indicate the fluid flow which is not characterized by the 2D fluid flow approximation.	135
9.2	Body immersed in a fluid	137
9.3	Forces acting on the top and bottom plate surfaces, Σ^t and Σ^b , respectively.	138
9.4	Plate's top surface partitioning, force discretization and the boundary element method.	138
9.5	Plate's midplane partitioning, force discretization and the slender body method.	139
9.7	a) Plate's partitioning $\mathcal{F}(\Omega_p)$ and b) integration scheme around the singularity when $\mathbf{x}_i^{\text{mp}} \in S_j$. The yellow circular region corresponds to the analytic integration domain. In the orange region, numerical integration is performed with triangular elements, and in the remaining domain, rectangular elements are employed.	142

9.8	Quadrature points x_i and limiting points $x_j^{(l)}$ in the Chebyshev-Gauss quadrature.	143
9.9	Real part of the pressure jump $\mathcal{R}(\Delta\hat{p})$ with the a) 2D and b) 3D fluid formulation for the mode 2:0 in air.	144
9.10	Cross-sections parallel to the x and y directions.	145
9.11	Real part of the pressure jump $\mathcal{R}(\Delta\hat{p})$ with the 2D and 3D fluid formulation for a slender beam in air.	146
9.12	Real part of the pressure jump $\mathcal{R}(\Delta\hat{p})$ with the 2D and 3D fluid formulation for a wide plate in air.	147
10.1	Resultant force $ F_{\text{resultant}} $ and convergence error $\epsilon_{\text{resultant}}$ for the a) 1:0, b) 1:1 and c) 2:0 mode.	150
10.2	Convergence as a function of the number of elements N_x in the FE-mesh of the plate with $r_a = 1/2$	152
10.3	Convergence as a function of the number of points \mathcal{M}_x in the fluid grid of the plate with $r_a = 1/2$ in air and water.	153
10.4	Dimensions of a cantilevered plate used in the convergence analysis.	154
10.5	Displacement spectrum of the slender beam with $b = 15 \mu\text{m}$ in water.	154
10.6	Spectrum displacement \hat{w}_t , Q-factor and f_d for the a) 1:0, b) 2:0, c) 3:0, d) 4:0 and e) 5:0 vibrational modes as a function of the fluid grid in water.	155
10.7	Convergence of the a) damped resonance frequency and b) Q-factor of the slender beam in water.	156
10.8	Quality factor of the vibrational modes of the slender beam in water obtained with the 3D fluid formulation, the 2D fluid formulation and Sader's method.	156
11.1	Example of plates with different widths a) $b = 15 \mu\text{m}$, b) $b = 100 \mu\text{m}$, c) $b = 200 \mu\text{m}$ and d) $b = 400 \mu\text{m}$ here investigated.	159
11.2	Symmetric and anti-symmetric forces applied at the plate's free corners.	159
11.3	Displacement spectrum of the slender beam with a) $b = 15 \mu\text{m}$, b) $b = 50 \mu\text{m}$, c) $b = 100 \mu\text{m}$ and d) $b = 200 \mu\text{m}$ in water under symmetric excitation.	160
11.4	Displacement spectrum of the slender beam with a) $b = 15 \mu\text{m}$, b) $b = 50 \mu\text{m}$, c) $b = 100 \mu\text{m}$ and d) $b = 200 \mu\text{m}$ in water under anti-symmetric excitation.	161
11.5	Difference in f_d obtained between 2D and 3D methods in water	162
11.6	In-phase fluid flow along the plate's center line ($y = 0$) for modes a) 1:0, b) 2:0, c) 3:0, d) 4:0 and e) 5:0.	164
11.7	Average computation time per frequency step for different values of \mathcal{M}_x	165
11.8	Quality factor of the vibrational modes of the plate with a) $b = 25 \mu\text{m}$, b) $b = 50 \mu\text{m}$, c) $b = 75 \mu\text{m}$ and d) $b = 100 \mu\text{m}$ in water obtained with the 3D and 2D fluid formulation.	166
11.9	Quality factor of the vibrational modes of the plate with a) $b = 150 \mu\text{m}$, b) $b = 200 \mu\text{m}$, c) $b = 300 \mu\text{m}$ and d) $b = 400 \mu\text{m}$ in water obtained with the 3D and 2D fluid formulation.	167

11.10	Quality factor of EB and torsional modes as the structure is altered from a slender beam with $b = 15 \mu\text{m}$ to a plate with $b = 400 \mu\text{m}$ in air	168
11.11	Difference in Q-factor obtained between 2D and 3D methods in air	169
11.12	Quality factor of EB and torsional modes as the structure is altered from a slender beam with $b = 12.5 \mu\text{m}$ to a plate with $b = 400 \mu\text{m}$ in air	170
11.13	Difference in Q-factor obtained between 2D and 3D methods in air	171
11.14	Difference in f_d for the w500 plate with the a) 2D and b) 3D fluid formulation.	171
11.15	Difference in f_d for the w750 plate with the a) 2D and b) 3D fluid formulation.	172
B.1	Convergence of the a) Q-factor and b) damped resonance frequency of the microplate used in [30]	183
B.2	Convergence of the a) Q-factor and b) damped resonance frequency of the microplate used in [66]	184
B.3	Convergence of the Q-factor and damped resonance frequency with the fluid grid for the plates in air.	185
B.4	Convergence of the Q-factor and damped resonance frequency with the fluid grid for the plates in water.	188
C.1	Influence of the τ_{Szz} in the displacement field	192
C.2	Average computation time per frequency step for different values of τ_{Szz}	192
D.1	Convergence of the Q-factor and damped resonance frequency with the fluid grid for the plates in air.	193
D.2	Convergence of the Q-factor and damped resonance frequency with the fluid grid for the plates in water.	196
D.3	Convergence of f_d and Q with the fluid grid for the a) w500 and b) w750 microplates in water.	199

List of Tables

1.1	Summary of existing semi-analytic methods for the micro-beams and micro-plates in fluids	8
2.1	Dimensions of beams and plates used in MEMS resonators.	20
2.2	Silicon properties approximated as an isotropic material	20
2.3	Properties of air and water at SATP.	23
3.1	Material properties of silicon as anisotropic material.	35
6.1	Average vacuum resonance frequencies and standard deviation of the beam-like modes 1:0 to 6:0 of the plates with aspect ratio from $r = 64/1$ to $r = 64/32$	87
A.1	Absolute viscosity μ_f , density ρ_f and kinematic viscosity ν_f of selected liquids and gases at SATP conditions [66].	181

List of symbols

\hat{w}	Spectral displacement
\hat{F}	Spectral force
m	Structure's (plate, beam) mass
f	Frequency
f_0	Resonance frequency
Q	Quality factor, Q-factor
Δf_0	Variation of the resonance frequency
E_{st}	Maximum stored energy
E_d	Dissipated energy in one oscillation cycle
$E_{d,surface}$	Dissipated energy in one cycle through surface losses
$E_{d,material}$	Dissipated energy in one cycle through material losses
$E_{d,anchor}$	Dissipated energy in one cycle through anchor losses
$E_{d,TED}$	Dissipated energy in one cycle through thermoelastic dissipation
$E_{d,viscous}$	Dissipated energy in one cycle through viscous fluidic dissipation
$E_{d,acoustic}$	Dissipated energy in one cycle through acoustic fluidic dissipation
T	Temperature
θ	Angle of rotation of the beam/Non-slender around the x -axis
v	Displacement of the beam/Non-slender in y -direction
w	Displacement of the beam/Non-slender in z -direction
l	Plate's length
b	Plate's width
h	Plate's thickness
E	Young's modulus
I	Moment of inertia
ρ	Beam or plate's density
F	External driving force
SF	Shear forces coefficient
κ	Timoshenko shear coefficient

G	Shear modulus
Ω_p	Plate's neutral plane or midplane
\mathbf{n}_p	Plate's transverse normal
ν	Poisson coefficient
r_a	Plate's aspect ratio
r_t	Plate's thickness ratio
Kn	Knudsen number
λ_{mfp}	Mean free path in a fluid
l_{char}	Characteristic length of a system
u_{wall}	Flow velocity at the wall
U_0	Free stream flow
ρ_f	Fluid's density
μ_f	Fluid's dynamic viscosity
ν_f	Fluid's kinematic viscosity
Ma	Mach number
c_s	Speed of sound in the fluid
λ_{ac}	Acoustic wavelength
λ_{st}	Spatial wavelength of the structure
δ_{char}	Characteristic displacement of the structure
u_{char}	Characteristic velocity of the structure
f_c	Limiting frequency between incompressible and compressible flows
f^{vac}	Resonance frequency in vacuum
f^f	Resonance frequency in a fluid
\mathbf{u}	Velocity field
p	Pressure
\mathbf{u}'	Non-dimensional velocity field
p'	Non-dimensional pressure
t'	Non-dimensional time
∇'	Non-dimensional gradient operator
γ_f	Ratio of specific heats
F_{hydro}	Hydrodynamic force acting on the plate
Σ^t	Plate's top surface
Σ^b	Plate's bottom surface
Σ^l	Plate's left surface
Σ^r	Plate's right surface
Σ^f	Plate's surface at the free end

$\hat{\sigma}^t$	Stress acting on the plate's top surface
$\hat{\sigma}^b$	Stress acting on the plate's bottom surface
$\hat{\sigma}^r$	Stress acting on the plate's right surface
$\hat{\sigma}^l$	Stress acting on the plate's left surface
$\hat{\sigma}^f$	Stress acting on the plate's free end surface
C	Fourth-order elasticity tensor
$\alpha\beta\gamma\delta$	Indices in the index notation to represent x and y directions
$C_{\alpha\beta\gamma\delta}$	Elements of the fourth-order elasticity tensor
$\delta_{\alpha\gamma}$	Kronecker delta
$\partial\Omega_p$	Union of all the boundaries of the plate's midplane
Γ_c	Edges of the plate's midplane where the displacement is restricted
g	Value of the displacement at one of the plate's boundaries
\mathbf{n}^b	Outward normal unity vector at the plate's boundaries
Γ_θ	Edges of the plate's midplane where the rotation angle is restricted
θ	Value of the rotation angle at one of the plate's boundaries
M	Specified moment at one of the plate's boundaries
Q_s	Specified shear force at one of the plate's boundaries
Γ_M	Edges of the plate's midplane where the momentum is restricted
Γ_Q	Edges of the plate's midplane where the shear force is restricted
\mathcal{W}	Hilbert space
\bar{w}	function in the Hilbert space
v	function in the Hilbert space
$a(,)$	bilinear form of a PDE
$l()$	linear form of a PDE
\mathcal{W}^h	Trial function space
\mathcal{V}^h	Test function space
\hat{w}^h	Trial function
v^h	Test function
$\mathcal{P}(\Omega_p)$	Partitioning of the plate's domain
E_i	Single triangular element of the plate's partitioning

N_x	Number of quadrilateral elements in x -direction
N_y	Number of quadrilateral elements in y -direction
N_t	Total number of triangular elements in $\mathcal{P}(\Omega_p)$
e_i	Single internal edge of $\mathcal{P}(\Omega_p)$
$\tilde{\Gamma}$	Union of all internal edges of $\mathcal{P}(\Omega_p)$
Γ	Union of all internal and external edges of $\mathcal{P}(\Omega_p)$
P^k	Lagrangian FE shape functions
k	Degree of the Lagrangian FE shape functions
x^*	Non-dimensional x -axis
y^*	Non-dimensional y -axis
\mathbf{n}^e	Normal unity vector at the internal edges e_i
$\langle - \rangle$	Average operator
$[[-]]$	Jump operator
τ^{IP}	Interior penalty coefficient
\mathcal{R}^h	Lifting operator trial function space
\mathcal{S}^h	Lifting operator test function space
r	Lifting operator trial function
s	Lifting operator test function
τ^{LO}	Lifting operator coefficient
E^θ	Elements at the clamped edge Γ_θ
w^{analytic}	Analytically obtained displacement
$\epsilon^{\text{analytic}}$	Error between analytic and numeric solution
$\epsilon^{\text{convergence}}$	Convergence error
\mathbf{K}	Elasticity matrix
\mathbf{M}	Mass matrix
λ	Eigenvalues
Φ	Eigenvectors
\hat{u}_x	x component of the fluid velocity
\hat{u}_y	y component of the fluid velocity
\hat{u}_z	z component of the fluid velocity
$\hat{\omega}$	Vorticity vector
$\hat{\psi}$	Stream vector
Ψ	Fundamental solution to the stream-function formulation of the Stokes equations
$\hat{\omega}_x$	x component of the vorticity
$\hat{\psi}_x$	x component of the stream vector

K_0	Modified Bessel function of the third kind and order zero
y'	Additional axis similar to y
z'	Additional axis similar to z
x^c	Position of a two-dimensional fluid flow cross-section
C	Cross-section of a plate
C^b	Lower edge of a plate's cross section
C^t	Top edge of a plate's cross section
$\hat{\omega}_x^t$	x component of the vorticity on the top surface of a plate
$\hat{\omega}_x^b$	x component of the vorticity on the lower surface of a plate
$\nabla \hat{\omega}_x$	x -component of the vorticity jump between top and lower surfaces of a plate
s	Tangent direction at the top and lower edge of a plate's cross section
n	Normal direction into the fluid flow at the top and lower edge of a plate's cross section
\mathcal{M}_y	Number of discretization points in y -direction
y_i	Discretization points in y -direction
$y_i^{(l)}$	Limits defined around each discretization point to be used in the analytic integration of the fundamental solution
\mathcal{F}	Function resultant of the analytic integration of the fundamental solution at a certain discretization scheme
Ker	Real value of the Kelvin function
Kei	Imaginary value of the Kelvin function
\mathbf{A}	Fluid response matrix
$\Delta \hat{\mathbf{p}}$	Pressure jump vector discretized with a certain discretization scheme
$\hat{\mathbf{w}}$	Plate's displacement discretized with a certain discretization scheme
I_y	Integral of the pressure jump in y -direction
ϵ_y	variable introduced to quantify the convergence of the numerical integration procedure in y -direction
\mathcal{M}_x	Number of discretization points in x -direction
x_i	Discretization points in x -direction

I_x	Integral of the pressure jump in x -direction
q_i	1/3 Simpson's rule weighting constants
ϵ_x	variable introduced to quantify the convergence of the numerical integration procedure in x -direction
$F_{\text{resultant}}$	Integral of the pressure jump in x -direction and y -direction
\mathcal{M}_t	Total number of discretization points in x -direction and y -direction
$\epsilon_{\text{resultant}}$	Variable introduced to quantify the convergence of the two-dimensional numerical integration procedure
ϵ_{fg}	Variable introduced to quantify the convergence of the method with the fluid grid
\hat{w}_t	Spectral displacement of the plate's free corner at $x = l$ and $y = b/2$
Δm	Fluid-added mass
γ	Fluidic damping coefficient
k	Modal stiffness
\hat{F}_m	Modal excitation force
m_p	Plate mass
\hat{q}	Displacement of the plate at a certain position
ω_d	Damped angular resonance frequency
m_t	Total mass
q_{dho}	Fit spectral response function
ϵ_Q	Variable introduced to quantify the convergence of the Q-factor of a vibrational mode
\mathcal{M}	Fluid-added-mass-per-plate-mass ratio
ϵ_f	Variable introduced to quantify the convergence of the damped resonance frequency of a vibrational mode
$\hat{\mathbf{u}}_{\text{IP}}$	In-phase fluid flow
$\hat{\mathbf{u}}_{\text{OP}}$	Out-of-phase fluid flow
Σ_k	Kinetic energy density
Σ_D	Dissipated energy density
\mathcal{W}^{md}	Trial function space
\mathcal{V}^{md}	Test function space
\hat{w}^{md}	Trial function
\hat{v}^{md}	Test function
N^{md}	Number of modes

ϵ_{modes}	Convergence error with the number of modes
u	Experimentally measured plate velocity
\bar{u}	Spatial average of the plate velocity
\hat{g}	Amplitude of arbitrary source in a fluid domain
\mathbf{x}_0	Pole position in the fluid domain
\mathbf{x}_f	Field position in the fluid domain
$\bar{\mathbf{p}}$	Distance vector between pole and field position
\mathcal{S}	Free space unsteady Stokeslet
\mathcal{T}	Free space unsteady Stresslet
r	Distance between pole and field points in the fluid domain
\mathbf{A}_{3D}	3D Fluid response matrix
τ_{Szz}	Tolerance constant for convergence of the numerical integration of the Stokeslet

List of acronyms

MEMS	Microelectromechanical systems
IC	Integrated circuit
AFM	Atomic force microscopy
DHO	Damped harmonic oscillator
TED	Thermoelastic dissipation
RTS	Roof tile-shaped (modes)
HOP	higher-order plate (modes)
IF	Inertial forces
VF	Viscous forces
2D	Two dimensional
3D	Three dimensional
FEM	Finite element method
PDE	Partial differential equation
SATP	Standard ambient temperature and pressure
FE	Finite element
C/DC	Continous-discontinuous (method)
IP	Interior penalty
LO	Lifting operator
BIEM	Boundary integral equation method
LEM	Lumped element model
GL-Q-inversion	Gas-liquid modal Q-factor inversion
VSC	Vienna Scientific Cluster
FMM	Fast multipole method

Bibliography

- [1] Y.-C. Tai, *Introduction to MEMS*, pp. 187–206. Berlin, Heidelberg: Springer Berlin Heidelberg, 2012.
- [2] N. Maluf and K. Williams, *An introduction to microelectromechanical systems engineering*. Artech House, 2004.
- [3] S. Fatikow and U. Rembold, *Microsystem technology and microrobotics*. Springer Science & Business Media, 2013.
- [4] D. Platz and U. Schmid, “Vibrational Modes in MEMS Resonators,” *Journal of Micromechanics and Microengineering*, vol. 29, no. 12, p. 123001, 2019.
- [5] O. Brand, I. Dufour, S. M. Heinrich, and F. Josse, eds., *Resonant MEMS: fundamentals, implementation, and application*. Wiley-VCH, 2015.
- [6] A. Raman, J. Melcher, and R. Tung, “Cantilever dynamics in atomic force microscopy,” *Nano Today*, vol. 3, no. 1-2, pp. 20–27, 2008.
- [7] G. E. Fantner, R. J. Barbero, D. S. Gray, and A. M. Belcher, “Kinetics of antimicrobial peptide activity measured on individual bacterial cells using high-speed atomic force microscopy,” *Nature Nanotechnology*, vol. 5, no. 4, pp. 280–285, 2010.
- [8] F. J. Giessibl, “Advances in atomic force microscopy,” *Reviews of Modern Physics*, vol. 75, no. 3, pp. 949–983, 2003.
- [9] S. Priya and D. J. Inman, *Energy harvesting technologies*, vol. 21. Springer, 2009.
- [10] Z. Chen, S. Shatara, and X. Tan, “Modeling of biomimetic robotic fish propelled by an ionic polymer-metal composite caudal fin,” *IEEE/ASME Transactions on Mechatronics*, vol. 15, no. 3, pp. 448–459, 2010.
- [11] A. Erturk and G. Delporte, “Underwater thrust and power generation using flexible piezoelectric composites: An experimental investigation toward self-powered swimmer-sensor platforms,” *Smart Materials and Structures*, vol. 20, no. 12, 2011.
- [12] W. Holzl, R. Behlert, M. Gehring, and G. Schrag, “Enhanced fluid flow by wavelike excitation of a micromechanical bending actuator,” *2019 20th International Conference on Thermal, Mechanical and Multi-Physics Simulation and Experiments in Microelectronics and Microsystems, EuroSimE 2019*, 2019.
- [13] C. Castille, I. Dufour, and C. Lucat, “Longitudinal vibration mode of piezoelectric thick-film cantilever-based sensors in liquid media,” *Applied Physics Letters*, vol. 96, no. 15, pp. 18–21, 2010.
- [14] H. Hosaka, K. Itao, and S. Kuroda, “Damping characteristics of beam-shaped micro-oscillators,” *Sensors and Actuators A: Physical*, vol. 49, no. 1-2, pp. 87–95, 1995.
- [15] F. Patocka, M. Schlögl, C. Schneidhofer, N. Dörr, M. Schneider, and U. Schmid, “Piezoelectrically excited MEMS sensor with integrated planar coil for the detection of ferrous particles in liquids,” *Sensors and Actuators, B: Chemical*, vol. 299, no. August, p. 126957, 2019.
- [16] P. Voigt, G. Schrag, and G. K. Wachutka, “Electrofluidic full-system modelling of a flap valve micropump based on Kirchhoffian network theory,” *Sensors and Actuators, A: Physical*, vol. 66, no. 1-3, pp. 9–14, 1998.
- [17] N. Jaber, S. Ilyas, O. Shekhah, M. Eddaoudi, and M. I. Younis, “Multimode mems resonator for simultaneous sensing of vapor concentration and temperature,” *IEEE Sensors Journal*, vol. 18, no. 24, pp. 10145–10153, 2018.
- [18] A. Hajjam and S. Pourkamali, “Fabrication and characterization of mems-based resonant organic gas sensors,” *IEEE Sensors Journal*, vol. 12, no. 6, pp. 1958–1964, 2011.

- [19] R. A. Bidkar, M. Kimber, A. Raman, A. K. Bajaj, and S. V. Garimella, "Nonlinear aerodynamic damping of sharp-edged flexible beams oscillating at low Keulegan-Carpenter numbers," *Journal of Fluid Mechanics*, vol. 634, pp. 269–289, 2009.
- [20] H. J. Pain and P. Rankin, *Introduction to vibrations and waves*. John Wiley & Sons, 2015.
- [21] G. E. Fantner, G. Schitter, J. H. Kindt, T. Ivanov, K. Ivanova, R. Patel, N. Holten-Andersen, J. Adams, P. J. Thurner, I. W. Rangelow, and P. K. Hansma, "Components for high speed atomic force microscopy," *Ultramicroscopy*, vol. 106, no. 8-9, pp. 881–887, 2006.
- [22] Y. H. Chen and W. H. Huang, "Resonant response of rectangular AFM cantilever in liquid," *Chinese Physics Letters*, vol. 24, no. 2, pp. 363–365, 2007.
- [23] H. S. Wasisto, S. Merzsch, A. Waag, E. Uhde, T. Salthammer, and E. Peiner, "Airborne engineered nanoparticle mass sensor based on a silicon resonant cantilever," *Sensors and Actuators B: Chemical*, vol. 180, pp. 77–89, 2013. Transducers 2011.
- [24] G. Pfusterschmied, J. Toledo, M. Kucera, W. Steindl, S. Zemann, V. Ruiz-Díez, M. Schneider, A. Bittner, J. L. Sanchez-Rojas, and U. Schmid, "Potential of piezoelectric MEMS resonators for grape must fermentation monitoring," *Micromachines*, vol. 8, no. 7, p. 200, 2017.
- [25] G. Pfusterschmied, C. Weinmann, M. Hospodka, B. Hofko, M. Schneider, and U. Schmid, "Sensing Fluid Properties of Super High Viscous Liquids Using Non-Conventional Vibration Modes in Piezoelectrically Excited MEMS Resonators," *Proceedings of the IEEE International Conference on Micro Electro Mechanical Systems (MEMS)*, vol. 2019-Janua, no. January, pp. 735–738, 2019.
- [26] S. Schmid, K. Jensen, K. Nielsen, and A. Boisen, "Damping mechanisms in high-q micro and nanomechanical string resonators," *Physical Review B*, vol. 84, no. 16, p. 165307, 2011.
- [27] I. Dufour, E. Lemaire, B. Caillard, H. Debéda, C. Lucat, S. M. Heinrich, F. Josse, and O. Brand, "Effect of hydrodynamic force on microcantilever vibrations: Applications to liquid-phase chemical sensing," *Sensors and Actuators B: Chemical*, vol. 192, pp. 664–672, 2014.
- [28] A. Frangi, A. Bugada, M. Martello, and P. Savadkoobi, "Validation of pml-based models for the evaluation of anchor dissipation in mems resonators," *European Journal of Mechanics-A/Solids*, vol. 37, pp. 256–265, 2013.
- [29] C. Zener, "Internal friction in solids. i. theory of internal friction in reeds," *Physical review*, vol. 52, no. 3, p. 230, 1937.
- [30] G. Pfusterschmied, C. Weinmann, M. Schneider, D. Platz, N. Shen, J. Sader, and U. Schmid, "Sound dissipation from plate-type resonators excited in non-conventional transversal modes in liquids," *Journal of Micromechanics and Microengineering*, vol. 30, no. 7, 2020.
- [31] J. E. Sader, "Frequency response of cantilever beams immersed in viscous fluids with applications to the atomic force microscope," *Journal of Applied Physics*, vol. 84, no. 1, pp. 64–76, 1998.
- [32] C. P. Green and J. E. Sader, "Small amplitude oscillations of a thin beam immersed in a viscous fluid near a solid surface," *Physics of Fluids*, vol. 17, no. 7, pp. 1–12, 2005.
- [33] C. P. Green and J. E. Sader, "Torsional frequency response of cantilever beams immersed in viscous fluids with applications to the atomic force microscope," *Journal of applied physics*, vol. 92, no. 10, pp. 6262–6274, 2002.
- [34] G. Wu, J. Xu, E. J. Ng, and W. Chen, "Mems resonators for frequency reference and timing applications," *Journal of Microelectromechanical Systems*, vol. 29, no. 5, pp. 1137–1166, 2020.
- [35] S. Basak, A. Raman, and S. V. Garimella, "Hydrodynamic loading of microcantilevers vibrating in viscous fluids," *Journal of Applied Physics*, vol. 99, no. 11, p. 114906, 2006.
- [36] M. K. Ghatkesar, T. Braun, V. Barwich, J. P. Ramseyer, C. Gerber, M. Hegner, and H. P. Lang, "Resonating modes of vibrating microcantilevers in liquid," *Applied Physics Letters*, vol. 92, no. 4, pp. 10–13, 2008.

- [37] J. W. Chon, P. Mulvaney, and J. E. Sader, “Experimental validation of theoretical models for the frequency response of atomic force microscope cantilever beams immersed in fluids,” *Journal of Applied Physics*, vol. 87, no. 8, pp. 3978–3988, 2000.
- [38] I. Dufour, F. Josse, S. M. Heinrich, C. Lucat, C. Ayela, F. M enil, and O. Brand, “Unconventional uses of microcantilevers as chemical sensors in gas and liquid media,” *Sensors and Actuators B: Chemical*, vol. 170, pp. 115–121, 2012.
- [39] L. A. Beardslee, K. S. Demirci, Y. Luzinova, B. Mizaikoff, S. M. Heinrich, F. Josse, and O. Brand, “Liquid-phase chemical sensing using lateral mode resonant cantilevers,” *Analytical Chemistry*, vol. 82, no. 18, pp. 7542–7549, 2010.
- [40] T. Manzanque, V. Ruiz, J. Hernando-Garc a, A. Ababneh, H. Seidel, and J. S anchez-Rojas, “Characterization and simulation of the first extensional mode of rectangular micro-plates in liquid media,” *Applied Physics Letters*, vol. 101, no. 15, p. 151904, 2012.
- [41] M. Kucera, E. Wistrela, G. Pfusterschmied, V. Ruiz-D iez, J. L. S anchez-Rojas, J. Schalko, A. Bittner, and U. Schmid, “Characterisation of multi roof tile-shaped out-of-plane vibrational modes in aluminium-nitride-actuated self-sensing micro-resonators in liquid media,” *Applied Physics Letters*, vol. 107, no. 5, pp. 1–5, 2015.
- [42] V. Ruiz-D iez, J. Hernando-Garc a, J. Toledo, T. Manzanque, M. Kucera, G. Pfusterschmied, U. Schmid, and J. L. S anchez-Rojas, “Modelling and characterization of the roof tile-shaped modes of AlN-based cantilever resonators in liquid media,” *Journal of Micromechanics and Microengineering*, vol. 26, no. 8, p. 084008, 2016.
- [43] A. W. Leissa, “The Free vibration of rectangular plates,” *Journal of Sound and Vibration*, vol. 31, no. 3, pp. 257–293, 1973.
- [44] S. N. Ahsan and M. Aureli, “Three-dimensional analysis of hydrodynamic forces and power dissipation in shape-morphing cantilevers oscillating in viscous fluids,” *International Journal of Mechanical Sciences*, vol. 149, pp. 436–451, 2018.
- [45] W. H. Chu, “Vibration of fully submerged cantilever plates in water,” tech. rep., South-West Research Institute, 1963.
- [46] U. S. Lindholm, D. D. Kana, W.-H. Chu, and H. N. Abramson, “Elastic vibration characteristics of cantilever plates in water,” *Journal of Ship Research*, vol. 9, no. 02, pp. 11–36, 1965.
- [47] C. A. Van Eysden and J. E. Sader, “Frequency response of cantilever beams immersed in viscous fluids with applications to the atomic force microscope: Arbitrary mode order,” *Journal of applied physics*, vol. 101, no. 4, p. 044908, 2007.
- [48] R. C. Tung, A. Jana, and A. Raman, “Hydrodynamic loading of microcantilevers oscillating near rigid walls,” *Journal of Applied Physics*, vol. 104, no. 11, p. 114905, 2008.
- [49] R. J. Clarke, O. E. Jensen, J. Billingham, A. P. Pearson, and P. M. Williams, “Stochastic elastohydrodynamics of a microcantilever oscillating near a wall,” *Physical Review Letters*, vol. 96, no. 5, pp. 2–5, 2006.
- [50] R. J. Clarke, V. Bachtiar, T. C. Lee, J. E. Cater, and J. Minton, “Response of a fluid-immersed microcantilever close to a deformable body,” *Journal of Applied Physics*, vol. 117, no. 9, 2015.
- [51] F. Cellini, C. Intartaglia, L. Soria, and M. Porfiri, “Effect of hydrodynamic interaction on energy harvesting in arrays of ionic polymer metal composites vibrating in a viscous fluid,” *Smart Materials and Structures*, vol. 23, no. 4, p. 045015, 2014.
- [52] C. Intartaglia, L. Soria, and M. Porfiri, “Hydrodynamic coupling of two sharp-edged beams vibrating in a viscous fluid,” *Proceedings of the Royal Society A: Mathematical, Physical and Engineering Sciences*, vol. 470, no. 2162, p. 20130397, 2014.

- [53] M. T. Clark and M. R. Paul, “The stochastic dynamics of an array of atomic force microscopes in a viscous fluid,” *International Journal of Non-Linear Mechanics*, vol. 42, no. 4, pp. 690–696, 2007.
- [54] C. A. Van Eysden and J. E. Sader, “Frequency response of cantilever beams immersed in compressible fluids with applications to the atomic force microscope,” *Journal of Applied Physics*, vol. 106, no. 9, p. 094904, 2009.
- [55] S. N. Ahsan and M. Aureli, “Finite amplitude torsional oscillations of shape-morphing plates immersed in viscous fluids,” *Physics of Fluids*, vol. 32, no. 5, p. 053101, 2020.
- [56] S. N. Ahsan and M. Aureli, “Small amplitude oscillations of a shape-morphing plate immersed in a viscous fluid near a solid wall,” *Journal of Applied Physics*, vol. 124, no. 13, p. 134502, 2018.
- [57] S. N. Ahsan and M. Aureli, “Torsional oscillations of a shape-morphing plate in viscous fluids,” *ASME 2019 Dynamic Systems and Control Conference, DSCC 2019*, vol. 2, pp. 1–9, 2019.
- [58] D. R. Brumley, M. Willcox, and J. E. Sader, “Oscillation of cylinders of rectangular cross section immersed in fluid,” *Physics of Fluids*, vol. 22, no. 5, pp. 1–15, 2010.
- [59] J. A. Schultz, S. M. Heinrich, F. Josse, I. Dufour, N. J. Nigro, L. A. Beardslee, and O. Brand, “Lateral-mode vibration of microcantilever-based sensors in viscous fluids using timoshenko beam theory,” *Journal of Microelectromechanical Systems*, vol. 24, no. 4, pp. 848–860, 2014.
- [60] N. Shen, D. Chakraborty, and J. E. Sader, “Resonant frequencies of cantilevered sheets under various clamping configurations immersed in fluid,” *Journal of Applied Physics*, vol. 120, no. 14, p. 144504, 2016.
- [61] N. Shen, D. Chakraborty, and J. E. Sader, “Frequency response of cantilevered plates of small aspect ratio immersed in viscous fluids,” *Journal of Applied Physics*, vol. 133, no. 3, p. 034501, 2023.
- [62] A. Maali, C. Hurth, R. Boisgard, C. Jai, T. Cohen-Bouhacina, and J. P. Aim, “Hydrodynamics of oscillating atomic force microscopy cantilevers in viscous fluids,” *Journal of Applied Physics*, vol. 97, no. 7, p. 074907, 2005.
- [63] A. T. Liem, A. B. Ari, C. Ti, M. J. Cops, J. G. McDaniel, and K. L. Ekinici, “Nanoflows induced by mems and nems: Limits of two-dimensional models,” *Physical Review Fluids*, vol. 6, no. 2, p. 024201, 2021.
- [64] A. L. Facci and M. Porfiri, “Analysis of three-dimensional effects in oscillating cantilevers immersed in viscous fluids,” *Journal of Fluids and Structures*, vol. 38, pp. 205–222, 2013.
- [65] J. N. Reddy, “Theory and Analysis of Elastic Plates and Shells,” 2007.
- [66] V. Ruiz-Díez, J. Hernando-García, T. Manzanique, M. Kucera, U. Schmid, and J. L. Sánchez-Rojas, “Modelling out-of-plane and in-plane resonant modes of microplates in liquid media,” *Journal of Micromechanics and Microengineering*, vol. 25, no. 7, p. 074005, 2015.
- [67] A. Ricci, G. Canavese, I. Ferrante, S. L. Marasso, and C. Ricciardi, “A finite element model for the frequency spectrum estimation of a resonating microplate in a microfluidic chamber,” *Microfluidics and Nanofluidics*, vol. 15, no. 2, pp. 275–284, 2013.
- [68] K. Takizawa and T. E. Tezduyar, “Multiscale space-time fluid-structure interaction techniques,” *Computational Mechanics*, vol. 48, no. 3, pp. 247–267, 2011.
- [69] R. J. Clarke, O. E. Jensen, and J. Billingham, “Three-dimensional elastohydrodynamics of a thin plate oscillating above a wall,” *Physical Review E - Statistical, Nonlinear, and Soft Matter Physics*, vol. 78, no. 5, pp. 1–17, 2008.
- [70] A. Gesing, D. Platz, and U. Schmid, “A numerical method to determine the displacement spectrum of micro-plates in viscous fluids,” *Computers & Structures*, vol. 260, p. 106716, 2022.

- [71] A. Gesing, D. Platz, and U. Schmid, “Viscous fluid-structure interaction of micro-resonators in the beam-plate transition,” *Journal of Applied Physics*, vol. 131, no. 13, p. 134502, 2022.
- [72] A. Gesing, T. Tran, D. Huber, D. Steinmüller-Nethl, G. Pfusterschmied, M. Schneider, D. Platz, and U. Schmid, “The gas-liquid-q-factor-inversion in mems plate resonators,” *Journal of Sound and Vibration*, vol. 559, p. 117777, 2023.
- [73] D. Kim, S. Hong, J. Jang, and J. Park, “Determination of fluid density and viscosity by analyzing flexural wave propagations on the vibrating micro-cantilever,” *Sensors*, vol. 17, no. 11, p. 2466, 2017.
- [74] M. A. Hopcroft, W. D. Nix, and T. W. Kenny, “What is the young’s modulus of silicon?,” *Journal of microelectromechanical systems*, vol. 19, no. 2, pp. 229–238, 2010.
- [75] B. J. Kirby, *Micro-and nanoscale fluid mechanics: transport in microfluidic devices*. Cambridge university press, 2010.
- [76] W.-M. Zhang, G. Meng, and X. Wei, “A review on slip models for gas microflows,” *Microfluidics and nanofluidics*, vol. 13, no. 6, pp. 845–882, 2012.
- [77] H. Brenner, “Beyond the no-slip boundary condition,” *Physical Review E*, vol. 84, no. 4, p. 046309, 2011.
- [78] G. Karniadakis, A. Beskok, and N. Aluru, *Microflows and nanoflows: fundamentals and simulation*, vol. 29. Springer Science & Business Media, 2006.
- [79] C. A. Van Eysden and J. E. Sader, “Small amplitude oscillations of a flexible thin blade in a viscous fluid: Exact analytical solution,” *Physics of Fluids*, vol. 18, no. 12, p. 123102, 2006.
- [80] M. D. Graham, *Microhydrodynamics, Brownian motion, and complex fluids*, vol. 58. Cambridge University Press, 2018.
- [81] T. J. Barth and D. Roose, *Finite Element Method Book*. Springer Science & Business Media, 10 ed., 2013.
- [82] G. Engel, K. Garikipati, T. J. Hughes, M. G. Larson, L. Mazzei, and R. L. Taylor, “Continuous/discontinuous finite element approximations of fourth-order elliptic problems in structural and continuum mechanics with applications to thin beams and plates, and strain gradient elasticity,” *Computer Methods in Applied Mechanics and Engineering*, vol. 191, no. 34, pp. 3669–3750, 2002.
- [83] G. N. Wells and N. T. Dung, “A C0 discontinuous Galerkin formulation for Kirchhoff plates,” *Computer Methods in Applied Mechanics and Engineering*, vol. 196, no. 35-36, pp. 3370–3380, 2007.
- [84] N. T. Dung and G. N. Wells, “A study of discontinuous Galerkin methods for thin bending problems,” *III European Conference on Computational Mechanics*, no. June, pp. 653–653, 2008.
- [85] D. Arnold, F. Brezzi, B. Cockburn, and L. D. Marini, “Unified analysis of Discontinuous Galerkin Method for elliptic problems,” *SIAM journal on numerical analysis*, vol. 39, no. 5, pp. 1749–1779, 2002.
- [86] A. Logg, L.-A. Mardak, and G. N. Wells, *Automated solution of differential equations by the finite element method: The FEniCS book*. Springer Science & Business Media, 84 ed., 2012.
- [87] F. Brezzi, G. Manzini, D. Marini, P. Pietra, and A. Russo, “Discontinuous Galerkin approximations for elliptic problems,” *Numerical Methods for Partial Differential Equations*, vol. 16, no. 4, pp. 365–378, 2000.
- [88] K. Larsson and M. G. Larson, “Continuous piecewise linear finite elements for the Kirchhoff-Love plate equation,” *Numerische Mathematik*, vol. 121, no. 1, pp. 65–97, 2012.
- [89] A. Embar, J. Dolbow, and I. Harari, “Imposing Dirichlet boundary conditions with Nitsche’s method and spline-based finite elements,” *International Journal for Numerical Methods in Engineering*, vol. 83, pp. 877–898, 2010.

- [90] F. Bassi and S. Rebay, “A High-Order Accurate Discontinuous Finite Element Method for the Numerical Solution of the Compressible Navier–Stokes Equations,” *Journal of Computational Physics*, vol. 131, no. 2, pp. 267–279, 1997.
- [91] K. B. Olgaard, A. Logg, and G. N. Wells, “Automated code generation for discontinuous galerkin methods,” *Society for Industrial and Applied Mathematics*, vol. 31, no. 2, pp. 849 – 864, 2007.
- [92] S. Fernández-Méndez and A. Huerta, “Imposing essential boundary conditions in mesh-free methods,” *Computer Methods in Applied Mechanics and Engineering*, vol. 193, no. 12-14, pp. 1257–1275, 2004.
- [93] C. Pozrikidis, “A singularity method for unsteady linearized flow,” *Physics of Fluids A*, vol. 1, no. 9, pp. 1508–1520, 1989.
- [94] C. Pozrikidis, *Boundary integral and singularity methods for linearized viscous flow*. Cambridge University Press, 1992.
- [95] E. O. Tuck, “Calculation of unsteady flows due to small motions of cylinders in a viscous fluid,” *Journal of Engineering Mathematics*, vol. 3, no. 1, pp. 29–44, 1969.
- [96] M. Abramowitz and I. A. Stegun, *Handbook of mathematical functions with formulas, graphs, and mathematical tables*, vol. 55. US Government printing office, 1948.
- [97] T. Sarpkaya, “On the parameter $\beta = re/kc = d^2/vt$,” *Journal of fluids and structures*, vol. 21, no. 4, pp. 435–440, 2005.
- [98] R. Kanwal, “Vibrations of an elliptic cylinder and a flat plate in a viscous fluid,” *ZAMM-Journal of Applied Mathematics and Mechanics/Zeitschrift für Angewandte Mathematik und Mechanik*, vol. 35, no. 1-2, pp. 17–22, 1955.
- [99] L. Ma, *Using superposition of undamped modes to model non-orthogonally damped systems*. PhD thesis, Massachusetts Institute of Technology, 2017.
- [100] L. Ma, T. L. Resvanis, and J. K. Vandiver, “The influence of mode dominance and traveling waves on flexible cylinder flow-induced vibration,” *Ocean Engineering*, vol. 264, p. 111750, 2022.
- [101] R. J. Clarke, O. E. Jensen, J. Billingham, and P. M. Williams, “Three-dimensional flow due to a microcantilever oscillating near a wall: An unsteady slender-body analysis,” *Proceedings of the Royal Society A: Mathematical, Physical and Engineering Sciences*, vol. 462, no. 2067, pp. 913–933, 2006.
- [102] L. Koens and E. Lauga, “The boundary integral formulation of stokes flows includes slender-body theory,” *Journal of Fluid Mechanics*, vol. 850, p. R1, 2018.
- [103] R. Cortez, L. Fauci, and A. Medovikov, “The method of regularized stokeslets in three dimensions: analysis, validation, and application to helical swimming,” *Physics of Fluids*, vol. 17, no. 3, p. 031504, 2005.
- [104] R. Cortez, “Regularized stokeslet segments,” *Journal of Computational Physics*, vol. 375, pp. 783–796, 2018.
- [105] V. Varanasi, M. Velten, T. Odatsu, A. Ilyas, S. Iqbal, and P. Aswath, “Surface modifications and surface characterization of biomaterials used in bone healing,” in *Materials for Bone Disorders*, pp. 405–452, Elsevier, 2017.
- [106] J. A. Hafner, *Ferroelectric polymer thin Films for MEMS applications: towards soft and high-speed AFM probes*. PhD thesis, TU Wien, 2021.
- [107] J. Hafner, D. Canena, D. Platz, M. Schneider, P. Hinterdorfer, and U. Schmid, “Scanning probes with high resonance frequency and low stiffness for high-speed afm applications in liquid environments,” in *8th Multifrequency AFM conference, Book of Abstracts*, p. 28, 2020.

- [108] E. Manconi and B. Mace, “Veering and strong coupling effects in structural dynamics,” *Journal of Vibration and Acoustics*, vol. 139, no. 2, p. 021009, 2017.
- [109] M. Asano, H. Yamaguchi, and H. Okamoto, “Free-access optomechanical liquid probes using a twin-microbottle resonator,” *Science Advances*, vol. 8, no. 44, p. eabq2502, 2022.
- [110] D. Demattio, “Simulation of Fluid-Structure Interactions in MEMS Resonators,” Master’s thesis, TU Wien, 2022.
- [111] M. Damircheli and B. Eslami, “Design of v-shaped cantilevers for enhanced multifrequency afm measurements,” *Beilstein Journal of Nanotechnology*, vol. 11, no. 1, pp. 1525–1541, 2020.
- [112] W. G. Dantas and A. Gusso, “Analysis of the chaotic dynamics of mems/nems doubly clamped beam resonators with two-sided electrodes,” *International Journal of Bifurcation and Chaos*, vol. 28, no. 10, p. 1850122, 2018.
- [113] M. Dorfmeister, M. Schneider, and U. Schmid, “Static and dynamic performance of bistable mems membranes,” *Sensors and Actuators A: Physical*, vol. 282, pp. 259–268, 2018.
- [114] T. van Opstal, E. van Brummelen, and G. van Zwieten, “A finite-element/boundary-element method for three-dimensional, large-displacement fluid–structure-interaction,” *Computer Methods in Applied Mechanics and Engineering*, vol. 284, pp. 637–663, 2015.
- [115] Y. Liu and N. Nishimura, “The fast multipole boundary element method for potential problems: a tutorial,” *Engineering Analysis with Boundary Elements*, vol. 30, no. 5, pp. 371–381, 2006.